ISSN:2538-516X

Journal of Civil Engineering Researchers

Volume: 7; Number: 2; June 2025

J-Researchers

J-Researchers

JOURNAL OF
CIVIL
ENGINEERING
RESEARCHERS

Volume 7, Number 2, June 2025

Contents

J-Researchers

Journal of Civil Engineering Researchers

Journal homepage: www.journals-researchers.com

The effect of Ash from Burning Industrial Waste on the Physical and Mechanical Properties of Ordinary Portland concrete

Mahdi Jalali,[a] Rasoul Shadnia,[b,*]

[a] *Department of Civil Engineering, Khayyam University of Mashhad, Mashhad, Iran*

[b] *Department of Civil Engineering, Hakim Sabzevari University, Sabzevar, Iran*

ABSTRACT

One of the ways to dispose of urban waste is to burn it in incinerators. In this research, it was tried to use the ash obtained from the waste incineration plant of Saveh city (Iran) as a substitute for part of the consumed cement in concrete production. To achieve this goal, the effects of waste ash on compressive strength, abrasion resistance, flexural strength, water absorption and unit weight of concrete were investigated using experimental methods. The concrete used was made with a compressive strength of 30 MPa. The results obtained from the laboratory tests showed that the addition of waste ash as a partial substitute of the cement in the amounts of 10, 20, and 30% in the tested concrete samples caused to decrease the compressive strength by 21, 42, and 49%, the flexural strength by 5, 15 and 22%, and the unit weight of concrete by 3, 5 and 7% respectively, and to increase the water absorption by 3, 6 and 12% respectively, compared to the control sample. Also, there is a slight decrease in the abrasion resistance of concrete including waste ash. However, the obtained strengths were still acceptable for the construction of concretes that require less strength. On the other hand, the use of this ash as a part of the cement used in concrete not only removes the concern of waste incineration plants to dispose of this pollution, but also reduces the consumption of cement and consequently reduces greenhouse gases caused by cement production.

ARTICLE INFO

Received: February 6, 2025
Accepted: March 1, 2025

Keywords:
Waste Ash
Compressive Strength
Flexural Strength
Abrasion Resistance
Ordinary Concrete

DOI: [10.61186/JCER.7.2.1](https://doi.org/10.61186/JCER.7.2.1)
DOR: 20.1001.1.2538516.2025.7.2.1.9

1. Introduction

Every year, thousands of tons of waste are produced from industries and cities, so the disposal of produced waste has become one of the main problems in developing countries. In other words, the increase in waste production has imposed huge costs on these countries. Also, the lack of landfills and high costs in this matter have increased the concern of many municipalities. All types of waste such as municipal, hospital, industrial waste and etc. are dangerous wastes that if get disposed improperly, will surely cause air, soil, surface and ground water pollution. One of the ways to prevent such pollution is to use waste incinerators.

On the other hand, concrete is the most widely used construction material in the world today [1-3]. The most polluting part of the concrete industry is the cement production process [4-7]. The annual consumption of natural resources for cement production is also significant

---

[*] Corresponding author. Tel.: +989000000000; e-mail: r.shadnia@hsu.ac.ir (R Shadnia).

[8-10]. In addition to the consumption of huge resources, a significant amount of air, water and soil pollution is also created due to cement production [11-14]. In addition to consuming large amounts of energy, this huge production of cement causes the release of large amounts of carbon dioxide gas [15-17]. Therefore, it is necessary to reduce the amount of cement used in concrete as much as possible.

One of these solutions can be replacing waste ash instead of part of the cement used in concrete. The main issue is that the concrete produced using ash obtained from waste burning has the required reliability and strengths and is economically justified. The effect of adding incinerated waste as a substitute for part of the aggregate on some characteristics of concrete has been investigated by different researchers [18-25].

The effect of incorporation of incinerated municipal waste materials as partial cement replacement in concrete has been also investigated in literature [26-32].

Different parameters such as the type, temperature and capacity of incinerator furnace as well as waste input can influence on the final compositions and as a result the characteristics of ashes obtained from burning industrial waste [32]. On the other hand, different compositions of ashes from such a complex combustion process with various reactions will result in different effects on the properties of concrete. Therefore, it seems to be necessary to investigate much further the effect of waste ash composition and its implications on the produced concrete. As an instance, the findings of Matos and Coutinho [26] indicate that the significant content of aluminum in the composition of waste ash may react with the alkaline media of cement paste and thus result in further pores and cracks in concrete because of hydrogen gas formation. Tyrer [29] stated that the existence of free aluminum in the composition of waste ash can disrupt the reactions of the cement paste due to the hydrolysis reactions at high pH.

Considering that the results obtained so far are exclusively related to the ashes used in those researches and it is possible that the wastes and the ashes obtained from their burning may have different compositions and so have different effects on the properties of produced concrete, in the current research the effect of replacing the different percentages of the ash obtained from industrial waste burned in Saveh Waste Technology Complex as a partial replacement of cement has been investigated on the physical and mechanical properties of ordinary concrete.

2. Specifications of Consumed Materials

The cement used in concrete is type 2 cement produced in the cement factory of Joveyn city with a relative specific gravity of 3.1 and a cement strength class (CSC) of 31.5 MPa. The water used is the drinking water of Sabzevar city, which has a suitable pH. The aggregates used in concrete, including sand and two types of gravel, were prepared from the construction materials of Rivand village, Sabzevar city, grading chart of which is shown in Figure 1. The ash needed to replace part of the cement was obtained from Saveh Waste Technology Complex. Due to the presence of some impurities in the ash to be used in concrete, the ash was passed through an 18 grade (1 mm) sieve before being used in concrete. Table 1 shows the components of waste ash obtained from the XRD test.

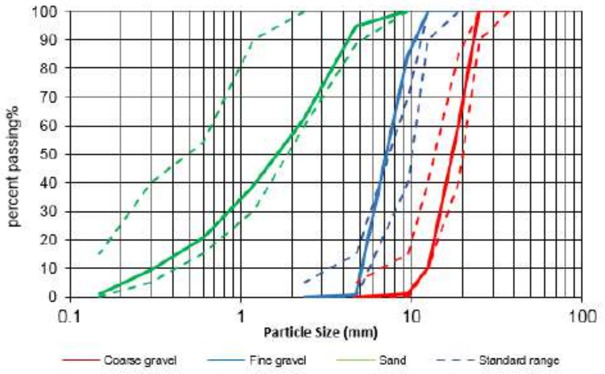

Figure 1. Particle size distribution curves

Table 1:
Chemical composition of waste ash

Chemical Analysis	*Sodium-Calcium-Aluminium (Na-Ca-Al)*	*Carbon disulfide (CS_2)*	*Carbon (C)*
(%)	*28*	*17*	*55*

3. Concrete Mixture Design

Concrete samples were made based on Iran's National Concrete Mixing Plant, Publication 479 [33]. After preparing the construction materials and mixing them for 5 minutes, a standard cube mold of 150 x 150 x 150 mm was used to make the samples. Also, the compaction of fresh concrete was done using a standard rod in three layers and each layer with 25 hits. Grading has been modified based on the regulations of Iran's National Mixing Plant and the modified grading chart is shown in Figure 2. All the samples were removed from the mold after 24 hours and placed in the lime water pool with a temperature of 25°C. The specifications of the tested samples are presented in Table 2. In all designs, all the conditions (cement type, water to cement ratio, granulation type, etc.) have been kept constant and only the amount of ash replacement has been changed.

Water to cement ratio (w/c): Using the Iran's National Mixing Plant Regulations and considering the compressive strength assumed in this research (equal to 30 MPa) for normal concrete (without ash) and also the standard deviation equal to 10.5 (obtained according to section 2-3-

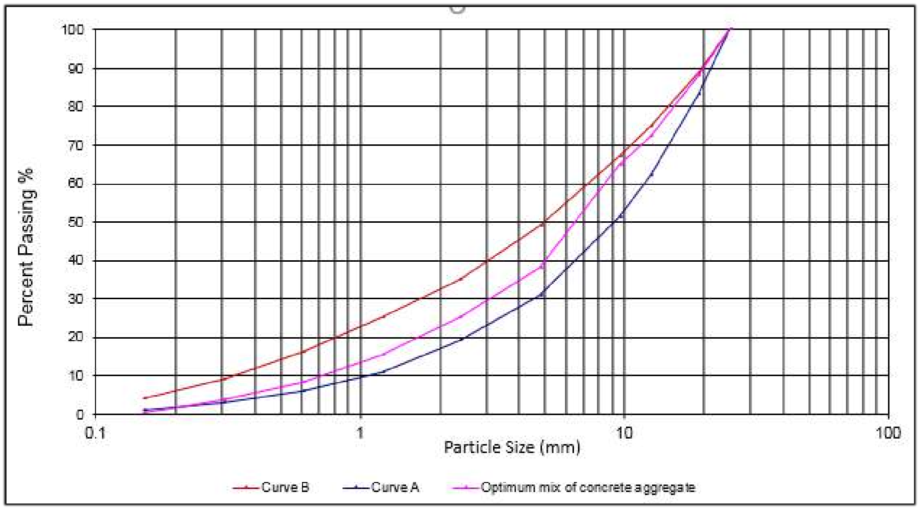

Figure 2: Modified granulation diagram

Table 2

concrete mixture design (For 1 m^3 of concrete)

Specimen Name	Ash (%)	Ash (kg/m^3)	Water (kg/m^3)	Cement (kg/m^3)	Coarse Gravel (kg/m^3)	Fine Gravel (kg/m^3)	Sand (kg/m^3)
A28	0	0	173	402.0	563	526	726
B28	10	40.2	173	361.8	563	526	726
C28	20	80.4	173	321.6	563	526	726
D28	30	120.6	173	281.4	563	526	726

-2, table 3-3 of the aforementioned regulations) and also consumed cement with CSC of 32.5 (the CSC of Portland cement type II is 31.5, which according to the regulations of the Iran's National mixing plant, it can be considered 32.5 when using the mentioned diagram) and finally, due to the angular aggregates, the ratio of water to cement was determined as 0.43.

4. Results and discussion

4.1. Compressive strength

The compressive strength of the samples was measured using a compressive test jack (Figure 3). These tests have been determined based on ASTM C39. In the compressive strength tests, the samples reach the ultimate strength by applying axial compressive force at a certain speed. The compressive strength has been then obtained by dividing the maximum force supported by the sample by the cross-sectional area of the sample.

Looking at the previous studies shows that the incorporation of waste ash as the partial replacement of cement might be successful, up to 30% of the binder mass (Kumar and Chandak (0-30%) [30], Kim et al. (0-30%) [34]). Some other researchers have even tested only one replacement level of waste ash (Tang et al. (30%) [35], Caprai et al. (25%) [28] and Alderete et al. (20%) [27]). Therefore, in the current research, in order to investigate the effect of waste ash on the compressive strength of ordinary concrete, the samples have been made with different percentages of waste ash, including 0 (as a control sample), 10, 20, and 30 percent ash as a substitute for cement. The number of samples for each replacement percentage was 3, and the average compressive strength of these three samples was reported as the corresponding concrete compressive strength.

Figure 3. Compressive strength measuring device

Figure 4 shows the compressive strength results of 7, 14, and 28-day concrete samples with zero, 10, 20, and 30 percent of ash replaced with cement. It can be seen carefully in the graph that the increase in the amount of ash causes a decrease in the compressive strength of concrete, and this decrease for 28-day samples (compared to the control sample without ash) for 10, 20 and 30% ash is 21%, 42% and 49% respectively. It is worth noting that despite the decrease in compressive strength with the increase of waste ash, the produced concrete can still be used to make concrete that needs less compressive strength, such as filler concrete or light concrete in building floors. The results also indicate that the effect of curing time on the compressive strength of the samples made with 20 and 30% ash is less compared to the other two types of samples.

Figure 5 shows the curvature created on the surface of different concrete samples. It can be seen carefully in the figure that there is no curvature in the concrete sample without ash. In other words, it can be seen that the amount of curvature increases in concrete samples including ash, which indicates an increase in concrete volume after initial setting probably due to the undesirable increase of Al (Table 1) by adding ash in concrete [30].

The existence of Al in waste ash can produce H2 (hydrogen gas) as described by the chemical reaction (1) [24, 25]. The hydrogen gas can be entrapped within the concrete and so can cause cracking of concrete and eventually reduce the strength [30, 31]:

$$2Al + 4OH + 2H_2O \rightarrow 2Al(OH)_3 + H_2 \uparrow \quad (1)$$

During the construction of concrete samples with ash compared to the control samples, some fat stains were observed in the concrete; The presence of these fat elements might be another reason for the reduction of compressive strength in concrete samples containing ash. Considering the increase in volume observed in concrete with the increase in the amount of replaced ash, perhaps this ash can be used in making concrete to fill cracks and repair concrete surfaces that do not need high strength.

It can also be seen from Figure 5 that the ash has an effect on the color of fresh concrete and as the amount of ash increases, the color of concrete becomes darker. But during drying, the color difference is reduced and almost all of them are close to the color of the control sample.

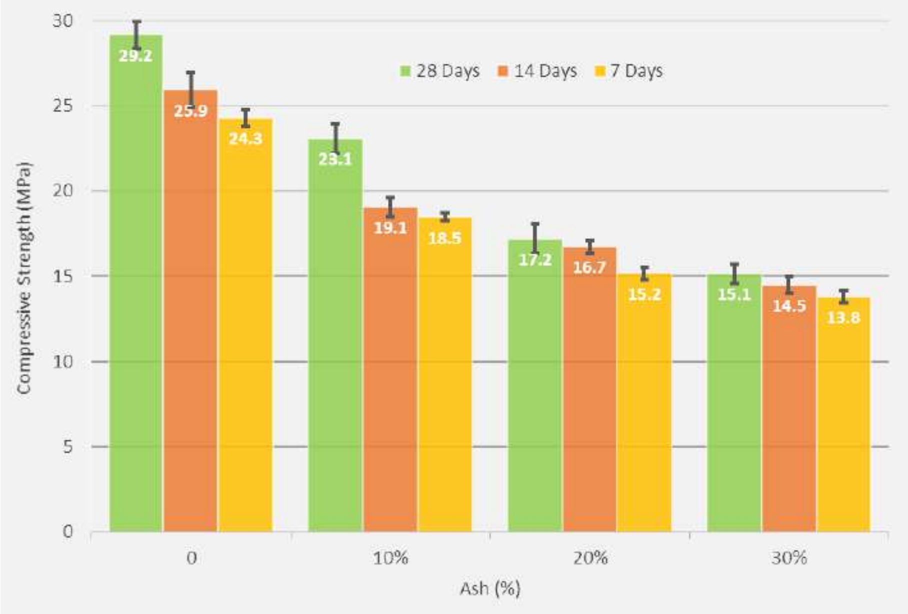

Figure 4. Compressive strength of concrete samples

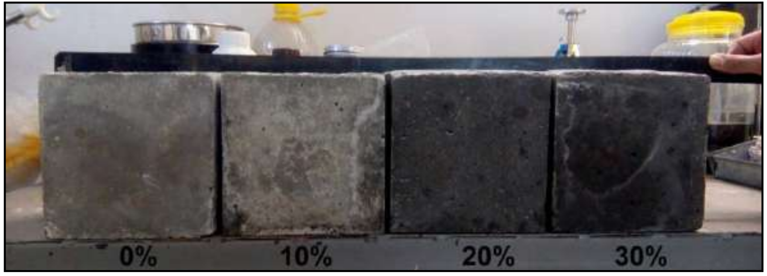

Figure 5. The curvature created on the concrete surface

4.2. Abrasion resistance

In this research, testing the abrasion resistance of concrete on 75x150x150 mm cube samples using the wide wheel abrasion test according to Iranian National Standardization Organization, INSO 12728 (Appendix C, Abrasion resistance measurement) [36] (taken from the European Standards, EN 1340 [37]) related to requirements and tests of concrete kerb units has been carried out. The grinding machine as shown in Figure 6 consists of a wide grinding wheel, a storage hopper with one or two control valves to regulate the output abrasive, a flow guide hopper, a clamped moving table or plate, and a weight. If two control valves are used, one of them should be used to adjust the flow rate and the other valve to turn off and on the flow.

Figure 6. Abrasion resistance testing device

The wide grinding wheel must be made of a steel conforming to EN 10083-2 with a hardness between HB 203 and HB 245. The diameter of the wheel should be (200±1) mm and its width (70±1) mm. The wheel must rotate 75 times in (3±60) seconds. In order to make the groove created on the samples easier to see, the samples were spray painted before testing as shown in Figure 7.

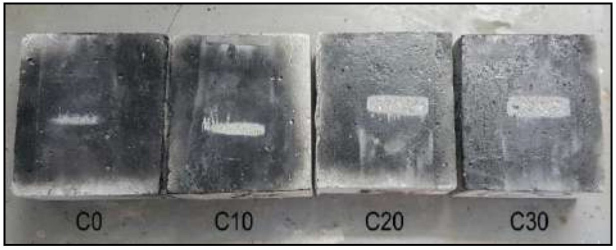

Figure 7. Preparing the sample to perform the abrasion resistance test

In order to choose the best amount of waste ash consumption, concrete samples with 0% ash as control samples and 10, 20, and 30% ash substitute for cement were examined for 30 MPa compressive strength with 50-90 mm slump. Abrasion resistance of the samples was measured after 28 days of curing using an abrasion resistance measuring device and measuring the groove created on the sample. The results obtained for each of the ash percentages are the average of three values obtained from three test samples.

4.2.1. Measurement of created groove

After creating the groove by the wide wheel machine, first, using a pencil, the outer boundary of the groove was marked and a line was drawn (l1 and l2 as shown in Figure 8). Then the line AB, from the middle of the created groove, was drawn perpendicular to the middle line. At the end, a caliper was placed on points A and B on the inner edge of the length of l1 and l2 of the groove, and measurements were made and recorded with an approximation of ±1 mm.

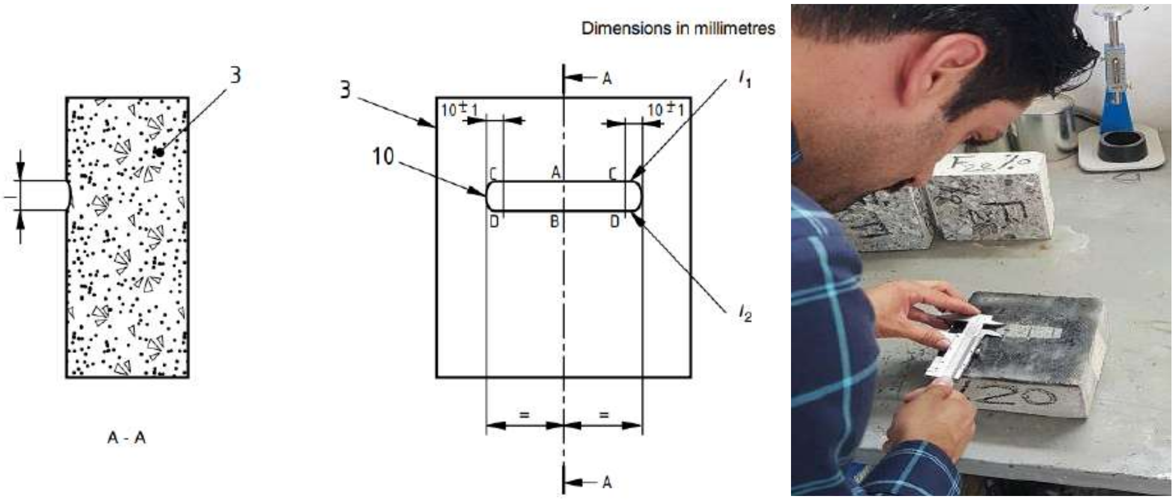

Figure 8. Groove measurement of samples

Table 3.
Size of grooves obtained from wear resistance

Specimen Name	Ash (%)	AB (mm)	CD1 (mm)	CD2 (mm)	Δ	Calibration factor	Final dimension (mm)
C0	0	8.8	8.2	7.3	8.1	11.9	20.5
C10	10	12.4	11.6	10.8	11.6	8.4	21
C20	20	17.9	17.1	16.3	17.1	2.9	21
C30	30	21.3	20.3	19.5	20.4	-0.4	21

In order to calibrate the created groove, measurements were recorded at a distance of (10±1) mm from each end of the groove (C and D) to obtain three results. The calibration value (Δ) is equal to the average of three measured values and is obtained from equation (1). The test result, which is the corrected dimension after applying calibration factor, is calculated from equation (2) and is reported after rounding with approximately 0.5 mm. It is worth mentioning that if two grooves are created in one test, the larger value should be reported as the desired result. The calibration factor according to equation (3) is the arithmetic difference between 20.0 and the recorded calibration value (Δ).

$$\Delta = \frac{(AB + CD_1 + CD_2)}{3} \quad (1)$$

$$\text{Corrected dimension} = AB + (20.0 - \Delta) \quad (2)$$

$$\text{Calibration factor} = 20.0 - \Delta \quad (3)$$

Table 3 and Figure 9 show the final dimension (corrected dimension) of the grooves resulting from the abrasion resistance test. According to the results obtained from the test and the grooves created on the samples with different percentages of waste ashes, it can be seen that with the increase in the amount of ash, the dimensions of the grooves created due to wear on the samples have slightly increased, which indicates a very little decrease in wear resistance with adding waste ash to concrete. Table 4 shows the requirements for abrasion resistance of concrete kerb units according to EN 1340 [37]. It is worth noting that the abrasion resistance of all concrete samples containing waste ash is in the H category (class 3) which is acceptable based on EN 1340.

4.3. Flexural

In concrete structures, the absence of cracks is an important factor in maintaining the stability of the structure due to the protection of steel rebars against corrosion. Since applying axial tensile force to concrete samples is a difficult task, the tensile strength of concrete is determined by indirect methods such as flexural and Brazilian (cracking) tests. These methods lead to strengths that are higher than the actual strength under axial tensile load. In the flexural test, the rupture modulus is the maximum theoretical tensile stress that occurs in the lower strands of the tested beam. The purpose of this test is to determine the flexural strength based on the ASTM C78, which was performed on prismatic samples of 50 x 10 x 10 cm by the flexural strength determination device (Figure 10) at a speed of 0.5 min/mm.

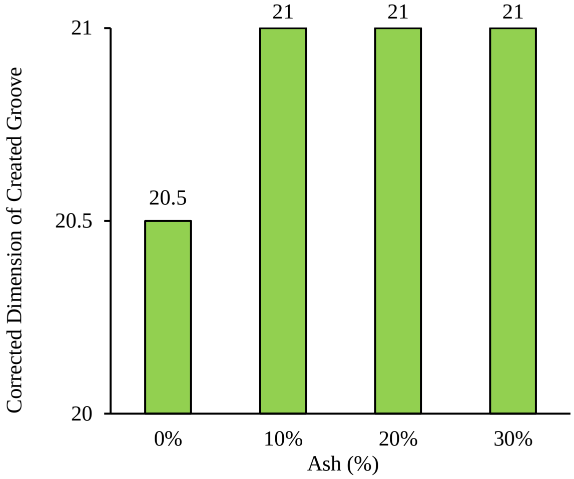

Figure 9. Abrasion resistance test results

Table 4.
Abrasion resistance classes [37]

Class	Maximum abrasion (mm) (wide wheel test)	Marking
1	No performance measured	F
3	≤ 23	H
4	≤ 20	I

Figure 10. Flexural strength testing device

If the crack is created outside the distance between two loads, provided that the distance to the loading point does not exceed 5% of the length of the sample, the flexural strength of the sample is obtained from equation (4).

$$f_b = \frac{\mathrm{My}}{\mathrm{I}} = \frac{3Pa}{d^3} \qquad (4)$$

where f_b is the rupture modulus of the section, M is the second moment of area, y is the maximum distance to the neutral beam, I is the second moment of area around the neutral axis, P is the maximum applied force, a is the distance between the cracked section and the nearest support (this distance is measured along the longitudinal axis of the bottom surface of the sample) and d is the height of the beam. It is reminded that if the crack is outside the distance between two loading points and the distance to the loading point is more than 5% of the length of the sample, the test must be repeated. ASTM allows rupture to occur outside the middle third of the beam at a distance of $a < 1/3$ from the nearest support.

Figure 11 shows the results of flexural strength of concrete samples with different percentages of waste ash. The results indicate that the addition of waste ash as a partial replacement of cement in the amount of 10, 20 and 30% in the tested concrete samples reduces the flexural strength by 5, 15 and 22% respectively compared to the control sample. The reason for the decrease in flexural strength can be related to the less cohesion of waste ash compared to cement and also the creation of more pores in concrete.

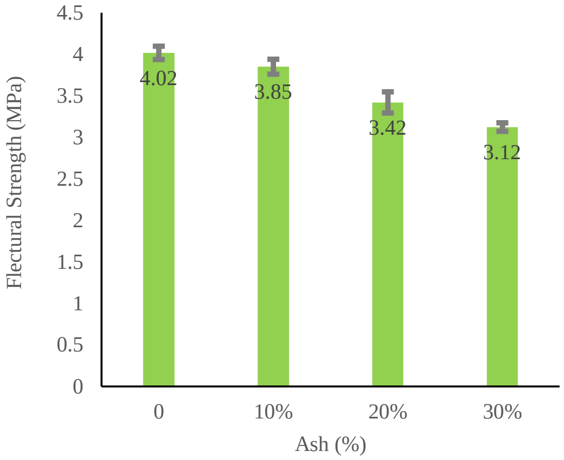

Figure 11. Flexural strength test results

4.4. Water absorption test

The purpose of this test is to determine the amount of water absorption based on to Iranian National Standardization Organization, INSO 12728 [36] (derived from the European Standards, EN 1340 [37]) related to the requirements and tests of concrete kerb units. The samples were immersed in a container containing drinking water with a temperature of 20+5 °C until it reached a constant mass (M1); Then the samples were placed at a distance of at least 15 mm from each other so that at least 20 mm of water was placed on the samples. The samples must be in water for at least 72 hours, and when the difference in mass of the samples after weighing 2 times within 24 hours is less than 0.1%, it means that the samples have reached constant mass.

Before each weighing, the samples were dried with a damp cloth so that their surface did not shine. Then, the samples were placed in a oven for at least 72 hours at a temperature of 105 ± 5 °C, so that there was a distance of at least 15 mm between them, and they were dried until they reached a constant mass. Before weighing the dried samples, they should be cooled in the laboratory environment. The water absorption percentage of the samples was calculated using equation (5):

$$W_a = \frac{(M_1 - M_2)}{M_2} \times 100 \qquad (5)$$

In which W_a is the water absorption percentage of each sample, M1 is the mass of the saturated sample in grams, and M2 is the mass of the dry sample in grams.

As can be seen in Figure 12, adding waste ash by 10, 20 and 30% increases the water absorption of concrete by 3, 6 and 12%, respectively, compared to the control sample

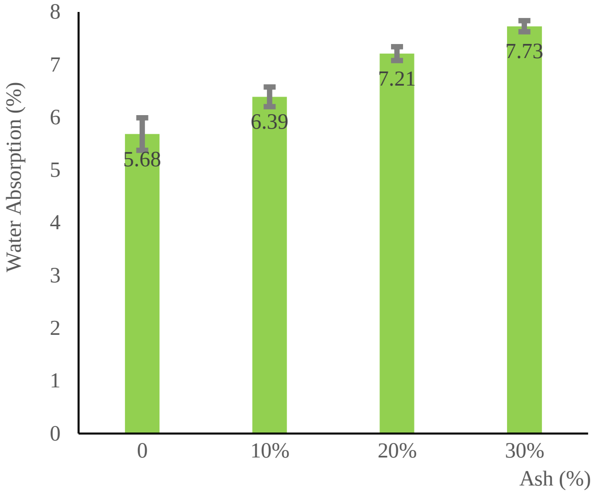

Figure 12. Water absorption test results

4.5. Unit weight test

This test is performed according to ASTM C138. The minimum volume of the container for the maximum nominal size of the aggregate of 25 mm, is about 5.5 liters, and for the maximum nominal size of 38 mm is about 11 liters. The volume of the container should be obtained by filling the container with distilled water and weighing it carefully. The upper level should be adjusted by placing a glass on top of the container (cup) so that it does not remain empty or has excess water. By controlling the temperature of distilled water and having the density of distilled water at this temperature, the volume of distilled water inside the container and as a result the volume of the container is obtained.

Concrete should be poured in standard forms in three layers with approximately equal height and compacted with a rod or vibrator. 25 hits are made in each layer. After each layer is compacted, the body of the mold containing concrete is hit 10 to 15 times with a rubber hammer or other suitable device, and then the next layer is compacted. Each layer is compacted by hitting the rod in such a way that about 25 mm descends in the bottom layer. The concrete of the last layer should be poured in such a way that after compaction, there is no shortage of concrete, and the excess concrete is removed with a sharp ruler and the said surface is smoothed. Additional concrete should not exceed 5 mm. As can be easily seen in Figure 13, the results indicate a decrease in unit weight with an increase in the amount of waste ash due to the creation of more pores in concrete including ash. This decrease in unit weight for adding waste ash to the amount of 10, 20 and 30% is equal to 3, 5 and 7%, respectively, compared to the control sample.

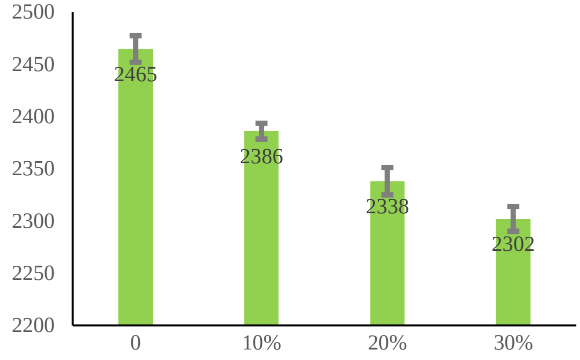

Figure 13. The results of the concrete unit weight test

5. Conclusion

Based on the laboratory results obtained from the present research, the following can be concluded:

- Based on the tests, it was found that the addition of waste ash as a partial replacement of the cement in the amount of 10, 20 and 30% in the tested concrete samples reduces the compressive strength by 21, 42 and 49%, reduces the flexural strength by 5, 15 and 22%, increases the water absorption by 3, 6 and 12% and reduces the unit weight by 3, 5 and 7%, respectively compared to the control sample and also a slight decrease in abrasion resistance in concrete.
- Despite the decrease in strength with the increase of waste ash, the produced concrete can still be used to make concrete that needs less strength, such as filler concrete or light concrete in building floors.
- Due to the increase in the volume of concrete with the increase in the amount of replaced ash, perhaps this ash can be used in making concrete to fill cracks and repair concrete surfaces that do not need much strength.
- It is also useful to remember that considering that the results obtained are exclusively related to the available ash and the methods used in this laboratory research and it is possible that each time the waste is burned, it has different compositions and have different effects on the results, so in order to express a more definite and accurate opinion, a wider laboratory program will be needed.

The suggestions for future research could include as:

1. Focus on Investigating the durability (such as thawing and freezing, shrinkage, creep, corrosion, and chloride infiltration of concrete) of concrete made with waste ash (from burning industrial waste).
2. Investigating the methods for improving the properties of concrete made with waste ash, such as increasing the strength and durability (for example, by adding pozzolans or suitable additives).

Acknowledgement

The Laboratory of Concrete Research Center of Hakim Sabzevari University and the respected officials of this university are grateful for providing the equipment and the possibility of using it.

References

[1] Naik, Tarun R. “Sustainability of Concrete Construction.” Practice Periodical on Structural Design and Construction 13.2 (2008): 98–103. DOI: https://doi.org/10.1061/(ASCE)1084-0680(2008)13:2(98)

[2] Barcelo, Lluís, et al. “Cement and Carbon Emissions.” Materials and Structures 47.6 (2014): 1055–1065. DOI: https://doi.org/10.1617/s11527-013-0119-5

[3] Bendapudi, S. C. K., and P. Saha. “Contribution of Fly Ash to the Properties of Mortar and Concrete.” International Journal of Earth Sciences and Engineering 4.6 (2011): 1017–1023.

[4] Van Oss, Hendrik G., and Anne C. Padovani. “Cement Manufacture and the Environment Part II: Environmental Challenges and Opportunities.” Journal of Industrial Ecology 7.1 (2003): 93–126. DOI: https://doi.org/10.1162/108819803766729212

[5] Felix, Eduardo F., and Emerson Possan. “Balance Emissions and CO_2 Uptake in Concrete Structures: Simulation Based on the Cement Content and Type.” Revista IBRACON de Estruturas e Materiais 11 (2018): 135–162. DOI: https://doi.org/10.1590/S1983-41952018000100006

[6] Mishra, Umesh C., et al. “A Systematic Review on the Impact of Cement Industries on the Natural Environment.” Environmental Science and Pollution Research 29.13 (2022): 18440–18451. DOI: https://doi.org/10.1007/s11356-021-17379-7

[7] Dunuweera, S. P., and R. M. G. Rajapakse. “Cement Types, Composition, Uses and Advantages of Nanocement, Environmental Impact on Cement Production, and Possible Solutions.” Advances in Materials Science and Engineering (2018): Article ID 4158682. DOI: https://doi.org/10.1155/2018/4158682

[8] Lim, Chanwoo, et al. “Global Trend of Cement Production and Utilization of Circular Resources.” Journal of Energy Engineering 2.3 (2020): 57–63.

[9] Schneider, M., et al. “Sustainable Cement Production—Present and Future.” Cement and Concrete Research 41.7 (2011): 642–650. DOI: https://doi.org/10.1016/j.cemconres.2011.03.019

[10] Mohamad, Noridah, et al. “Environmental Impact of Cement Production and Solutions: A Review.” Materials Today: Proceedings 48 (2022): 741–746. DOI: https://doi.org/10.1016/j.matpr.2021.04.192

[11] Al-Taai, S. H. H. “Soil Pollution-Causes and Effects.” IOP Conference Series: Earth and Environmental Science 790.1 (2021): 012009. DOI: https://doi.org/10.1088/1755-1315/790/1/012009

[12] Aprianti, E. “A Huge Number of Artificial Waste Material Can Be Supplementary Cementitious Material (SCM) for Concrete Production – A Review Part II.” Journal of Cleaner Production 142 (2017): 4178–4194. DOI: https://doi.org/10.1016/j.jclepro.2016.11.153

[13] Shah, S. N. “Impact of Industrial Pollution on Our Society.” Pakistan Journal of Science 73.1 (2021).

[14] Jadoon, S., et al. “Soil Pollution by the Cement Industry in the Bazian Vicinity, Kurdistan Region.” Journal of Environmental & Analytical Toxicology 6 (2016): 1000413. DOI: https://doi.org/10.4172/2161-0525.1000413

[15] Kramer, David. “Negative Carbon Dioxide Emissions.” Physics Today 73.1 (2020): 44–51. DOI: https://doi.org/10.1063/PT.3.4394

[16] Martens, J. A., et al. “The Chemical Route to a Carbon Dioxide Neutral World.” ChemSusChem 10.6 (2017): 1039–1055. DOI: https://doi.org/10.1002/cssc.201601546

[17] Hunt, A. J., et al. “Generation, Capture, and Utilization of Industrial Carbon Dioxide.” ChemSusChem 3.3 (2010): 306–322. DOI: https://doi.org/10.1002/cssc.200900169

[18] Aggarwal, Y., and R. Siddique. “Microstructure and Properties of Concrete Using Bottom Ash and Waste Foundry Sand as Partial Replacement of Fine Aggregates.” Construction and Building Materials 54 (2014): 210–223. DOI: https://doi.org/10.1016/j.conbuildmat.2013.12.067

[19] Pavlík, Z., et al. “Environmental Friendly Concrete Production Using Municipal Solid Waste Incineration Materials.” WIT Transactions on Ecology and the Environment 148 (2011): 325–334. DOI: https://doi.org/10.2495/SDP110271

[20] Keppert, M., et al. “Properties of Concrete with Municipal Solid Waste Incinerator Bottom Ash.” International Proceedings of Computer Science and Information Technology 28 (2012): 127–131.

[21] Park, J. S., et al. “Solidification and Recycling of Incinerator Bottom Ash through the Addition of Colloidal Silica (SiO_2) Solution.” Waste Management 27.9 (2007): 1207–1212. DOI: https://doi.org/10.1016/j.wasman.2006.08.002

[22] Liu, J., et al. “Novel Recycling Application of High Volume Municipal Solid Waste Incineration Bottom Ash (MSWIBA) into Sustainable Concrete.” Science of the Total Environment 838 (2022): 156124. DOI: https://doi.org/10.1016/j.scitotenv.2022.156124

[23] Shen, P., et al. “Utilization of Municipal Solid Waste Incineration Bottom Ash (IBA) Aggregates in High-Strength Pervious Concrete.” Resources, Conservation and Recycling 174 (2021): 105736. DOI: https://doi.org/10.1016/j.resconrec.2021.105736

[24] Müller, U., and K. Rübner. “The Microstructure of Concrete Made with Municipal Waste Incinerator Bottom Ash as an Aggregate Component.” Cement and Concrete Research 36.8 (2006): 1434–1443. DOI: https://doi.org/10.1016/j.cemconres.2006.03.020

[25] Sorlini, S., et al. “Recovery of MSWI and Soil Washing Residues as Concrete Aggregates.” Waste Management 31.2 (2011): 289–297. DOI: https://doi.org/10.1016/j.wasman.2010.09.001

[26] Matos, A. M., and J. Sousa-Coutinho. “Municipal Solid Waste Incineration Bottom Ash Recycling in Concrete: Preliminary Approach with Oporto Wastes.” Construction and Building Materials 323 (2022): 126548. DOI: https://doi.org/10.1016/j.conbuildmat.2022.126548

[27] Alderete, N. M., et al. “Effective and Sustainable Use of Municipal Solid Waste Incineration Bottom Ash in Concrete Regarding Strength and Durability.” Resources, Conservation and Recycling 167 (2021): 105356. DOI: https://doi.org/10.1016/j.resconrec.2020.105356

[28] Caprai, V., et al. “Evaluation of the Influence of Mechanical Activation on Physical and Chemical Properties of Municipal Solid Waste Incineration Sludge.” Journal of Environmental Management 216 (2018): 133–144. DOI: https://doi.org/10.1016/j.jenvman.2017.04.083

[29] Tyrer, M. “Municipal Solid Waste Incinerator (MSWI) Concrete.” Eco-Efficient Concrete, Woodhead Publishing, 2013: 273–310.

[30] Gupta, A. K., and R. Chandak. “Effect on Compressive Strength of Concrete with Partial Replacement of Cement by Municipal Solid Waste Incinerator Ash.” International Research Journal of Engineering and Technology (IRJET) 4.2 (2017): 1972–1976.

[31] Bertolini, L., et al. “MSWI Ashes as Mineral Additions in Concrete.” Cement and Concrete Research 34.10 (2004): 1899–1906. DOI: https://doi.org/10.1016/j.cemconres.2004.02.005

[32] Chang, F. Y., and M. Y. Wey. “Comparison of the Characteristics of Bottom and Fly Ashes Generated from Various Incineration Processes.” Journal of Hazardous Materials 138.3 (2006): 594–603. DOI: https://doi.org/10.1016/j.jhazmat.2006.05.088

[33] Ministry of Housing and Urban Development, Building and Housing Research Center. National Method of Concrete Mix Plan. Iran; Publication No. Z-479, 2016.

[34] Kim, H. K., et al. “Flow, Water Absorption, and Mechanical Characteristics of Normal- and High-Strength Mortar Incorporating Fine Bottom Ash Aggregates.” Construction and Building Materials 26.1 (2012): 249–256. DOI: https://doi.org/10.1016/j.conbuildmat.2011.06.054

[35] Tang, P., et al. “The Investigation of the MSWI Bottom Ash Fines (0–2 mm) as Binder Substitute after Combined Treatments.” EurAsia Waste Management Symposium, 28–30 April 2014: 126–130.

[36] Iranian National Standardization Organization. Concrete Kerb Units – Specifications and Test Methods, INSO 12728, 2013.

[37] European Standards. Concrete Kerb Units. Requirements and Test Methods, EN 1340:2003.

Journal of Civil Engineering Researchers

Journal homepage: www.journals-researchers.com

Numerical Investigation of the Parameters Influencing Site Effects

Sadegh Rezaei,[a] Majid Moradi,[a] Ali Hasanzadeh[b,*]

[a] Department of Civil Engineering, University of Science and Technology of Mazandaran, Behshahr, P. O. BOX 48518-78195, Iran

[b] Department of Civil Engineeing, Babol Noshirvani University of Technology, Babol, P. O. BOX 484, Iran

ABSTRACT

One of the most important topics in geotechnical earthquake engineering is the examination of site effects. This phenomenon alters the characteristics of seismic waves, leading to amplified vibrations and consequently increasing financial and human losses. Today, various methods exist for assessing site effects, among which numerical methods are among the most widely used due to their reasonable costs, reduced time, and high accuracy. In this research, a problem was subjected to the effects of three different earthquakes (Bam, Naghan, and Tabas). By comparing the results of each earthquake, the site effects were identified in terms of changes in peak gorund acceleration (PGA), frequency content, and shaking duration. Additionally, to investigate the effects of soil layering, the position of the layers was altered, revealing significant impacts of layer changes on seismic wave characteristics. Finally, to assess the effect of earthquake source type, one earthquake was evaluated at two different stations (near/far field). Results indicated a significant influence of the epicentral distance on the amplification and attenuation of waves.

ARTICLE INFO

Received: February 27, 2025
Accepted: April 1, 2025

Keywords:
Site Effect
PGA
Frequency Content
Soil Layering
Epicentral Distance

DOI: 10.61186/JCER.7.1.10
DOR: 20.1001.1.2538516.2025.7.2.2.0

1. Introduction

The dynamic characteristic of a motion at a point on the ground surface in the frequency domain is expressed as follows:

$$Q(f) = F(f).T(f).S(f) \qquad (1)$$

where $Q(f)$ is the Fourier spectrum of motion at a point on the ground surface. $Q(f)$ is a function of the wave source $F(f)$, the path of propagation $T(f)$, and the dynamic characteristics of the layers near the surface of the ground beneath the point of interest, or site effects $S(f)$. These factors collectively and independently influence how the ground responds. Numerous studies have shown that among the three factors, site effects $S(f)$ have the most significant impact on the propagation of waves [1-6].

Site effects refer to the change in the nature of seismic waves, which leads to the amplification of input movements from the bedrock and intensification of damages. Examination of past earthquakes has shown that local geotechnical conditions have a profound impact on the distribution of damages in residential areas and vital lifelines. Previous research has indicated that during an

---

[*] Corresponding author. Tel.: +989113120260; e-mail: a_hasanzade64@yahoo.com.

earthquake, the soil acts like a filter, altering the motion characteristics of the ground during the event. The intensity of strong ground motion depends on several factors such as earthquake magnitude, distance to the surface, seismic source characteristics, soil layering, surface topography, and local soil conditions. Among these factors, local geotechnics and soil layering are the most significant determinants of site response variations at any specific location [7-12].

MacMurdo stated in 1824 that during the 1819 earthquake in Cutch, India, buildings founded on rock were not as affected as buildings whose foundations did not reach the bottom of the soil layer. Mallet, in his 1862 report on the 1857 Neapolitan earthquake, referred to the effects of local geological conditions on earthquake damage. Wood in 1908 and Reid in 1910 showed that the intensity of ground shaking in the San Francisco earthquake was related to local soil and geological conditions. Since these early observations, the effects of local site conditions on ground motions have been described in earthquakes around the world [13].

There are various methods for estimating site effects. The best method is to record ground motion generated by a large earthquake. However, in areas where this phenomenon is not very frequent, such an assessment is not possible, making this method less practical for site effect analysis [11-13].

The importance of selecting appropriate methods for evaluating site effects is evident. There are two general methods for estimating site response: a) Theoretical and numerical methods, b) Operational methods [11-13]. One of these methods or a combination of both should be selected for optimal research advancement, depending on the project's significance, the sensitivity of the subject, and the available budget.

2. Research objective

In this research, in order to investigate site effects as well as the influences of soil type, layering, and earthquake source, a comprehensive set of analyses was conducted using the finite element method. By applying different earthquakes, changing the layer configurations, and varying the epicentral distances, multiple analyses were performed. Fig. 1 shows different layering of the study.

First, appropriate parameters for each of the layers were obtained using credible references, and then modeling and analysis were carried out using the finite element method. Finally, the accelerograms at points A, B, and C were determined and analyzed. It is worth mentioning that the location of earthquake application was at the interface between bedrock and soil, with the applied earthquakes being those of Bam, Tabas, and Naghan. Fig. 2 illustrates the accelerograms of the aforementioned earthquakes.

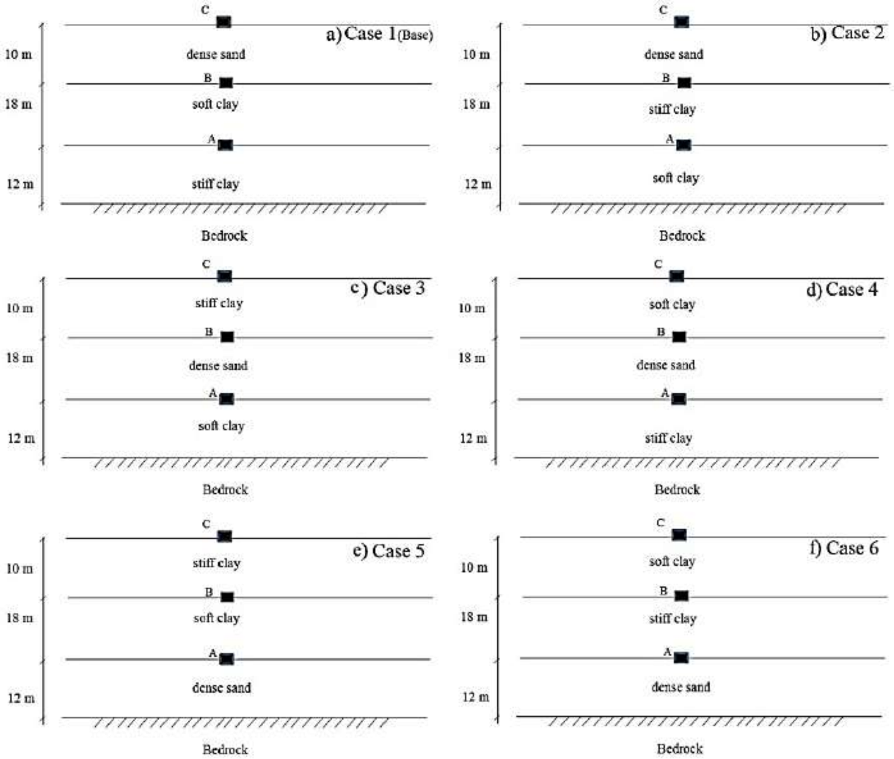

Fig.1 Layering of the study a) Case 1 (Base) b) Case 2 c) Case 3 d) Case 4 e) Case 5 f) Case 6

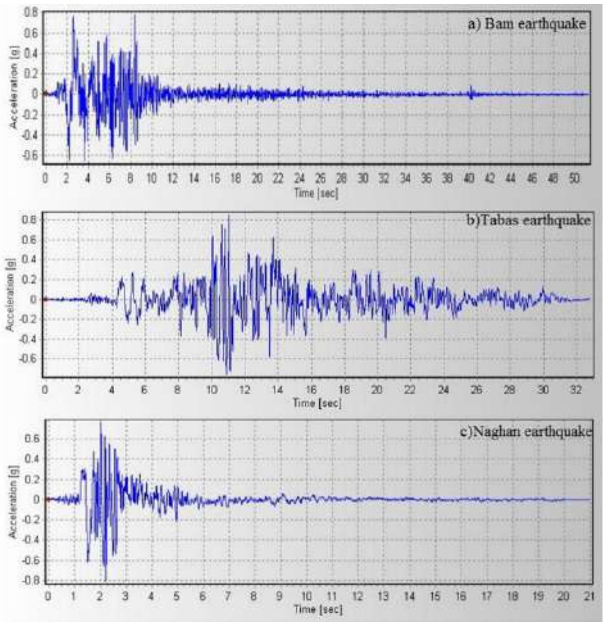

Fig. 2 The accelerograms of the a) Bam b) Tabas c) Naghan earthquakes

3. Applied earthquakes in the research

3.1. Bam earthquake

The Bam earthquake occurred on December 26, 2003 in the historical city of Bam, located in the southeastern part of Iran country, Kerman province. Official casualty statistics reported over 25,000 deaths and approximately 50,000 injuries, with many people left homeless. The epicenter of the earthquake (based on data obtained from the main shock and aftershocks recorded by seismographs and accelerographs stationed in Bam) was located within the city borders of Bam. Investigations revealed that a section of the Bam fault, which runs alongside the city, was activated during this earthquake. Additionally, based on observations of the main shock and aftershocks, the focal depth of the Bam earthquake was estimated to be 8 km. The Bam fault (with a north-south orientation) passes near the city of Bam. In summary, it can be stated that the Bam earthquake, with a magnitude of 6.5, devastated the city due to the effects of the near-field fault [14].

3.2. Tabas earthquake

The Tabas earthquake occurred on September 16, 1978 with a magnitude of 7.4 and tragically resulted in the deaths of approximately 40% of the residents (14800 out of a population of around 36000) of Tabas. The study of the records of this earthquake and the seismicity of the region indicates that the hypocenter was located at a depth of approximately 10 km below the ground surface. Researchers have estimated that the fault responsible for this earthquake had a length of about 80 km. This fault passed approximately 10 km from the city of Tabas. The hypocenter of this earthquake was also near the village of Krite in Tabas.

3.3. Naghan earthquake

The Geophysics Center of the University of Tehran has stated that on April 6, 1977, a destructive and devastating earthquake with a magnitude of 6.1 occurred in the mountainous areas of Chaharmahal and Bakhtiari province, severely damaging the villages of Naghan, Ardal, Duplan, Gandoman, and Avorgan. The focal depth of the earthquake was 33 km. In the Naghan earthquake, 350 out of a total of 450 houses were destroyed. The death toll from this earthquake was 384, with the village of Naghan suffering more damage than other areas.

4. Soil parameters and modeling

Before modeling, appropriate parameters are determined for each layer. These parameters are extracted from various references [15-19]. Table 1 shows the values for different soil layers used in modeling with finite element. In this Table, E is Young's modulus, ν is Poisson's ratio, φ is the internal friction angle, c is cohesion, ψ is the dilation angle, γ_{unsat} is the unsaturated unit weight, and γ_{sat} is the saturated unit weight.

Table 1

Parameters of soil layers

Parameter Soil type	E (kPa)	ν	φ (°)	c (kPa)	ψ (°)	γ_{unsat} (kN/m^3)	γ_{sat} (kN/m^3)
Stiff clay	60000	0.25	20	200	0	20	22
Soft clay	10000	0.35	18	20	0	16	18
Dense sand	70000	0.3	38	1	15	19	20

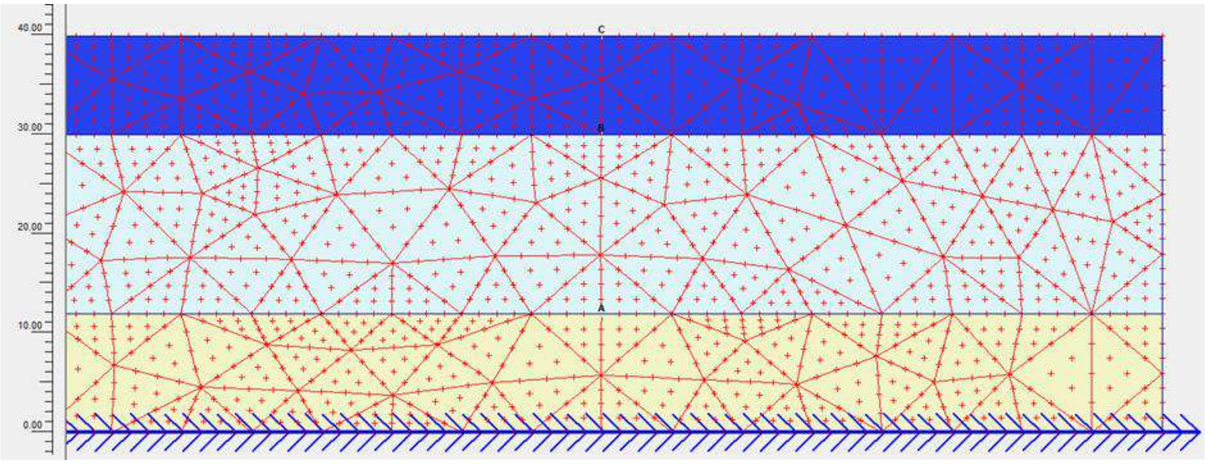

Fig. 3 Meshing the model and selecting points A, B, and C on the layer boundaries

Soil and structures are often subjected not only to static loads but also to dynamic loads. These dynamic loads can be strong enough to cause severe damage during earthquakes. Through dynamic analysis, the effects of vibrations on the soil can be assessed. In this study, after drawing the problem geometry, suitable parameters are assigned to the soil layers. Under dynamic conditions, absorbent boundaries should be chosen. Thus, absorbent boundaries will be considered for the left and right sides. The mesh used in this study is based on triangular elements. Mesh generation encompasses all points and lines within the geometric model. Smaller meshes lead to higher accuracy. In this study, the fine mesh was employed. Additionally, 15-node elements are used for plane strain conditions along with the Mohr-Coulomb model. The steps for analyzing the site include: general settings, defining the problem geometry, defining materials and assigning them to layers, determining boundary conditions and loading, meshing, initial conditions, performing analysis operations and displaying analysis results. Fig. 3 illustrates how the problem was modeled.

5. Results and discussion

5.1. Effect of different earthquakes on the base case

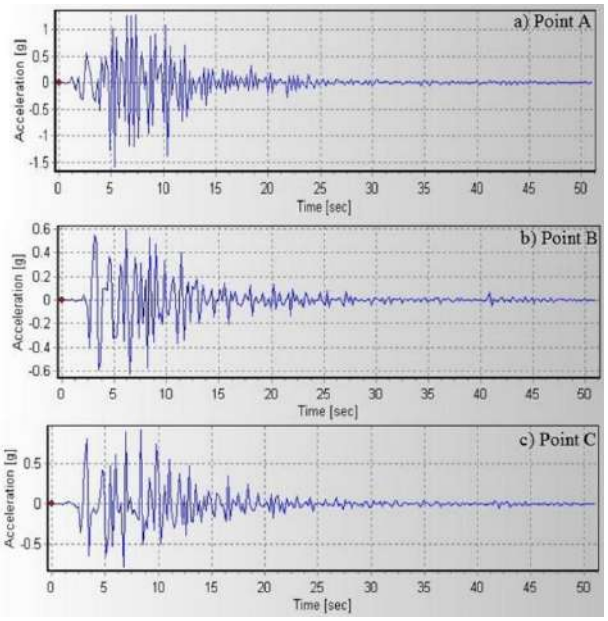

Fig. 4 Accelerogram during Bam earthquake for base layering a) point A b) point B c) point C

The Bam earthquake in the bedrock had a Peak Ground Acceleration (PGA) of 0.79g (Fig. 2 (a)). According to Fig. 4(a), this earthquake was amplified after passing through the stiff clay layer, reaching a PGA of 1.59g. Subsequently, as shown in Fig. 4(b), after the seismic waves passed through the soft clay layer, the PGA decreased to 0.62g. Finally, after the waves passed through the dense sand, the PGA reached 0.91g, indicating an amplification (Fig.4(c)). It is noteworthy that PGA is amplified in dense sand but does not reach the PGA value in stiff clay since soft clay filters the high frequency characteristics of the earthquake waves and alters the frequency content of the earthquake.

Investigations indicate that the location of the Bam earthquake recording is less than 60 km from the epicenter (according to reports from the Road, Housing and Urban Development Research Center of Iran, it is 6 km), thus classifying it as a near-field earthquake. Near-field earthquakes have high frequency content and dominant frequencies. Therefore, in such earthquakes, stiff soils with high frequencies amplify ground motion, while soft soils with low frequencies attenuate it. Consequently, dense sand and stiff clay layers amplify seismic motion, while soft clay diminishes it. From a duration perspective, it can also be stated that soft soil increases earthquake duration due to trapping seismic waves (in this research, the duration of the earthquake is considered as the time between the first and last accelerations greater than 0.05 g).

Now, the impact of nonlinear soil behavior on the amplification and attenuation of seismic waves is studied. The Bam earthquake has a greater magnitude compared to the Naghan earthquake. As earthquakes increase in magnitude, more attenuation occurs. With increased acceleration levels, greater strains are generated and stiffness decreases. Additionally, this high acceleration level causes nonlinear soil behavior and results in greater damping, consequently reducing amplification. Investigations show that the amplification levels in the Naghan and Bam earthquakes are 1.53 and 1.15, respectively, which aligns with nonlinear soil behavior.

The Tabas earthquake had a PGA of 0.85g in the bedrock (Fig.2(b)). According to Fig.5(a), after passing through the stiff clay layer, the earthquake is amplified, reaching a PGA of 2.42g. Subsequently, as the seismic waves traverse the soft clay layer, the PGA decreases to 1.55g (Fig.5(b)). Finally, after passing through the dense sand layer, the PGA increases to 2.04g, indicating a further amplification (Fig. 5(c)). It is noteworthy that PGA is amplified in dense sand but does not reach the PGA level in stiff clay, as the soft clay filters the high-frequency characteristics of the seismic waves and alters the earthquake's frequency content. The significant amplification of this earthquake by soil layers is likely due to the proximity of the dominant frequencies of the soil and the input motion, along with the phenomenon of relative resonance.

Studies indicate that the recording location of the Tabas earthquake is within a distance of fewer than 60 km from the hypocenter, thus it is considered a near-field earthquake. Near-field earthquakes have high frequency content and a high dominant frequency. Therefore, in this type of earthquake, stiff soils with high frequencies amplify ground motion, while soft soils with low frequencies attenuate ground motion. For this reason, the dense sand and stiff clay layers amplify earthquake motion, whereas the soft clay layer attenuates it. From the perspective of earthquake duration, it can also be stated that soft soil increases the earthquake's duration due to trapping seismic waves.

The Naghan earthquake had a PGA of 0.81g in the bedrock (Fig.2(c)). According to Fig.6(a), after passing through the stiff clay layer, the earthquake is amplified, reaching a PGA of 1.62g. Subsequently, as the seismic waves traverse the soft clay layer, the PGA decreases to 0.72g (Fig.6(b)). Finally, after passing through the dense sand layer, the PGA increases to 1.42g, indicating a further amplification (Fig. 6(c)). It is noteworthy that PGA is amplified in dense sand but does not reach the PGA level in stiff clay, as the soft clay filters the high-frequency characteristics of the seismic waves and alters the earthquake's frequency content.

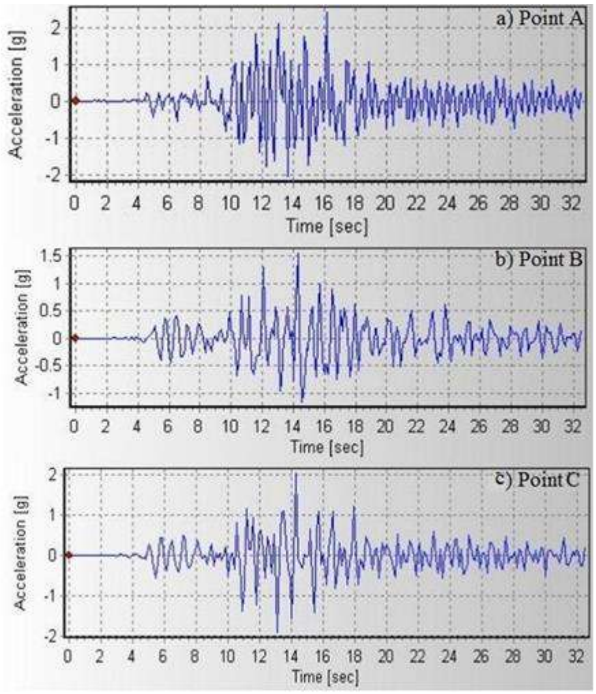

Fig. 5 Accelerogram during Tabas earthquake for base layering a) point A b) point B c) point C

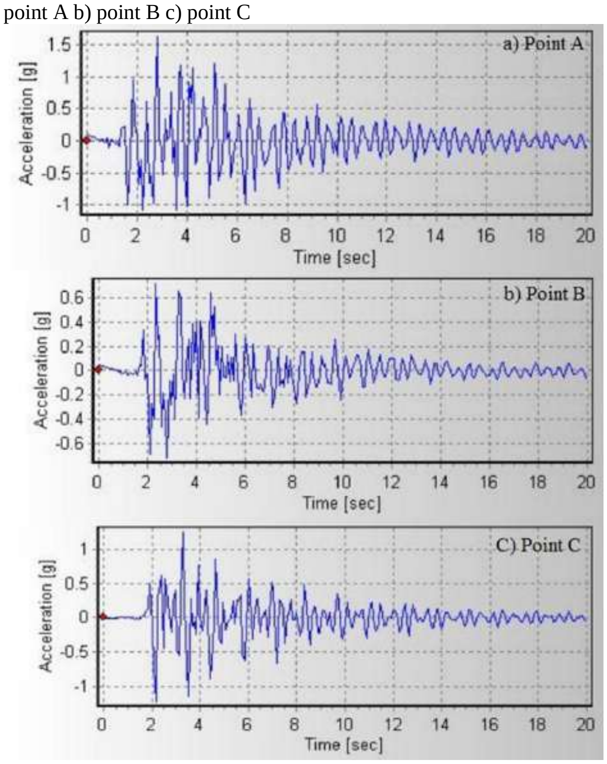

Fig. 6 Accelerogram during Naghan earthquake for base layering a) point A b) point B c) point C

Investigations indicate that the location of the Naghan earthquake recording is less than 60 km from the epicenter (according to reports from the Road, Housing and Urban Development Research Center, it is 5 km), thus classifying it as a near-field earthquake. Near-field earthquakes have high frequency content and dominant frequencies. Therefore, in such earthquakes, stiff soils with high frequencies amplify ground motion, while soft soils with low frequencies attenuate it. Consequently, dense sand and stiff clay layers amplify seismic motion, while soft clay diminishes it.

5.2. Examination of soil layering effects

To examine the effects of soil layering, in addition to the base layering status of the research (Fig. 1(a)), five other different layering scenarios have also been considered. The Naghan earthquake is applied as the input motion on the bedrock for these scenarios, and the results are analyzed.

Fig. 1(b) shows the layering configuration for case 2. The Naghan earthquake in the bedrock has a PGA of 0.81g (Fig. 2(c)). According to Fig. 7(a), this earthquake is attenuated after passing through the soft clay layer, reaching a PGA of 0.34g. Subsequently, as shown in Fig. 7(b), after the seismic waves pass through the stiff clay layer, the PGA decreases to 0.31g. Finally, after passing through the dense sand, the PGA reaches 0.59g, indicating amplification (Fig. 7(c)).

The Naghan earthquake is considered a near-field event. Near-field earthquakes have high frequency content and dominant frequencies. In this layering scenario, the soft clay layer, having a low frequency and being distant from the dominant frequency of the input motion, attenuates the characteristics of the earthquake. Additionally, soft clay filters out high-frequency seismic waves, resulting in lower frequency waves entering the stiff clay layer, which also contributes to the attenuation of ground motion. Ultimately, after passing through the stiff clay layer, the dominant frequency of motion increases again, leading to amplified acceleration in dense sand.

Fig. 1(c) shows the layering configuration for case 3. According to Fig. 8(a), this earthquake is attenuated after passing through the soft clay layer, reaching a PGA of 0.29g. Subsequently, as shown in Fig. 8(b), after passing through the dense sand layer, the PGA decreases to 0.25g. Finally, after passing through the stiff clay layer, the PGA reaches 0.58g, indicating amplification (Fig.8(c)).

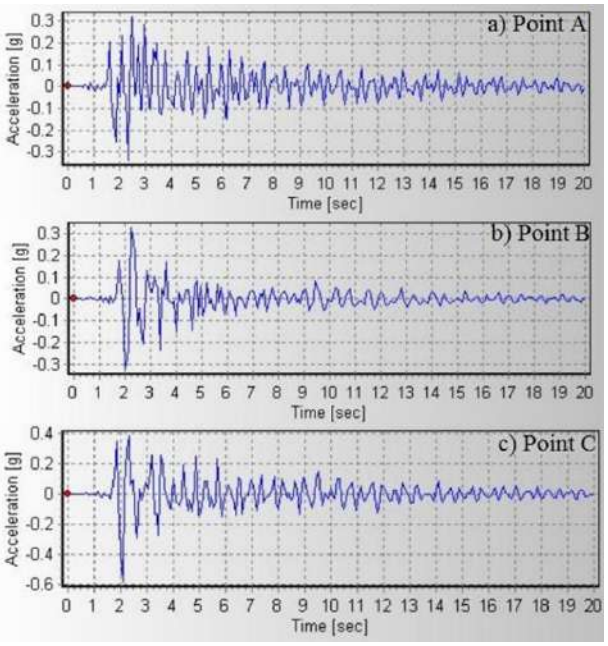

Fig. 7 Accelerogram during Naghan earthquake for layering case 2 a) point A b) point B c) point C

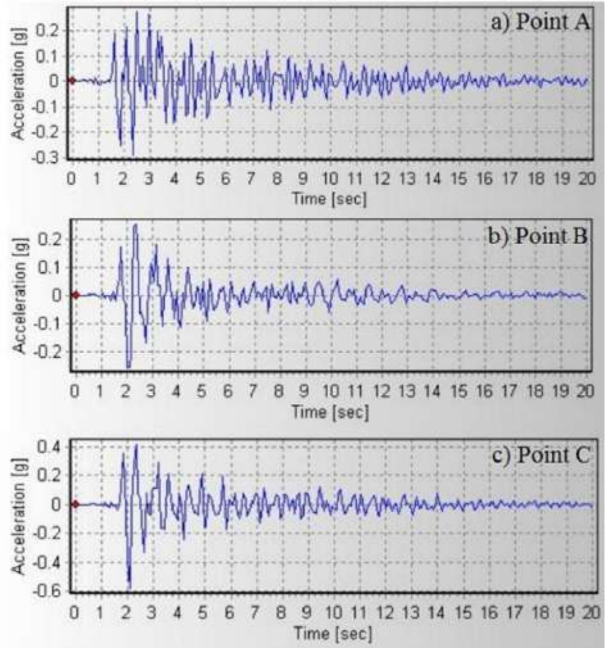

Fig. 8 Accelerogram during Naghan earthquake for layering case 3 a) point A b) point B c) point C

In this layering scenario, since soft clay has a low frequency and is distant from the dominant frequency of input motion, it attenuates earthquake characteristics. Additionally, soft clay filters high-frequency seismic waves, resulting in lower frequency waves entering the dense sand layer and contributing to ground motion attenuation. Ultimately, after passing through dense sand, the dominant frequency of motion increases again, leading to amplified acceleration in stiff clay. From a duration perspective, it can be stated that soft soil increases earthquake duration due to trapping seismic waves.

Fig.1(d) shows the layering condition of case 4. According to Fig. 9(a), this earthquake is amplified after passing through the stiff clay layer, reaching a PGA of

1.46g. Then, according to Fig.9(b), after the earthquake waves pass through the dense sand layer, the PGA decreases to 1.44g. Finally, after passing through the soft clay, the PGA reaches 0.83g, indicating attenuation (Fig.9(c)).

In this layering, the stiff clay, having a high frequency and being close to the dominant frequency of the input motion, amplifies the earthquake characteristics. In the dense sand, a very small amount of attenuation occurs, possibly because the frequency content of the stiff clay layer is closer to the frequency content of the input motion than that of the dense sand, resulting in greater amplification. Another reason could be the thick layer of dense sand causing wave attenuation. Finally, after passing through the soft clay, attenuation occurs because the lower layers filter out low-frequency waves. Thus, the dominant frequency moves away from the frequency of the soft clay, which is the reason for the attenuation of the earthquake in this layer. From the perspective of earthquake duration, soft soil can increase the duration by trapping seismic waves.

Fig.1(e) shows the layering condition of case 5. According to Fig.10(a), this earthquake is amplified after passing through the dense sand layer, reaching a PGA of 1.98g. Then, according to Fig.10(b), after the earthquake waves pass through the soft clay layer, the PGA decreases to 0.52g. Finally, after passing through the stiff clay, the PGA reaches 1.43g, indicating re-amplification (Fig.10(c)). It is noted that PGA is amplified in stiff clay but does not reach the PGA level in dense sand because the soft clay filters out high-frequency components of the earthquake waves, altering their frequency content.

Near-field earthquakes have high-frequency content and dominant frequency. Therefore, in these types of earthquakes, stiff soils with high frequencies amplify ground motion, while soft soils with low frequencies attenuate it. Thus, dense sand and stiff clay layers enhance earthquake motion, whereas soft clay attenuates it.

Fig.1(f) shows the layering condition of case 6. According to Fig.11(a), this earthquake is amplified after passing through the dense sand layer, reaching a PGA of 1.53g. Then, according to Fig.11(b), after the earthquake waves pass through the stiff clay layer, the PGA decreases to 1.41g. Finally, after passing through the soft clay, the PGA reaches 0.85g, indicating attenuation (Fig.11(c)).

In this layering, the dense sand, having a high frequency and being close to the dominant frequency of the input motion, amplifies the earthquake characteristics. In the stiff clay, a very small amount of attenuation occurs, possibly due to the thick layer of stiff clay causing wave attenuation. Finally, after passing through the soft clay, attenuation occurs because the lower layers filter out low-frequency waves.

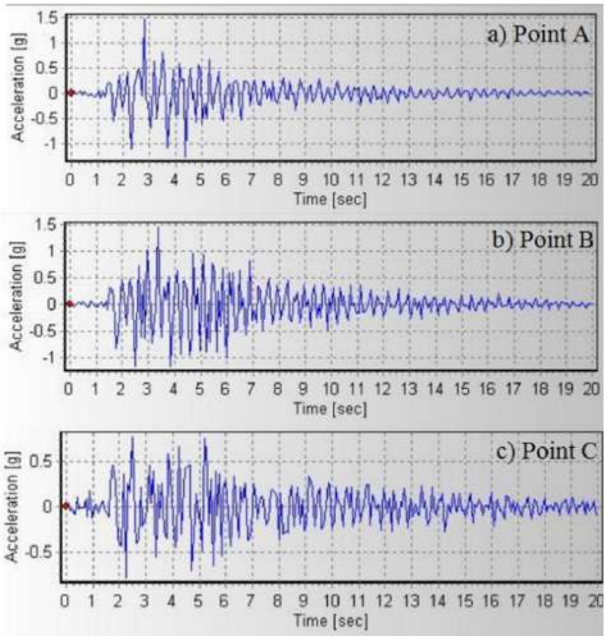

Fig. 9 Accelerogram during Naghan earthquake for layering case 4 a) point A b) point B c) point C

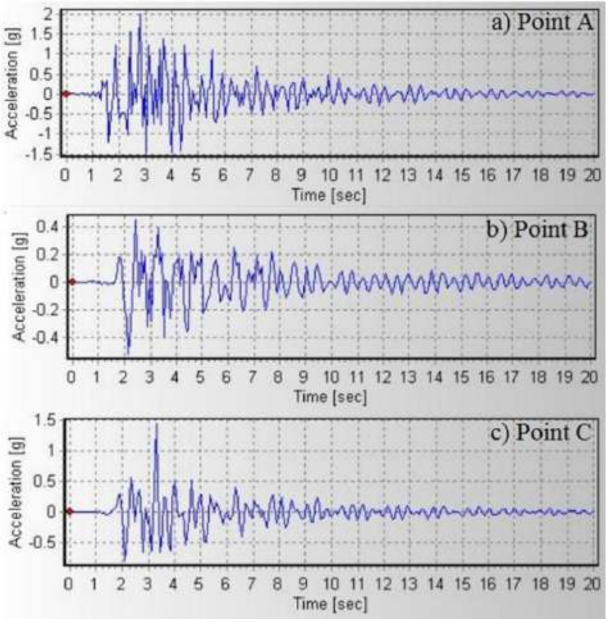

Fig. 10 Accelerogram during Naghan earthquake for layering case 5 a) point A b) point B c) point C

5.3. The effect of distance from the earthquake epicenter

In this section, the effect of distance from the earthquake epicenter will be examined. For this study, the Tabas earthquake recorded at the Kashmar station is used. Kashmar is 227 km away from the epicenter of the earthquake, thus categorizing it as a far-field earthquake. The Tabas earthquake recorded at the Kashmar station was applied to the base layering condition of the project (Case 1), and the time history of acceleration at points A, B, and C is presented.

The earthquake at the Kashmar station has a PGA of 0.04g in the bedrock (Fig.12(a)). According to Fig. 12(b), the PGA of this earthquake shows little change after passing through the stiff clay layer, with the PGA remaining approximately 0.04g. Then, according to Fig.12(c), after the earthquake waves pass through the soft clay layer, the PGA increases to 0.09g. Finally, after passing through the dense sand, the PGA reaches 0.06g, indicating attenuation (Fig.12(d)).

Studies indicate that the location of the earthquake recording at the Kashmar station is approximately 227 km away from the epicenter, thus considered a far-field earthquake. Far-field earthquakes have low-frequency content and dominant frequency. Therefore, in these types of earthquakes, stiff soils with high frequencies attenuate ground motion, while soft soils with low frequencies amplify it. Consequently, the dense sand layer causes attenuation of earthquake motion, whereas the soft clay amplifies it. In other words, under these specific conditions, the behavior of soil layers is exactly opposite to that in near-field earthquakes. This is because at such low acceleration levels, soil behavior is linear. Table 2 presents the PGA and its occurrence time at different points for all analyses of this study.

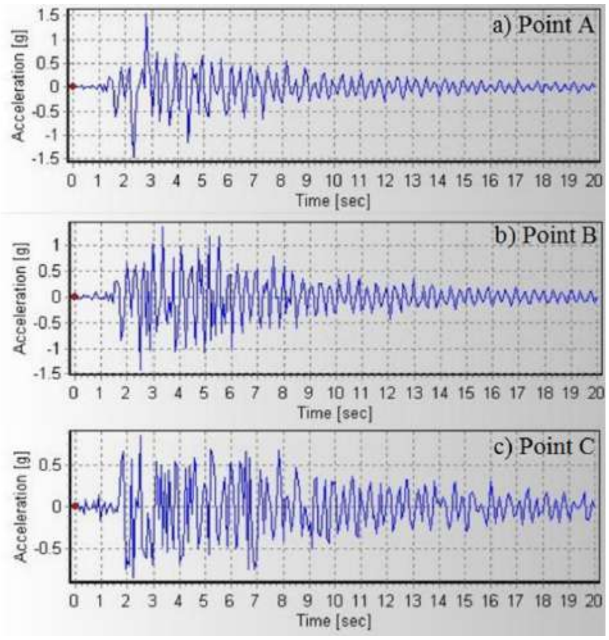

Fig. 11 Accelerogram during Naghan earthquake for layering case 6 a) point A b) point B c) point C

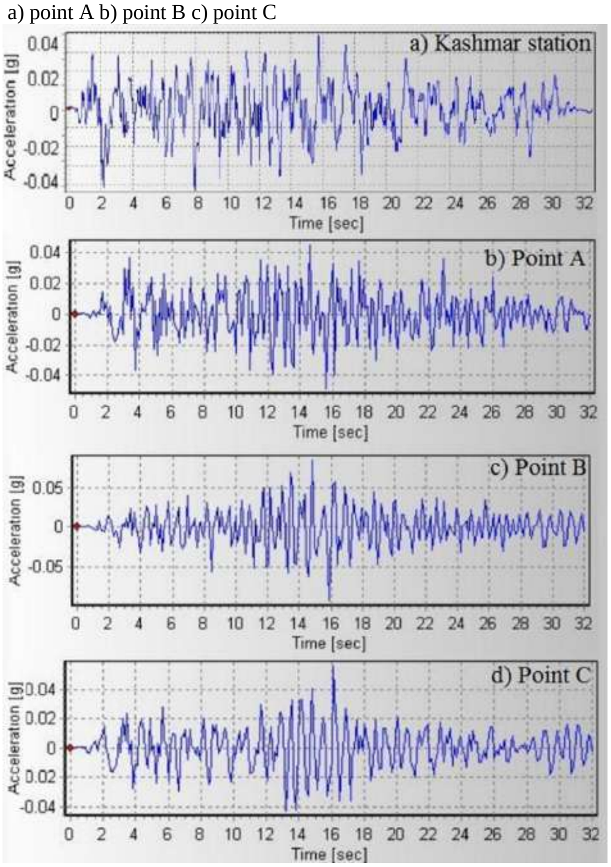

Fig. 12 Accelerogram during Tabas earthquake a) Kashmar station b) point A c) point B d) point C

6. Conclusions

In this study, a soil with specific layering (case 1) was subjected to three different earthquakes (Bam, Naghan, and Tabas), and by comparing the PGA values at the top of each layer, the effect of various earthquakes was determined. Additionally, to investigate the influence of soil layering, the positions of different layers were changed, and six possible conditions were evaluated. Furthermore, to examine the effect of distance from the earthquake epicenter, the recorded data from the Kashmar station related to the Tabas earthquake was used to compare the results from the Kashmar and Tabas stations and determine the impact of far-field and near-field earthquakes. Among the most significant results obtained are the following:

1. In the Bam earthquake, the seismic waves were amplified after passing through the stiff clay layer, reaching a PGA of 1.59g. Subsequently, after passing through the soft clay layer, the PGA decreased to 0.62g. Finally, after passing through the dense sand, the PGA reached 0.91g, indicating re-amplification. Studies show that the Bam earthquake site is located less than 60 km from the epicenter (6 km according to the Road, Housing, and Urban Development Research Center of Iran) and is

Table 2
PGA values and the time of their occurrence for all analyses of the study

Type of analysis	Type of layering	Name of earthquake	Locations	Time (s)	PGA (g)	Relevant Fig.
Effect of different earthquakes	Case1 (Base)	Bam	Bedrock	8.36	0.79	2. a
			Point A	5.30	1.59	4. a
			Point B	6.52	0.62	4. b
			Point C	8.12	0.91	4. c
		Tabas	Bedrock	11.04	0.85	2. b
			Point A	16.12	2.42	5. a
			Point B	14.30	1.55	5. b
			Point C	14.60	2.04	5. c
		Naghan	Bedrock	2.22	0.81	2. c
			Point A	2.57	1.62	6. a
			Point B	2.83	0.72	6. b
			Point C	3.28	1.24	6. c
Effect of soil layering	Case 2	Naghan	Bedrock	2.22	0.81	2. c
			Point A	2.32	0.34	7. a
			Point B	2.24	0.31	7. b
			Point C	2.08	0.59	7. c
	Case 3	Naghan	Bedrock	2.22	0.81	2. c
			Point A	2.32	0.29	8. a
			Point B	2.10	0.25	8. b
			Point C	2.08	0.28	8. c
	Case 4	Naghan	Bedrock	2.22	0.81	2. c
			Point A	2.80	1.46	9. a
			Point B	3.36	1.44	9. b
			Point C	2.24	0.83	9. c
	Case 5	Naghan	Bedrock	2.22	0.81	2. c
			Point A	2.80	1.98	10. a
			Point B	2.16	0.52	10. b
			Point C	3.28	1.43	10. c
	Case 6	Naghan	Bedrock	2.22	0.81	2. c
			Point A	2.80	1.53	11. a
			Point B	2.48	1.41	11. b
			Point C	2.36	0.85	11. c
Effect of epicentral distance	Case 1 (Base)	Tabas (Kashmar station)	Bedrock	7.92	0.04	12. a
			Point A	15.61	0.04	12. b
			Point B	15.87	0.09	12. c
			Point C	16.12	0.06	12. d

thus considered a near-field earthquake. Near-field earthquakes have high-frequency content and dominant frequency. Therefore, in these types of earthquakes, stiff soils with high frequencies amplify ground motion, while soft soils with low frequencies attenuate it. Consequently, the dense sand and stiff clay layers enhance earthquake motion, whereas the soft clay attenuates it.

2. In the Tabas earthquake, the seismic waves were amplified after passing through the stiff clay layer, reaching a PGA of 2.42g. In continuation, after passing through the soft clay layer, the PGA decreased to 1.55g. Finally, after passing through the dense sand, the PGA reached 2.04g, indicating re-amplification. The reason for the significant amplification of this earthquake by the soil layers is likely due to the proximity of the dominant frequencies of the soil and the input motion and the phenomenon of relative resonance.
3. In the Naghan earthquake, the seismic waves were amplified after passing through the stiff clay layer, reaching a PGA of 1.62g. Then, after passing through the soft clay layer, the PGA decreased to 0.72g. Finally, after passing through the dense sand, the PGA reached 1.24g, indicating re-amplification. It is noted that PGA is amplified in dense sand but does not reach the PGA level in stiff clay because the soft clay filters out high-frequency

components of the earthquake waves, altering their frequency content.

4. The nonlinear behavior of soil also affects the results. The Bam earthquake, compared to the Naghan earthquake, has a larger magnitude. As the earthquake magnitude increases, more attenuation occurs. With an increase in acceleration level, larger strains are created, and stiffness decreases. This high acceleration level also causes the soil behavior to become nonlinear, resulting in greater damping and reduced amplification. Studies show that the amplification in the Naghan and Bam earthquakes is 1.53 and 1.15, respectively, which is consistent with the nonlinear behavior of soil.
5. The change in soil layering has a significant impact on the results. In conditions where soft soil is placed on the bedrock, because soft clay has a low frequency and is far from the dominant frequency of the input motion, it attenuates the earthquake characteristics. Additionally, soft clay filters out high-frequency earthquake waves, causing the input waves to the stiff soil layer to have low frequencies, which in turn leads to attenuation of earthquake motion. Finally, after the waves pass through the first stiff soil layer (stiff clay/dense sand), the dominant frequency of the motion increases again, and this phenomenon causes amplification of PGA in the second stiff soil layer. In conditions where the first two soil layers are stiff, seismic waves are amplified, and when they reach the soft clay layer, attenuation occurs. Moreover, in conditions where soft layer is between two stiff layers, amplification is observed in the first layer and attenuation is observed after passing through the soft soil. Finally, re-amplification occurs when the waves reach the top of the last layer, but it does not reach the PGA values at the top of the first stiff layer.
6. The Tabas earthquake recorded at the Kashmar station has a PGA of 0.04g in the bedrock. This value shows little change after passing through the stiff clay layer, with the PGA remaining approximately 0.04g. Then, after the earthquake waves pass through the soft clay layer, the PGA increases to 0.09g. Finally, after passing through the dense sand, the PGA reaches 0.06g, indicating attenuation. The location of the earthquake recording at the Kashmar station is approximately 227 km away from the epicenter, thus considered a far-field earthquake. Far-field earthquakes have low-frequency content and dominant frequency. Therefore, in these types of earthquakes, stiff soils with high frequencies attenuate ground motion, while soft soils with low frequencies amplify it. Consequently, the dense sand layer causes attenuation of earthquake motion, whereas the soft clay amplifies it. In other words, under these specific conditions, the behavior of soil layers is exactly opposite to that in near-field earthquakes. This is because at such low acceleration levels, soil behavior is linear.

References

[1] Maass, Regina, Ka Lok Li, and Christopher J. Bean. “Improving passive reflection seismic imaging in complex geological settings through site effect reduction: Application to Krafla volcano, Iceland.” Geophysical Journal International (2025): ggaf072. DOI: https://doi.org/10.1093/gji/ggaf072.

[2] Choudhary, Romani, et al. “A transfer learning-based ground motion model for Western Himalayas.” Acta Geophysica (2025): 1–24. DOI: https://doi.org/10.1007/s11600-025-01000-3.

[3] Zaoui, Mohammed Akram Ismail, Boumédiène Derras, and Julie Régnier. “Impact of several site-condition proxies and ground-motion intensity measures on the spectral amplification factor using neuro-fuzzy approach: An example on the KiK-Net dataset.” Natural Hazards (2025): 1–30. DOI: https://doi.org/10.1007/s11069-025-07151-0.

[4] Pilz, Marco, Fabrice Cotton, and Chuanbin Zhu. “Site-response high-frequency frontiers and the added value of site-specific earthquake record-based measurements of velocity and attenuation.” Earthquake Spectra (2025): 87552930241311312. DOI: https://doi.org/10.1177/87552930241311312.

[5] Kuncar, Felipe, et al. “Methods to account for shallow site effects in hybrid broadband ground-motion simulations.” Earthquake Spectra (2025): 87552930241301059. DOI: https://doi.org/10.1177/87552930241301059.

[6] Uyanık, O., et al. “Seismic microzonation and geotechnical modeling studies considering local site effects for İnegöl Plain (Bursa-Turkey).” Earth and Space Science 11.11 (2024): e2023EA003460. DOI: https://doi.org/10.1029/2023EA003460.

[7] Pavlenko, Olga V. “Methods for Calculation of Ground Response During Strong Earthquakes.” In Seismic Waves in Soil Layers: Soil Behaviour During Recent Strong Earthquakes, Cham: Springer Nature Switzerland, 2024. 51–94. DOI: https://doi.org/10.1007/978-3-031-43171-9_3.

[8] Tao, Zhengru, et al. “Regional study of site effects on the high-frequency spectral-decay parameter.” Soil Dynamics and Earthquake Engineering 187 (2024): 109030. DOI: https://doi.org/10.1016/j.soildyn.2024.109030.

[9] Kakhki, Mohsen Kazemnia, et al. “Directional variations of site response in a landslide area using ambient noise analysis via Nakamura’s and polarization-based method.” Soil Dynamics and Earthquake Engineering 141 (2021): 106492. DOI: https://doi.org/10.1016/j.soildyn.2020.106492.

[10] Rezaei, Sadegh, Issa Shooshpasha, and Hamed Rezaei. “Evaluation of ground dynamic characteristics using ambient noise

measurements in a landslide area." Bulletin of Engineering Geology and the Environment 79.4 (2020): 1749–1763. DOI: https://doi.org/10.1007/s10064-019-01614-3.

[11] Choobbasti, Asskar Janalizadeh, et al. "Evaluation of site response characteristic using nonlinear method (Case study: Babol, Iran)." Frontiers of Structural and Civil Engineering 8 (2014): 69–82. DOI: https://doi.org/10.1007/s11709-014-0256-7.

[12] Rezaei, Sadegh, and Ali Hasanzadeh. "The site effect investigation using nonlinear and Iranian seismic code methods in Babol city." Magazine of Civil Engineering 110.2 (2022): 11008. DOI: https://doi.org/10.34910/MCE.110.8.

[13] Kramer, Steven L., and Jonathan P. Stewart. Geotechnical Earthquake Engineering. CRC Press, 2024.

[14] Kavand, Ali, et al. "Local Site Effects on the Damage Distribution during the 2003 Bam Earthquake (Southeastern Iran) and Its Implementation in Preparation of Earthquake Design Spectra for the City of Bam." Iranian Journal of Science and Technology, Transactions of Civil Engineering (2024): 1–21. DOI: https://doi.org/10.1007/s40996-024-01526-z.

[15] Bowles, Joseph E., and Yingzhong Guo. Foundation Analysis and Design. Vol. 5. New York: McGraw-Hill, 1996.

[16] Budhu, Muniram. Soil Mechanics and Foundations. John Wiley and Sons, 2010.

[17] Arman, Ara, et al. Geotechnical and Foundation Engineering Module 1: Subsurface Investigations. No. FHWA-HI-97-021, 1997.

[18] Kwasniewski, M., and P. Rodriguez-Oitaben. "Study on the dilatancy angle of rocks in the pre-failure domain." ISRM Congress. ISRM, 2011.

[19] Ameratunga, Jay, Nagaratnam Sivakugan, and Braja M. Das. Correlations of Soil and Rock Properties in Geotechnical Engineering. 2016.

J-Researchers

Journal of Civil Engineering Researchers

Journal homepage: www.journals-researchers.com

3D Free Vibration Analysis of Nanocomposite Beams Carbon Nanotube Reinforced FGM Using DQ Method

Kouros Nekoufar,[a,*] Shahrzad Farrokhi[a]

[a] *Associate Professor, Department of Mechanical Engineering, Cha.c., Islamic Azad University, Chalus, Iran*

ABSTRACT

Beams are always noteworthy as an engineering structure due to their wide application in industry such as bridges, railway tracks, floors and ceilings of buildings and many other cases. Therefore, considering the wide application of these materials in industry, the analysis of this category of structures becomes important in the overall design process of these parts in a structure. With the increasing use of beams in industry and the need to increase their efficiency and ensure their proper functioning, the use of new materials such as functionally graded materials has increased. The use of composite materials, shape memory alloys, piezoelectric materials, etc. and the expansion of the scope of use of these materials has led to increased efforts by researchers to achieve the construction and design of structures and parts with better efficiency and quality. On the other hand, conducting experimental analyses on these materials is associated with problems such as size, price, complexity of the laboratory model, etc., hence the presentation of general theoretical models. In this research, the vibration analysis of a nanobeam is considered. Unidirectional FGM (functional properties along the beam thickness) with carbon nanotubes and a layer Metal and ceramic supports on various types of supports Sometimes. The solutions, including simple, complex, etc., were discussed. The solution method in question was the mixing method, and in line with the thickness of the numerical method, the differential function. It has been DQ based on this, relationships have been extracted regarding how to increase the natural frequency and the lowest natural frequency, as well as the length-to-thickness ratio, natural frequency changes, and dimensionless natural frequency changes in the beam.

ARTICLE INFO

Received: March 6, 2025
Accepted: May 22, 2025

Keywords:
Nanocomposite
Carbon Nanotube
Method GDQ
FGM
Eshelby-Mori-Tanaka method

DOI: 10.61186/JCER.7.2.21
DOR: 20.1001.1.2538516.2025.7.2.3.1

1. Introduction

Currently, the use of functionally graded nanobeams, plates, and layered structures is expanding significantly in industry. In this way, the bending stiffness and strength of functionally graded nanobeams exceed the bending stiffness of each of its components alone, which is achieved at the lowest possible weight of this type of structure ¬are usually used somewhere¬. Weight is a critical factor, meaning that the weight of the structure must be low. For example, in the aerospace, mining, and sports equipment industries. In recent years, much attention has been paid to the development of nanostructures with functionally graded properties and their applications. The general

---

[*] Corresponding author. Tel.: +98 912 525 86 98; e-mail: kouros.nekoufar@iau.ac.ir (Associate Prof. Kouros Nekoufar).

properties of these structures are high thermal resistance, high strength-to-weight ratio, good sound and energy absorption, and often low production costs. These structures have a very good light-stiffness ratio. Many applications of nanostructures with functionally graded properties require the production of complex shapes, which has made the analysis of these materials more complex. Also, to make the structure lighter and structures that require high bending stiffness, nanomaterials with functionally graded properties are used in structures. A nanocomposite is also a composite in which one or more components have dimensions less than 100 nanometers. Nanocomposite are composed of two phases. The first phase is a crystalline structure, which is actually the base or matrix of the nanocomposite and may be made of polymer, metal or ceramic. The second phase is particles on the nanometer scale. May they be Title: Filler Reinforcement for specific purposes such as strength, resistance, electrical conductivity, magnetic properties, and... are distributed within the first phase (base material).

1.1. Functionally graded materials

Functionally graded materials are composite materials that are microscopically heterogeneous and in which the properties and characteristics of the material change continuously and gradually from one level to another. In these materials, the properties change as a function of position, which may occur naturally or as a result of manufacturing processes [1]. Materials generally exhibit one property, while in functionally graded materials the properties of one side are different from the other. For example, one side may have high mechanical strength and the other side may have high thermal resistance. Figure (1-1) shows the material and its properties in different structures.

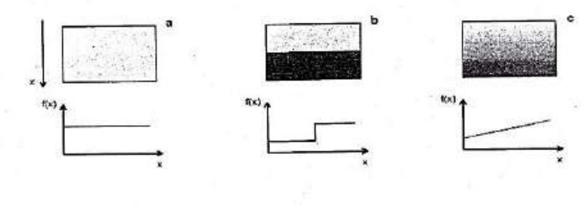

Figure 1: Types of material structures and their properties [1]

As can be seen in Figure 1, in the structure (a) the material is homogeneous and the properties are the same at all points of the material. In the structure (b) a new material is obtained by joining two materials together and the properties of the new material change in the form of bridges. Also, a boundary is created at the junction. In the structure (c) which is a functional graded structure, the properties change uniformly from one side to the other, and no boundaries can be determined between the constituent materials within the material.

So in graded materials, there is a continuous change in properties. That is, this material is formed by bonding materials to. Individually to It is not easy to obtain both comes, because in this case a boundary is created in the material. In other words, by mixing several materials with different properties, continuous and gradual changes are created in the manufactured material without creating a boundary. Due to the continuous and gradual changes that occur in the body, this manufactured material is called a functional material. The gradual change in the properties of functionally graded materials, unlike the sudden change in discrete layered materials such as fiber-matrix composites, is used to modify the fracture performance and crack growth that is clearly visible in the intermediate surface of the composite materials. These properties and characteristics are designed by manufacturers according to the needs and uses. Examples of these characteristics include crystal structures, crystal orientation, grain diameter and boundaries, particle distribution conditions, hardness and ductility values, thermal resistance, etc., which can be in any direction (horizontal or vertical). In the simplest FGMs consist of two different material components. Continuously from one to the other, as in Figure.2a it is explained that the composition of the materials can also change.

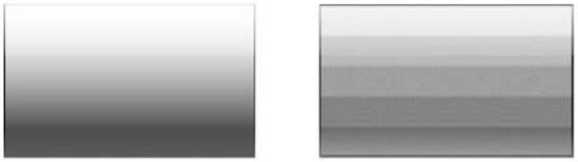

(a) (b)

Figure 2: Different designs in functionally graded structures [1]

Discontinuous face and step by step (Figure 2(b)). Both of these cases are considered structurally FGM. The basic idea of this structure was first presented in 1972 for composites and polymeric materials, and various models for the composite components in polymerization were proposed with possible applications for hierarchical structures. However, until 1980 there was no real investigation and research on how to build and evaluate hierarchical structures.

Functionally graded materials are also found in nature. It is found in the biological tissues of plants and animals and even in our own bodies, such as bones and teeth. Bamboo, oysters, and coconuts are good examples. Both bamboo and oysters are very hard on the outside and soft and durable on the inside. On the other hand, bamboo plants have other good qualities. They are lightweight, strong, and flexible. It organisms have a very suitable structure for living in the environment. All living things in nature are best created with structures and tissues that include functional materials.

In Figure 3Cross section of a clam shell It is shown. The continuous change of material on the surface of this shell is clearly evident in its appearance. The variety of material and its relationship to appearance is noteworthy. Teeth, shells, bone Example There are studies that show how nature shapes the microscopic structure of materials by placing stronger elements where stress and strain are highest. It is, it gives order.

Figure 3: Cross section of an oyster shell [1]

The basic idea of hierarchical structures was first proposed in 1972 for composites and polymeric materials, and various models for the components of the composite in polymerization were proposed with possible applications for hierarchical structures. However, it was not until 1980 that there was any real investigation and research into how to design, fabricate, and evaluate these structures.

Functionally graded materials were developed around 1984. Two researchers, one studying aeronautics and astronautics and the other advanced materials, worked together on spacecraft. The outer shell of spacecraft is exposed to very high temperatures (about 1700 degrees), so it needs to be able to withstand the harsh conditions of the large temperature difference between the inside and outside. No single material could withstand such conditions. The researchers came up with a concept called functionally graded materials. (FGM) thought of producing a material for spacecraft bodies by gradually changing its properties, which would have both enhanced thermal resistance and good mechanical properties. They decided to use ceramics for the external surface exposed to very high temperatures and heat-conducting materials for the internal surface. This was the beginning of research activities on functionally graded materials. In 1987, their research The research project on functionally graded materials became a major project of the Ministry of Science and Research. Between 1987 and 1991, the research project It was started when many researchers from universities, laboratories and companies participated in the work. They discussed the development methods of functionally graded materials and the production steps such as material design, production and evaluation. Finally, the thermal stress-releasing material (FGM) was developed. In 1990, the first international conference on functionally graded materials was held in Sendai, Japan, and in 1992, functionally graded materials (FGM) were announced as one of the top ten technologies and attracted much attention worldwide.

1.2. Relationships governing functionally graded materials

Consider a case where the sheet is made of a material with a functional property of ceramic and metal. The material properties vary continuously along the thickness according to the following relationships:

$$E(z) = E_m + E_{cm}V_f(z) \quad (1)$$
$$\nu(z) = \nu_m + \nu_{cm}V_f(z)$$
$$\rho(z) = \rho_m + \rho_{cm}V_f(z)$$

$$\mathrm{E_{cm}} = \mathrm{E_c} - \mathrm{E_m}$$
$$\nu_{\mathrm{cm}} = \nu_{\mathrm{c}} - \nu_{\mathrm{m}} \quad (2)$$
$$\rho_{\mathrm{cm}} = \rho_{\mathrm{c}} - \rho_{\mathrm{m}}$$

Which refers to materials with the properties of metals and ceramics and $V_f(z)$is the volume fraction of structural materials is most often expressed by power law or sigmoid functions. For power-functionally graded materials, the volume fraction is expressed as:

$$\mathrm{V_f}(z) = \left(\frac{z}{h} + \frac{1}{2}\right)^N \quad (3)$$

Where N represents the power law, the material index, which shows the index of change of the material in its thickness.

For sigmoid functionally graded materials, the volume fraction function is expressed as follows:

$$\mathrm{V_f}(z) = \begin{cases} 1 - \frac{1}{2}\left(1 - \frac{2z}{h}\right)^N & 0 \leq z \leq \frac{h}{2} \\ \frac{1}{2}\left(1 + \frac{2z}{h}\right)^N & -\frac{h}{2} \leq z \leq 0 \end{cases} \quad (4)$$

Similarly, N represents the thickness change profile of the material, which controls the change in Young's modulus.

For two-layer functionally graded materials:

$$\mathrm{V_f}(z) = \begin{cases} \left(1 - \frac{2z}{h}\right)^N & 0 \leq z \leq \frac{h}{2} \\ \left(1 + \frac{2z}{h}\right)^N & -\frac{h}{2} \leq z \leq 0 \end{cases} \quad (5)$$

There is another type of functionally graded material in which the material properties follow an exponential distribution and are expressed as follows:

$$E(z) = E_m e^{\frac{1}{h}\ln\frac{E_c}{E_m}\left(z+\frac{h}{2}\right)} \quad (6)$$
$$\nu(z) = \nu_m e^{\frac{1}{h}\ln\frac{\nu_c}{\nu_m}\left(z+\frac{h}{2}\right)}$$
$$\rho(z) = \rho_m e^{\frac{1}{h}\ln\frac{\rho_c}{\rho_m}\left(z+\frac{h}{2}\right)}$$

The exponential change model of properties in functionally graded materials is a suitable model for obtaining an accurate solution of elasticity.

1.3. History of studies

In 2001, Sankar, a bullet from the barrel–Bernoulli made of materials FGM with simple supports has been statically investigated. An orthotropic beam is under normal stress only and all desired elastic parameters are proportional to which is constant and z is the coordinate component in the thickness direction which has obtained the exact solution. (The beam is only mechanically loaded in a sinusoidal form and Poisson's ratio is assumed to be constant). [3]

In 2002, Chakraborty and his colleagues used the finite element method based on the first-order shear deformation theory to calculate the change in elastic and thermal properties through the thickness. Both exponential and power-law deformations of the material properties were used to represent the changes in different stresses. (The beam was considered under both thermal and mechanical forces.)). [4]

In 2003, Chakraborty and his colleagues used a finite element method based on the first-order shear deformation theory to study the effects of geometric nonlinearity on the dynamic and static response of isotropic, composite, and material beams. FGM has been used. The general Lagrange equation of the linear beam element for the displacement analysis and rotation Big ones to the work has been done. Both frequencies High and low pulse Loading curves are used to show the nonlinear effect on the transient response. (Power distribution is considered for material properties.) [5]

In 2004, Shi and colleagues, Analytical solution of a single-ended piezoelectric beam made of materials FGM has been studied under different loads. A piezoelectric beam with a continuously varying elastic parameter and material density is considered. A pair of stress and induction functions are assumed and determined as polynomials. Based on these functions, a set of solutions of this paper is obtained. Such as problems such as a piezoelectrically engaged one-ended beam with a constant body force or without body force, etc. In this research, the direct and inverse behavior of a piezoelectrically restrained one-ended beam is investigated. The Airy stress function method is used to find the solution. The result is that the stress function used to analyze a one-ended beam made of FGM materials and piezoelectric layers is similar to the function used for a similar beam made of homogeneous elastic materials. Also, if the body forces are ignored, some effects such as the effect of the FGM material parameter and layers are eliminated in the analytical solution. [6]

In 2006, Ding and his colleagues have investigated the plane stress problem of non-isotropic beams, assuming that the desired elastic parameters are arbitrary functions of the thickness coordinate direction. Partial differential equations, which are expressed by the Airy stress function for the plane problem of materials the non-isotropic FGM is satisfied and includes body forces. The solutions performed are: solution for beam under pure tension and bending, solution for single-ended fixed beams with free ends under shear force, solution for single-ended fixed beams or beams with simple supports under uniform force, solution for double-ended fixed beams under uniform force and solution for beam under body force and can be easily solved. The elasticity values for homogeneous beams decrease. In this case Research the Silverman 1964 method has been generalized to provide a general way of obtaining the stress function for beams made of materials with non-isotropic functional properties. No assumptions are made for the variation of the desired elastic quantities through the thickness. In addition, the change in physical force with coordinates has been taken into account.[7]

In 2007, Kapoor and his colleagues third-order zigzag theory based on a model for beams made of materials layered FGM in combination with the modified law of mixtures for effective elastic modulus have been validated with tests for free and static vibration response.

Two sets, using powder metallurgy and technique respectivelyAl/sicNi/〖AL〗_2 O_3Heat dissipation generated are being considered for validation effect of number of layers the accuracy of the theoretical model is discussed. A finite element model for dynamic analysis of material beams with layered functional properties, efficient zigzag theory for layer mechanics, modified mixed method the elastic modulus effect has been estimated and validated in laboratory experiments. Two models of three-layer and five-layer materials have been used FGM has been used for calculations. The volume fraction of the material is assumed to be it varies exponentially along the thickness slow.[8]

In 2007, Kaduli and his colleagues developed a displacement field based on higher-order shear deformation theory to study the static behavior of beams made of materials. Metal-ceramic FGMs are used under ambient temperature. Beams made of materials FGM with varying metal and ceramic volume fractions are considered based on the power law. Using the static potential energy law, the finite element form of the static equilibrium equation for a beam made of FGM materials is shown. Numerical results of vertical deflection and axial and shear stresses in a thick FGM beam in equilibrium under uniform load distribution for clamped boundary conditions–The effect of power distribution for different metal compositions is discussed. – Ceramic beam made of materials with FGM on deflection and stresses has been explained. The study reveals that the static deflection and static stresses will not be the same depending on whether the load is applied to a pure metal or pure ceramic surface.[9]

In 2007, Lee, an integrated method (analytical solution) for static and dynamic analysis of beams made of materials FGM, considering rotational inertia and shear deformation. All material properties are optionally considered as a function of the beam thickness. The results obtained cover the homogeneous Timoshenko beam with fixed elements without material properties. The proposed method for laminated Timoshenko beams is applicable to they are used the equations are obtained assuming the Timoshenko theory. It is assumed that the shear deformation and deflection in the direction Z depend only on X and temperature and are constant at any cross section. Numerical results for a beam that obeys a power law Multilayer Euler-Bernoulli and Timoshenko beams and beams obtained w When shear deformation and rotational inertia are Simultaneously disregarded, Euler's results–Bernoulli gets Come.[10]

In 2007, Tao and his colleagues used the Airy stress function method for a piezoelectric single-ended beam made of materials with functional properties. It is assumed that the feature t the mechanical and electrical properties of the material have similar variations along the thickness. and, a two-dimensional plane elasticity solution for coupling of electric fields–The elasticity of the beam under different loads has been obtained. This solution is for analyzing a beam made of functional materials with a layer Piezoelectric material with optional changes in properties. The properties of the materials will also be affected. Material properties with functional properties on the structural response of the beam under various loads have been studied in numerical examples. (A single-ended beam with a free end under a uniform load on the upper edge is assumed).[11]

In 2007, Chen His colleagues have investigated the bending problem of a non-isotropic single-ended beam made of a material with linearly distributed functional properties under load. Analysis based on exact elasticity equations for plane stress problems. The stress function is given by the form of a polynomial function of the longitudinal component is introduced.[12]

The analytical solution shows a good agreement compared to the finite element calculations. The desired elastic parameters are functions of the beam thickness only. The analytical solution can be easily reduced to the solution for a homogeneous beam.

In 2007, Chen and colleagues investigated the bending problem of a non-isotropic single-ended beam made of functionally-proper materials under thermal and uniform spread loads. are, where the material parameters are functions of the thickness coordinates. The thermal conductivity problem behaves like a one-dimensional problem along the thickness. Based on the initial equations for the plane stress problem, The stress function is the form of a polynomial function of the longitudinal coordinates in such a way that the stress it is assumed that they are obtainable.[13]

In 2007, Chen and his colleagues presented an exact solution for the bending and free vibration of a beam made of functional material on an elastic base based on the two-dimensional elasticity theory. The beam is assumed to be orthotropic at all points, while the material properties vary exponentially throughout the thickness. The system of governing partial differential equations is reduced to a normal state in the thickness limit by expanding the state variables into a series. Infinite sinusoidal waves decrease. The problem is finally solved using the state space method.[14]

In 2007, Zhong His colleagues, an elasticity solution for beam bending FGM using inverse methods in Airy stress function sentences was reported. [15]

In 2007, Ding and his colleagues, a series of analytical solutions for beams anisotropic FGM with various support conditions were extracted using an Airy stress function in general polynomial form. [16]

In 2009, Farhatnia and his colleagues developed analytical and numerical solutions for beams FGM under stress. They presented thermomechanical equations; they used the Euler-Bernoulli beam theory for analytical solution and the finite element method for numerical solution.[17]

In 2010, Ali Bigelow Thermoelasticity analysis for the beam FGM with integrated piezoelectric surfaces is presented, the properties in the thickness direction are assumed to be exponential and the Poisson's ratio is assumed to be constant. Beam in the support condition. Sometimes simple, with a limited length, and subjected to uniform pressure and thermal force, and in a state of plate tension. It is and at its lower level the temperature is considered to be zero.[18]

In 2010, Shimshak Beam base frequency analysis FGM with theory examined various higher-order [19]

In 2012, Tai and colleagues, beam bending and vibration FGM with theory various higher-order shear deformation models were investigated.[20]

In 2013, the Pardahan and his colleagues, free vibration of the beam Eulerian and Timoshenko investigated the FGM using the Rayleigh-Ritz method. [21]

In 2013, Thomas and his colleagues, a nanocomposite beam FGM with nanotubes. They modeled randomly placed beams using finite elements and investigated their free vibrations. For this analysis, Timoshenko beam theory was used. Also, Mori Tanaka approach was used to analyze the beam properties and the equations of motion were extracted using Hamilton's laws. The obtained results provide the most accurate representation of the nanotube placement. [22]

In 2013, Mohammadi Mehr and his colleagues analyzed the bending and vibration of a nanocomposite beam with functional properties based on the Timoshenko beam model based on coupled stress theory. The equations of motion were obtained using Hamilton's theory and Navier equations, and the functional properties FGM is considered as exponential functions.[23]

In 2013, Heshmati and his colleagues performed the free vibration analysis of a nanocomposite beam with carbon nanotube fibers with functionally graded properties using the Ashleby, Mori, Tanaka approach. In this project, the governing equations were derived based on the virtual work rules and assuming the Euler-Bernoulli beam theory. The finite element method was also used for better approximation. [24]

In 2015, Moradi Dastjerdi and colleagues performed vibration analysis for a composite beam. FGM reinforced with carbon nanotube fibers and placed on an elastic substrate. For the analysis of free vibrations, shear deformation theory was used and the equations of motion were obtained using Hamilton's energy laws and Navier's method. The substrate considered in this project is the classical Winkler-Pasternak substrate and the functional properties of the materials are in the thickness direction and the placement of the nanotubes carbon nanotubes were prepared according to Mori Tanaka principles. [25]

Zarehparvar-Shoja et al. [26], utilizes carbon nanotubes, to improve the mechanical characteristics of concrete as a building material.

2. Method of square differences

Numerical method of square differences It is a numerical method for solving differential equations. It was first introduced by Bellman and his colleagues before 1970. It approximates the derivatives of a function at each location by a linear series of all the values of the function at the sample points. The key to the method is the use of the method of square differences in determining the weighting coefficients. Bellman initially proposed two methods for calculating the weighting coefficients for first-order weighted derivatives. The first method is based on a system of algebraic equations of anomalous conditions. and the second method uses a simple algebraic formulation, but the coordinates of the points are determined by the roots of the Legendre polynomial. The method of square differences has been used as a powerful numerical discretization tool. Compared to the finite difference method Low order and finite element methods The square difference method produces much more accurate results with fewer node points, resulting in fewer calculations.

2.1. Introduction to the method of square differences and its governing equations

Many engineering problems or sets of partial differential equations It is accompanied by appropriate boundary conditions. For example, Newton's laws in fluids are modeled by the Navier-Stokes equations, the vibration of thin shells is modeled by fourth-order differential equations, and also waves acoustics and micro can be solved by the Helmholtz equation Model. In the usual case, solving such differential equations directly is a very difficult task. The method of square differences for similar the modeling of incompressible viscous flow, free vibration of beams, plates, and shells, and wave analysis in one and multidimensional domains, in Cartesian and curved coordinates, have been applied by Xu Cheng and his colleagues.

In most cases, approximate solutions are computed using function values at a series of sample points. At this point, the question may arise as to what is the relationship between partial differential equations and function values at sample points. In fact, it seems that there should be a bridge between them. The numerical gridding technique is in fact the bridge between the two.

Currently, there are many numerical techniques available. Among them, we can mention methods such as finite difference, finite element, and finite volume. The finite difference method is based on the use of Taylor expansion or polynomial approximation, while the finite element method uses the calculus of variations. and weighted residuals are used. In the finite volume method, the direct application of the stability principle to the cells is used. To achieve an acceptable accurate answer, in many of the numerical solutions mentioned, the number of sample points can be increased. Vibration analysis can be used as an example for this. Of course, it should be noted that in many problems, applying a larger number of sample points is necessary to achieve an accurate answer with high accuracy, which is one of the disadvantages of these methods. To solve many problems, a series of differential equations must be solved, the analytical solution of which is difficult and complex. Therefore, approximate methods must be used. In most cases, the approximate solution is expressed by a series of function values at certain points (node points or grid points).

The method of square differences is a numerical method with high accuracy while the number of nodes points it considers is less than other numerical methods. In this method, the partial derivative of a function with respect to a coordinate direction is expressed as an algebraic sum of all the values of the function at all grid points along the desired direction. Instead of the methods proposed by Bellman, other researchers have used Lagrange's interpolated polynomials.

2.2. Approximating derivatives by the method of square differences

The method of square differences is a numerical method that approximates the derivatives of a function by a linear series. This numerical method is based on the idea of squaring the integral. It is derived from. In this section, a brief explanation of the integral squaring method is first given, and then the method of square differences is examined. One of the problems that usually arises in engineering problems is the measurement and calculation of $\int_a^b f(x)dx$ In the distance*[a,b]*. If there is a function *F* such that it is, then the value of this integral will be equal to *F(b)-F(a)*. Unfortunately, in many engineering problems it is very difficult or impossible to find the function *F*. Instead, in many problems only the values of f are known in the interval, in which case a numerical method is necessary $df/\mathrm{dx} = F$.

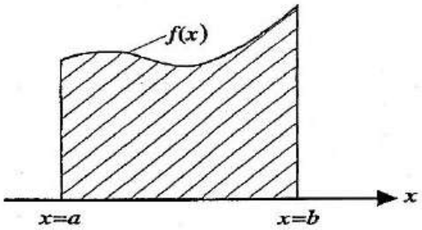

Figure 4: Calculating the integral of a function f(x)In the interval[a,b]

On the other hand, the integral of the function f(x)In the interval [a,b] represents the area under the curve of the function f(x). Therefore, calculating this integral is equivalent to approximating the area under the curve. Using this simple principle, various numerical methods have been introduced. In general, the approximation of this integral is represented in the following form:

$$\int_a^b f(x)dx = g_1 f_1 + g_2 f_2 + \cdots + g_N f_N = \sum_{k=1}^{N} g_k f_k \tag{7}$$

in which g_k the weighting coefficient functions and the f_k are the values of the function *f* at the points X_k. The equation mentioned is called the integral square, which is used to calculate the integral of the function. Now we will examine the differential squaring method.

Consider a one-dimensional problem, as shown in Figure (4). It is assumed that the function *f(x)*It has good uniformity at all points of the range.

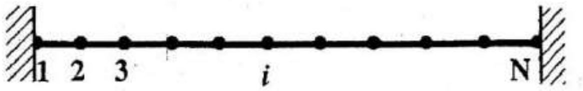

Figure 5: A one-dimensional problem

Using the idea of integral squaring, Bellman proposed in 1972 that the first-order derivatives of the function f(x)At the nodes Xi, can be approximated by a sum of function values over the entire domain as follows.

$$f_x(x_i) = \left(\frac{df}{dx}\right)_{x=x_i} = \sum_{j=1}^{N} g_{ij}\,.\,f(x_i) \quad , \text{ for } i = 1,2,\dots,N \tag{8}$$

in which g_{ij} weighting coefficients and Nis the number of sample points in the entire domain. The above equation is a differential quadrature equation or it is called DQ. It should be noted that the weight coefficients are different at different positions of Xi. Therefore, the key to solving the differential quadrature approximation is to determine the weight coefficients. So, in the method of square differences, to find the unknown of the differential equation, the derivatives of the function are considered to be equivalent to the sum of a series of products of the weight coefficients at certain points of the function and then the unknown is obtained from solving the system.

The main relationship of the method of square differences is generally defined as follows:

$$\left(\frac{\partial^n f(x)}{\partial x^n}\right)_{x=x_i} = \sum_{r=1}^{N} g_{ir}^{(n)}\,.\,f(x_r) \tag{9}$$

$$n = 1,2,\dots,N \quad , \quad i = 1,2,\dots,N$$

in which f is the desired function, N is the number of sample points, Xi is the i-th sample point of the function interval, and g_{ij} is the weighting coefficients for the derivative. Therefore, it can be seen that two very important and determining factors in the accuracy of the square difference method are the weighting coefficients and the selection of sample points, which will be mentioned below.

2.2.1. Selecting sample points

The method of selecting sample points is one of the most important parameters affecting the accuracy of the answers. There are several methods for selecting sample points, three of which will be mentioned here.

a) Sample points with equal distances

The first and simplest method for selecting sample points is to define the scope of the problem as N the point should be divided by equal distances. That is:

$$\Delta x = x_2 - x_1 = x_i - x_{i-1} = x_N - x_{N-1} \tag{10}$$

The division is done using the following relationship:

$$x_i = a + \left[\frac{i-1}{N-1}\right](b-a) \tag{11}$$

$$i = 1,2,\dots,N \quad , \quad a \le x_i \le b$$

3. Roots of Chebyshev polynomials

Usually, choosing points with equal distances does not yield accurate results. Experience has shown that choosing sample points with unequal distances gives accurate answers. The use of orthogonal polynomial roots is one of the common methods for selecting sample points with unequal distances. For example, Chebyshev polynomial roots are widely used in solving lubrication problems and orthotropic plates. In the field of using orthogonal polynomial roots, extensive studies were conducted by Kwan and Chang in 1989, during which it was shown that in the field of solving chemical engineering problems and applying the method of square differences, using Chebyshev polynomial roots as sample points leads to better results. On the other hand, Malik, in 1993, showed that using Legendre orthogonal polynomial roots is more useful than Chebyshev polynomials in solving elasticity and plate problems. In any case, depending on the type of problem, one of the mentioned methods can be used to select sample points.

The division using Chebyshev polynomials is as follows:

$$x_{\mathrm{i}} = \left[\mathrm{a}, \mathrm{a} + \frac{1}{2}\left(1 - \cos\left[\frac{2\mathrm{i}-1}{2\mathrm{N}}\right]\right)(\mathrm{b}-\mathrm{a}), \mathrm{b}\right] \tag{12}$$

$i = 2,3,\dots,N-1 \ \ , \ \ a \le x_i \le b \ \ , \ \ x_l = a\&x_N = b$

Roots of Legendre polynomials:

In order to divide the interval using the roots of the Legendre polynomial, first the polynomial of degree. We define n of the Legendre function:

$$\mathrm{p_n}(\mathrm{x}) = \frac{1}{2^{\mathrm{n}}\,\mathrm{n}!}\left[\frac{\mathrm{d}^{\mathrm{n}}}{\mathrm{dx}^{\mathrm{n}}}(\mathrm{x}^2-1)^{\mathrm{n}}\right] \tag{13}$$

And the division of points with this method will be using the following relations:

$$x_{\mathrm{i}} = \left[\mathrm{a}, \mathrm{a} + \frac{1}{2}\left(1 - \cos\left[\frac{(2\mathrm{i}-1)\pi}{2\mathrm{N}-4}\right]\right)(\mathrm{b}-\mathrm{a}), \mathrm{b}\right] \tag{14}$$

$i = 2,3,\dots,N-1 \ \ , \ \ a \le x_i \le b \ \ , \ \ x_l = a\&x_N = b$

What is observed in these relations is that the density of the number of nodes at the two ends of the interval is more than in the middle, which leads to better results. Of course, one of the shortcomings of the mentioned polynomials is that they do not include the beginning and end points of the interval, while in many engineering problems there is a need to apply boundary conditions at the beginning or end points of the interval.

In 1992, in two papers examining fluid mechanics problems and solving Navier-Stokes equations, Shaw and Richards proposed a formula that, in addition to selecting sample points with unequal distances, also includes the beginning and end points of the interval:

$$x_i = \left[\frac{1}{2}\left(1 - cos\left[\frac{(i-1)\pi}{N-1}\right]\right)\right] \tag{15}$$

$i = 1,2,\dots,N \ \ , \ \ a \le x_i \le b \ \ , \ \ x_i = a\,, x_N = b$

Of course, it should be noted that in problems whose derivatives the higher the order, the more sample points are needed.

4. Selecting the weighting coefficient function

When the weight coefficients were first determined, a bridge was established to connect the derivatives in the governing differential equations and the function values at the sample points. In other words, with the weight coefficients, the function values can easily be used to calculate its derivatives. To apply the differential squaring method to solve a differential equation, we must write the derivatives as the matrix product of the weight coefficients in the vector of unknowns, as mentioned above. Therefore, we must look for a solution to obtain the matrix of weight coefficients. Various methods have been proposed to calculate the matrix of weight coefficients. In these methods, first the function f_A known function is assumed. By taking the derivative of this function and satisfying the equality of the right and left sides of the above equation, the weight coefficients are obtained. This function, which is used to obtain the weight coefficient function, is called the test function or experimental function. After inventing the method in 1971, Bellman introduced two ways to obtain the weight coefficient matrix. The first method was the Gauss method, which obtains the weight coefficients by solving the Vandermonde apparatus. Unfortunately, in this method, when the number of the number of sample points increases, the Vandermonde matrix conditions will become abnormal and the solution of the device will be difficult. Bellman presented his second method to solve this problem. In this method, Legendre's transferred polynomials are used. In this method, the sample points are the roots of Legendre's polynomials, which is of course a big problem in using this method because in many engineering problems, it is necessary to choose the sample points arbitrarily and freely. Considering the many problems that existed in both methods presented by Bellman, many scholars tried to solve this problem with various test functions. In the following, we will examine and define several different methods.

4.1. Bellman's first method

In the first Bellman method, the function introduced as the test function is of the following form:

$$h(x) = x^k \quad and \quad k = 1,2,\dots,(N-1) \tag{16}$$

It is clear that the above relationship N test functions are given. To find these weighting coefficients, N test functions must be obtained at N sample points, namely $X_1,\dots,X_N$.

By substituting this function into the original relation of square differences, we will have:

$$\sum_{j=1}^{N} g_{ij} x_j^{k} = k x_i^{(k-1)} \tag{17}$$

$$k = 0,1,\dots,(N-1) \quad , \quad i = 1,2,\dots,N$$

So the number of weight coefficients per i,j=1,...,N is equal to N×N So we have a matrix N×N We have (i.e. N Equation and N unknown) which is calculated by solving a system, the vector of the weight coefficient matrix. The system of equations above has a unique solution, because its matrix is in the form of the Vandermonde matrix. Unfortunately, when N increases, the matrix is placed in an abnormal condition and it becomes difficult to find its inverse. To obtain results using this method, it is usually N it must be less than 13.

4.1.1. Bellman's second method

This method is similar to Bellman's first method, but it uses other test functions. Bellman defined another test function using Legendre's transformed orthogonal polynomials according to the following relation:

$$h_j(x) = \frac{L_N(x)}{(x - x_j) L_N^{(1)}(x_j)} \quad , \quad j = 1,2,\dots,N \tag{18}$$

So that in it N Number of sample points, $L_N(x)$ Legendre polynomial of order N and $L^{(1)}_N(x)$ is the first derivative of $L_N(x)$. By choosing the roots of the Legendre polynomial and using the above relation for N points, Bellman and his colleagues obtained a simple relation for calculating the weighting coefficients, which is as follows:

$$g_{ij} = \frac{L_N^{(1)}(x_i)}{(x_i - x_j) L_N^{(1)}(x_j)} \quad , \quad j \neq i \tag{19}$$

$$g_{ij} = \frac{1 - 2x_i}{2x_i(x_i - 1)} \tag{20}$$

Therefore, with the help of the above relations, calculating weight coefficients is an easy task.

As you can see in this method, unlike the first Bellman method, the selection of sample points is not free. This means that in this method, the selection of sample points is exactly based on the roots of the Legendre polynomials and is not free, whereas in many engineering problems, the selection of sample points should be completely arbitrary.

4.2. The Kwan Chang Method

To improve Bellman's methods in finding weight coefficients, many efforts have been made by researchers. One of the most important methods was introduced by Kwan and Chang. Kwan and Chang from the Lagrange median polynomial Below to they used it as a test function.

$$\begin{gathered} h_j(x) = \frac{M(x)}{(x - x_j).M^{(1)}(x_j)} \quad , \quad j = 1,2,\dots,N \\ M(x) = (x - x_1)(x - x_2)\dots(x - x_N) \\ M^{(1)}(x_i) = \prod_{j=1, r\neq i}^{N} (x_i - x_j) \end{gathered} \tag{21}$$

Therefore, the weighting factor in the N sample points are obtained as follows:

$$\begin{gathered} g_{ij} = \frac{1}{x_j - x_i} \prod_{j=1, r\neq i}^{N} \frac{x_i - x_r}{x_j - x_r} \quad , \quad j \neq i \\ g_{ij} = \sum_{r=1, r\neq i}^{N} \frac{1}{x_i - x_r} \end{gathered} \tag{22}$$

The advantage of this method over Bellman's second method was that there was no longer any restriction on the selection of sample points.

4.3. Method GDQ or Generalized Show Method

The general method of Shaw is inspired by Bellman methods. This method includes all other methods. Choosing a suitable test function that does not have two defects of Bellman functions is a very important task. One of the important parameters involved in this choice is a correct understanding of the logic governing the method of square differences and the role of the test function on these equations, because Shaw and Richards were able to achieve better results by choosing different test functions. The reason for this is that the test function is a function with the help of which we obtain the weight coefficients. By placing this function in the main formula of the method of square differences, the weight coefficients are obtained. After obtaining the weight coefficients, we use them in solving various differential equations, while the weight coefficients are extracted only for the derivative of the test function and only calculate the derivatives of the test function accurately. In fact, by using the weight coefficients obtained from the test function, we approximate the function governing the differential equation with the test function. Therefore, any test function that can better approximate other functions will result in more accurate answers. Four examples of basic polynomials are given below:

$$\begin{gathered} h_j(x) = x^{j-1} \quad , \quad j = 1,2,\dots,N \\ h_j(x) = \frac{L_N(x)}{(x - x_j) L_N^{(1)}(x_j)} \quad , \quad j = 1,2,\dots,N \\ h_j(x) = \frac{M(x)}{(x - x_j).M^{(1)}(x_j)} \quad , \quad j = 1,2,\dots,N \\ h_1(x) = 1 \quad , \qquad h_j(x) = (x - x_{j-1}).h_{j-1}(x) \quad , \quad j = 2,3,\dots,N \end{gathered} \tag{23}$$

in which $L_N(x)$ is a Legendre polynomial of degree N. It is also assumed that the degree of the approximation polynomial in relation (a) is *N-1*. Among these four original polynomials, equations (b) and (c) are Newton's median polynomials. The difference between equations (b) and (c) is in the distribution of sample points. If equation (c) is defined at the sample points of the Legendre polynomial. Equation (c) becomes (b). So, in fact, equation (b) is a special case of equation (c). As a result, the weighting coefficients for the first-order derivative are obtained from the following relationship:

$$g_{ir}^{(1)} = \frac{\prod_{j=1,j\neq i}^{N}(x_i - x_j)}{(x_i - x_r)\prod_{j=1,j\neq r}^{N}(x_r - x_j)} \qquad (24)$$

$$i,j,r = 1,2,\dots,N$$

Using the existing relationships, the weight coefficients for the remaining derivative orders can be obtained, which are:

$$\mathrm{g}_{\mathrm{ir}}^{(\mathrm{n})} = n\left[\mathrm{g}_{ii}^{(n-1)}\mathrm{g}_{ir}^{(1)} - \frac{\mathrm{g}_{ir}^{(n-1)}}{x_i - x_r}\right] \qquad (25)$$

$$i,r = 1,2,\dots,N \quad and\ n = 2,3,\dots,N-1$$

$$\mathrm{g}_{ii}^{(n)} = -\sum_{r=1,r\neq i}^{N}\mathrm{g}_{ir}^{(n)}\ ,\ \ i = 1,2,\dots,N \qquad (26)$$

$$i = 1,2,\dots,N \text{ and } \ n = 1,2,\dots,N-1$$

To calculate higher-order derivatives, we will have:

$$\left[g^{(n)}\right] = \left[g^{(1)}\right]\left[g^{(n-1)}\right] \qquad (27)$$

The above relations are independent of the number and location of the sample points and on the other hand led to more accurate solutions due to the smaller error caused by rounding. In addition, the number of mathematical operations is also less and saves on calculation time. It is necessary to mention again that in this numerical method, unlike conventional numerical methods, adding the number of sample points does not necessarily lead to a better solution. This can be mentioned as one of the disadvantages of this method, but of course, considering the speed of convergence to the solution, this disadvantage can be ignored with a smaller number of sample points.

5. Calculation of mechanical properties of beam CNTRC

As you saw in Chapter 3, there are various methods for finding the mechanical properties of beams. There are CNTRC, among which we can mention the mixing law and the Eshelby-Mori-Tanaka method. It is worth noting that a number of articles have calculated mechanical properties using both methods, and in this Paper, the mixing law was used.

5.1. Method Eshel by-Mori-Tanaka

In this method, the stiffness matrix is calculated from the following equation:

$$C = C_m + V_{CNT}\big((C_{CNT} - C_m).A\big).\left[V_m I + V_{CNT}A\right]^{-1} \qquad (28)$$

$$A = \left[I + S.C_m^{-1}.(\,C_{CNT} - C_m)\right]^{-1} \qquad (29)$$

Which we have:

Stiffness matrix matrix C_m:

C_{CNT}: Hardness matrix of carbon nanotubes

I: Fourth-order unit tensor

S: Fourth-order Ashlabian tensor.

5.2. Mixing law

One of the most general and basic relationships used to determine the elastic modulus of composites is the mixing law. In this model, the filler is considered as long fibers and the Young's and shear moduli of the composite are obtained. In this model, the complete transfer of any stress applied to the system from the matrix material to the filler is assumed. For nanotube reinforced composites, the mixing law relationships are used with the difference that the efficiency parameters CNT, have been added to the equations. In Fig.6 the distribution of carbon nanotubes in the composite beam is shown. As is clearly seen, the first case is a uniform distribution and the other case is a non-uniform and functionally graded distribution.

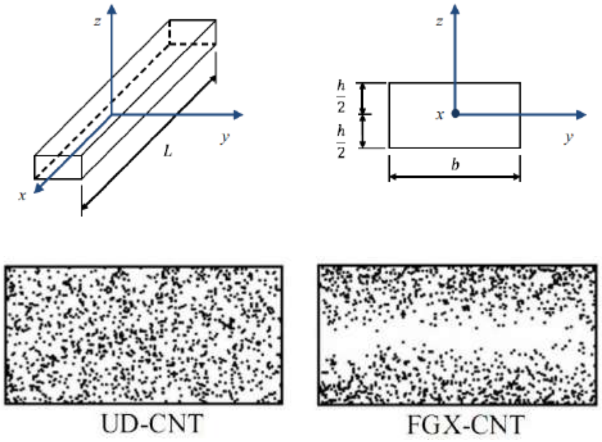

(a) (b)

Figure 6: Problem geometry and nanotube distribution in the beam CNTRC. (a) Uniform distribution. (b) Non-uniform and graded functional distribution

The relationships governing the shear and tensile moduli of a beam based on the mixing law are as follows:

$$E_{11} = \eta_1 V_{CNT}E_{11}^{CNT} + V_m E^m$$
$$\frac{\eta_2}{E_{22}} = \frac{V_{CNT}}{E_{22}^{CNT}} + \frac{V_m}{E^m} \qquad (30)$$
$$\frac{\eta_3}{G_{12}} = \frac{V_{CNT}}{G_{12}^{CNT}} + \frac{V_m}{G^m}$$

Which:

${E_{11}}^{CNT}, {E_{22}}^{CNT}, {G_{12}}^{CNT}$: Shear and tensile moduli of nanotubes

E^m, G^m: ModuleShear and tensile modulus of the matrix material

η_j $(j = 1, 2, 3)$: Nanotube efficiency coefficients

V_{CNT}, V_m: Volume fraction of matrix and nanotubes

It is worth noting that the effect of carbon nanotube size on the efficiency parameter definition CNT is considered, and this parameter is calculated by matching the results from molecular dynamics simulations and the mixing rule for the elastic modulus of CNTRCs.

As shown in Figure (1), each of the nanotube distribution states has its own volume fraction, which is obtained from the following relations:

$$V_{CNT} = V_{CNT}^{*} \qquad (UD\ CNTRC) \qquad (31)$$

$$V_{CNT}(z) = \left(\frac{4|z|}{h}\right) V_{CNT}^{*} \qquad (FG - X\ CNTRC)$$

Which:

$$V_{CNT}^{*} = \frac{w_{CNT}}{w_{CNT} + (\rho^{CNT}/\rho^{m}) - (\rho^{CNT}/\rho^{m}) w_{CNT}} \qquad (32)$$

Also, other properties of the beam CNTRC, including Poisson's ratio, density, coefficient of thermal expansion in the longitudinal direction, and coefficient of thermal expansion in the transverse direction, can be obtained similarly to other properties of the sheet as follows:

$$\nu_{12} \rho \alpha_{11} \alpha_{22}$$

$$\begin{aligned} \nu_{12} &= V_{CNT}^{*}\, \nu_{12}^{CNT} + V_m \nu^{m} \\ \rho &= V_{CNT} \rho^{CNT} + V_m \rho^{m} \\ \alpha_{11} &= V_{CNT} \alpha_{11}^{CNT} + V_m \alpha^{m} \\ \alpha_{22} &= (1 + \nu_{12}^{CNT}) V_{CNT} \alpha_{22}^{CNT} + (1 + \nu^{m}) V_m \alpha^{m} - \nu_{12} \alpha_{11} \end{aligned} \qquad (33)$$

Which:

ν_{12}^{CNT} , ν^{m}: Poisson's ratio of matrix and nanotube

ρ^{m} , ρ^{CNT}: Nanotube density and matrix

α_{22}^{CNT} , α_{11}^{CNT}: Thermal expansion coefficient of the nanotube in the longitudinal and transverse directions, respectively

α^{m}: Matrix thermal expansion coefficient

The results of the mixing law are in very good agreement with the experimental results.

6. Extraction of state space equations

Without considering the volume forces, the equations of motion can be written as the following equation:

$$\begin{aligned} \sigma_{x,x} + \tau_{xz,z} &= \rho \frac{\partial^2 u}{\partial t^2} \\ \tau_{xz,x} + \sigma_{z,z} &= \rho \frac{\partial^2 w}{\partial t^2} \end{aligned} \qquad (34)$$

in which σ_z and σ_x Axial stresses, τ_{xz} Shear stress, wandu Mechanical displacement in the transverse and axial directions, respectively, ρ Density of materials and t they are time. The relationship between strain and mechanical displacement for small deformations can be expressed as Equation 35.

$$\begin{aligned} \varepsilon_x &= \frac{\partial u}{\partial x} \\ \varepsilon_z &= \frac{\partial w}{\partial z} \\ \gamma_{xz} &= \frac{\partial u}{\partial z} + \frac{\partial w}{\partial x} \end{aligned} \qquad (35)$$

That u and w Displacements and Normal strains in the direction of the coordinate axes, respectively x and z they are. Shear strain in the plane it is xz. Using Hooke's law and strain-displacement equations, the stress-displacement equations are obtained in the following form:

$$\begin{aligned} \sigma_x &= Q_{11} \frac{\partial u}{\partial x} + Q_{13} \frac{\partial w}{\partial z} \\ \sigma_z &= Q_{11} \frac{\partial u}{\partial x} + Q_{33} \frac{\partial w}{\partial z} \\ \tau_{xz} &= Q_{55} \left[\frac{\partial w}{\partial x} + \frac{\partial u}{\partial z} \right] \end{aligned} \qquad (36)$$

That *Q11*, *Q33*, *Q13* and *Q55* they are calculated as follows:

$$Q_{11} = \frac{E_{11}}{\Delta}, \qquad Q_{33} = \frac{E_{33}}{\Delta}, \qquad Q_{13} = \nu_{31} \frac{E11}{\Delta}, \qquad Q_{55} = G_{13} \qquad \Delta = 1 - \nu_{31} \nu_{313} \qquad (37)$$

It should be noted that the degree of functional or homogeneity of a material is reflected in the stress-strain relationships. In a homogeneous material, the modulus of elasticity E is constant in all directions. Using equations (2) and (4), the state space equations are obtained in the following form:

$$\begin{aligned} \frac{\partial \sigma_z}{\partial z} &= -\frac{\partial \tau_{xz}}{\partial x} + \rho \frac{\partial^2 w}{\partial t^2} \\ \frac{\partial u}{\partial z} &= -\frac{\partial w}{\partial x} + \frac{1}{Q_{55}} \tau_{xz} \\ \frac{\partial w}{\partial z} &= \frac{1}{Q_{33}} \sigma_z - \frac{Q_{11}}{Q_{33}} \frac{\partial u}{\partial x} \\ \frac{\partial \tau_{xz}}{\partial z} &= -\frac{Q_{13}}{Q_{33}} \frac{\partial \sigma_z}{\partial x} - \left(Q_{11} - \frac{Q_{13} Q_{11}}{Q_{33}} \right) \frac{\partial^2 u}{\partial x^2} + \rho \frac{\partial^2 u}{\partial t^2} \end{aligned} \qquad (38)$$

The boundary conditions for the various supports are as follows:

Simple support $\qquad \sigma_x = w = 0 \qquad (39)$

Free support $\sigma_x = \tau_{xz} = 0$

7. Analytical solution of a simply supported beam

First, the state space matrix is calculated for each layer, then the surface conditions between the layers and the continuity of stress and displacement are applied, and the overall state space matrix is obtained. Finally, by applying the surface conditions of the lower and upper surfaces (Equation 40), the equations are solved.

The surface conditions at the top and bottom surfaces of the beam are as follows:

$$\sigma_z = \tau_{xz} = 0, \qquad at\ z = -\frac{h}{2}, \frac{h}{2} \tag{40}$$

The boundary conditions at the simple support are as follows:

$$\sigma_x = w = 0, \qquad at\ x = 0, L \tag{41}$$

Considering the boundary conditions, the following Fourier expansions have been considered for stresses and displacements

$$\begin{aligned}
u &= \sum_{m=1}^{\infty} \bar{U}(\mathrm{z}) \cos\left(p_m x\right) e^{(i\omega t)} \\
w &= \sum_{m=1}^{\infty} \bar{W}(\mathrm{z}) \sin\left(p_m x\right) e^{(i\omega t)} \\
\sigma_z &= \sum_{m=1}^{\infty} \bar{\sigma}_z(\mathrm{z}) \sin\left(p_m x\right) e^{(i\omega t)} \\
\tau_{xz} &= \sum_{m=1}^{\infty} \bar{\tau}_{xz}(\mathrm{z}) \cos\left(p_m x\right) e^{(i\omega t)} \\
\sigma_x &= \sum_{m=1}^{\infty} \bar{\sigma}_x(\mathrm{z}) \sin\left(p_m x\right) e^{(i\omega t)}
\end{aligned} \tag{42}$$

In the above relationship ωt the natural frequency of the beam and t is the time. By substituting the above equations into the state space equations (4-15), the following relations are obtained.

$$\begin{aligned}
\frac{\partial \bar{\sigma}_z}{\partial z} &= p_m \bar{\tau}_{xz} - \rho\omega^2 \bar{W} \\
\frac{\partial \bar{U}}{\partial z} &= -p_m \bar{W} + \frac{1}{Q_{55}} \bar{\tau}_{xz} \\
\frac{\partial \bar{W}}{\partial z} &= \frac{1}{Q_{33}} \bar{\sigma}_z + \frac{Q_{11}}{Q_{33}} p_m \bar{U}
\end{aligned} \tag{43}$$

Vector δ which includes state space variables is considered as follows.

$$\delta = \left\{ \bar{\sigma}_z \quad \bar{U} \quad \bar{W} \quad \bar{\tau}_{xz} \right\} \tag{44}$$

Using the defined vector, Equations (45) can be written in matrix form as follows.

$$\frac{d\delta}{dz} = G\delta \tag{45}$$

That G is defined as follows.

$$G = \begin{bmatrix} 0 & 0 & -\rho\omega^2 & p_m \\ 0 & 0 & -p_m & \dfrac{1}{Q_{55}} \\ \dfrac{1}{Q_{33}} & \dfrac{Q_{11}}{Q_{33}} p_m & 0 & 0 \\ -\dfrac{Q_{13}}{Q_{33}} p_m & (\mathrm{Q}_{11} - \dfrac{Q_{13}Q_{11}}{Q_{33}}) p_m^2 - \rho\omega^2 & 0 & 0 \end{bmatrix} \tag{46}$$

The solution to the differential Equations (47) in matrix form is as follows.

$$\delta(z) = e^{\int_{z_0}^{z} G dz} \delta(z_0) \tag{47}$$

8. Semi-analytical solution of a beam with various supports using the differential square method

Initially, a semi-analytical solution is performed for the simple support and compared with the analytical solution presented in the previous section, which allows the best case for the number of sample points to be obtained.

To solve the semi-analytical state space equations, the beam is oriented in the direction *x* is discretized using the method of difference of squares with the help of *N* points:

$$x_i = \frac{L}{2}\left(1 - \cos\frac{(i-1)\pi}{N-1}\right) \tag{48}$$

in which xi is the length of the it *h* point and *L* is the total length of the beam. The derivatives with respect to x are discretized as follows:

$$\left(\frac{\partial^{\mathrm{n}} \mathrm{f}(\mathrm{x},\mathrm{z})}{\partial \mathrm{x}^{\mathrm{n}}}\right)_{\mathrm{x}=\mathrm{x}_{\mathrm{i}}} = \sum_{\mathrm{j}=1}^{\mathrm{N}} \mathrm{A}_{\mathrm{ij}}^{(\mathrm{n})} \ \mathrm{f}\left(\mathrm{x}_{\mathrm{j}}, \mathrm{z}\right) \tag{49}$$

Values of the weight coefficients are calculated based on the Quan-Chang method according to the following formula:

$$\begin{aligned}
\mathrm{A}_{\mathrm{ij}} &= \frac{1}{x_j - x_i} \prod_{j=1, r \neq i}^{N} \frac{x_i - x_r}{x_j - x_r} \quad , \ i \neq j \\
\mathrm{A}_{\mathrm{ij}} &= \sum_{r=1, r \neq i}^{N} \frac{1}{x_i - x_r} \qquad , \ i = j
\end{aligned} \tag{50}$$

In this case, the solution process is similar to the analytical case for a simple support, with the difference that the dependence of the state space equations on the variables x and its derivatives are solved using the differential square method and the matrices that are calculated have much larger dimensions than the analytical solution. First, the state space matrix is calculated for each layer, then the boundary conditions between the layers and the continuity of stress and displacement are applied and the overall state space matrix is obtained. Finally, using the stress and displacement relationship of the upper and lower surfaces of the beam, the equations are solved.

Mode CS:

$$\begin{aligned} &u = w = 0, \quad \frac{\partial w}{\partial x} = 0, \quad && at\ x = 0 \\ &\sigma_x = w = 0, && at\ x = L \end{aligned} \tag{51}$$

Mode CF:

$$\begin{aligned} &u = w = 0, \quad \frac{\partial w}{\partial x} = 0, \quad && at\ \mathrm{x} = 0 \\ &\sigma_x = \tau_{xz} = 0, && at\ x = L \end{aligned} \tag{52}$$

Mode CC:

$$\begin{aligned} &u = w = 0, \quad \frac{\partial w}{\partial x} = 0, \quad && at\ x = 0 \\ &u = w = 0, \quad \frac{\partial w}{\partial x} = 0, && at\ x = L \end{aligned} \tag{53}$$

State space variables at a point(i)th are:

$$\delta_{(\mathrm{i})} = \left\{ \sigma_{\mathrm{z}_{(\mathrm{i})}},\ \mathrm{u}_{(\mathrm{i})},\ \mathrm{w}_{(\mathrm{i})},\ \tau_{\mathrm{xz}(\mathrm{i})} \right\}^{\mathrm{T}} \tag{54}$$

According to Equation 54, the point state space equations are (i) will be as follows:

$$\frac{\mathrm{d}\delta_{(\mathrm{i})}}{\mathrm{dz}} = \mathrm{G}_{(\mathrm{i})}\ \delta_{(\mathrm{i})} \tag{55}$$

By writing Equation 55 for different points in the solution domain, the system of total equations is obtained:

$$\frac{\partial \Delta}{\partial \mathrm{z}} = \mathrm{M}\Delta \tag{56}$$

In which, the matrix is called the general matrix and is defined as follows:

$$\Delta = \left\{ \sigma_z, u, w, \tau_{xz} \right\}^{T}_{1\times(6\times N)} \tag{57}$$

That:

$$\begin{aligned} \sigma_z &= \left\{ \sigma_{\mathrm{z}_1}, \sigma_{\mathrm{z}_2}, \ldots, \sigma_{\mathrm{z}_{\mathrm{N_x \times N_y}}} \right\}^{T}_{1\times N} \\ u &= \left\{ \mathrm{u}_1, \mathrm{u}_2, \ldots, \mathrm{u}_{\mathrm{N_x \times N_y}} \right\}^{T}_{1\times N} \\ w &= \left\{ \mathrm{w}_1, \mathrm{w}_2, \ldots, \mathrm{w}_{\mathrm{N_x \times N_y}} \right\}^{T}_{1\times N} \\ \tau_{xz} &= \left\{ \tau_{\mathrm{xz1}}, \tau_{\mathrm{xz2}}, \ldots, \tau_{\mathrm{xzN_x \times N_y}} \right\}^{T}_{1\times N} \end{aligned} \tag{58}$$

Considering the removal of dependency M to x and its derivatives, the solution to Equation (57) can be easily obtained. But before that, boundary conditions in the x direction for the boundary points must be determined and applied. After applying the boundary conditions, the dimensions of the overall matrix are reduced and Equations (59) change to the following form.

$$\frac{\partial \Delta_{\mathrm{b}}}{\partial \mathrm{z}} = \mathrm{M}\Delta_{\mathrm{b}} \tag{59}$$

The analytical solution of Equations 59 is as follows:

$$\Delta_{\mathrm{b}} = \mathrm{e}^{\int_{z_0}^{z} \mathrm{M_b z}} \left\{ \mathrm{c} \right\} \tag{60}$$

that the column matrix constants *C* column vector value It is at the bottom of the layer.

9. Applying surface conditions to the upper and lower surfaces

According to Equation 60, it can be written:

$$\begin{bmatrix} \bar{\sigma}_z\left(h/2\right) \\ \bar{U}\left(h/2\right) \\ \bar{W}\left(h/2\right) \\ \bar{\tau}_{xz}\left(h/2\right) \end{bmatrix} = \begin{bmatrix} s_{11} & s_{12} & s_{13} & s_{14} \\ s_{21} & s_{22} & s_{23} & s_{24} \\ s_{31} & s_{32} & s_{33} & s_{34} \\ s_{41} & s_{42} & s_{43} & s_{44} \end{bmatrix} \begin{bmatrix} \bar{\sigma}_z\left(-h/2\right) \\ \bar{U}\left(-h/2\right) \\ \bar{W} -\left(h/2\right) \\ \bar{\tau}_{xz}\left(-h/2\right) \end{bmatrix} \tag{61}$$

Which we will have by applying boundary conditions.

$$\begin{bmatrix} 0 \\ \bar{U}\left(h/2\right) \\ \bar{W}\left(h/2\right) \\ 0 \end{bmatrix} = \begin{bmatrix} s_{11} & s_{12} & s_{13} & s_{14} \\ s_{21} & s_{22} & s_{23} & s_{24} \\ s_{31} & s_{32} & s_{33} & s_{34} \\ s_{41} & s_{42} & s_{43} & s_{44} \end{bmatrix} \begin{bmatrix} 0 \\ \bar{U}\left(-h/2\right) \\ \bar{W} -\left(h/2\right) \\ 0 \end{bmatrix} \tag{62}$$

The previous equations are solved by removing unnecessary rows and columns.

$$\begin{bmatrix} 0 \\ 0 \end{bmatrix} = \begin{bmatrix} s_{12} & s_{13} \\ s_{42} & s_{43} \end{bmatrix} \begin{bmatrix} \bar{U}\left(-h/2\right) \\ \bar{W}\left(-h/2\right) \end{bmatrix} \tag{63}$$

To analyze the free vibrations of the beam, considering that the left side of Equations 63 becomes zero, the natural frequencies of the beam have been calculated by setting the determinants of the coefficients equal.

The natural frequencies in the analytical solution are calculated using the following equation.

$$\left| S_A \right| = 0 \tag{64}$$

The natural frequencies in the semi-analytical solution are calculated using the following equation.

$$\left| S_D \right| = 0 \tag{65}$$

To demonstrate the accuracy and precision of the calculations in the previous chapter, numerical results are presented in the form of graphs and tables for various problems and materials in this chapter. The results include the calculation of the natural frequency of the nanocomposite beam FG, which has been validated according to the results in authoritative papers. First, the convergence of the numerical solution (DQ) for a simple support is shown and compared with the analytical solution. Then, to ensure the accuracy and precision of the method used, the results for different boundary conditions are compared and validated with authoritative papers. Next, the effect of the dimensions and percentage of nanotube presence (V*CNT) on the natural frequencies is investigated and their results are presented for comparison. In Table 1, the values of nanotube efficiency (iη) are shown for the studied nanocomposite beams.

Table 1
Nanotube efficiency values (*Iη*)

CNT efficiency parameters	VCNT		
	0.12	0.17	0.28
1η	1.2833	1.3414	1.3238
2η	1.0556	1.7101	1.7380
3η	1.0556	1.7101	1.7380

10. Solution convergence DQ and comparison with analytical solution

In this section, the convergence of the differential square solution with increasing number of sample points is investigated and compared with the analytical solution. In Table 2, the first three modes of natural frequencies for a uniform distribution of nanotubes (UD) and functional graded distribution (FG-X) are presented. The frequencies presented in the table are for a nanocomposite beam with simply supported SS boundary conditions. According to the table, at the number of sample points of 9 and 10, the results of the semi-analytical solution have good convergence, and it is also seen that with increasing the vibration mode, the number of sample points of convergence increases. It is observed that the numerical solution provides very fast and good convergence, and its results are very close to the results of the analytical solution.

Table 2
Convergence of the results of the first three modes of natural frequencies in the numerical solution and comparison with the analytical solution

Mode	Method	UD	FG-X
1	DQM (N=5)	1.2243	1.3575
	(N=6)	1.2284	1.3619
	(N=7)	1.2287	1.3621
	(N=8)	1.2287	1.3621
	(N=9)	1.2287	1.3621
	Exact	1.2290	1.3624
2	DQM (N=5)	3.656	3.8071
	(N=6)	3.1823	3.3353
	(N=7)	3.2402	3.3929
	(N=8)	3.2383	3.3910
	(N=9)	3.2384	3.3912
	Exact	3.2384	3.3914
3	DQM (N=5)	4.8918	5.0376
	(N=6)	4.9453	5.1269
	(N=7)	5.0769	5.2219
	(N=8)	5.2929	5.4372
	(N=9)	5.2646	5.4089
	(N=10)	5.2700	5.4130
	Exact	5.2675	5.4121

11. Validation of the problem-solving method

In this section, the accuracy of the presented solution is examined and validation is performed. For this purpose, the problem conditions that are described in the articles [31] and [32] have been considered and the numerical results of the present study have been compared with the results of the aforementioned articles. Table 3 shows the changes of the first mode of the dimensionless natural frequency for simple-simple (SS), simple-clamped (CS) and clamped-clamped (CC) supports. The results in this table have been considered in two completely analytical and numerical (DQ) methods for the simple support and in the numerical (DQ) method for the other supports. A comparison can be made between the results obtained from the analytical solution, the numerical solution and the results of the aforementioned articles. The results presented; compliance it shows a very good agreement between the two methods used.

12. Effect of various boundary conditions on natural frequency

To better compare the effect of boundary conditions on beam behavior, the first four dimensionless natural frequency modes for different boundary conditions are shown together in Table 4.

Table 3
First mode dimensionless natural frequency for simple-simple (SS), simple-clamped (CS) and clamped-clamped (CC) supports and comparison with the results of papers [31] and [32]

CNT distribution	Boundary conditions	Present Perfect	Present DQM	Reference [1]	Reference [2]
UD-CNT	CC	-	1.6817	1.6691	1.6678
	CS	-	1.4495	1.4565	1.4556
	SS	1.229	1.2287	1.2581	1.2576
FGX-CNT	CC	-	1.7477	1.7242	1.7230
	CS	-	1.5414	1.5394	1.5385
	SS	1.3624	1.3621	1.3859	1.3852

Table 4
The first four dimensionless natural frequency modes for different boundary conditions

BC	Mode			
	1	2	3	4
CF	0.5727	2.1128	4.2359	6.3008
SS	1.3624	3.3914	5.4121	7.4261
CS	1.5414	3.4651	5.4543	7.5711
CC	1.7477	3.5353	5.5040	7.6071

According to Table 4, the stiffer or more restricted the plate is in the support, the higher the natural frequency it will have. In the case CC has the highest natural frequency and CF has the lowest natural frequency.

13. The effect of length to thickness ratio (L/h) at natural frequencies

At this stage, the aim is to investigate the effect of the length to thickness ratio (L/h) in the dimensionless natural frequency of a nanocomposite beam with nanotube distribution FG-X. In Figure 7, the changes in the dimensionless natural frequency as a function of the ratio (L/h) for the FG-X nanocomposite beam can be seen. With increasing L/h, the natural frequency increases, and at low values, the changes in the natural frequency are very severe.

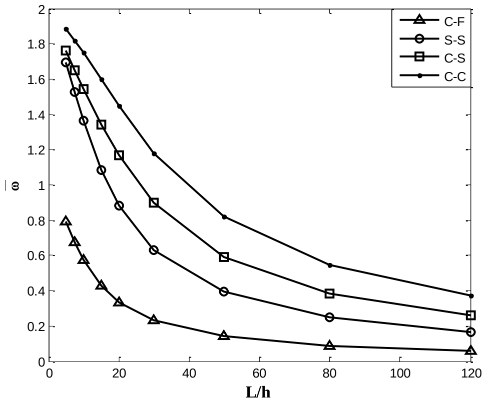

Figure 7: Variations of dimensionless natural frequency in terms of ratio (L/h) for FG-X nanocomposite beam

14. The effect of the volume fraction of the presence of nanotubes (V*CNT) in nanocomposite beam

At this stage, the aim is to investigate the effect of the volume fraction of the presence of nanotubes (V*CNT) in the natural frequency of the FG-X and UD nanocomposite beam. With increasing V*CNT, the percentage of mixing method and, in the direction of thickness, the numerical method of differential quadrature DQ and the nanotubes increases. Tables 5, 6, 7 and 8 show the changes in the first three modes of the dimensionless natural frequency of the beam with CC, CS, SS and CF supports in terms of V*CNT, respectively. It is observed that with increasing the V*CNT parameter, the dimensionless natural frequency increases.

Table 5
Variations of the first three modes of the dimensionless natural frequency of the beam with CC supports in terms of V*CNT(L/h=20)

V*CNT		Mode		
		1	2	3
0.12	UD	1.6817	3.4196	5.3825
	FG-X	1.7477	3.5353	5.5040
0.17	UD	2.1524	4.3955	6.9415
	FG-X	2.2368	4.5264	7.0914
0.28	UD	2.3796	4.8195	7.5578
	FG-X	2.4299	4.9131	7.6625

Table 6
Variations of the first three modes of the dimensionless natural frequency of the beam with CS supports in terms of V*CNT(L/h=20)

V*CNT		Mode		
		1	2	3
0.12	UD	1.0351	2.6928	4.6294
	FG-X	1.1674	2.9170	4.8939
0.17	UD	1.2817	3.3878	5.8838
	FG-X	1.4518	3.6784	6.2224
0.28	UD	1.6807	4.1134	6.8294
	FG-X	2.1597	4.8186	7.6215

Table 7
Variations of the first three modes of the dimensionless natural frequency of the beam with SS supports in terms of V*CNT(L/h=20)

V*CNT		Mode		
		1	2	3
0.12	UD	0.7536	2.4580	4.4434
	FG-X	0.8842	2.7247	4.7494
0.17	UD	0.9203	3.0632	5.6188
	FG-X	1.0839	3.4085	6.0155
0.28	UD	1.1262	3.5825	6.3696
	FG-X	1.3053	3.8759	6.6379

Table 8
Variations of the first three modes of the dimensionless natural frequency of the beam with CF supports in terms of V*CNT(L/h=20)

V*CNT		Mode		
		1	2	3
0.12	UD	0.3361	1.6040	3.5326
	FG-X	0.2814	1.4311	3.2575
0.17	UD	0.3416	1.7765	4.0979
	FG-X	0.4092	1.9990	4.4523
0.28	UD	0.4237	2.0963	4.6998
	FG-X	0.5033	2.3040	4.9895

15. Conclusion

In this research to the vibration analysis of a Nano-beam unidirectional FGM (functional properties along the beam thickness) with carbon nanotubes and a Layer-Metal and ceramic braces on various supports w whether simple, complex, etc. became. The solution method used is the assumptions in this research in this way it is that the material properties change along the thickness as an exponential function slow, the beam is under plane tension, no there is no thickness variation or discontinuity in the longitudinal direction of the beam, Poisson's ratio in the layer FGM is constant along its thickness. Accordingly, the following results have been obtained:

1. The stiffer, or more constrained, the sheet in the support will have a higher natural frequency.
2. In the state CC has the highest natural frequency and CF has the lowest natural frequency.
3. By increasing the length to thickness ratio L/h the natural frequency increases.
4. When the length to thickness ratio is low, the natural frequency changes are very severe.
5. By increasing the volume fraction parameter of the presence of nanotubes V*CNT increases the dimensionless natural frequency.
6. In the case where the volume fraction of nanotubes in the beam FGM is fixed, relying sometimes YRadar-GYRadar has the highest natural frequency in all modes.
7. In the case where the volume fraction of nanotubes in the beam FGM is fixed, relying sometimes YRadar-free has the lowest natural frequency of all modes.
8. In any case of the volume fraction of nanotubes in the beam FGM the first mode has the lowest frequency and subsequent modes have a higher frequency than the previous mode.

References

[1] Ichikawa, Kiyoshi, ed. Functionally graded materials in the 21st century: a workshop on trends and forecasts. Springer Science & Business Media, 2001.26-28. DOI: 10.1007/978-1-4615-4373-2

[2] Suresh, Subra, and Andreas Mortensen. “Fundamentals of Functionally Graded Materials.” London: IOM Communications Ltd., 1998.

[3] Sankar, B.V. “An elasticity solution for functionally graded beams.” Composites Science and Technology 61.5 (2001): 689–696. DOI: https://doi.org/10.1016/S0266-3538(01)00007-0.

[4] Chakraborty, A., and S. Gopalakrishnan. “A spectrally formulated finite element for wave propagation analysis in functionally graded beams.” International Journal of Solids and Structures 40.10 (2003): 2421–2448. DOI: https://doi.org/10.1016/S0020-7683(03)00029-5.

[5] Chakraborty, A., S. Gopalakrishnan, and J.N. Reddy. “A new beam finite element for the analysis of functionally graded materials.” International Journal of Mechanical Sciences 45.3 (2003): 519–539. DOI: https://doi.org/10.1016/S0020-7403(03)00058-4.

[6] Shi, Z.F., and Y. Chen. “Functionally graded piezoelectric cantilever beam under load.” Archive of Applied Mechanics 74.3–4 (2004): 237–247. DOI: https://doi.org/10.1007/BF02637199.

[7] Ding, H. J., D. J. Huang, and WQ2304402 Chen. "Elasticity solutions for plane anisotropic functionally graded beams." International Journal of Solids and Structures 44.1 (2007): 176-196. https://doi.org/10.1016/j.ijsolstr.2006.04.026

[8] Kapuria, S., M. Bhattacharyya, and A.N. Kumar. “Bending and free vibration response of layered functionally graded beams: A theoretical model and experimental validation.” Composite Structures 82.3 (2008): 390–402. DOI: https://doi.org/10.1016/j.compstruct.2007.01.019 .

[9] Kadoli, Ravikiran, Kashif Akhtar, and N. Ganesan. “Static analysis of functionally graded beams using higher order shear deformation theory.” Applied Mathematical Modelling 32.12 (2008): 2509–2525. DOI: https://doi.org/10.1016/j.apm.2007.09.015 .

[10] Li, X.F. “A unified approach for analyzing static and dynamic behaviors of functionally graded Timoshenko and Euler–Bernoulli beams.” Journal of Sound and Vibration 318.4–5 (2008): 1210–1229. DOI: https://doi.org/10.1016/j.jsv.2008.04.017 .

[11] Tao, Yu, and Zhong Zheng. “Bending analysis of a functionally graded piezoelectric cantilever beam.” Science in China Series G: Physics, Mechanics & Astronomy 50.1 (2007): 97–108. DOI: https://doi.org/10.1007/s11433-007-2006-6 .

[12] Huang, De-jin, Hao-jiang Ding, and Wei-qiu Chen. “Analytical solution for functionally graded anisotropic cantilever beam subjected to linearly distributed load.” Applied Mathematics and Mechanics 28.7 (2007): 855–860. DOI: https://doi.org/10.1007/s10483-007-0702-1.

[13] Huang, De-jin, Hao-jiang Ding, and Wei-qiu Chen. “Analytical solution for functionally graded anisotropic cantilever beam under thermal and uniformly distributed load.” Journal of Zhejiang University-SCIENCE A 8.9 (2007): 1351–1355. DOI: https://doi.org/10.1631/jzus.2007.A1351.

[14] Ying, Ji, Chuan-Fu Lu, and Wei-Qiu Chen. “Two-dimensional elasticity solutions for functionally graded beams resting on elastic foundations.” Composite Structures 84.3 (2008): 209–219. DOI: https://doi.org/10.1016/j.compstruct.2006.12.004.

[15] Zhong, Zhihong, and Tianyu Yu. “Analytical solution of a cantilever functionally graded beam.” Composites Science and Technology 67.3–4 (2007): 481–488. DOI: https://doi.org/10.1016/j.compscitech.2006.08.023.

[16] Ding, Hao-jiang, De-jin Huang, and Wei-qiu Chen. “Elasticity solutions for plane anisotropic functionally graded beams.” International Journal of Solids and Structures 44.1 (2007): 176–196. DOI: https://doi.org/10.1016/j.ijsolstr.2006.04.036.

[17] Farhatnia, Farhad, Ghasem Sharifi, and Sadegh Rasouli. “Numerical and analytical approach of thermo-mechanical stresses in FGM beams.” Proceedings of the World Congress on Engineering 2 (2009): [No page range]. DOI: Not available.

[18] Alibeigloo, Akbar. “Thermoelasticity analysis of functionally graded beam with integrated surface piezoelectric layers.” Composite Structures 92.7 (2010): 1535–1543. DOI: https://doi.org/10.1016/j.compstruct.2009.10.015.

[19] Simsek, Mehmet. “Fundamental frequency analysis of functionally graded beams by using different higher-order beam theories.” Nuclear Engineering and Design 240.4 (2010): 697–705. DOI: https://doi.org/10.1016/j.nucengdes.2009.12.013.

[20] Thai, Hoc, and Tuan Vo. “Bending and free vibration of functionally graded beams using various higher-order shear deformation beam theories.” Nuclear Engineering and Design 262 (2012): 57–66. DOI: https://doi.org/10.1016/j.nucengdes.2013.03.001.

[21] Pradhan, Krishna, and Snehashish Chakraverty. “Free vibration of Euler and Timoshenko functionally graded beams by Rayleigh-Ritz method.” Composites Part B: Engineering 51 (2013): 175–184. DOI: https://doi.org/10.1016/j.compositesb.2013.02.030.

[22] Thomas, Biju, Pravin Inamdar, Tapas Roy, and B. K. Nada. “Finite element modeling and free vibration analysis of functionally graded nanocomposite beam reinforced by randomly oriented carbon nanotubes.” International Journal of Theoretical and Applied

Research in Mechanical Engineering 2 (2013): 2319–3182. DOI: Not available.

[23] Mohammadimehr, Mohammad, and Mahdi Mahmudian. “Bending and free vibration analysis of nonlocal functionally graded nanocomposite Timoshenko beam model reinforced by SWBNNT based on modified coupled stress theory.” Journal of Nanostructures 3.4 (2013): 483–492. DOI: Not available.

[24] Heshmati, Mohammad, and Mohammad Yas. “Free vibration analysis of functionally graded CNT-reinforced nanocomposite beam using Eshelby-Mori-Tanaka approach.” Journal of Mechanical Science and Technology 27.11 (2013): 3403–3408. DOI: https://doi.org/10.1007/s12206-013-0857-4.

[25] Moradi-dastjerdi, Reza, Gholamreza Payganeh, and Hamed Malek-mohammadi. “Free vibration analysis of functionally graded CNT-reinforced nanocomposite sandwich plates resting on elastic foundation.” Journal of Solid Mechanics 7.2 (2015): 158–172. DOI: Not available.

[26] Bellman, Richard, and John Casti. “Differential quadrature and long-time integration.” Journal of Mathematical Analysis and Applications 235.2 (1997): 235–238. DOI: https://doi.org/10.1006/jmaa.1997.5717.

[27] Bellman, Richard, B. G. Kashef, and John Casti. “Differential quadrature: A technique for the rapid solution of nonlinear partial differential equations.” Journal of Computational Physics 10.1 (1972): 40–52. DOI: https://doi.org/10.1016/0021-9991(72)90045-9.

[28] Hu, Li-Chung, and Chin-Rong Hu. “Identification of rate constants by differential quadrature in partially measurable compartmental models.” Mathematical Biosciences 21.1 (1974): 71–78. DOI: https://doi.org/10.1016/0025-5564(74)90054-5.

[29] Civan, Faruk, and Charles M. Sliepcevich. “Application of differential quadrature to transport processes.” Journal of Mathematical Analysis and Applications 93.1 (1983): 206–221. DOI: https://doi.org/10.1016/0022-247X(83)90116-0.

[30] Naadimuthu, G., Richard Bellman, and K. M. Wang. “Differential quadrature and partial differential equation: Some numerical results.” Acta Mechanica 24.1 (1995): 85–94. DOI: https://doi.org/10.1007/BF01176994.

[31] Yas, Mohammad Hossein, and Nima Samadi. “Free vibration and buckling analysis of carbon nanotube-reinforced composite Timoshenko beam on elastic foundation.” International Journal of Pressure Vessels and Piping 98 (2012): 119–128. DOI: https://doi.org/10.1016/j.ijpvp.2012.07.003.

[32] Yang, Liao-Liang, and Supachai Kitipornchai. “Nonlinear free vibration of functionally graded carbon nanotube-reinforced composite beams.” Composite Structures 92.3 (2010): 676–683. DOI: https://doi.org/10.1016/j.compstruct.2009.09.004.

[33] Zarehparvar-Shoja, Mohammad, Reza Shadnia, and Amin Kazemi Beydokhti. “Physical and chemical surface modifiers of carbon nanotubes on the mechanical and physical properties of concrete.” Journal of Civil Engineering Researchers 7.1 (2025): 34–47. DOI: https://doi.org/10.61186/JCER.7.1.34.

J-Researchers

Journal of Civil Engineering Researchers

Journal homepage: www.journals-researchers.com

Numerical Investigation of the Seismic and Axial Performance of Circular Steel Columns Filled with Double-Layer Concrete with Inner Bracing

Hadi Faghihmaleki,[a,*] Seyedeh Sara Farahpour[a]

[a] *Faculty of Civil Engineering, Ayandegan Institute of Higher Education, Tonekabon, Iran*

ABSTRACT

Concrete-filled double-shell circular steel columns consist of two concentric steel tubes with the space between them filled with concrete. These columns are a suitable option for high-rise construction due to their lower weight and also allow the passage of cables and utilities. In this research, modelling was carried out in Abaqus software and parametric analysis was performed based on variables such as the shape and dimensions of the stiffeners. The results show that concrete-filled double-shell columns perform better against axial and seismic loads than columns without concrete. The total and square stiffeners give the best performance, but it is not possible to increase their number due to space constraints. Trapezoidal stiffeners are also effective in improving axial and lateral performance, but result in a reduction in ductility. Circular stiffeners have the greatest reduction in ductility and their use is limited. In general, the choice of stiffener type has a significant effect on the performance of double shell columns.

ARTICLE INFO

Received: February 2, 2025
Accepted: April 1, 2025

Keywords:
Seismic Performance
Axial Performance
Double Shell Steel Column
Internal Stiffener
Finite Element Analysis

DOI: 10.61186/JCER.7.2.38
DOR: 20.1001.1.2538516.2025.7.2.4.2

1. Introduction

Concrete-filled double-shell steel columns (CFDST) have the advantages of concrete-filled steel columns (CFST) and are lighter, which is an advantage in high-rise construction due to their high performance with less weight [1]. In addition, the hollow section of these columns allows the passage of cables and utilities for power transmission towers and special structures [2]. The lighter weight and high efficiency of these columns has led to their use in applications such as offshore wind turbine support structures and tall power transmission towers. Concrete-filled double-shell steel columns (CFDST) are not yet common in our country due to their wide range of applications, which may call into question their practicality. Further research is needed to make these structures practical. One of the main disadvantages of CFST structures is that local buckling and delamination may occur under uniaxial compression due to the surface contact between concrete and steel. This problem may also

---

[*] Corresponding author. Tel.: +989112923228; e-mail: h.faghihmaleki@gmail.com.

be present in CFDST structures, but due to the presence of two inner and outer shells, it requires more detailed investigation in this area. One solution to reduce local delamination between concrete and steel is to use internal stiffeners. These stiffeners are installed in such a way that the two shells fit together easily, and then concrete is poured into the space between the two shells. The shape and dimensions of the stiffeners, as well as their spacing in the cross-section height, have a great influence on the seismic and axial performance of the columns [3,4].

Ding [5] showed that steel and steel sections can provide effective confinement for the core concrete. A study was also conducted on the effect of outer steel column confinement on the core concrete and the interaction between concrete and section steel, which showed that the models in Eurocode 4 may underestimate the load-bearing capacity of composite steel-concrete columns. Al-Ramaili et al. [6] showed that confinement by a steel column can significantly increase the load-bearing capacity of the column and inhibit diagonal shear cracking. Chitawadagi et al [7] in their research on 27 cold-rolled rectangular concrete filled steel columns found that increasing the wall thickness delayed local buckling failure. It increases the ultimate axial load capacity. Tawu et al. [8] performed a linear analysis of concrete filled square stainless-steel columns (CFSST) under axial compression and presented a formula for calculating the ultimate load capacity. Le Hewitt [9] used numerical methods to investigate the compressive behaviour of high-strength circular steel columns that had reached high strength by laboratory methods. Yuan et al. [10] presented an experimental investigation and numerical analysis of the performance of concrete-filled double-shell composite columns (CFDSCT) under axial loading.

This study investigates the effect of buried internal stiffeners in the cross-section of concrete-filled double-shell circular steel columns (CFDST) under compressive and lateral loading. In particular, this study addresses the reduction of local separation between concrete and steel in CFDST structures having two inner and outer shells. The effect of the shape, location and number of stiffeners on the axial and lateral behaviour of the columns is also one of the innovations of this study. The use of non-linear quasi-static analysis and finite element methods to accurately evaluate the axial and lateral performance of CFDST columns is one of the main objectives of this study.

2. Research Methods

2.1. Numerical modelling for verification

For verification, a numerical model must be created that matches the laboratory model, so in Abaqus software, all laboratory properties must be converted to a numerical model, and the laboratory results are obtained by compressing the numerical model, which will be discussed below. The design process in Abaqus software starts in the Parts module. This process involves three separate elements that are created in the Part module and then each element is assembled into its corresponding part in the Assembly module.

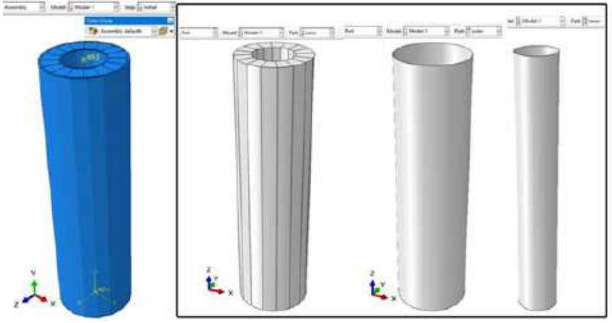

Figure 1 - In the Part module (right image) and the model assembly in the Assembly module (left image) of the Abaqus software.

Material properties in terms of shell thickness, steel yield stress and concrete strength between shells are created in the Material Properties module and assigned to the specimens (Figure 1). To solve the problem, the elements of the desired specimen should be divided into smaller sections in the Mesh module, so the optimum division rate of 5 mm was selected for each element, naturally the element type of the inner and outer shells is shell type and the concrete specimen is solid type. In order to apply the load and boundary conditions of the lower beam in the Interaction module of the Abaqus software, two reference points are created at the top and bottom of the specimen and a coupling constraint is created between these points (to facilitate the application of the load and boundary conditions of the beam). Also, in the same module, the direction of action and interaction of the space between the steel and concrete in the two shells should be defined by applying the coefficient of friction between the steel and concrete (of 0.30) and activating the surface interaction. To apply the load and support conditions in the Loading module of the Abaqus software, first define the gravity loading of the specimen and then fully constrain the lower coupler reference point in terms of displacement and rotation and load the upper coupler reference point (of the displacement control type) in increments of up to 20 mm (according to the laboratory specimen). After applying the load, to obtain the best and most accurate results, since the sample is under compressive load and there are buckling conditions in the steel section, one file should be run with buckling analysis and the other file with quasi-static analysis. These definitions are made in the STEP module of the Abaqus software. Therefore, in the first file, the sample is analysed under 9 buckling modes.

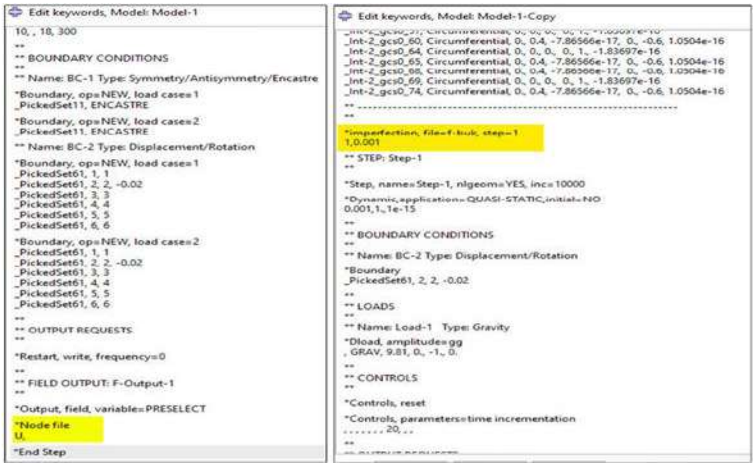

```
Edit keywords, Model: Model-1
10, , 18, 300
**
** BOUNDARY CONDITIONS
**
** Name: BC-1 Type: Symmetry/Antisymmetry/Encastre
*Boundary, op=NEW, load case=1
_PickedSet11, ENCASTRE
*Boundary, op=NEW, load case=2
_PickedSet11, ENCASTRE
** Name: BC-2 Type: Displacement/Rotation
*Boundary, op=NEW, load case=1
_PickedSet61, 1, 1
_PickedSet61, 2, 2, -0.02
_PickedSet61, 3, 3
_PickedSet61, 4, 4
_PickedSet61, 5, 5
_PickedSet61, 6, 6
*Boundary, op=NEW, load case=2
_PickedSet61, 1, 1
_PickedSet61, 2, 2, -0.02
_PickedSet61, 3, 3
_PickedSet61, 4, 4
_PickedSet61, 5, 5
_PickedSet61, 6, 6
**
** OUTPUT REQUESTS
**
*Restart, write, frequency=0
**
** FIELD OUTPUT: F-Output-1
**
*Output, field, variable=PRESELECT
*Node file
U,
*End Step
```

```
Edit keywords, Model: Model-1-Copy
_Int-2_gcs0_60, Circumferential, 0., 0.4, -7.86566e-17, 0., -0.6, 1.0504e-16
_Int-2_gcs0_64, Circumferential, 0., 0., 0., 0., 1., -1.83697e-16
_Int-2_gcs0_65, Circumferential, 0., 0.4, -7.86566e-17, 0., -0.6, 1.0504e-16
_Int-2_gcs0_68, Circumferential, 0., 0.4, -7.86566e-17, 0., -0.6, 1.0504e-16
_Int-2_gcs0_69, Circumferential, 0., 0., 0., 0., 1., -1.83697e-16
_Int-2_gcs0_74, Circumferential, 0., 0.4, -7.86566e-17, 0., -0.6, 1.0504e-16
** ----------------------------------------------------------------
**
*imperfection, file=f-buk, step=1
1,0.001
** STEP: Step-1
**
*Step, name=Step-1, nlgeom=YES, inc=10000
*Dynamic,application=QUASI-STATIC,initial=NO
0.001,1.,1e-15
**
** BOUNDARY CONDITIONS
**
** Name: BC-2 Type: Displacement/Rotation
*Boundary
_PickedSet61, 2, 2, -0.02
**
** LOADS
**
** Name: Load-1   Type: Gravity
*Dload, amplitude=gg
, GRAV, 9.81, 0., -1., 0.
**
** CONTROLS
**
*Controls, reset
*Controls, parameters=time incrementation
, , , , , , , 20, , ,
**
```

Figure 2 - Coding for transfer of displacement values from buckling analysis to quasi-static analysis.

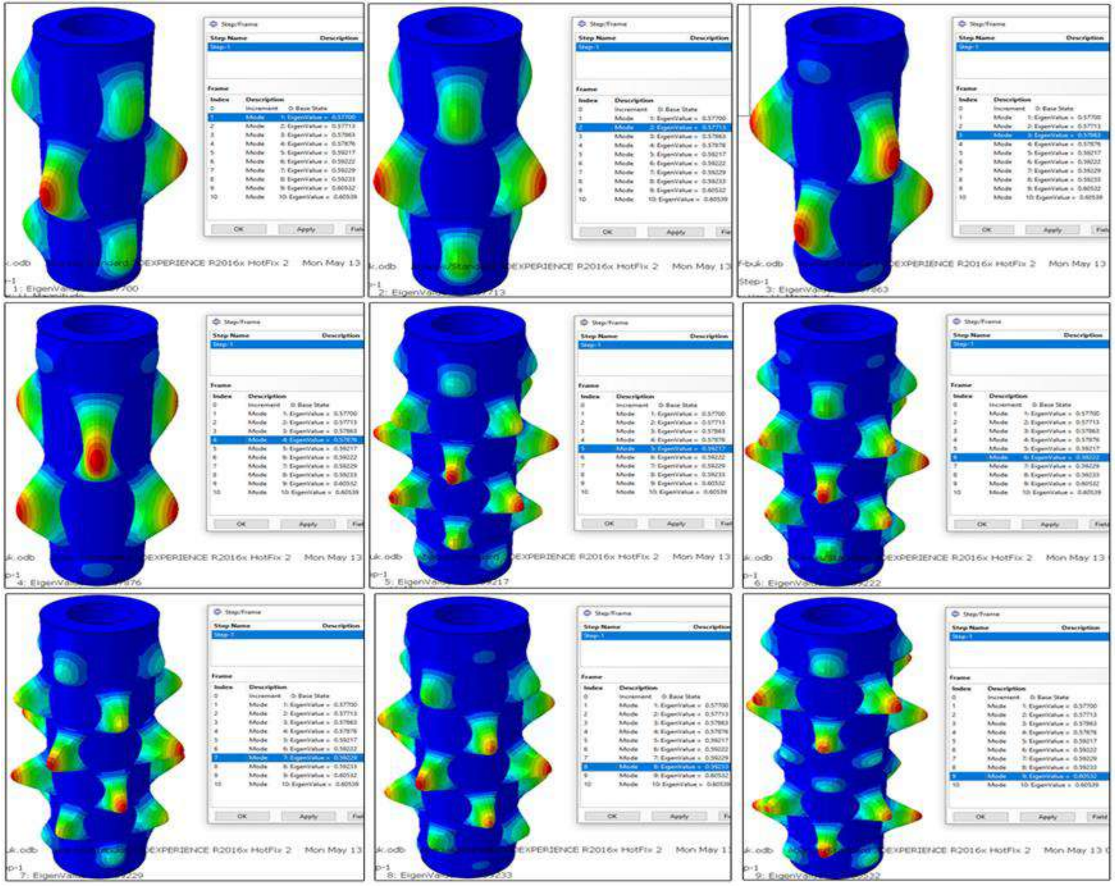

Figure 3 - Coding for transfer of displacement values from buckling analysis to quasi-static analysis

The deformation results of these buckling modes should be stored in a separate file and these results should be retrieved in the main quasi-static analysis file.

Meanwhile, the buckling modes of a double-shell steel column filled with prestressed concrete are shown in Figure 3.

After performing the above operations, the column specimen in question should be analysed using quasi-static analysis by applying compressive load, so by applying analysis in the work module, the results can be viewed in the results visualisation module. The results obtained after applying compressive loading show that compressive loading of the double-shell steel column specimen filled with concrete causes significant deformation in the outer and inner shell sections, as shown, and according to the same figure, the concrete has deformed more in the middle section. The results of the load-displacement and stress diagrams of the numerical specimen are also shown in

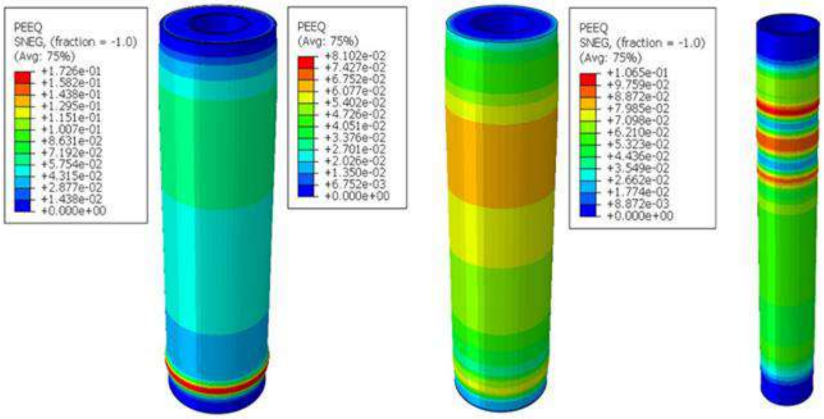

Figure 4 - Display of permanent deformation of concrete-filled double-shell steel column elements in relation to compressive loading in the results visualisation module of the Abaqus software.

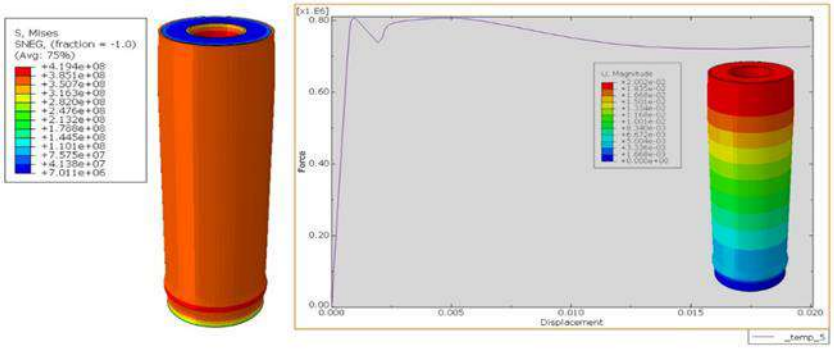

Figure 5 - Display of the von Mises stress of the specimen and the load-displacement diagram of the numerical specimen in the results visualisation module of the Abaqus software

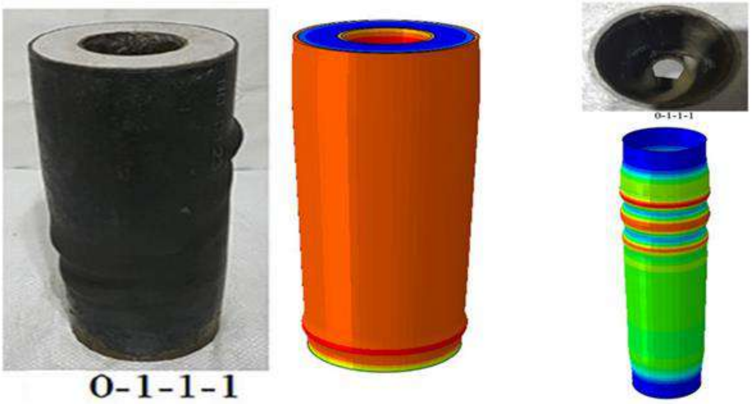

Figure 6 - Comparison and agreement of permanent deformation of specimens after completion of compressive loading between two numerical specimens and laboratory work (in specimen "0-1-1-1") Talha Akmakyapar et al

Figure 5.

2.2. Comparison and validation

In order to compare and validate the laboratory work of the concrete-filled double-shell steel column specimen (specimen "0-1-1-1") by Talha Ekmekiapar et al [11]. which was tested under quasi-static loading and additional axial (compressive) loading, and the numerical work, several parts of this comparison and validation should be carried out.

According to Figure 6, the permanent deformation of the specimen is observed in the two parts of the outer shell as a hump outward, i.e. the lower and middle parts upwards, as in the laboratory specimen, which is the same deformation observed in the numerical specimen. This outward hump is also observed in the inner shell between the two samples. Therefore, a shape match is observed between the two numerical and laboratory samples.

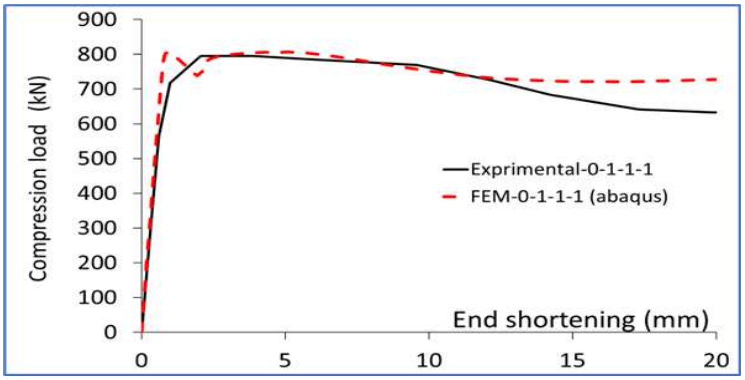

Figure 7 - Comparison and matching of load-displacement diagrams of specimens between two numerical specimens and laboratory work (in the "0-1-1-1" specimen) by Talha Ekmekiapar et al [11].

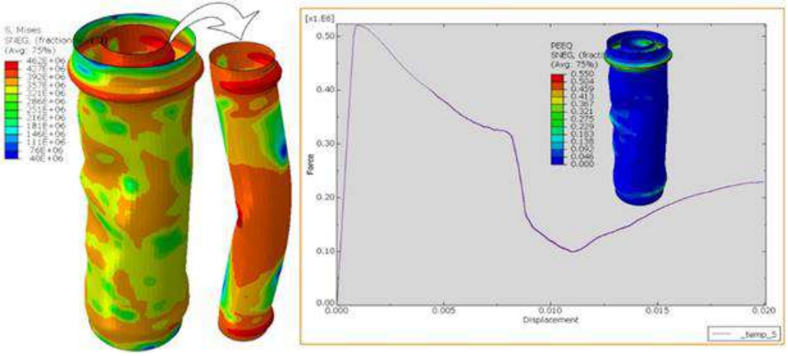

Figure 8 - Axial load results of a bare double shell steel column specimen without concrete and its axial load-displacement diagram in Abaqus software.

The second part of the comparison and matching can be done on the output results obtained from the experiment. The load-displacement diagram is the best option for this comparison and matching, so first the laboratory load-displacement diagram is converted to numerical data and then the diagram obtained from the Abaqus software is placed on top of it and the two are compared. Figure 7 shows the comparison between the two load-displacement diagrams of the laboratory and numerical samples.

According to Figure 7, as is also clear from the load-displacement diagram of the laboratory specimen, the maximum resistance of the "0-1-1-1" specimen is recorded at 790 kN, which is 800 kN for the numerical specimen, which is 1.2% of the difference in resistance criterion between the two specimens. In addition, the hardness of the specimen, which is the initial slope of the load-displacement diagram, is almost the same. According to the load-displacement diagram of the laboratory specimen, the hardness of the "0-1-1-1" specimen is 995 kN/mm, while the hardness of the numerical specimen is 1020 kN/mm, which is 2.9% of the difference in the hardness criterion between the two specimens. Also, in terms of the overall shape between the two laboratory and numerical diagrams, these two diagrams are almost the same, and the small difference may be due to various laboratory and numerical reasons.

Therefore, the two numerical and experimental models are in relatively good agreement and it can be said that the numerical model has been validated against the experimental model. Also, the studies in this part of the research can be used (both in terms of the Abaqus file and in terms of a reference model of a double-shell steel column filled with concrete) as the assumptions of section 3.

3. Analysis of the research results

Comparison of the axial and lateral performance of the base sample of a double-shell column without concrete with a double-shell column filled with concrete (between the two shells) In this part of the research, because there must be samples as a reference to compare the rest of the parametric samples with them, this part deals with the question of how much axial and lateral performance the base samples of the research have. The reference sample is the same sample that was tested in the third chapter, because the laboratory test results of this sample matched the numerical results, so the double-shell steel column filled with concrete is called "Ref", meaning the reference and base sample of this research. Another sample based on this research is a sample that is a double-shell steel column without concrete, and in order to be able to compare the samples well, this sample is the same verified sample but without concrete between the two shells. Because the steel column is without concrete and bare, this column is introduced as "Bare".

The compressive (axial) loading results of the first sample "Ref" were presented in the second section, but the double shell steel column sample without concrete has not been loaded yet, so in the Abaqus software the results are obtained by copying the first file, removing the concrete and reloading the axial load. Figure 8 shows the axial load results of the double shell steel column without concrete. According to the result obtained from the load-displacement diagram of the concreteless double-shell steel column sample in Figure 8, the concreteless double-shell steel column reaches the axial yield point and buckles when subjected to a compressive load with an axial displacement of about 1 mm and an axial resistance of 521 kN. The von Mises stress and deformation of the sample in both the inner and outer shells are shown in Figure 8.

As mentioned above, the "Bare" specimen is identical to the "Ref" specimen in all dimensional and material properties, except that in the "Bare" specimen there is no concrete between the two shells. By plotting the results of the reference samples in the form of a load-displacement diagram, we can comment on the results obtained. Figure 9 shows the axial load-displacement diagram of the two reference specimens. As can be seen from Figure 9, the double-shell steel column without concrete, because it does not have a concrete column in its body and because of the buckling of the steel body in the inner and outer shells, buckles earlier and has a lower compressive performance than the double-shell steel column filled with concrete. These functions are clearly visible in the initial slope of the load-displacement diagram (representing the initial axial stiffness of the specimens) and the maximum axial strength (representing the axial strength criterion). Also, in the load-displacement diagram and axial loading of the specimens, the curve of the diagram changes slope (stiffness) at the yield point and the specimens only deforms. According to Figure 9, in the sample of double-shell steel column filled with concrete, after the yield point, the resistance diagram remains almost constant, slightly less than the maximum resistance, but in the double-shell steel column without concrete, the resistance decreases sharply and becomes a decrease, which is a phenomenon in the ductility criterion.

By bilinearising the load-displacement diagram with the equivalent energy model, multi-line diagrams are transformed into just two lines and these two lines represent the diagram so that the area lost and the area gained are equal in the resulting diagram. By bilinearising the load-displacement diagram, the yield point of the diagrams can be calculated and with the yield point the axial power can be calculated and compared. Therefore, according to Figure 10, the graphs become two lines and according to this figure, all the information of the yield point, the performance endpoints and the maximum recorded resistance is shown. According to Figure 10, the axial performance endpoint of the "Bare" specimen occurs at a displacement of 4.6 mm and, due to the compressive buckling of the column without concrete, the continuation of its axial load-displacement diagram is not part of the axial performance, whereas in the "Ref" specimen, due to the presence of concrete in the column, the entire load length, i.e. 20 mm, is considered part of the performance. This is taken into account in the calculation of the axial ductility and it is obvious that the ductility of the specimen with concrete is much higher than that of the column without concrete.

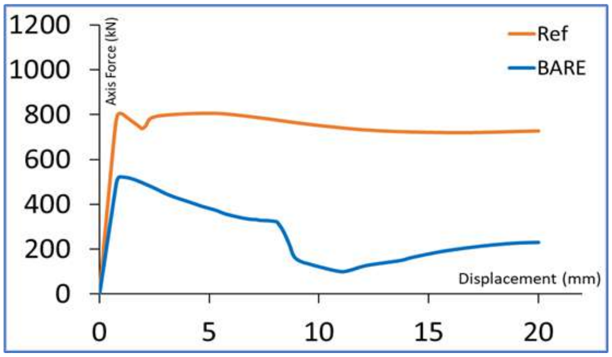

Figure 9 - Comparison of the axial load-displacement diagram of the "Ref" concrete-filled and the "Bare" concrete-free double-shell steel column specimens

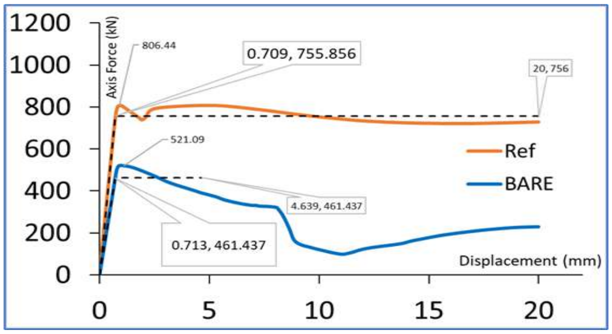

Figure 10 - Comparison of the two-line load-axial displacement diagram data of the "Ref" concrete-filled double-shell steel column and the "Bare" concrete-free double-shell steel column

Table 1 shows the comparison of axial performance between two concrete filled double shell steel column base specimens "Ref" and a concrete free double shell steel column specimen "Bare".

According to Table 1, the yield point in the displacement section of the concrete-filled double-shell steel column "Ref" specimen is only 1% lower than the same case of the concrete-free double-shell steel column "Bare" specimen, but its yield point load is 64% higher, so the slope (stiffness) of the load-displacement diagram should also be higher. Similarly, the axial stiffness of the

"Ref" specimen is 65% higher than that of the "Bare" specimen. According to the table, the ultimate displacement yield point of the "Bare" specimen occurs earlier and the ductility, which is the result of dividing the ultimate displacement yield point by the yield displacement yield point, should be lower. For example, the axial ductility of the "Bare" sample is 6.5 and the axial ductility of the "Ref" sample is 28.2, which is more than 3 times. In terms of strength, the strength of the "Ref" sample is 55% higher than that of the "Bare" sample. It is therefore clear how its axial performance is increased by filling the space between the two shells with concrete.

Table 1
Comparative axial performance data between the two baseline samples 'Ref' and 'Bare'.

Spectrum	Δy (mm)	V_y (kN)	Δu (mm)	P_{sh} (kN)	K_{sh} (kN/mm)	μ_{sh}
Ref	0.709	756	20	806	1066	28.20
Bare	0.713	461	4.64	521	647	6.50
	-1%	64%	331%	55%	65%	334%

In the case of lateral loading in two specimens, a double-skinned steel column filled with concrete "Ref" and a double-skinned steel column without concrete "Bare", all features of the application of software properties (except the loading path) are fixed. In this way, the load path is applied laterally to the specimens instead of axially as a displacement control. First, the double-shell steel column specimen filled with concrete "Ref" and then the double-shell steel column specimen without concrete "Bare" are subjected to lateral loading, and the results of applying lateral loading are shown in Figures 11 and 12, respectively.

The von Mises stress and deformation of the specimen in both the inner and outer shells are known for both the concrete-filled double-shell steel column "Ref" and the concrete-free double-shell steel column "Bare". Also, by bilinearising the lateral load-displacement diagram, the yield point of the diagrams can be calculated, and with the yield point, the lateral performance can be calculated and compared. Therefore, Figure 13 shows the yield points of the diagrams side by side and compares them.

Table 2 shows the comparison of lateral performance between two concrete filled double shell steel column base specimens "Ref" and a concrete free double shell steel column specimen "Bare".

According to Table 2, the lateral strength criterion of the "Ref" concrete-filled double-shell steel column base specimen is 19% higher than that of the "Bare" concrete-free double-shell steel column base specimen. Also, the lateral initial stiffness criterion of the concrete-filled double-shell steel column base specimen "Ref" is 39% higher than that of the concrete-free double-shell steel column specimen "Bare", and the lateral ductility criterion of the concrete-filled double-shell steel column base specimen "Ref" is 14% higher than that of the concrete-free double-shell steel column specimen "Bare". It is therefore clear how the lateral performance is increased by filling the space between the two shells with concrete.

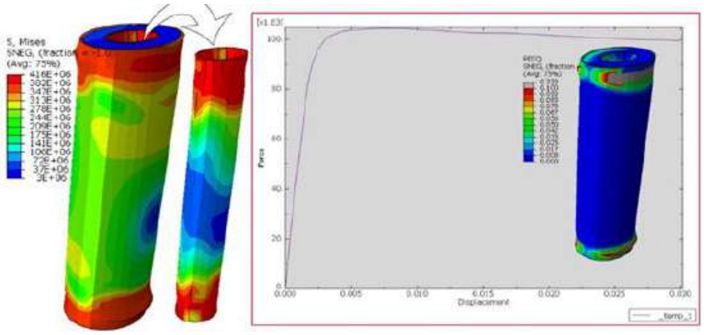

Figure 11 - Lateral loading results of concrete filled steel column "Ref" sample and its lateral load-displacement diagram

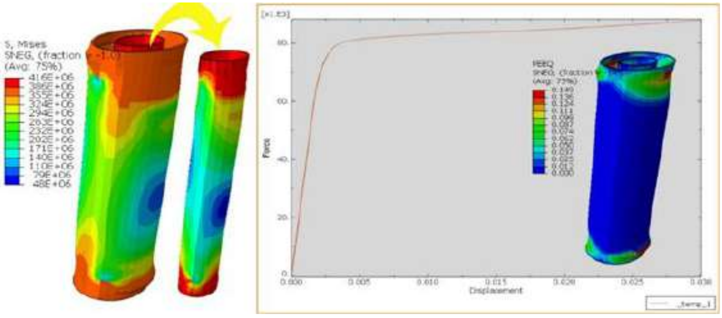

Figure 12 - Results of the lateral loading of a double-shell steel column with no 'bare' concrete and the lateral load-displacement diagram

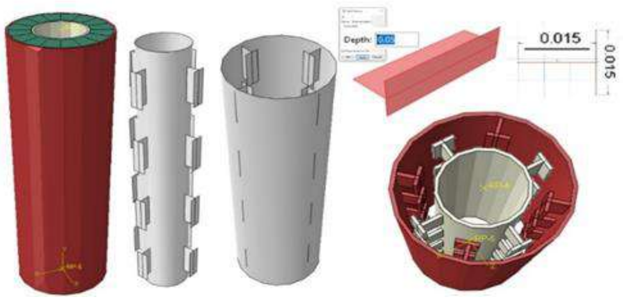

Figure 14 - Example of a double shell steel column filled with concrete with a T-shaped stiffener, section at 4 parts of the column height (example "T8-4").

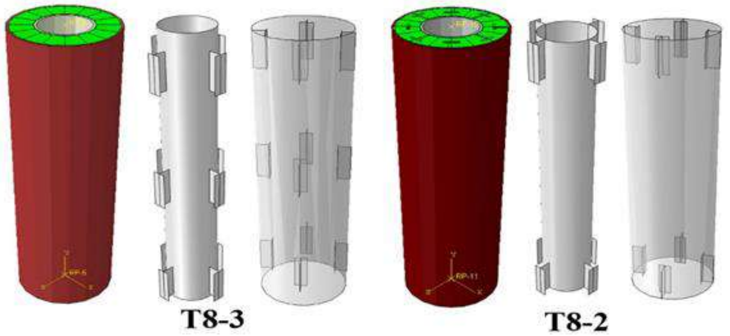

Figure 15 - Examples of double shell steel columns filled with concrete with T-shaped stiffeners at 3 and 2 parts of the column height (examples "T8-3" and "T8-2").

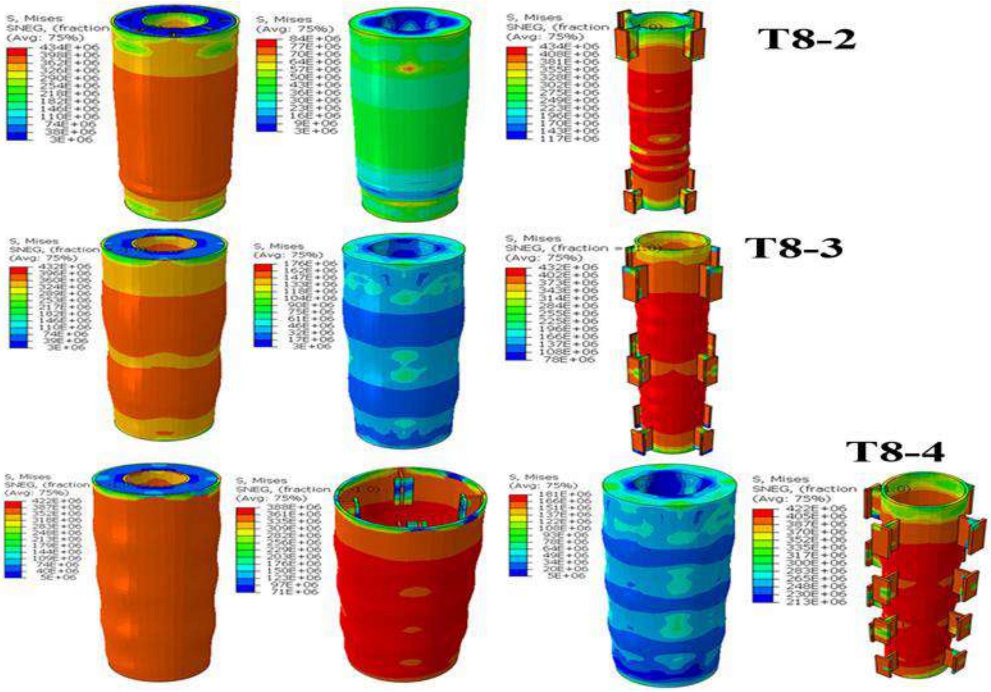

Figure 16 - Axial loading results - von Mises stress in concrete filled double shell steel column specimens with T-shaped section stiffeners at 2, 3 and 4 parts of column height (specimens "T8-2", "T8-3" and "T8-4").

3.1. Comparison of the axial behaviour of concrete-filled double-shell columns with a T-shaped stiffener in the cross-section and with a global T-shaped stiffener

In this part of the research, the problem is addressed: if steel stiffeners are used in the space between the two shells, how will the axial performance factors of a double-shell steel column filled with concrete change? Therefore, a T-section stiffener is proposed, modelled with a flange and web of 1.5 cm, a height of 5 cm and a thickness of 2.7 mm. Four of them are welded to the inner shell and the other four to the outer shell. During installation, they are placed at a 45-degree angle to each other so that they do not collide. Finally, the space between the stiffeners is filled with concrete. In Figure 4-8, these stiffeners are placed at 4 different heights in the column. This column has a total of 8 T-shaped stiffeners in the radial direction. The name "T8-4" has been considered for this example, which is located at 4 column heights with 8 T-shaped stiffeners.

The fact that the cross-sectional stiffeners are located at 3 and 2 parts of the column height has resulted in the steel column specimens "T8-3" and "T8-2" shown in Figure 15.

The results of the axial loading of the three new specimens in terms of von Mises stress and the results of the force-displacement diagram are shown in Figures 16 and 17 respectively.

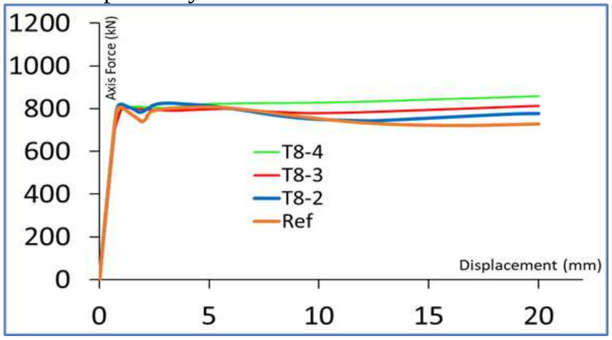

Figure 17 - Comparison of axial load-displacement diagrams of a concrete filled double shell steel column specimen with T-shaped section stiffeners at 2, 3 and 4 parts of the column height (specimens "T8-2" and "T8-3" and "T8-4").

According to Figure 16, the von Mises stress of the concrete-filled double-shell steel column specimens with T-shaped sectional stiffeners at 2, 3 and 4 parts of the column height (specimens "T8-2" and "T8-3" and "T8-4") is shown in accordance with the axial loading results. Figure 17 shows that the stress in the inner shell is higher than the rest of the parts and the type of stiffener is effective in the deformations caused by axial loading. Figure 17 also shows that the specimens with sectional reinforcement with T-shaped stiffeners have a slight increase in ultimate strength compared to the reference specimen "Ref", so that as the number of stiffeners in height increases, the ultimate strength also increases. For a better comparison between the results of the specimens studied, their axial performance is also calculated by bilinearising the load-displacement diagram, the results of which are shown in Table 3.

According to Table 3, the column strength criterion increases as the number of stiffeners in the column height increases, so that this increase is 2.5, 1 and 6.5% for samples "T8-2", "T8-3" and "T8-4" respectively.

In this part of the research, the question is: if a global steel stiffener is used in the space between the two shells instead of a sectional steel stiffener, what is the change in the axial performance factors of a double-shell steel column filled with concrete? Therefore, the same stiffener is modelled according to Figure 18 with a height equal to the height of the column, so that these columns are named according to the number of T-shaped stiffeners.

Table 3 - Comparison of axial performance data between concrete filled double shell steel column specimens with T-shaped section stiffeners at 2, 3 and 4 parts of the column height (specimens "T8-2" and "T8-3" and "T8-4")

Spectrum	Δy (mm)	Vy (kN)	Δu (mm)	Psh (kN)	Ksh (kN/mm)	μax
Ref	0.709	756	20	806	1066	28.20
T8-2	0.735	776	20	826	1056	27.22
T8-3	0.747	794	20	814	1063	26.77
T8-4	0.775	831	20	859	1072	25.82

According to Figure 18, the double shell steel columns filled with concrete with T-shaped global stiffeners, which have 2 stiffeners in the inner shell and 2 stiffeners in the outer shell, have a total of 4 T-shaped global stiffeners, named "T4", and similarly, the "T6" and "T8" specimens have 6 and 8 T-shaped global stiffeners, respectively. Figure 19 shows the von Mises stress results of the specimens.

Figure 19 shows that the stress in the inner shell is higher than the rest of the outer shell and that the type of stiffener is effective in the deformations caused by the axial load, so that in sample "T4" the column has deformed in the upper part of the outer shell. Figure 20 shows the results of the force-displacement diagram.

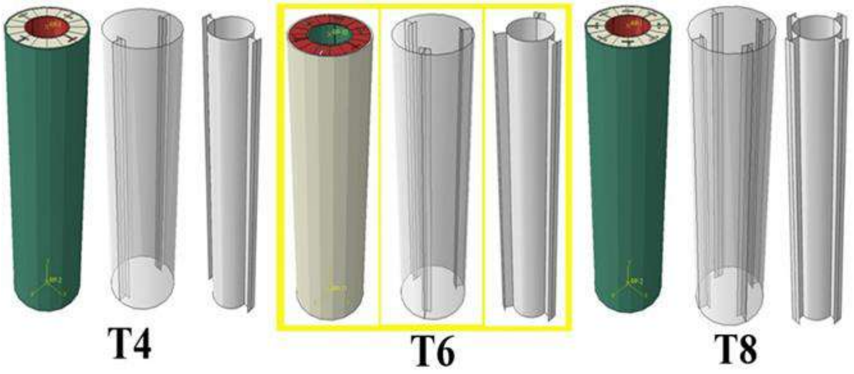

Figure 18 - Examples of concrete filled double shell steel columns with continuous T-shaped stiffeners (examples "T4", "T6" and "T8").

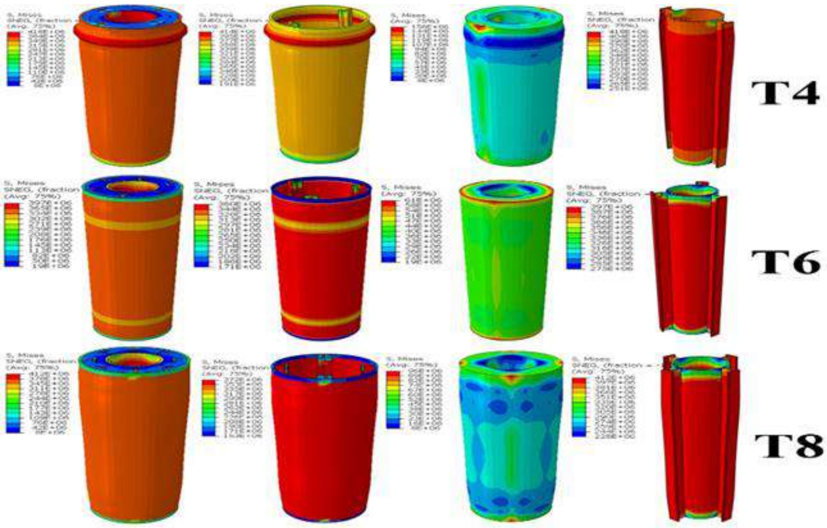

Figure 19 - Axial load results - von Mises stress in concrete filled double shell steel column specimens with global T-shaped stiffeners (specimens "T4", "T6" and "T8").

For a better comparison between the results of the specimens studied, their axial performance is also calculated by bilinearising the load-displacement diagram, the results of which are shown in Table 4.

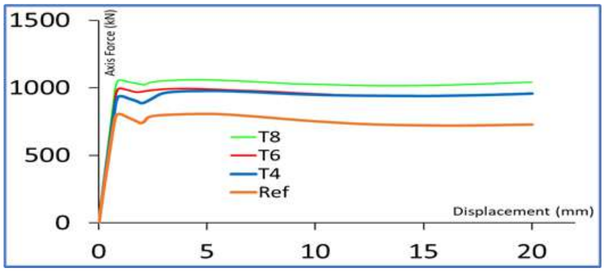

Figure 20 - Comparison of axial load-displacement diagrams of concrete filled double shell steel column specimens with global T-shaped stiffeners (specimens "T4", "T6" and "T8").

Table 4

Comparison of axial performance data between concrete filled double shell steel column specimens with global T-shaped stiffeners (specimens "T4", "T6" and "T8").

Spectrum	Δy (mm)	Vy (kN)	Δu (mm)	Psh (kN)	Ksh (kN/mm)	μax
Ref	0.709	756	20	806	1066	18.20
T4	0.823	950	20	977	1155	24.31
T6	0.785	964	20	997	1227	25.47
T8	0.797	1034	20	1060	1298	25.11

According to Table 4, as the number of T-shaped stiffeners in the column increases, the axial stiffness criterion of the column increases, so that this increase is 21, 24 and 31% for samples "T4", "T6" and "T8" respectively. Table 4 also shows that as the number of T-shaped stiffeners in the column increases, the axial stiffness criterion of the column increases, so that this increase is 8, 15 and 22% for samples "T4", "T6" and "T8" respectively. However, as far as the ductility of the column is concerned, as the number of stiffeners in the height of the column increases, the axial ductility criterion decreases, so that for samples "T4", "T6" and "T8" it decreases by 14, 10 and 11% respectively. Now, if the results of the total axial performance information of the samples with cross-sectional and global T-shaped stiffeners are placed side by side, this can be discussed, so this comparison is made in Table 5.

Table 5 - Comparison of the axial performance data between the concrete filled double shell steel column specimens with a T-shaped cross-section and with global stiffeners

Spectrum	Δy (mm)	Vy (kN)	Δu (mm)	Psh (kN)	Ksh (kN/mm)	μax
T8	0.797	1034	20	1060	1298	25.11
T6	0.785	964	20	997	1227	25.47
T4	0.823	950	20	977	1155	24.31
T8-4	0.775	831	20	859	1072	25.82
T8-2	0.735	776	20	826	1056	27.22
T8-3	0.747	795	20	814	1063	26.77
Ref	0.709	756	20	806	1066	18.20

According to Table 5, the concrete-filled double-shell steel column specimens with T-shaped global stiffeners have higher strength and stiffness criteria than the concrete-filled double-shell steel column specimens with T-shaped cross-sectional stiffeners due to the direct participation of the stiffeners in axial load transfer. Also, the number of T-shaped stiffeners in both cross-sectional and global specimens has a direct relationship in increasing the axial strength and stiffness criteria. Figure 21 also shows the performance of each specimen divided by the performance of the base specimen and its details.

According to Figure 21, by comparing the relative performance of the concrete-filled double-shell steel column specimens with T-shaped cross-sectional and global stiffeners with the base specimen, it can be

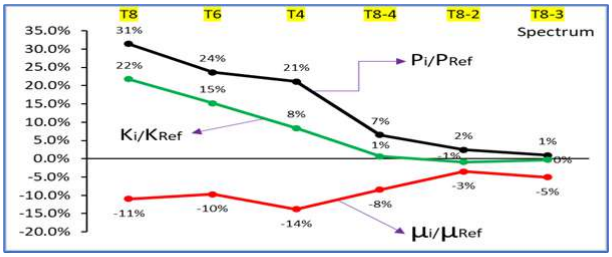

Figure 21 - Comparison of the relative performance of concrete filled double shell steel column specimens with sectional and global T-stiffeners compared to the base specimen

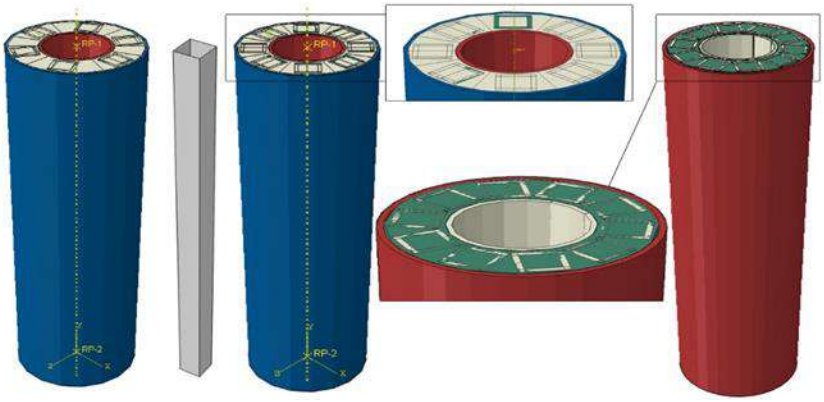

Figure 22 - Example of a double shell steel column filled with concrete with a continuous square stiffener (examples "Box6", "Box8" and "Box10")

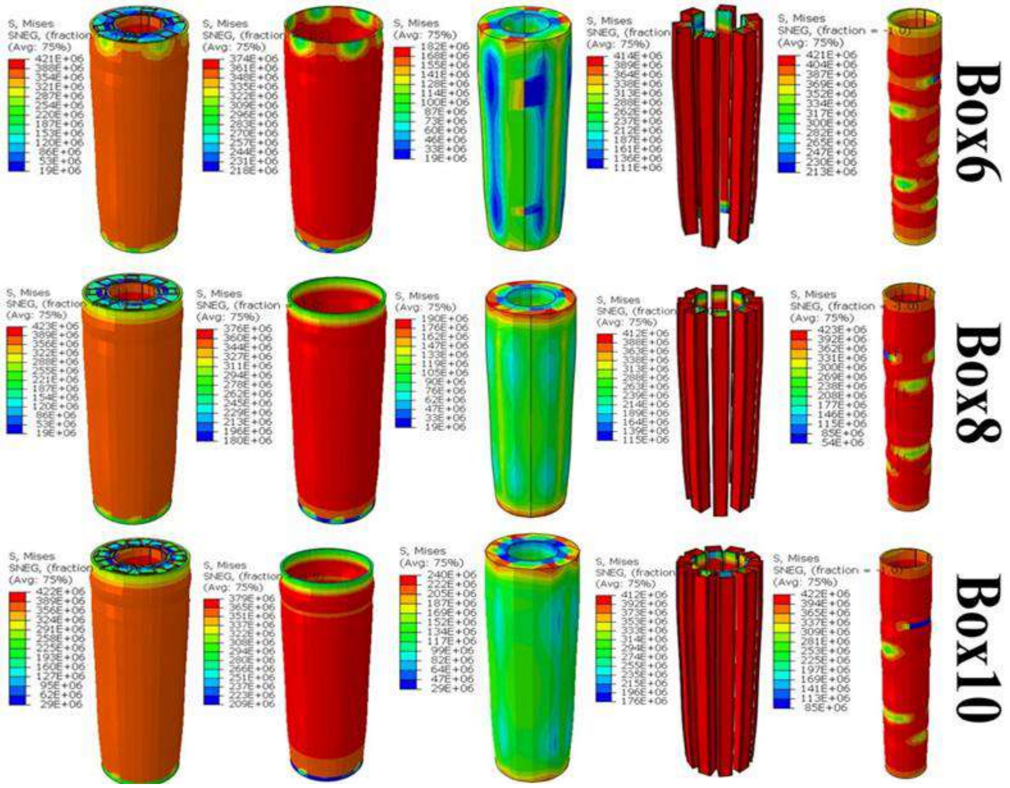

Figure 23 - Axial load results - von Mises stress in concrete filled double shell steel column specimens with square stiffeners throughout (examples "Box6", "Box8" and "Box10").

concluded that the concrete-filled double-shell steel column specimens with T-shaped cross-sectional stiffeners do not have very high axial performance, but the concrete-filled double-shell steel column specimens with T-shaped global stiffeners have higher axial performance.

3.2. Comparison of axial behaviour of concrete filled double shelled columns and square stiffening

This part of the research deals with the question of how the axial performance factors of a double-shell steel column filled with concrete change when a square steel stiffener is used in the space between the two shells. Therefore, a square stiffener is proposed that is considered without welding to the shells and only by placing it inside the shells and then pouring concrete in the space between the two concrete shells. These stiffeners have dimensions of 2 x 2 cm and a height of 40 cm. These columns have a total of 6, 8 and 10 square stiffeners in the radial direction, called "Box6", "Box8" and "Box10" respectively. Obviously, the criteria for the number of these stiffeners are the same for all stiffeners, namely 6 and 8, and the number 10 is used because more than 10 square stiffeners cannot fit into this column and will collide with each other (Figure 22).

Figure 23 shows the von Mises stress results for the specimens investigated. It shows that the highest stresses are in the outer shell, followed by the square stiffeners and then the outer shell. Figure 24 also shows the results of the force-displacement diagram. For a better comparison between the results of the specimens studied, their axial performance is also calculated by bilinearising the load-displacement diagram, the results of which are shown in Table 6.

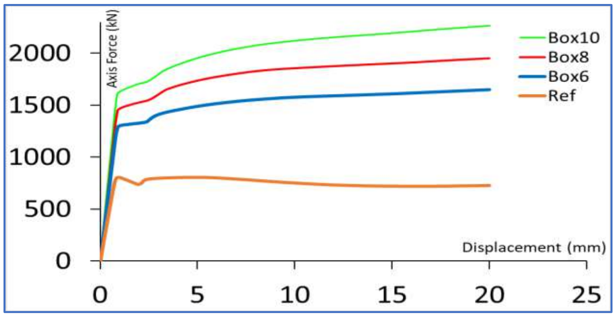

Figure 24 - Comparison of axial load-displacement diagrams of concrete filled double shell steel column specimens with continuous square stiffeners (specimens "Box6", "Box8" and "Box10").

Table 6
Comparison of axial performance data between concrete filled double shell steel column specimens with universal square stiffeners ("Box6", "Box8" and "Box10" specimens).

Spectrum	Δy (mm)	Vy (kN)	Δu (mm)	Psh (kN)	Ksh (kN/mm)	µax
Ref	0.709	759	20	806	1066	28.20
Box6	0.999	1547	20	1651	1549	20.02
Box8	1.049	1813	20	1729	1729	19.07
Box10	1.084	2072	20	1911	1911	18.45

According to Table 6, as the number of square stiffeners in the column increases, the axial stiffness criterion of the column increases so that this increase is 105, 142 and 181% for samples "Box6", "Box8" and "Box10" respectively. Table 6 also shows that as the number of square stiffeners in the column increases, the axial stiffness criterion of the column increases, so that this increase is 45, 62 and 79% for the "Box6", "Box8" and "Box10" samples respectively. However, as far as the ductility of the column is concerned, the axial ductility criterion decreases as the number of stiffeners increases, so that it decreases by 29, 32 and 35% respectively for samples "Box6", "Box8" and "Box10".

3.3. Comparison of axial performance of concrete-filled double-shell columns and circular stiffeners

This part of the research is concerned with how the axial performance factors of a concrete-filled double-shell steel column change when a circular steel stiffener is used in the space between the two shells. Therefore, a circular stiffener is proposed that is not welded to the shells, but is simply placed inside the shells and then concrete is poured into the space between the two concrete shells. These stiffeners have a diameter of 2.35 cm and a height of 40 cm. These columns have a total of 6, 8 and 11 circular stiffeners in the radial direction, named "Cir6", "Cir8" and "Cir11" respectively. Obviously, as far as the number of these stiffeners is concerned, the criteria of the two numbers 6 and 8 are constant for all stiffeners and the number 11 is used because more than 11 circular stiffeners cannot fit into this column and they will collide with each other (Figure 25).

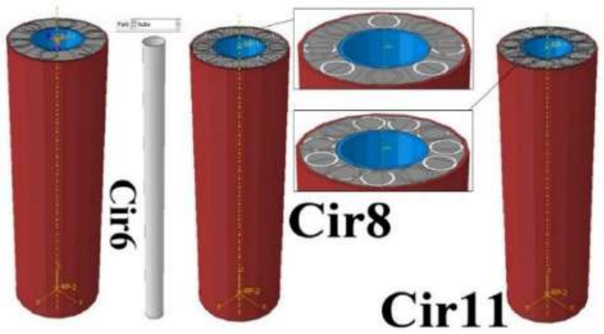

Figure 25 - Example of a concrete filled double shell steel column with global circular stiffener (examples "Cir6", "Cir8" and "Cir11").

Figure 26 shows the von Mises stress results for the specimens investigated. It shows that the highest stresses are in the outer shell, followed by the circular stiffeners and then the outer shell. Figure 27 also shows the results of the force-displacement diagram. For a better comparison between the results of the specimens studied, the axial performance is also calculated by bilinearising the load-displacement diagram, the results of which are shown in Table 7.

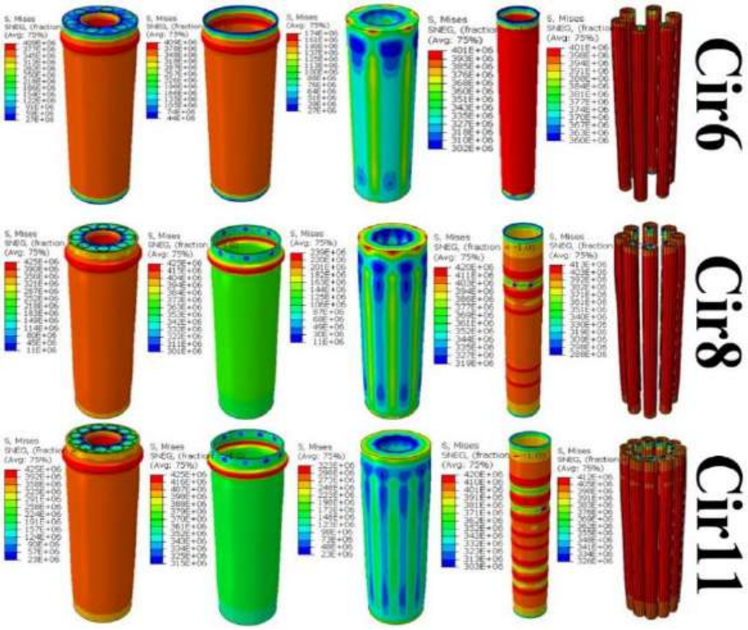

Figure 26 - Axial loading results - von Mises stress in concrete filled double shell steel column specimens with global circular stiffeners (specimens "Cir6", "Cir8" and "Cir11").

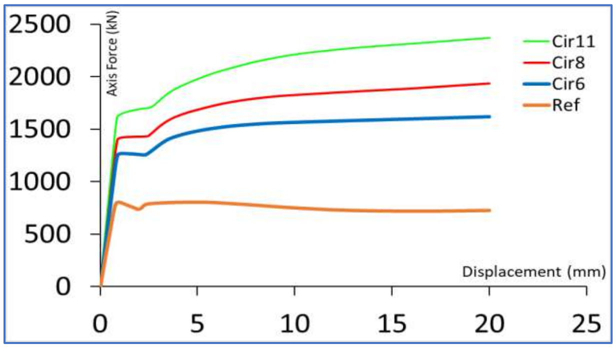

Figure 27 - Comparison of axial load-displacement diagrams of concrete filled double shell steel column specimens with global circular stiffeners (specimens "Cir6", "Cir8" and "Cir11")

Table 7
Comparison of axial performance data between concrete filled double shell steel column specimens with global circular stiffeners (specimens "Cir6", "Cir8" and "Cir11").

Spectrum	Δy (mm)	Vy (kN)	Δu (mm)	Psh (kN)	Ksh (kN/mm)	μax
Ref	0.709	759	20	806	1066	28.20
Cir6	1.013	1527	20	1620	1507	19.75
Cir8	1.061	1775	20	1973	1673	18.85
Cir11	1.116	2144	20	1922	1922	1793

According to Table 7, as the number of global circular stiffeners in the column increases, the axial stiffness criterion of the column increases so that this increase is 101, 140 and 194% for samples "Cir6", "Cir8" and "Cir11" respectively. Table 7 also shows that as the number of global circular stiffeners in the column increases, the axial stiffness criterion of the column also increases, so that this increase is 41, 57 and 80% for samples "Cir6", "Cir8" and "Cir11" respectively. However, as far as the ductility of the column is concerned, the axial ductility criterion decreases as the number of stiffeners increases, so that for samples "Cir6", "Cir8" and "Cir11" it decreases by 30, 33 and 36% respectively.

3.4. Comparison of axial performance of concrete-filled double-shell columns and trapezoidal stiffeners

This part of the research deals with the question of how the axial performance factors of a concrete-filled double-shell steel column change when a global trapezoidal steel stiffener is used in the space between the two shells. Therefore, the global trapezoidal stiffener is recommended due to its suitable dimensional adaptation to the space between the two shells, which is considered without welding to the shells and only by placing it inside the shells and then pouring concrete in the space between the two concrete shells. These stiffeners have a trapezoidal base width of 1.24 and 2 cm, a trapezoidal base height of 2 cm and a column height of 40 cm. These columns have a total of 6, 8 and 16 trapezoidal stiffeners in the radial direction, designated "Tra6", "Tra8" and "Tra16" respectively. Obviously, as far as the number of these stiffeners is concerned, the criteria of the two numbers 6 and 8 are constant for all the stiffeners, and the number 16 is also used because 16 trapezoidal stiffeners are placed inside this column in such a way as to include the entire capacity of the stiffeners without the sections colliding. It is explained that this number of stiffeners (16) is the maximum number of stiffeners that could be placed in the space between the two shells because the trapezoidal shape has a suitable dimensional fit for the space between the two shells (Figure 28). Figure 29 also shows the results of the force-displacement diagram. In order to better compare the results of the specimens studied, their axial performance is also calculated by bilinearising the force-displacement diagram, the results of which are shown in Table 8.

According to Table 8, as the number of trapezoidal stiffeners in the column increases, the axial stiffness criterion of the column increases, so that this increase is 86, 120 and 250% for samples "Tra6", "Tra8" and "Tra16" respectively. Table 8 also shows that as the number of trapezoidal stiffeners in the column increases, the axial stiffness criterion of the column also increases, so that this increase is 41, 56 and 119% for samples "Tra6", "Tra8" and "Tra16" respectively. On the other hand, as far as the ductility of the column is concerned, the axial ductility criterion decreases as the number of stiffeners increases, so that it decreases by 25, 29 and 35% respectively for samples "Tra6", "Tra8" and "Tra16".

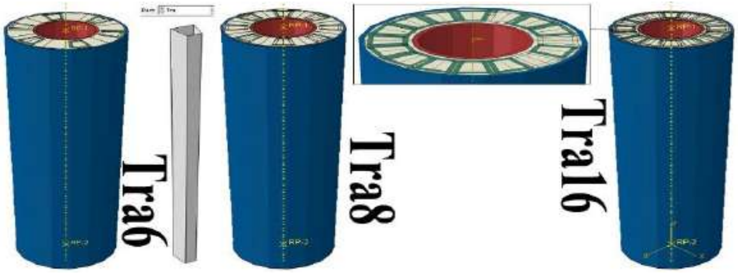

Figure 28- Example of concrete filled double shell column with trapezoidal stiffener (examples "Tra6", "Tra8" and "Tra16")

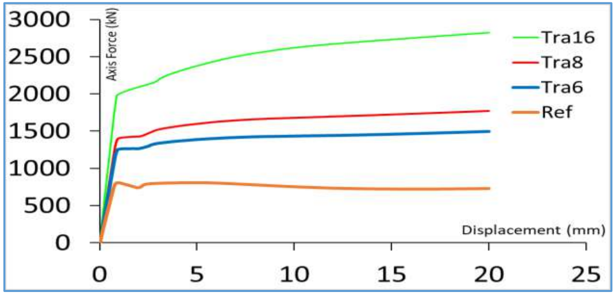

Figure 29 - Comparison of axial load-displacement diagrams of concrete filled double shell steel column specimens with continuous trapezoidal stiffeners (specimens "Tra6", "Tra8" and "Tra16")

Table 8 - Comparison of axial performance data between concrete filled double shell steel column specimens with continuous trapezoidal stiffeners (specimens "Tra6", "Tra8" and "Tra16").

Spectrum	Δy (mm)	Vy (kN)	Δu (mm)	Psh (kN)	Ksh kN/mm	Max
Ref	0.709	759	20	806	1066	28.20
Cir6	1.013	١٤٢٠	20	١٤٩٧	١٥٠٣	٢١,١٦
Cir8	1.061	١٦٥٩	20	١٧٧٤	١٦٦٧	٢٠,١٦
Cir16	1.116	٢٥٦٠	20	٢٨٢٤	٢٣٣٣	١٨,٢٣

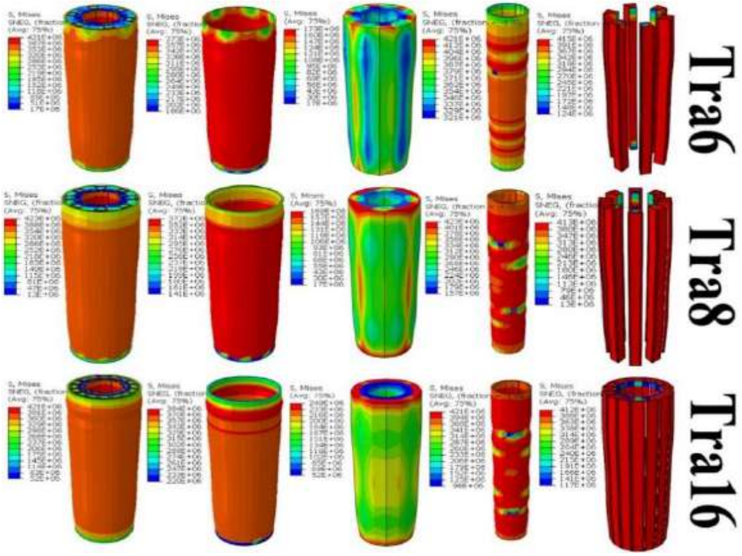

Figure 30 - Axial load results - von Mises stress in concrete filled double shell steel column specimens with continuous trapezoidal stiffeners (specimens "Tra6", "Tra8" and "Tra16").

3.5. Comparison of axial performance of concrete-filled double-shell columns and square, circular and trapezoidal stiffeners

T-shaped stiffeners were used as stiffeners in concrete-filled double-shell columns, which had to be welded to the inner or outer shell, but stiffeners such as square, circular and trapezoidal stiffeners are placed without welding only in the space between the two shells and then concrete is poured in the space between the two shells. In the previous sections, the axial performance comparison was made between concrete-filled double-shell columns with T-shaped stiffeners, but here the axial performance comparison is made between concrete-filled double-shell columns and square, circular and trapezoidal stiffeners. To begin the comparison, the force-displacement diagrams of three concrete-filled double-shell columns with square, circular and trapezoidal stiffeners with 8 stiffeners are compared side by side in Figure 31. According to Figure 31, the three samples of concrete-filled double-shell columns with square, circular and trapezoidal stiffeners with 8 stiffeners behave almost the same, with the difference that the concrete-filled double-shell column sample with 8 trapezoidal stiffeners has a lower axial performance in strength and stiffness than the square and circular samples, then the circular sample and finally the square sample have higher performances. It seems that if the force-displacement diagram of all the concrete-filled double-shell column samples with square, circular and trapezoidal stiffeners is compared side by side, the comparison of the samples will be clearer. This is therefore shown in Figure 4-26. In addition, Table 9 shows the side-by-side comparison of the axial performance data of the concrete-filled double-shell steel column specimens with square, circular and trapezoidal stiffeners.

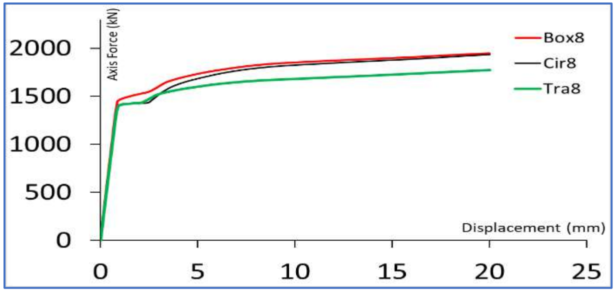

Figure 31 - Comparison of axial load-displacement diagram of concrete filled double shell column with square, circular and trapezoidal stiffeners for a total of 8 stiffeners

According to Table 9, the concrete-filled double-shell steel column specimen with 16-foot trapezoidal stiffener has a higher strength and stiffness criterion due to the direct involvement of the stiffeners in the axial load transfer, followed by the concrete-filled double-shell steel column specimen with 11-foot circular stiffener and the concrete-filled double-shell steel column specimen with 10-foot square stiffener. This shows that the shape of the internal stiffener section, where appropriate, allows a greater number of that section to fit inside the column and increases performance. In other cases, where the maximum number is not taken into account, these are square, circular and trapezoidal sections respectively. Figure 33 also divides the performance of each sample by the performance of the base sample and shows its details.

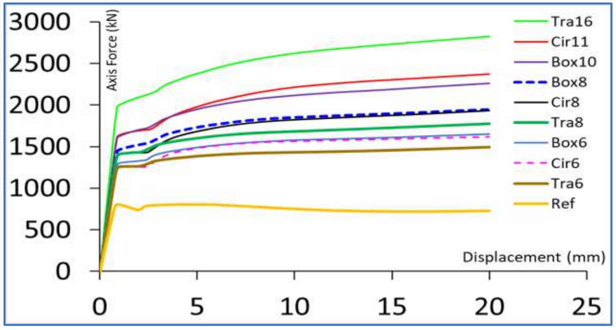

Figure 32 - Comparison of axial load-displacement diagrams of all concrete filled double shell steel column specimens with square, circular and trapezoidal stiffeners

Table 9

Comparison of the axial performance data of all the concrete filled double shell steel column specimens with square stiffeners, circular stiffeners and trapezoidal stiffeners.

Spectrum	Δy (mm)	Vy (kN)	Δu (mm)	Psh (kN)	Ksh (kN/mm)	μax
Tar16	1.097	2560	20	2824	2333	18.23
Cir11	1.116	2144	20	2372	1922	17.93
Box10	1.084	2072	20	2264	1911	18.45
Cir8	1.049	1813	20	1950	1729	19.07
Box8	1.061	1775	20	1934	1673	18.85
Tra8	0.995	1659	20	1774	1667	20.10
Cir6	0.999	1547	20	1651	1549	20.02
Box6	1.013	1527	20	1620	1507	19.75
Tra6	0.945	1420	20	1497	1503	21.16
Ref	0.709	756	20	806	1066	28.20

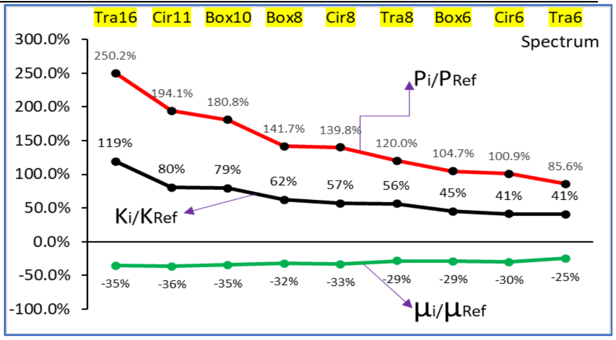

Figure 33 - Comparison of relative performance of concrete filled double shell steel column specimens with square, circular and trapezoidal stiffeners against the base specimen

From Figure 33, comparing the relative performance of the concrete filled double shell steel column specimens with square, circular and trapezoidal stiffeners compared to the base specimen, it can be concluded that the number of stiffeners has a direct relationship with the axial performance and that the shape of the stiffener also affects the axial performance of the specimens.

3.6. Investigation of lateral performance, double-shell column filled with concrete and types of stiffeners

In this part of the research, assuming that all the characteristics of the model, including the software characteristics, remain constant, the problem is addressed: what is the lateral performance of the specimens when lateral loading is applied to the specimens under investigation instead of axial loading? The problem is that the load path is applied to the specimens laterally instead of axially as a displacement control. For a better comparison of the specimens, specimens were selected where the number of stiffeners was constant, so all specimens with 8 stiffeners (specimens "T8-4", "T8", "Box8", "Cir8" and "Tra8") were selected for lateral loading. Figure 34 shows the von Mises stress of the specimens studied.

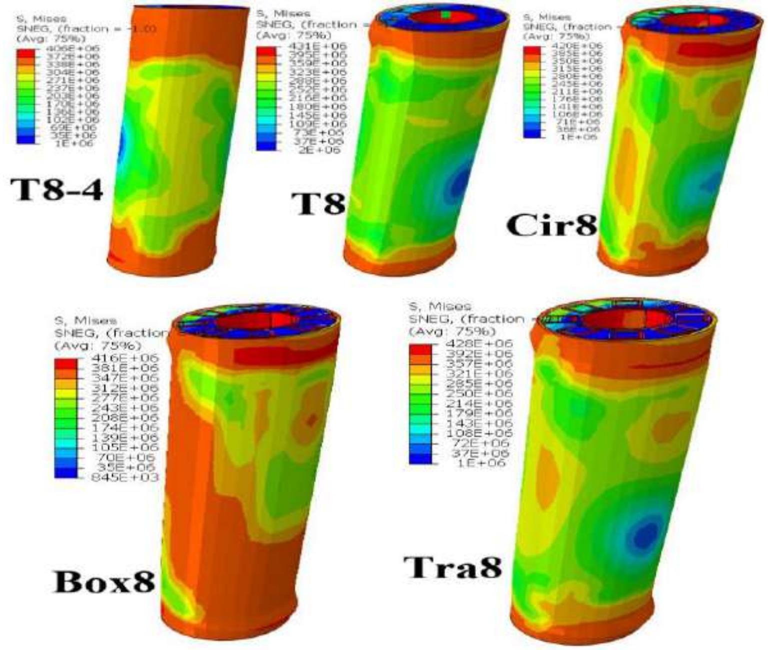

Figure 34 - Von Mises stress of lateral loading in the concrete filled double shell steel column specimens with 8 stiffeners (specimens "T8-4", "T8", "Box8", "Cir8" and "Tra8").

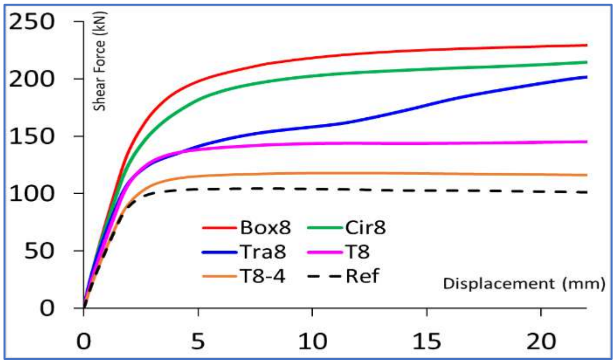

Figure 35 - Comparison of lateral load-displacement diagrams of concrete filled double shell steel columns with 8 stiffeners (samples "T8-4", "T8", "Box8", "Cir8" and "Tra8")

Meanwhile, Figure 34 shows the results of the lateral force-displacement diagram and the lateral performance information table for the specimens tested.

As can be seen in Figure 36, the lateral performance of the specimens studied, which include double-shell steel columns filled with concrete with 8 stiffeners "T8-4", "T8", "Box8", "Cir8" and "Tra8", are different from each other, which proves that the stiffener shape (assuming a constant number of stiffeners) is effective in their lateral performance. For a more detailed examination, Figure 37 shows the sorted relative lateral performance, which involves dividing the performance of each specimen by the performance of the base specimen, in three parts: relative lateral strength, relative lateral stiffness and relative lateral ductility.

The results of the relative lateral performance of the concrete-filled double-shell steel column specimens with 8 stiffeners (specimens "T8-4", "T8", "Box8", "Cir8" and "Tra8") compared to the base specimen show the effect of the stiffener shape (assuming a constant number of

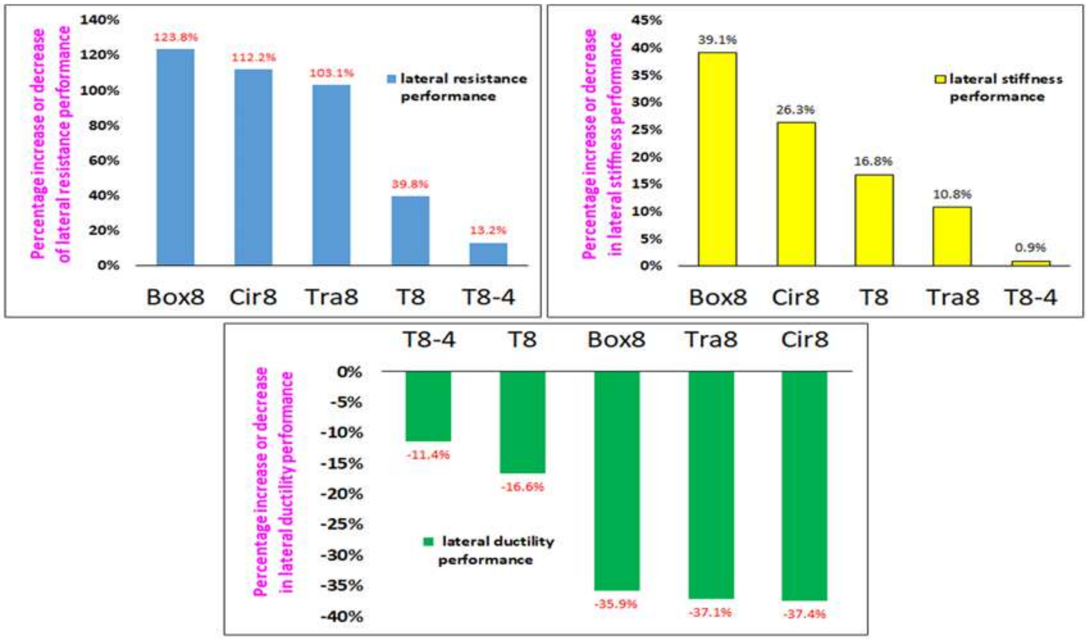

Figure 36 - Comparison of the lateral relative performance of concrete-filled steel tube columns with eight internal stiffeners (samples "T8-4," "T8," "Box8," "Cir8," and "Tra8") compared to the baseline sample.

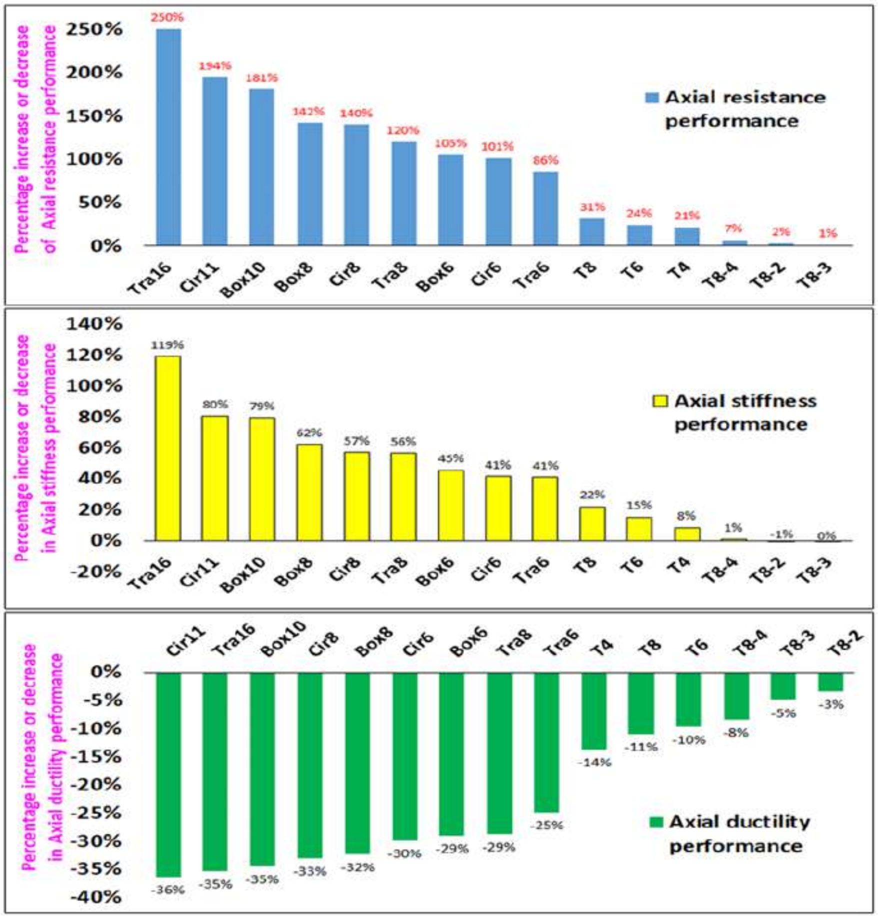

Figure 37 - Comparison of relative axial performance of all samples of double-shell steel columns filled with concrete with internal stiffener compared to the base sample

stiffeners), the details of which are presented in Chapter 5 of this study.

3.7. Investigation of the axial performance of the concrete-filled double-shell column and types of stiffeners

In this part of the study, which is also the final part of the research findings, the issue of comparing the axial performance of all the specimens under study is addressed. Therefore, the axial performance of all the specimens under study is shown along with the percentage increase or decrease in the axial performance compared to the base specimen (relative performance). The axial performance of the specimens under study, which includes concrete-filled double-shell steel columns with internal stiffeners, is shown. For a more detailed examination, in Figure 38, the sorted relative axial performance, which includes dividing the performance of each sample by the performance of the base sample, is shown in three parts: relative axial strength, relative axial stiffness, and relative axial ductility. Translate

The results of the relative axial performance of all samples of double-shell steel columns filled with concrete with internal stiffener compared to the base sample indicate the effect of the stiffener on the axial performance, the details of which are presented in Chapter 4 of this study.

4. Conclusion

According to the study, it has been determined that if the space between the two shells (inner and outer) of a double-shell steel column is filled with concrete, its axial and lateral performance is greatly improved. (So that in this study, the axial performance, which includes strength, stiffness and ductility, is improved by 55, 65 and 334% respectively, and its lateral performance is improved by 19, 39 and 14%).

1. A notable point in filling the space between the two shells with concrete is the axial ductility performance of the double-shell steel column, and the reason for this can be related to the fact that when a bare steel column (without concrete) is subjected to pure pressure, after the axial strength of the column reaches the yield point, it undergoes distortion and premature buckling, and this causes a decrease in uΔ and its axial ductility is greatly reduced. On the other hand, the problem of premature buckling does not occur in a double-shell steel column filled with concrete, and as a result, its axial ductility performance is higher than that of the steel column sample. The bare steel column becomes much higher.
2. In the studies conducted on the stresses created in the samples and components of the double-shell steel column filled with concrete with internal stiffeners, it can be seen that in terms of axial loading, the inner shell, the internal stiffener, the outer shell and the concrete between the two shells have the largest share in load transfer, and in terms of lateral loading, the inner shell, the outer shell and the concrete between the two shells have the largest share in load transfer. Therefore, considering the high share of the internal stiffener in load transfer, it is possible to understand the importance of this issue.
3. The results of the research showed that by increasing the number of stiffeners in the height of the double-shell steel column filled with concrete, the axial strength and stiffness of the column increase, but its ductility decreases.
4. The research showed that the use of overall stiffeners in the double-shell steel column filled with concrete is preferable to sectional stiffeners, and the reason for this can be attributed to the direct participation of stiffeners in axial and lateral load transfer.
5. Research has also proven that instead of using all the energy spent on welding stiffeners in the column body, only placing stiffeners inside the space between the two shells (provided they fit) and pouring concrete results in better results in terms of axial and lateral performance.
6. The results show that by using square stiffeners inside the space between the two shells, double-shell steel columns filled with concrete have the best performance in terms of axial and lateral performance in terms of two criteria of strength and stiffness, but due to their geometric shape, a large number of these stiffeners cannot be used inside the space between the two shells, because these stiffeners collide with each other and cannot be placed in large numbers.
7. The results also show that in terms of axial and lateral performance in terms of two criteria of strength and stiffness, after the overall square stiffeners, there are two circular and trapezoidal shapes, respectively, and then finally the T-shape.
8. Research has shown that as the number of global stiffeners inside the space between the two shells increases, the axial and lateral performance in the two criteria of strength and stiffness also increases. In addition, the trapezoidal shape is the best shape for placing the stiffener inside the space between the two shells, so that in this research, 16 trapezoidal stiffeners, 11 circular

stiffeners, and 10 square stiffeners were placed inside the space between the two shells.

9. Research shows that using stiffeners inside the space between the two shells in a double-shell steel column filled with concrete reduces the axial and lateral ductility criteria, and columns with circular stiffeners showed the greatest reduction in ductility compared to the others.

References

[1] Ezoji, Reyhaneh. "A Review on Behaviour and Strength of Concrete Filled Steel Tubular Columns." Journal of Civil Engineering Researchers, vol. 1, no. 7, 2017, pp. 12–16.

[2] Hadi Faghihmaleki and Gholamreza Abdollahzadeh. “Using Risk-Based Robustness Index for Seismic Improvement of Structures.” KSCE Journal of Civil Engineering 23.3 (2019): 1207–1218. DOI: https://doi.org/10.1007/s12205-019-0350-5 .

[3] Hadi Faghihmaleki and Mohammad Sayadi. “Evaluation of the Performance of Moment Resisting Steel Frames under Near Field and Far Field Earthquakes Based on Energy Conception.” Sigma Journal of Engineering and Natural Sciences 40.1 (2022): 1–8. DOI: https://doi.org/10.14744/sigma.2022.00001 .

[4] Mohammadreza Noori Shirazi. “Seismic Strength of RC Columns Using Enhanced Steel Jacket. FE Modeling.” Journal of Civil Engineering Researchers 4.1 (2022): 39–54. DOI: https://doi.org/10.52547/JCER.4.1.39 .

[5] Zhiwei Ding, Faxing Li, Gang Gong, and Yuzhong Yu. “Behavior of Tubular Stub Columns of Axially Loaded Steel-Reinforced Concrete-Filled Circular Steel.” Journal of Central South University 43 (2012): 3625–3630.

[6] Ahmed Elremaily and Atorod Azizinamini. “Behavior and Strength of Circular Concrete-Filled Tube Columns.” Journal of Constructional Steel Research 58.12 (2019): 1567–1591. DOI: https://doi.org/10.1016/S0143-974X(02)00005-6 .

[7] M. V. Chitawadagi, M. C. Narasimhan, and S. M. Kulkarni. “Axial Capacity of Rectangular Concrete-Filled Steel Tube Columns – DOE Approach.” Construction and Building Materials 24.4 (2010): 585–595. DOI: https://doi.org/10.1016/j.conbuildmat.2009.09.006 .

[8] Zhong Tao, Brian Uy, Feiyan Liao, and Lianghua Han. “Nonlinear Analysis of Concrete-Filled Square Stainless Steel Stub Columns under Axial Compression.” Journal of Constructional Steel Research 67.11 (2021): 1719–1732. DOI: https://doi.org/10.1016/j.jcsr.2011.04.012 .

[9] Mahmoud M. El-Heweity. “On the Performance of Circular Concrete-Filled High Strength Steel Columns under Axial Loading.” Alexandria Engineering Journal 51.2 (2022): 109–119. DOI: https://doi.org/10.1016/j.aej.2012.05.006 .

[10] Wenbin Yuan and Jinjun Yang. “Experimental and Numerical Studies of Short Concrete-Filled Double Skin Composite Tube Columns under Axially Compressive Loads.” Journal of Constructional Steel Research 80 (2023): 23–31. DOI: https://doi.org/10.1016/j.jcsr.2012.09.014 .

[11] Tamer Ekmekyapar, Omar H. Alwan, Hozan G. Hasan, Bashar A. Shehab, and Bashar J. M. AL-Eliwi. “Comparison of Classical, Double Skin and Double Section CFST Stub Columns: Experiments and Design Formulations.” Journal of Constructional Steel Research 155 (2019): 192–204. DOI: https://doi.org/10.1016/j.jcsr.2018.12.025 .

Journal of Civil Engineering Researchers

Journal homepage: www.journals-researchers.com

Evaluation of Seismic Response of Multi-Story Structures: A Comparative Study of Buckling Restrained Braces and Viscous Dampers

Mansour Bagheri,[a,*] Seyed Abbas Hosseini[b]

[a] *Department of Civil Engineering, Birjand University of Technology, Birjand, Iran*

[b] *Faculty of Technology and Mining, Yasouj University,Yasouj, Iran*

ABSTRACT

In buckling restrained bracing systems, earthquake-induced elongation problems are solved, and BRB-equipped structures have a much more effective performance in energy absorption in addition to high lateral stiffness. Systems equipped with viscous dampers (VD) also have great potential to absorb seismic energy. To assess the vulnerability of structures equipped with buckling restrained bracing (BRB) and VD systems, three structures (6-, 10- and 15-story) were chosen as representatives of mid-rise, high-rise and super high-rise buildings and modeled in four states of moment-resisting frame (MRF): the frame equipped with VD, the frame equipped with BRB, and the frame equipped with BRB and viscous damper simultaneously (BRB+VD) using OpenSees-2.4.6 software under incremental dynamic analysis (IDA). Seven seismic records were applied, and the maximum inter-story drift response and fragility curves were determined. The results indicated that although the simultaneous application of BRB+VD causes a significant decline in the response of all structures, each of these two systems is able to provide structural safety at various levels in mid-rise structures. It is required to apply both systems simultaneously to provide safety for slight and moderate levels of damage in high-rise buildings, while super high-rise buildings are vulnerable to whole levels of damage, and their structural safety involves the simultaneous use of both systems.

ARTICLE INFO

Received: April 11, 2025
Accepted: April 23, 2025

Keywords:
Viscous Damper (VD)
Buckling Restrained Brace (BRB)
Incremental Dynamic Analysis (IDA)
Seismic Response
Multi-Story Structures

DOI: 10.61186/JCER.7.2.57
DOR: 20.1001.1.2538516.2025.7.2.5.3

1. Introduction

High lateral forces are applied to the structure during an earthquake. Since the philosophy of most design methods is based on the prevention of structural collapse and energy absorption and dissipation, the building must exit the elastic region, and inelastic cyclic displacements should occur when the structure is exposed to seismic forces. Hence, this may lead to irreparable damage to the structure due to plastic hinges formed in specific points. Researchers have examined the effect of modern technologies on structural safety and strength against seismic forces in recent years. The systems are based on energy absorption and changing the frequency of the structure, which eventually withstand the seismic energy and cause less damage to structural elements. Fluid viscous dampers

---

[*] Corresponding author. Tel.: +98915543091; e-mail: mnsrbagheri@gmail.com.

(FVDs) are among the systems that consist of a cylinder, a stainless-steel piston, and a perforated bronze cap which has a high capacity to absorb energy and plays a crucial role in the seismic energy dissipation of structures.

On the other hand, there are other resistant systems to retrofit structures against seismic loads that most of which are based on the distribution of seismic force among structural elements such as braced frames. To eliminate the drawbacks of bracing systems, i.e., buckling behavior and yielding, the braces should reach the yield point without bucking under compression and tension. A system equipped with this type of bracing is known as buckling restrained braced frame (BRBF). Bucking restrained bracing system is a new technology which can absorb far more energy than conventional bracing systems due to the prevention of buckling. BRBFs include a variety of components such as a steel brace to withstand axial forces, a gusset plate linked to the connection and brace, a casing to resist buckling, and grout to fill the gap between the steel core and casing. A small gap is also provided to allow the steel core moving freely in the grout infill and decrease friction effects. The steel core is usually designed like a bone with decreased cross-section to concentrate yielding in the region.

Hatzigeorgiou et al. [1] studied the behavior of structures equipped with VDs under near-field earthquakes and evaluated the effect of structural parameters, attached damper parameters, and type of fault on maximum seismic velocity and damping force. Results revealed the profound and significant impact of effective damping ratio of VD on the inelastic seismic response of structures. Introducing the super-elastic VDs, Silwal et al. [2] studied the seismic collapse resistance of steel frames equipped with such dampers. The super-elastic dampers are hybrid passive control devices (HPCDs) combined with viscoelastic materials and alloy cables, possessing higher energy dissipation capacity compared to other VDs. The main results of the research showed a better performance of damping system in comparison with conventional MRF and BRB. Hsu and Halim [3] studied a curved steel damper embedded in the beam-to-column connection. The results of research demonstrated that as curvature angle increases in the damper, the strength of frames rises, and damper considerably enhances the strength, stiffness, and energy dissipation. Banazadeh et al. [4] investigated the performance of structures designing two linear and nonlinear dampers with the same damping ratio for 6, 8 and 12-story frames. Applying incremental dynamic analysis (IDA); the results showed the improved performance of structures equipped with the damper compared to moment resisting frame structures for the same damping ratios. Kazemi et al. [5] investigated the effect of linear FVDs on the seismic vulnerability of buildings. Survey results showed that the installation of linear VD reduces the maximum impact force and duration of impacts exerted to adjacent structures, postpones the collapse of the structures. Abdi et al. [6] investigated the response modification factors for reinforced concrete (RC) structures equipped with VDs. The results suggested that response modification factors for RC structures equipped with VDs are more than those without VDs, and the number of dampers and building height have significant influences on response modification factors. Guo et al. [7] tried to control structural vibration under powerful earthquake excitation. To achieve this goal, they implemented a nine-story benchmark steel building and three different and typical types of dampers. VD, and BRB were mounted to this prototype to examine its response to 10 earthquake records. The fragility curves showed that the largest collapse margin ratio was with the viscoelastic damper, and the greatest drift control was provided by the VD. The floor acceleration responses in the mid-rise building can be reduced effectively by both of the BRB and VDs.

Ataei and Anaraki [8] evaluated seismic response of structures developing a design procedure based on corrected response spectrums. The effectiveness of the proposed method was explored through nonlinear time series analysis of 3, 5 and 7-story steel frames. Consequently, the obtained results were verified with the collapse fragility curves of the generic structures according to the ASCE 7-10 and displacement-based design methodology. survay results show that models designed according to the proposed procedure indicated great performance using degrading dampers. Rofooei and Mohammadzadeh [9] studied the optimal distribution of fluid VDs to control the seismic response of moment-resisting concrete structures by using a previously defined center of damping constant. Findings revealed that the stiffness eccentricity, which is the major parameter in determining the location of the optimal center of damping constant, tended to be smaller than the optimal damping constant eccentricity in the linear range of structural behavior.

Jae-Do Kang and Hiroshi Tagawa [10] designed experimental and numerical research on a seesaw energy dissipation system using FVDs. The results indicated that the system had enough damping capacity to reduce seismic response of frames. He and Lu [11] used three numerical models of a super-tall building to investigate the inter-story drift control effect under different hybrid control schemes using buckling restrained braces and VDs. The results revealed that in fragility analysis, peak ground velocity (PGV) according to its high efficiency is suitable for IDA in high-rise buildings. Kariniotakis and Karavasilis [12] established different steel moment-resisting frames designed according to Eurocode 8 equipped by VDs. Collapse fragility curves were generated performing IDA for 44 ground motions. The design criteria were compared according to Eurocode 8. Yahyazadeh and Yakhchalian [13] investigated the effects of linear and nonlinear FVDs on the maximum residual inter-story drift ratio response of steel special MRF.

Nomura et al. [14] examined how effective viscous dampers are for retrofitting steel moment frames. Through simulations of different seismic scenarios, they discovered that the dampers considerably decreased peak accelerations and inter-story drifts during earthquakes. The findings underscored that viscous dampers not only enhance the structural resilience of buildings but also present a cost-effective alternative to conventional retrofitting methods. Chen et al. [15], introduced a performance-based methodology for retrofitting steel moment frames using viscous dampers. They created a detailed design framework that takes into account various seismic design criteria and also examined an existing steel frame building that was retrofitted with viscous dampers. The findings revealed that this retrofit not only increased the building's energy dissipation capacity but also significantly enhanced its overall performance, resulting in a marked reduction in seismic vulnerability. Kim et al. [16] investigated the integrated design considerations involved in retrofitting steel moment frames using viscous dampers. The authors introduced an innovative design methodology that merges performance-based design principles with numerical simulation techniques to determine the optimal placement and sizing of the dampers. Results indicated that strategically positioning the dampers notably improves energy dissipation and enhances the overall seismic resilience of the structures.

Wakabayashi [17] introduced BRBs for seismic hazard for steel structures. Choi and Kim [18] studied the energy dissipation capacity and seismic response of steel structures equipped with BRBs. They concluded that as the stiffness of BRBs increases, the equivalent damping ratio of single-degree-of-freedom (SDOF) structures rises, and the maximum displacement of buildings declines in general. Sahoo and Chao [19] investigated the performance of the plastic design method for buckling restrained braced frames. The results revealed that the frames designed through the performance-based design (PBD) method could successfully limit the maximum displacements to the predetermined target displacement. Chang and Chiu [20] investigated a 6-story office building equipped with BRBs. Seismic performance of building and capacity and requirements of BRBs through test results and response analysis were studied. Findings showed that BRBs could provide high confidence levels, which guarantee the proper satisfaction of immediate occupancy and life safety performance levels in the building. Guo et al. [21] studied BRBs with two individual cores and evaluated its load-bearing capacity and hysteresis response. The results indicated a good compatibly between test results and finite element analyses and showed that even proposed equations could be used to design the braces; this reveals that buckling does not happen in the independent cores of BRBs before global buckling of bracing system. Bing et al. [22] assessed a new type of BRBs with replaceable angular steel fuses. They tested seven braces to examine the seismic behavior of these BRBs. Given the tests, it was concluded that the hysteretic behavior of these braces resembles conventional BRBs, and the proposed braces can show a stable hysteretic behavior to relatively high levels of strain in the fuses.

Park et al. [23] examined the seismic performance of steel buckling-restrained braces (BRBs) by integrating experimental testing with numerical simulations. The authors performed full-scale tests to evaluate the behavior of the braces under different seismic loading scenarios. The results indicated that BRBs effectively dissipated energy and retained their strength even during intense earthquake events. Morales et al. [24] explored the dynamic behavior of steel structures fitted with buckling-restrained braces (BRBs) when subjected to seismic excitation. They employed sophisticated numerical modeling methods to evaluate the impact of BRBs on the overall performance of these structures during earthquakes. Their findings demonstrated that buildings with BRBs experienced considerably lower inter-story drifts and enhanced energy dissipation compared to those using conventional bracing systems.

Given the increasing development of new technologies for structural improvement using buckling restrained bracing system and promotion of their safety level and seismic resistance using a variety of dampers, particularly VDs, this study attempts to find out how their individual or simultaneous application affects the performance of structures of different stories, ranging from low-rise to high-rise. The vulnerability of structures is evaluated at slight, moderate, extensive and complete levels of damage in order to introduce a suitable system amongst steel moment resisting frame (MRF), moment resisting frame with viscous damper (VD), moment resisting frame with BRB (BRB) and moment resisting frame with BRB and viscous damper (MRF+VD).

2. Investigated models

To evaluate the behavior of structures equipped with BRB or VD, three 6-, 10- and 15-story structures with 4 spans 4m in length, 3m in height are selected as representatives of mid-rise, high-rise and super high-rise building, respectively. These three structures are initially designed as MRF under the requirements of seismic considerations, AISC 360 and AISC 341 codes, respectively [25,26], as shown in the plan in Fig.1 Then, the outer frame of each structure is chosen and modeled by OpenSees software [27]. Fig.2 demonstrates the arrangement of VDs and BRBs within the frames; the sections used for these structures are listed in Table 1. According to the table, W sections are used for beams, and TUB sections are used for columns, both made of steel with the yield strength of 2400 kg/cm2 and elastic modulus of 2.1 × 16 kg/cm2. The buckling restrained braced span should satisfy specific seismic criteria due to the forces applied by the BRB, where the sections must be stronger than other structural members.

2.1. Verification of modeling

In order to ensure the reliability of BRB modeling, a frame illustrated in Fig. 3 was modeled and exposed to cyclic analysis. The BRB is modeled by OpenSees using Corotational truss element and Steel02 material. Fig. 4 shows the results of analysis of modeled bracing system compared with the results of an experimental specimen utilized by Burkholder [28]. To model the VD by OpenSees software, the Viscous Damper material defined by Lignos is used and assigned to a two Node Link element.

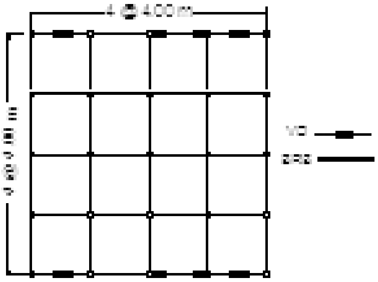

Fig. 1. Plan of investigated models

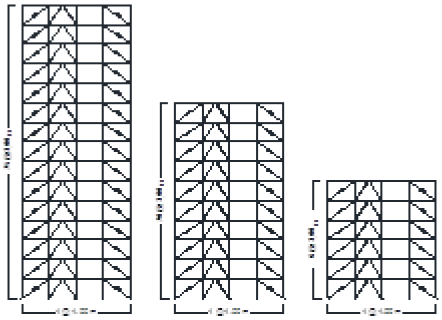

Fig. 2. Arrangement of BRBs and VD in models

Table 1
Frame sections

Element Type	Beam			Column		
Story No.	6 story	10 story	15 story	6 story	10 story	15 story
1	W 12×35	W 12×35	W 14×38	TUB 280×20	TUB 320×28	TUB 320×28
2	W 12×35	W 12×35	W 14×38	TUB 280×20	TUB 320×28	TUB 320×28
3	W 12×19	W 12×26	W 14×38	TUB 220×16	TUB 280×20	TUB 320×28
4	W 12×19	W 12×26	W 12×35	TUB 220×16	TUB 280×20	TUB 320×28
5	W 12×14	W 12×26	W 12×35	TUB 180×16	TUB 260×20	TUB 280×20
6	W 12×14	W 12×26	W 12×35	TUB 180×16	TUB 260×20	TUB 280×20
7	-	W 12×26	W 12×26	-	TUB 220×16	TUB 280×20
8	-	W 12×14	W 12×26	-	TUB 220×16	TUB 280×20
9	-	W 12×14	W 12×26	-	TUB 180×16	TUB 260×20
10	-	W 12×14	W 12×19	-	TUB 180×16	TUB 260×20
11	-	-	W 12×19	-	-	TUB 260×20
12	-	-	W 12×19	-	-	TUB 260×20
13	-	-	W 12×14	-	-	TUB 220×16
14	-	-	W 12×14	-	-	TUB 220×16
15	-	-	W 12×14	-	-	TUB 220×16

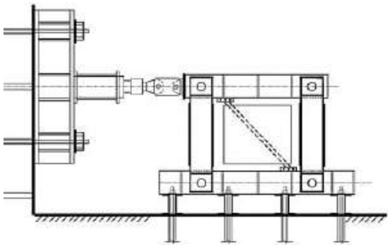

Fig. 3. Prototype of BRB modelling [29]

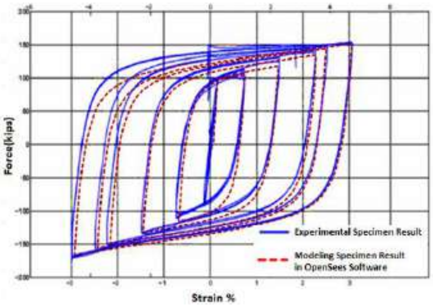

Fig. 4. Verification of BRB modelling

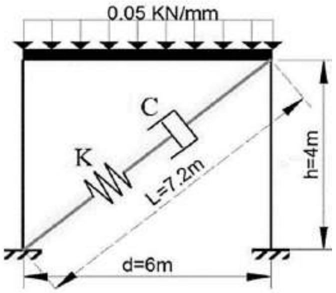

Fig. 5. Prototype of VD modelling [4]

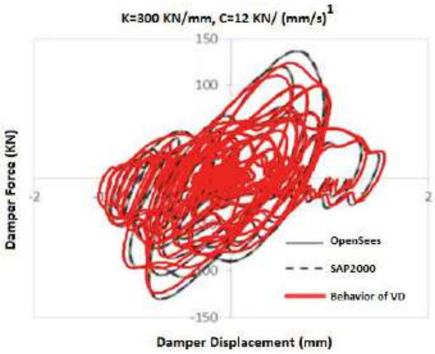

Fig. 6. Verification of VD modelling

Table 2
Specifications of BRBs

Model	6 story	10 story	15 story
Base shear coefficient	0.0933	0.0723	0.0590
Base shear (ton)	91	120	145
Brace axial force (ton)	41.2	53.3	65.3
Brace core area (cm^2)	19.08 ~ 20	24.67 ~ 25	30 ~ 30.23

Table 3
Specifications of VDs

Model	Type	Damping ratio (%)	Magnification factor	Damping Coefficient (ton.sec/m)	Damper Stiffness (ton/m)
6 story	Diagonal	25	f_v=0.6	305.97	4320.88
10 story	Diagonal	25		666.12	5388.43
15 story	Diagonal	25	f_h= 0.8	1310.25	6749.47

To validate the modeling of the behavior of viscous damper, the response presented in a study by Banazadeh [4] is employed, where a 1-story single-span frame is modeled using SAP and OpenSees according to Fig. 5. The frame is made of sections including TUB 200×20 for columns and W 5×16 for beams and subjected to a distributed load of 0.05 KN/mm and the time history analysis is conducted using the Kobe earthquake record at a scale factor of 0.5. In this study, the VD is similarly modeled in a 1-story single-span frame and its response to time history analysis under the Kobe earthquake record at a scale factor of 0.5 is compared with that of study by Banazadeh [4] according to Fig. 6; the acceptable compatibility between the results implies the proper performance of modeled VD in this study.

2.2. BRB and VD modelling

Given the symmetry of braces on both sides of structure for each frame, half of total base shear force calculated for the structure is taken into account in this study and the axial force of the brace and area of BRB steel core are then obtained. Tables 2 and 3 represent the specifications of BRBs and VDs, respectively.

3. Incremental Dynamic Analysis and results

Incremental dynamic analysis (IDA) using 7 earthquake records normalized in acceleration of gravity on 10 scales ranging from 0.1g to 1.0g is performed. The specifications of applied records are given in Table 4. The results of the analysis of each structure are then plotted as IDA curves, i.e. MRF, frame equipped with VD, frame equipped with BRB and frame equipped with BRB+VD. The fragility curves and maximum inter-story drift response of each structure as a failure index at 1PGA are compared with each other in order to estimate the vulnerability of structures during various earthquakes at different performance levels using statistical and probabilistic functions. Fig.7 illustrates the IDA curve of 15-story structure with moment resisting frame system. Table 5 represents the period of 6-, 10- and 15-story models of three states.

Fig. 8 shows that the maximum drift response occurs in middle stories at about 0.4-0.6 of total height in high-rise MRF. The chart of the Tabas earthquake also indicates the instability of mid-rise structure under the record; except for this earthquake, the inter-story drift of structure gradually decreases at the bottom and top floors for other earthquakes.

Given the fragility curve of 10-story MRF in Fig. 9, the exceedance probability (EP) of a slight level of damage between 0.1PGA and 0.4PGA increases dramatically and reaches about 50% at 0.4PGA; then, the slope of the curve lowers and finally reaches about 69% at 1PGA. At the moderate level of damage, the EP uniformly rises for different accelerations and finally reaches about 65% at 1PGA. At extensive level of damage, the EP approximately equals zero up to 0.3PGA and then gently increases to 0.7PGA; the slope continues to grow significantly and then reaches about 50%. A complete level of damage, the EP equals zero up to 0.7PGA and then gradually reaches 13%; so that sudden changes in the slope of curves at 0.7PGA can represent the formation of plastic hinges in the structure and its vulnerability at these accelerations.

Table 4
Applied seismic records [30]

NO	Earthquake	Site	Year	PGA(g)
1	Bam	Bam	2003	0.81
2	Erzincan	Erzincan	1992	0.5
3	Izmir	Izmir	1997	0.42
4	Kobe	Takarazuka	1995	0.67
5	Loma printa	Los Gatos	1989	0.41
6	Northridge	24087 Arleta –Nordhoff Fire	1994	0.34
7	Tabas	Tabas	1999	0.84

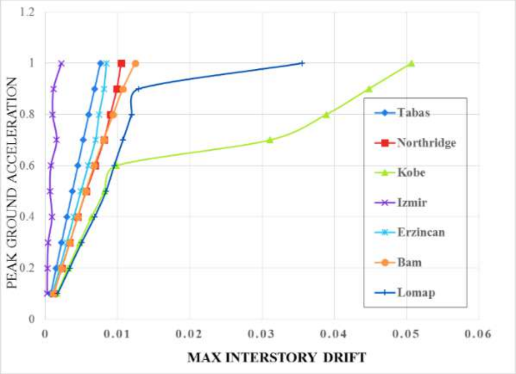

Fig. 7. IDA curve for 15-story structure equipped with VD

Table 5
Period of models (sec)

Model	MRF	VD	BRB	BRB+VD
6 story	0.45	0.45	0.22	0.22
10 story	0.77	0.77	0.32	0.32
15 story	1.22	1.22	0.44	0.44

According to Fig. 10, when seismic dampers are attached to the structures, e.g. mid-rise structures, the maximum responses occur on lower stories at about 0.2-0.4 of building height in comparison with the MRF. According to the fragility curve of the 10-story structure equipped with VD in Fig. 11, the EP of structure at slight level of damage equals zero up to 0.3PGA and then rises uniformly until reaches 38% at 1PGA, indicating a 30% decrease in comparison with the MRF. At the moderate level of damage, the EP equals zero up to 0.5PGA and then constantly reaches 18% at 1PGA, which shows a 50% decrease in comparison with MRF. For the extensive and complete levels of damage, the EP is about zero throughout the analysis, where the structure possesses adequate safety level, which respectively 50% and 15% decreases show a good seismic performance in these structures compared to the MRF.

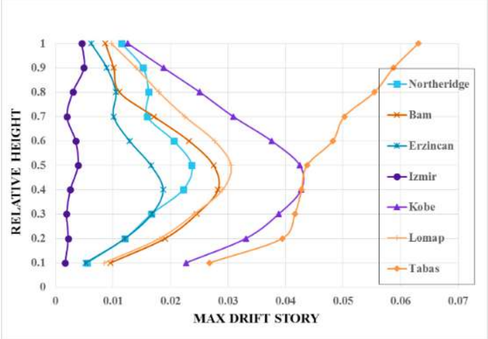

Fig. 8. Inter-story drift responses of 10-story MRF

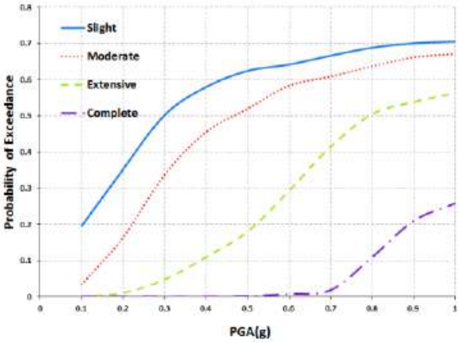

Fig. 9. Fragility curve of 10-story MRF

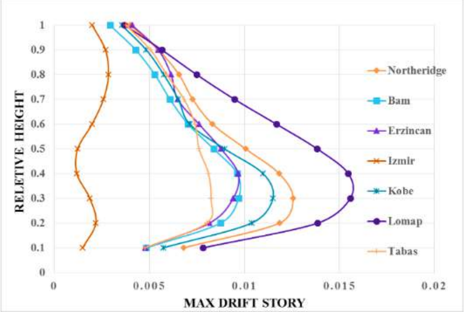

Fig. 10. Inter-story drift responses of a 10-story structure equipped with VD

Fig. 12 shows that in high-rise structures equipped with BRBs, the maximum drift response occurs on the floors at 0.2-0.4 of total building height but the responses on upper floors decrease more intensively compared to

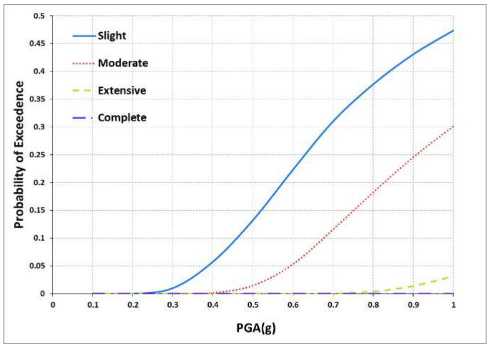

Fig. 11. Fragility curve of a 10-story structure equipped with VD

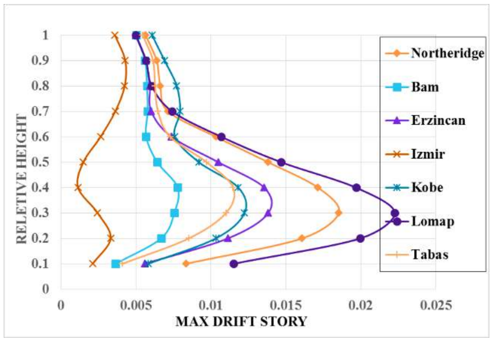

Fig. 12. Inter-story drift responses of a 10-story structure equipped with BRB

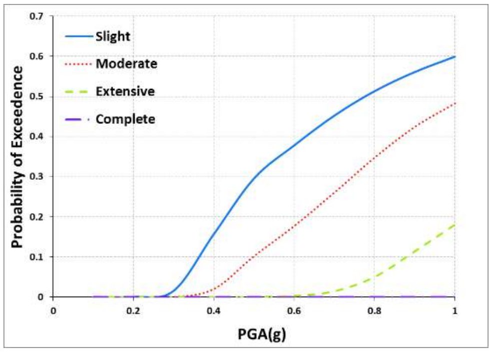

Fig. 13. Fragility curve of a 10-story structure equipped with BRB

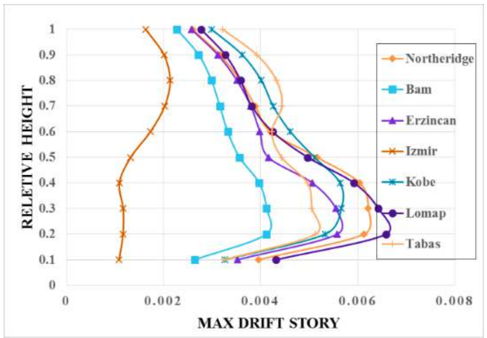

Fig. 14. Inter-story drift responses of a 10-story structure equipped with BRB+VD

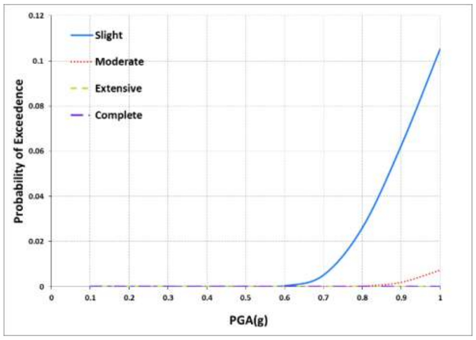

Fig. 15. Fragility curve of a 10-story structure equipped with BRB+VD

mid-rise structures; hence the probability of formation of plastic hinges and their number would be relatively higher than that for mid-rise frames. Given the fragility curve in Fig. 13, it is observed that the EP of 10-story structure equipped with BRB at the slight level of damage equals zero up to 0.3PGA and eventually surges to 53% on a constant steep slope at 1PGA, indicating a 40% decrease at 0.3PGA and a 15% decrease at 1PGA compared to the MRF. At the moderate level of damage, the EP equals zero up to 0.3PGA and then steadily reaches about 53% at 1PGA, showing a 12% decrease compared to the MRF. At extensive level of damage, the EP equals zero up to 0.7PGA and finally reaches about 18%, indicating a 30% decrease compared to the MRF. A complete level of damage, the EP of structure equals zero at all accelerations, which indicates a 13% decrease compared to the MRF.

As shown in Fig. 14, in high-rise structures equipped with BRB+VD, bottom floors are more vulnerable than other floors and the maximum drift response occurs at about 0.2 of building height; this indicates that the maximum response in these structures is still transferred to bottom floors compared to other high-rise structures. In Fig. 15, the fragility curve of a 10-story structure equipped with BRB+VD demonstrates a very low EP for slight level of damage at accelerations above 0.7PGA; so that the EP equals zero up to that acceleration and then reaches 3% at 1PGA on a constant slope. For other performance levels, the EP equals zero up to 1PGA. In Table 6, the changes in drift responses and the decrease in EP for the structure equipped with BRB+VD is compared to those for structures equipped with MRF, VD, and BRB.

According to Table 6, it can be concluded that the simultaneous use of BRB+VD in mid-rise structures causes a 98%, 93% and 53% decrease in inter-story drift response compared to MRF, VD and BRB, respectively, which indicates the good performance of these two systems in the reduction of structural response. It is also seen that although the simultaneous application of BRB+VD leads to a 65%, 55% and 22% decrease compared to the MRF at slight, moderate and extensive levels of damage, respectively, the changes in PE of model equals almost to zero compared to mid-rise BRB or VD structures at different levels; this implies that mid-rise structures equipped with BRB or VD can lonely meet safety requirements at different performance levels and the simultaneous use of both systems seems very conservative and unnecessary in spite of considerable decrease in maximum drift response.

For high-rise structures, the simultaneous use of BRB+VD leads to an 89%, 58%, and 70% decrease compared to MRF, VD and BRB respectively, which indicates the good performance of both systems to reduce the maximum response of structure; but the decrease in maximum structural responses is less than those for mid-rise models. Moreover, the simultaneous use of BRB+VD in high-rise structures reduces the PE by 69%, 38% and 53% at slight level of damage and by 65%, 18% and 40% at moderate level of damage compared to the MRF, VD and BRB, respectively. So, it can be concluded that these structures need to meet safety requirements at 1PGA. At extensive and complete levels of damage, the PE declines by 50% and 13% in BRB+VD compared MRF, respectively; but the decrease in PE equals almost to zero compared to VD or BRB. Results implies that the structure can adequately meet safety requirements at these levels by the installation of BRB or VD alone and the simultaneous use of both systems leads to no changes in PE at these levels. Hence it can be concluded that if it is required to provide safety at slight and moderate levels of damage, the unique performance of both systems can be employed simultaneously; but if safety at extensive and complete levels of damage is required, the BRB or VD can lonely meet the requirements and their simultaneous use is not cost-efficient.

Given the values for super high-rise structures equipped with BRB+VD, it is also observed that the maximum drift response of these structures is reduced by 86%, 86% and 78% compared to the MRF, VD and BRB, respectively. Hence these structures show a good performance by limiting the maximum structural response to allowable values of the code. The structural response decreases by 53%, 51% and 48% at slight level of damage, 68%, 66% and 42% at moderate level of damage, 57%, 57% and 40% at extensive level of damage and 25%, 25% and 4% at complete level of damage compared to the MRF, VD and BRB, respectively. Thus, these structures are vulnerable at all performance levels and just the frame equipped with BRB has relative safety at complete level of damage. Therefore, the simultaneous use of BRB+VD is crucial in super high-rise structures to meet safety requirements at 1PGA.

4. Discussion and interpretation of results

In mid-rise structures equipped with MRF and BRB, the floors at 0.4-0.6 of building height have the maximum inter-story drift during earthquakes and are the most vulnerable points. These structures equipped with MRF system experience higher damage probability in earthquakes above 0.5PGA for slight and moderate levels of damage. So these structures experience PE of 65% and 55% at 1PGA for the performance levels, respectively. This indicates their vulnerability at these performance levels, while PE is zero up to 0.6PGA for extensive level of damage and reaches 20% at 1PGA. The PE equals zero throughout the analysis for complete level of damage; hence the structure generally possesses adequate safety at these performance levels. In the system equipped with VD, the floors at 0.3-0.4 of total building height show the maximum drift responses. These structures have PE of zero throughout the analysis for slight, moderate, extensive and complete levels of damage, indicating 50%, 47%, and 20% reductions compared to the MRF structure for slight, moderate and extensive levels of damage respectively. Therefore, the model has adequate safety at 1PGA for all performance levels. In mid-rise structures equipped with VD, the variation of inter-story drift is linear, which implies that plastic hinges are not formed and the structure does not exceed the elastic region; the maximum drift response is reduced by 74% compared to MRF.

The PE of mid-rise structures equipped with BRB is zero for whole slight, moderate, extensive and complete levels of damage, which shows that BRBs can properly meet safety requirements of these structures at 1PGA. Similar to structures equipped with VD, the variation of maximum drift response in mid-rise structures equipped with BRB is linear, which indicates the elastic conditions and formation of no plastic hinges. In structures equipped with BRB+VD, the maximum drift responses occur at about 0.3 of total building height. Which demonstrates that the model has adequate safety at the performance levels and the variation of maximum drift response is linear.

In high-rise structures equipped with MRF system, the floors at 0.4-0.6 of total building height experience the maximum drift response, which occurs on the floors at 0.2-0.4 of total building height in the structures equipped with

Table 6
BRB+VD Compared to other models

Model	6 Story (mid-rise structure)						10 Story (high-rise structure)						15 Story (super high-rise structure)					
	Loss of PE of damage state				Max. response	Response reduction (%)	Loss of PE of damage state				Max. response	Response reduction (%)	Loss of PE of damage state				Max. response	Response reduction (%)
	slight	moderate	extensive	complete			slight	moderate	extensive	complete			slight	moderate	extensive	complete		
MRF	65	55	22	0	0.034	98	69	65	50	13	0.063	89	53	68	57	25	0.051	86
VD	9	1	0	0	0.008	93	38	18	0	0	0.016	58	51	66	57	25	0.05	86
BRB	0	0	0	0	0.001	53	53	40	8	0	0.022	70	48	42	40	4	0.032	78

VD or BRB and at 0.2 of total building height in the structures equipped with BRB+VD, considered as the most vulnerable floors. Compared to initial accelerations, the PE of MRF system undertakes a significant increase at different performance levels, i.e. 69%, 65%, 50% and 13% at 1PGA for slight, moderate, extensive and complete levels of damage, respectively that shows the vulnerability of structure at these levels. In these models, the variation of drift response also increases at accelerations above 0.7PGA, which refers to the formation of plastic hinges. In the models equipped with VD, the PE at 1PGA is 38% and 18% for slight and moderate levels of damage, respectively, and almost zero for both extensive and complete levels of damage with 30%, 50%, 50%, and 15% decrease for slight, moderate, extensive and complete levels of damage, respectively. Which reveals the adequate safety of these structures up to 1PGA. In these structures, the variation of drift response is almost linear, indicating that the structure is in the elastic region during the analysis.

In high-rise structures equipped with BRB, the PE at 1PGA is 53%, 40%, 8% and 0% for slight, moderate, extensive and complete levels of damage and the variation of maximum drift is non-linear at accelerations above 0.4PGA, that demonstrates the relative formation of plastic hinges. For the structures equipped with BRB+VD, reductions of 53%, 40%, and 8% are also observed at slight, moderate and extensive levels of damage compared to the corresponding structure equipped with BRB. In high-rise structures equipped with BRB+VD, the maximum drift response shows a 58% decrease in comparison with the structure equipped with BRB.

The maximum drift response occurs on floors at 0.4-0.6 of building height in super high-rise structures equipped with MRF or VD and on floors at 0.2-0.4 of building height in structures equipped with BRB or BRB+VD, representing the vulnerability of these floors in super high-rise structures. In the structures equipped with MRF, the PE is so great even at low earthquake accelerations for slight and moderate levels of damage, i.e. 73% and 70% at 1PGA, respectively. It increases considerably at accelerations above 0.7PGA for extensive and complete levels of damage, i.e. 58% and 25% at 1PGA, respectively, which represents significant vulnerability of these structures. For the MRF system, the variation of maximum drift response often has a considerable slope at accelerations above 0.4PGA and the non-linear trend indicates the formation of plastic hinges, which mostly exceeds allowable values and reaches twice as much as them in some cases.

In addition, VDs does not have a reliable performance in super high-rise structures and practically lose their efficiency in some seismic records. In these structures, the PE decreases suitably at low accelerations, i.e. 40%, 38% and 35% at 0.6PGA for slight, moderate and extensive levels of damage, respectively. However, they are not efficient at higher accelerations and show negligible variations at 1PGA compared to the MRF structure. In super high-rise structures equipped with VD, the variation of maximum drift response is linear up to 0.6PGA that represents the elastic state, but it abruptly rises at higher accelerations in some earthquakes; hence it does not seem so reasonable to apply dampers in super high-rise structures.

The PEs of super high-rise structures equipped with BRB exhibit the high vulnerability of model for various performance levels, particularly at accelerations above 0.5PGA. The variation of maximum drift response starts to increase significantly at accelerations above 0.4PGA and exceeds allowable values at higher accelerations, which indicates the inefficiency of BRBs to meet safety requirements of the structure. In super high-rise structures equipped with BRB+VD, the PE equals to zero at entire performance levels, indicating appropriate safety at all performance levels. Despite significant decreases in these structures, the variation of maximum drift response at accelerations above 0.4PGA follows an irregular trend compared to other structures, which is due to the distribution of seismic forces applied to structural members, BRB+VD, considering the low values of structural response. Super high-rise structures equipped with BRB+VD show a very good performance due to the 78% decrease in the maximum structural response compared to structures equipped with BRB and the limitation of maximum structural response to allowable values of the code. The super high-rise structure equipped with BRB+VD shows 48%, 42%, 40%, and 4% decreases for slight, moderate, extensive and complete levels of damage, respectively, compared to the structure equipped with BRB.

5. Conclusions

In this study, three 6-, 10- and 15-story structures are considered to investigate the effect of VDs on the response of structures equipped with BRBs. Four systems, e.g. MRF, frame equipped with VD, frame equipped with BRB and frame equipped with BRB+VD, are then modeled using OpenSees. The IDA is conducted for the structures at different accelerations and frequencies under 7 seismic records and the results are finally examined in form of IDA, fragility and inter-story drift curves.

Investigating the IDA results and fragility curves of the structures, it is concluded that the simultaneous use of BRB+VD provides no reduction of PE for mid-rise structures at slight, moderate, extensive and complete levels of damage in comparison to the systems equipped with BRB or VD. Therefore, these structures can meet safety requirements at different performance levels merely by BRBs or VDs and the simultaneous application of both systems seems highly conservative in spite of significant decrease in maximum drift response.

Moreover, high-rise structures equipped with BRBs or VDs can meet safety requirements at extensive and complete levels of damage, but both BRBs and VDs should be utilized to provide safety at slight and moderate levels of damage. One of the key findings of the research is that super high-rise structures equipped with MRF, BRB or VD are vulnerable at the entire slight, moderate, extensive and complete levels of damage; hence it is required to employ structures equipped with BRB+VD to meet safety requirements at accelerations up to 1PGA. This means that structural engineers can significantly enhance the safety of high-rise and super high-rise buildings by ensuring both BRB and VD systems work together. Overall, this study highlights the importance of earthquake resistance structural systems ensuring the safety of the occupants during seismic events.

References

[1] Hatzigeorgiou, D. G., and Pnevmatikos, G. N. “Maximum Damping Forces for Structures with Viscous Dampers under Near-Source Earthquakes.” Engineering Structures 68.1 (2014): 1–13. DOI: https://doi.org/10.1016/j.engstruct.2014.02.018.

[2] Silwal, B., Ozbulut, E. O., and Michael, J. R. “Seismic Collapse Evaluation of Steel Moment Resisting Frames with Superelastic Viscous Damper.” Journal of Constructional Steel Research 126.1 (2016): 26–36. DOI: https://doi.org/10.1016/j.jcsr.2016.03.004.

[3] Hsu, H. L., and Halim, H. “Improving Seismic Performance of Framed Structures with Steel Curved Dampers.” Engineering Structures 130.1 (2017): 99–111. DOI: https://doi.org/10.1016/j.engstruct.2016.10.026.

[4] Banazadeh, M., and Ghanbari, A. “Seismic Performance Assessment of Steel Moment-Resisting Frames Equipped with Linear and Nonlinear Fluid Viscous Dampers with the Same Damping Ratio.” Journal of Constructional Steel Research 136.1 (2017): 215–228. DOI: https://doi.org/10.1016/j.jcsr.2017.08.020.

[5] Kazemi, F., Mohebi, B., and Yakhchalian, M. “Enhancing the Seismic Performance of Adjacent Pounding Structures Using Viscous Dampers.” 16th European Conference on Earthquake Engineering (16ECEE), Thessaloniki, Greece (2018).

[6] Abdi, H., Hejazi, F., Jaafar, M. S., and Karim, I. B. A. “Response Modification Factors for Reinforced Concrete Structures Equipped with Viscous Damper Devices.” Periodica Polytechnica Civil Engineering 62.1 (2018): 11–25. DOI: https://doi.org/10.3311/PPci.9938.

[7] Guo, W., Wu, J., Hu, Y., Li, Y., and Yang, T. Y. “Seismic Performance Evaluation of Typical Dampers Designed by Chinese

Building Code." Earthquake Engineering and Engineering Vibration 18.2 (2019): 433–446. DOI: https://doi.org/10.1007/s11803-019-00478-4.

[8] Ataei, H., and Anaraki, K. K. "A Proposed Structural Design Method Considering Fluid Viscous Damper Degradations." Structural Design of Tall and Special Buildings 27.15 (2018). DOI: https://doi.org/10.1002/tal.1344.

[9] Rofooei, F. R., and Mohammadzadeh, S. "Improving the Seismic Torsional Behavior of Plan-Asymmetric, Single-Story, Concrete Moment Resisting Buildings with Fluid Viscous Dampers." Earthquake Engineering and Engineering Vibration 15.1 (2016): 61–78. DOI: https://doi.org/10.1007/s11803-016-0311-z.

[10] Kang, J. D., and Tagawa, H. "Comparison between Experimental and Analytical Results for Seesaw Energy Dissipation Systems Using Fluid Viscous Dampers." Earthquake Engineering and Engineering Vibration 15.1 (2016): 79–90. DOI: https://doi.org/10.1007/s11803-016-0312-y.

[11] He, X., and Lu, Z. "Seismic Fragility Assessment of a Super Tall Building with Hybrid Control Strategy Using IDA Method." Soil Dynamics and Earthquake Engineering 123.1 (2019): 278–291. DOI: https://doi.org/10.1016/j.soildyn.2019.03.002.

[12] Kariniotakis, K., and Karavasilis, T. L. "Limits for the Interstory Drift Sensitivity Coefficient θ of Steel MRFs with Viscous Dampers Designed According to Eurocode 8." Soil Dynamics and Earthquake Engineering 117.1 (2019): 203–215. DOI: https://doi.org/10.1016/j.soildyn.2018.10.014.

[13] Yahyazadeh, A., and Yakhchalian, M. "Probabilistic Residual Drift Assessment of SMRFs with Linear and Nonlinear Viscous Dampers." Journal of Constructional Steel Research 148.1 (2018): 409–421. DOI: https://doi.org/10.1016/j.jcsr.2018.09.020.

[14] Nomura, R., Sato, H., and Watanabe, Y. "Seismic Retrofitting of Steel Moment Frames with Viscous Dampers: A Numerical Study." Journal of Structural Engineering 148.4 (2022): 04022032. DOI: https://doi.org/10.1061/JSTU2.0001475.

[15] Chen, L., Zhou, M., and Li, T. "Performance-Based Seismic Retrofit of Steel Frames Using Viscous Dampers." Earthquake Engineering & Structural Dynamics 52.1 (2023): 122–144. DOI: https://doi.org/10.1002/eqe.3515.

[16] Kim, J., Lee, H., and Choi, D. "Integrated Design of Steel Moment Frames Retrofitted with Viscous Dampers." Journal of Civil Engineering and Management 30.2 (2024): 132–145. DOI: https://doi.org/10.3846/jcem.2024.15149.

[17] Wakabayashi, M., et al. "Experimental Studies on Precast Concrete Wall Including Un-Bonded Braces under Cyclic Loading Part 1." Annual Meeting AIJ 48.1 (1973): 1041–1042.

[18] Kim, J., and Choi, H. "Behavior and Design of Structures with Buckling-Restrained Braces." Engineering Structures 26.6 (2004): 693–706. DOI: https://doi.org/10.1016/j.engstruct.2004.01.022.

[19] Sahoo, D. R., and Chao, S. H. "Performance-Based Plastic Design Method for Buckling-Restrained Braced Frames." Engineering Structures 32.9 (2010): 2950–2958. DOI: https://doi.org/10.1016/j.engstruct.2010.05.013.

[20] Chang, Y., and Chiu, Y. "Performance Assessment of Buckling Restrained Braces." Procedia Engineering 14.1 (2011): 2187–2195. DOI: https://doi.org/10.1016/j.proeng.2011.07.272.

[21] Guo, Y. L., Zhang, B. H., Zhu, B. L., Zhou, P., Zhang, Y. H., and Tong, J. Z. "Theoretical and Experimental Studies of Battened Buckling-Restrained Braces." Engineering Structures 136.1 (2017): 312–328. DOI: https://doi.org/10.1016/j.engstruct.2017.01.002.

[22] Bing, Q., Xiaofang, M. L., Hetao, H., Canxing, Q., and Dazhu, H. "Testing of Buckling-Restrained Braces with Replaceable Steel Angle Fuses." Journal of Structural Engineering, ASCE 144.3 (2018). DOI: https://doi.org/10.1061/(ASCE)ST.1943-541X.0001931.

[23] Park, K. J., Chen, M. T., and Smith, A. R. "Seismic Performance of Steel Buckling Restrained Braces: Experimental and Numerical Studies." Journal of Structural Engineering 150.1 (2024): 04023234. DOI: https://doi.org/10.1061/(ASCE)ST.1943-541X.0002958.

[24] Morales, L. G., Patel, D. A., and Bennett, R. K. "Dynamic Response of Steel Structures with Buckling Restrained Braces under Earthquake Excitation." Earthquake Engineering and Structural Dynamics 54.5 (2025): 1045–1062. DOI: https://doi.org/10.1002/eqe.3673.

[25] Zhang, G., Wu, X., and Zhao, J. "Kriging-Assisted Hybrid Reliability Design and Optimization of Offshore Wind Turbine Support Structure Based on a Portfolio Allocation Strategy." Renewable Energy 196.1 (2022): 888–906. DOI: https://doi.org/10.1016/j.renene.2022.05.086.

[26] Liu, Y., Guo, F., and Li, H. "A Novel Hybrid Adaptive Kriging and Water Cycle Algorithm for Reliability-Based Design and Optimization Strategy: Application in Offshore Wind Turbine Monopile." Structural Safety 97.1 (2022): 101975. DOI: https://doi.org/10.1016/j.strusafe.2022.101975.

[27] Chen, J., Xie, Y., and Peng, Z. "Intelligent-Inspired Framework for Fatigue Reliability Evaluation of Offshore Wind Turbine Support Structures under Hybrid Uncertainty." Engineering Structures 283.1 (2023): 115372. DOI: https://doi.org/10.1016/j.engstruct.2022.115372.

Journal of Civil Engineering Researchers

Journal homepage: www.journals-researchers.com

Laboratory Study of Weight Loss and Ultrasonic Wave Propagation Velocity in Conventional Concrete Under High Temperature, Along with Validation by SEM and XRD Analysis

Mohammadhossein Mansourghanaei,[a,*]

[a] Department of Civil Engineering, Chalous Branch, Islamic Azad University, Chalous, Iran

ABSTRACT

In this laboratory study, a mixed concrete design containing Portland cement type 2 with a grade of 500 kg/m3 was made. Weight loss and ultrasonic pulse velocity (UPV) tests were performed on concrete samples at a curing age of 90 days at room temperature (21 °C) and under a temperature of 600 °C. In order to further investigate and verify the results, scanning electron microscopy (SEM) and X-ray diffraction (XRD) analyses were performed on concrete samples at a curing age of 90 days. The results of the tests in this study were evaluated together and compared and analysed with the results of other researchers. Applying high heat to concrete samples caused a decrease in results. In this regard, in the weight loss test of concrete samples, the weight of the concrete sample decreased from 2378 to 2225 grams, which was a decrease of 72.6%, and in the UPV test, the speed of ultrasonic waves decreased from 6179 to 3411 m/s, which was a decrease of 79.44%. At the end of this study, the results of SEM and XRD analysis at room temperature and under high temperature, while coordinating with each other, overlapped with the results of the weight loss test and the ultrasonic wave velocity test in concrete samples.

ARTICLE INFO

Received: March 7, 2025
Accepted: April 4, 2025

Keywords:
Ultrasonic Pulse Velocity (UPV)
Temperature
Scanning Electron Microscopy (SEM)
X-ray Diffraction Spectroscopy (XRD)
Conventional Concrete

DOI: 10.61186/JCER.7.2.68
DOR: 20.1001.1.2538516.2025.7.2.6.4

1. Introduction

In order to develop national security and passive defense in the field of civil engineering infrastructure, a lot of laboratory work has been carried out to produce structural concrete for strategic and sensitive centers of the country [1-3]. The strength of reinforced concrete structures of these centers plays an important role in reducing destruction and human injuries caused by enemy defense operations. Improving the strength of concrete can be achieved through the type of materials used in its mixture composition [4-10]. One of the methods for evaluating the durability of concrete against various physical factors is to examine changes in the density of concrete in different temperature ranges. Concretes with low durability against heat lose more water in the pores and interlayer capillary pores in hydrated gels, therefore experiencing greater weight loss. UPV testing is one of the

---

[*] Corresponding author. Tel.: +989121712070; e-mail: Mhm.Ghanaei@iauc.ac.ir.

types of non-destructive tests for measuring the homogeneity and strength of concrete. In various studies, this test has been used to qualitatively evaluate the strength of concrete [2-5,7]. Research has shown that with increasing curing age in concrete, the UPV improvement process is divided into three parts based on the time-rate curve. In the first part, called the stationary period, UPV is very small. In the second part, with the development of the polymerization process (hydration or polymerization), UPV increases rapidly until, with the emergence of a solid network (final setting), the rate of increase decreases, which is characterized as the third part [11].

Portland cement is one of the major types of cements that is most widely used in the construction and production of ordinary concrete. Portland cement is a type of hydraulic cement that mainly consists of CaO, SiO2, Al2O3 and Fe2O3, these oxides are mainly present in the concrete in a bonded form [12]. In ordinary concrete paste containing Portland cement, calcium silicate-hydrate (C-S-H) gel is formed from silicon groups [13]. This gel constitutes a high volume (between 50 and 60%) of the Portland cement paste. Many models have been proposed to describe the exact structure of C-S-H. According to the Powers-Bronwar model, this structure is in the form of layers with a large surface area. The specific surface area of C-S-H is estimated to be about 100 to 700 m2/g [14]. The strength of this structure is attributed to van der Waals forces. In the Feldman-Serda model, the C-S-H structure is represented as a series of irregular layers that are randomly placed together to create interlayer spaces with various sizes and shapes, ranging from 5 to 25 angstroms [4]. The C-S-H gel is a factor in improving the strength of the hardened cement paste matrix structure. One of the methods for improving the results of the aforementioned tests (weight reduction and UPV) in conventional concrete is to increase the cement content in the concrete. Research has shown that by increasing the cement content from 275 to 400 kg/m3 in conventional concrete, the density of the concrete increases [15]. By increasing the density of the concrete, the mechanical properties and durability of the concrete will improve [1,6].

On the other hand, by increasing the cement content in the concrete and keeping the water-to-cement ratio low, the mechanical properties of the concrete can be increased, and the poor performance of the concrete in these conditions can be compensated by adding a superplasticizer [16]. As the cement content of concrete increases, the volume of C-S-H gel produced in the chemical process increases. This gel increases the density and strength of concrete by filling the pores and bonding the bonds, especially in the interfacial transition zones (ITZ), the interface between the paste and the aggregates. However, the high consumption of cement has always been accompanied by environmental concerns. In this regard, research shows that cement factories are responsible for the emission of about 5% of the total carbon dioxide entering the Earth's atmosphere [17]. In the microstructure of ordinary concrete containing Portland cement, hydrated calcium silicate (C-S-H) known as tobermorite gel accounts for 50 to 60 percent, calcium hydroxide (Ca (OH)2) or portlandite accounts for 20 to 25 percent, and hydrated calcium aluminum silicate (C-A-S-H) or ettringite gel accounts for 15 to 20 percent of the cement paste volume, with the remainder being non-hydrated clinker grains [18]. The effect of increasing temperature on the hardened hydrated cement paste depends on various factors, including the degree of polymerization and the moisture content of the cement paste. A well-hydrated and saturated cement paste contains large amounts of capillary water and free water in excess of surface water. The collapse of the concrete structure occurs when the rate of increase in the pressure of the vapor gas inside the material exceeds the rate of decrease in pressure due to the release of vapor into the atmosphere. When the temperature in the concrete reaches 300 ℃, the interlayer water in the hydrated calcium silicate gel and some of the water that is chemically combined and results from C-S-H and sulfoaluminate hydrates are lost. The subsequent dehydration of the cement paste due to the decomposition of calcium hydroxide (hydrated lime with the chemical formula Ca(OH)2) begins in the temperature range of 600 ℃, but a temperature of about 900 ℃ is required for complete decomposition of C-S-H [14]. Hertz reported that the C-S-H structure decomposes at 600 ℃ and is destroyed at 800 ℃ [19]. Applying high temperatures to concrete causes a decrease in the results of weight loss tests [1,6] and UPV [3-5] in concrete. Weight loss of conventional concrete samples under high temperatures has also been reported in other studies [20]. Using SEM and XRD image analysis is an effective way to evaluate the microstructure and the extent of chemical changes in the hardened cement matrix structure [3,4].

By examining the results of these tests, it is possible to have a good understanding of the performance of concrete in tests on the evaluation of mechanical properties and durability of concrete at room temperature and high temperatures. The investigation of mechanical, durability, microstructural and chemical properties in conventional concrete with high grade (500 kg/m3) of Portland cement at room temperature and under high temperatures is proposed in this article as an innovative design that can be used in structures requiring high mechanical properties and durability.

2. Sample Construction and Laboratory Program

2.1. Consumable Materials

In this study, Portland cement type 2 with chemical and physical characteristics according to Tables 1 and 2 was used. This cement is a product of Gilan Sabz Cement Industries Company (Dilman) and is produced under the EN 197-1 standard. The water used to prepare lime water and make the mixture design in the present study is from the drinking water of Lahijan city, this water has a pH in the range of 6.5 to 7.5 and a density of 1000 kg/m3. According to Section 9-10-4-2 and 9-10-4-3 of the fourth edition of the National Building Regulations of Iran, water that is drinkable, has no distinct taste or odor, and is clean and clear can be used in concrete without testing, unless previous records indicate that this water is unsuitable for concrete [21].

The aggregate grading curve used is within the ASTM C33 standard range, as shown in Figure 1. The aggregates used were supplied from sand and gravel factories in Lahijan city and were cleaned to remove organic impurities. Some of the characteristics of the fine and coarse aggregates used in this study were determined based on Table 3. The ideal aggregate grading is of particular importance because the aggregates with the highest density and the least amount of pores are the most economical materials used in concrete construction, which, if of appropriate quality, will require the least amount of cement paste [18]. The superplasticizer used in this study is a fourth-generation normal polycarboxylate-based product from Durochem Middle East Company under the trade name Flowcem R700. This material is used to compensate for the poor efficiency and maintain the fluidity of the mortar mixture due to the high cement content in concrete. Some characteristics of normal polycarboxylate superlubricants are presented in Table 4.

Table 1.
Chemical Characteristics of Portland Cement Type II

L.O.I	MAX 1/5
C_3A	5.5-7.5
I.R	MAX 0/7
$Na_2O+0.658K_2O$	MAX 0.6
SO_3	2-2.3
MgO	MAX 4/5
Cao	42-43
Fe_2O_3	3.5-3.8
Al_2O_3	4.5-4.8
SiO_2	21-22
Cl	MAX 0/003

2.2. Mix Design and Curing Concrete

In this laboratory study, the mixture design recommended by ACI 211.1-89 was used to make regular concrete. In this regard, the mixture design of concrete samples in this study was prepared and adjusted based on Table 5. In order to make concrete samples, dry materials (aggregate and cement) were first poured into a rotating mixer and the mixing process lasted for 2 minutes, then water and superplasticizer were added to the mixture and the mixing of the materials continued for another 2 minutes. Finally, the prepared concrete mixture was poured into pre-lubricated molds in three stages and in each stage, the concrete mixture was compacted with 25 rod blows. After the first 24 hours of concrete pouring and the samples were kept in a dry environment and at room temperature (21 ℃), the samples were separated from the mold and kept in lime water at room temperature until the test.

Table 2.
Physical Characteristics of Portland Cement Type II

Density (kg/m^3)	3250
Specific Surface Area (cm^2/g)	3000-3200
Initial Setting (min)	115< <130
Secondary Setting (min)	190< <205

Table 3.
Aggregate Specifications

Concrete Aggregates	Gravel	Sand
Minimum Diameter	4.75 (mm)	75 (μm)
Maximum Diameter (mm)	19	4.75
Modulus of Elasticity (mm)	5.7	2.85
Density (kg/m^3)	2750	2650
Water Absorption (%)	2.2	2.9

Table 4.
Superplasticizer Characteristics

Chemical Formula	Normal Polycarboxylate
Physical Condition	Liquid
Color	Light Brown
Density (kg/m^3)	1100
Consumption Standard	ASTM C494
pH	About 7

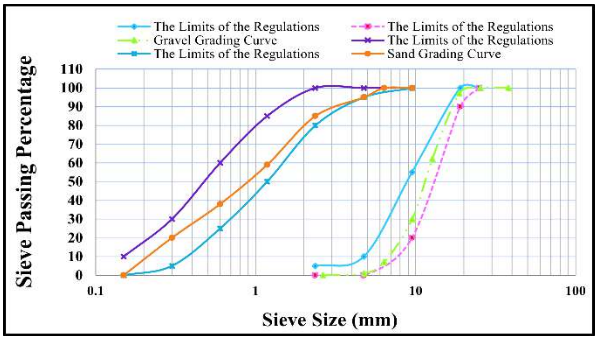

Fig. 1. Aggregate Curve

Table 5.
Specifications of Concrete Mix Design

Materials	**kg/m^3**	**%**
Cement	500	20.02
Water	225	9.01
Gravel	1000	40.04
Sand	765	30.63
Superplasticizer	7	0.0028

- Curing Conditions After Demolding = In the water
- Density of Concrete Mix = 2497 kg/m^3
- W/C = 45 %

2.3. Test Methods and Standards

The weight loss test of concrete at a curing age of 90 days at room temperature and under high heat was carried out in accordance with the ISO834 standard on cubic samples with dimensions of 10×10×10. In this standard, the temperature applied to concrete samples is recommended to be up to 1000 ℃ and the duration of heat application is one hour [1,6]. The samples were first weighed at room temperature, then the samples were exposed to a temperature of 600 ℃ for 1 hour in an oven, this action causes water to evaporate from the capillary spaces and possible pores in the concrete, at the end of the heating time and after the temperature of the samples reached room temperature, the samples were re-weighed and the average weight loss of the samples was entered as the final result. UPV test in concrete was measured under ASTM C597 standard on cubic samples with dimensions of 10×10×10 cm at room temperature and high temperature, with a Dundee type device with a vibration frequency of 55 kHz and an accuracy of 0.1 and ±2% of the time interval of the waves. In this regard, at a curing age of 90 days, the surface dimensions of the samples that were in contact with the mold bottom were measured by calipers, then a suitable acoustic connection was achieved between the concrete surface (smooth surfaces that were in contact with the mold faces) and the transducer surface to remove air pockets through Vaseline on the surface of the samples. After determining the time of wave passage through the concrete sample, using the relationships in the mentioned standard, UPV was obtained in meters per second. XRD analysis of concrete at a curing age of 90 days under room temperature and high temperature was performed using an XRD device with a Philips PW1730 model. In this regard, crushed samples taken from the center of the concrete sample were placed inside the device and during the test, a diffraction diagram of concrete crystals was prepared. The data obtained from X-ray diffraction is in the form of photon intensity in terms of detector angle 2θ, which is presented as a list of peak locations and their intensities on the graphs. SEM analysis was performed at a curing age of 90 days at room temperature and under high temperature using a scanning electron microscope with the FEI Quanta200 model. In this regard, the crushed concrete sample was placed in the device and images were recorded at the desired magnification and then microstructurally examined. Before performing high-temperature tests (600 ℃) at a curing age of 90 days, according to ISO834 standard, concrete samples were placed in a furnace at a temperature of 600 ℃ for 1 hour, then the samples remained in the furnace for another 1 hour to avoid the effect of thermal shock. After the samples were removed from the furnace, the samples were kept at room temperature for 24 hours to reach temperature equilibrium. The use of this standard in other research on high-temperature tests in concrete has been reported [3,4,5,22].

3. Laboratory Results

3.1. Weight Loss Test Results

The results of the weight loss test of concrete samples at a curing age of 90 days at room temperature and under a temperature of 600 ℃ are shown in Figure 2. In this regard, the weight of the concrete sample has experienced a 6.81% decrease from 2387 to 2225 grams. Considering the passage of 90 days of concrete curing age, a significant part of the polymerization process has been completed in the concrete. In this regard, most of the cement binder and hydrated filler particles such as calcium hydroxide have participated in the chemical process, and the result is the production of a large volume of hydrated calcium silicate gel (C-S-H) in the concrete structure, which, while filling the pores and cavities, has caused a bond in the ITZ between the aggregates and the cement paste, and in this way has increased the compaction, density and strength of the concrete. These characteristics cause the resulting concrete to have less weight loss against the applied heat [1,6]. Researchers have reported that the decrease in strength is mainly attributed to the decomposition of calcium hydroxide, and this phenomenon usually occurs in the temperature range between 450 and 500 ℃ [23,24]. Therefore, in high-strength concrete, greater strength occurs in this temperature range. Heating up to 100 ℃ causes water to evaporate from the pores and capillary spaces in the concrete structure and intensifies the porosity in the concrete. At temperatures above 100 ℃, due to the exit of water from the concrete structures and the start of the polymerization process, the sample shrinks and cracks form due to drying caused by the evaporation of water in the concrete. According to the study of other researchers, when the vapor pressure reaches its maximum, the dense structure of concrete with low permeability is unable to control the thermal stresses, and this causes thermal cracks to appear on the surface of the sample due to shrinkage. In concrete, this phenomenon is called the "vapor effect" [25].

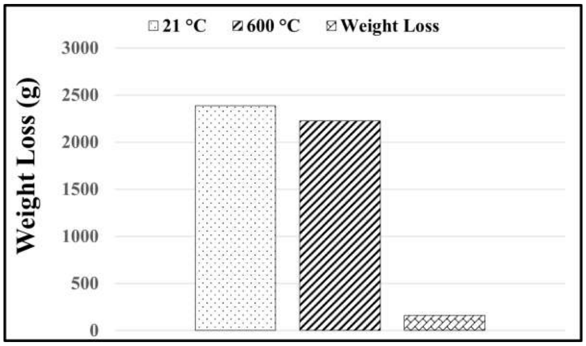

Fig. 2. Results of Weight Loss Test of Concrete Sample

Also, the evaporation of water from the concrete structure is accompanied by weight loss, which can cause thermal cracks due to shrinkage. The results of XRD and SEM analysis in this study confirm the results of the weight loss test.

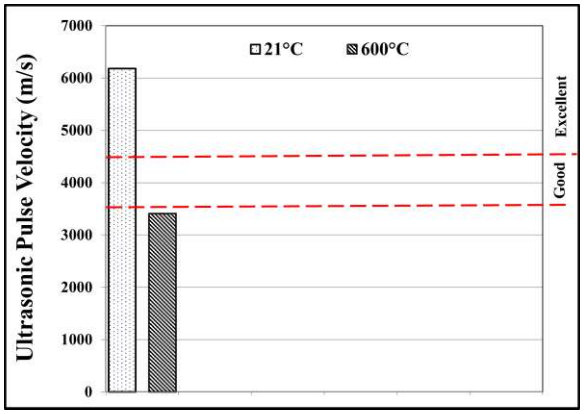

Fig. 3. UPV Test Results

3.2. UPV Test Results

In this study, the results of the UPV test at the 90-day curing age of concrete at room temperature and under high temperature are shown in the graph of Figure 3. Research has shown that the UPV in ordinary concrete at the 90-day curing age has the least changes compared to the ages of 7 and 28 days due to the completion of a large part of the polymerization process [26]. Based on the results of Figure 3, it is observed that at room temperature and 600 ℃, the UPV rate has reached 6179 and 3411 m/s, respectively, which shows a 79.44% drop in UPV at high temperature. The IS 13311-1 standard shows the quality range of concrete in the UPV test [27]. The use of this standard for classifying the quality of ultrasonic wave velocity has also been reported in other studies [2-5,7,28]. In this study, at room temperature, the concrete is in the excellent quality range. According to IS 13311-1, as long as the UPV values are in the “excellent” category, it means that the concrete in question does not have large cracks or voids that affect the structural integrity of the specimen [29].

The resistance of concrete to heat depends on various factors such as the chemical composition of the concrete ingredients, temperature, and curing method [4,30]. Heat causes water to evaporate from the pores and cavities in the concrete, and while weakening the polymerization process and destroying the C-S-H gel structure, it will increase the porosity in the concrete [3,5]. The presence of any porosity and cracks in the concrete will lead to a decrease in the UPV in the concrete. Considering the 90-day curing time of the concrete in this study, the participation of the filler and cementitious adhesive particles in the polymerization process has reached its maximum, and this has led to the production of a high volume of C-S-H gel in the concrete, which has contributed to increasing the compaction and density of the concrete (according to the SEM result in Figure 5) by filling the cracks and improving the bond in the ITZ. The bond in conventional concretes is formed based on polymerization reactions between calcium oxide and silicon dioxide to form hydrated calcium silicate (C-S-H).

3.3. XRD Analysis Results

In this laboratory study, X-ray diffraction (XRD) spectroscopy was used to study and analyze the crystalline structure of materials and to investigate the size of grains and particles in concrete. The results of XRD analysis at a curing age of 90 days at 21 and 600 ℃ are shown in Figure 4. Based on these results, it is observed that at 21 ℃, aluminum phosphate compounds with a maximum peak height of 2670 at an angle of 59.85 degrees, followed by calcium hydroxide with a maximum peak height of 2452 at an angle of 24.41 degrees, titanium oxide with a maximum peak height of 1794 at an angle of 24.29 degrees, calcite with a maximum peak height of 1600 at an angle of 26.45 degrees, and dolomite with a maximum peak height of 671 at an angle of 17.92 degrees, have the highest dispersion. The presence of calcium hydroxide with the highest dispersion in XRD indicates that a large part of this hydrated material has not been able to fully participate in the chemical process, and this could be due to the high cement content in concrete, which increased the polymerization rate and did not allow some cementitious materials to participate chemically. After the removal of some elements in the calcination process at high temperature, compounds such as calcium manganese carbonate with a maximum peak height of 2092 at an angle of 29.47 degrees, carbon with a maximum peak height of 1865 at an angle of 27.9 degrees, hydrated potassium iron manganese aluminum silicate with a maximum peak height of 1712 at an angle of 28.13 degrees, and hydrated calcium aluminum silicate with a maximum peak height of 726 at an angle of 26.42 degrees have the highest dispersion. The application of high heat reduced the height of the peaks due to the presence of compounds, in this regard, the difference in peak height in the XRD graph at 21 ℃ (with a height of 2092), compared to 600 ℃ (with a height of 2670), is 21.64%. Research has shown that at high temperatures, CH gel does not convert into calcium carbonates such as Calcite, and as is clear from the results of the table, CH disappears at high temperatures and is actually converted into Carbon and C-A, which is the main cause of concrete weakness at high temperatures [31,32]. Research has shown that after the materials used in the preparation and manufacture of concrete are combined, the chemical reaction process (polymerization) between cementitious materials and water begins, the speed and extent of formation of hydrated calcium silicate gel (C-S-H), which is the final product of the chemical composition, mainly depends on the properties and ratios of cementitious materials and water [1,2].

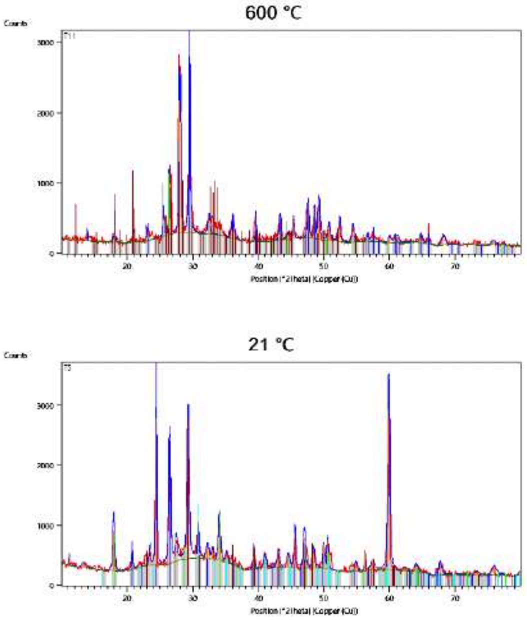

Fig. 4. XRD Analysis Results

3.4. SEM Analysis Results

The results of SEM analysis at a curing age of 90 days at a scale of 5 µm and a magnification of 13,000 times at temperatures of 20 and 600 °C are shown in Figure 5. Based on these images, the microstructure of concrete in all mix designs can be summarized in three basic phases as follows [5,1-7]:

1. The first phase consists of polymerization products including hydrated gels, which are mainly dark in color in the images. After formation and in combination with other concrete components, these gels are known to be the main factor in strengthening the microstructure of concrete by filling pores and cavities, as well as improving the bond in the ITZ and interlayer (in the hydrated gels themselves).
2. The second phase consists of unreacted crystals that are formed as a result of impurities in the raw materials or unreacted particles in the polymerization process and are mainly white in the images.
3. The third phase includes the bonding of cement paste with aggregate in ITZ, as well as the bonding of interlayers in the structure of hydrated gels.

According to SEM images at 21 °C, it is clear that the presence of hydrated C-S-H gel in the concrete sample has caused the connection of fracture surfaces, the homogeneity of the hydration product, and the densification of the Portland cement paste structure. Also, this gel, by filling the ITZ space, causes reinforcement at the paste-aggregate boundary or the adhesion zone between aggregate and cement paste (ITZ). The presence of some small crystals, fracture surfaces, and white spherical particles caused by calcium hydroxide crystals that did not participate in the production of hydrated gel in the concrete structure of this design, which can be seen in the images, can be attributed to the high grade of cement used, which leads to the phenomenon of nucleation and agglomeration of particles (due to the high speed of the hydration process). Also, the presence of pores and capillary pores can often be considered the result of water evaporation from the interlayer capillary spaces in the hydrated calcium silicate gel (C-S-H), which contributes to the creation of cracks and shrinkage phenomena due to drying.

Research has shown that in the bulk part of Portland cement paste, ions such as calcium, sulfate, hydroxide, and aluminate, which are formed through aerobic dissolution into calcium silicate and calcium aluminate, combine to form ettringite gel (C-A-S-H) and calcium hydroxide (Ca(OH)2), meaning that ettringite is formed by the reaction of calcium aluminate with calcium sulfate, and as the hydration stage progresses, weak C-S-H crystals and the second generation of crystals formed from calcium hydroxide and ettringite gel begin to fill the empty spaces in the ettringite and calcium hydroxide network (called portlandite), and this operation increases the density, hardness, and ITZ strength of the concrete [18]. Research has shown that the main factor of strength in concrete is hydrated gels resulting from the polymerization process, which increase in strength as the curing age of concrete increases [5,1-7].

Applying high heat (600 °C) to the concrete sample has affected the microstructure of the concrete. According to the SEM image at 600 °C, the formation of a tree structure, the presence of numerous capillary pores due to the evaporation of water between the capillary spaces in the hydrated calcium silicate gel (C-S-H), and the reduction of the amount of hydrated C-S-H gel (dark areas) following destruction are evident in the concrete sample, which indicates a weakness in the microstructure of the concrete after heating. Previous studies [3-5] show that the C-S-H gel present in the microstructure of concrete containing Portland cement will cause the most breakage in the concrete from a temperature of 450 °C onwards. In the images, the increase in volume and pore size can be attributed to the release of water under heat from capillary pores in the concrete microstructure, and this amount can also be increased by increasing the water-to-cement (W/C) ratio in the preparation of the concrete mix design, and contribute to the porosity and embrittlement of the concrete structure. According to the SEM images in Figure 5, the hexagonal structure of portlandite changes at a temperature of 500 ℃ and the C-S-H nanostructure also decomposes [21].

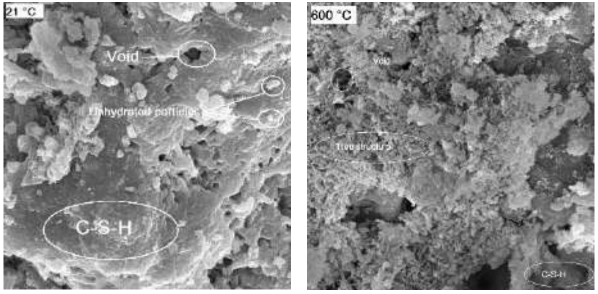

Fig. 5. SEM Analysis Results

4. Conclusion

In this study, the weight loss and UPV were tested at a curing age of 90 days at room temperature and high temperature in ordinary concrete with a cement content of 500 kg/m3. The results were evaluated based on XRD and SEM analysis. The main results of this laboratory study are presented as follows.

1) In the weight loss test of concrete samples, the weight of the concrete sample decreased from 2387 to 2225 grams, which was a decrease of 786.6%. As a result of the increase in temperature in the concrete samples, the results in the weight loss test of concrete were decreased. Similar results were obtained in the research of others [1,6].

2) In the UPV test, the speed of ultrasonic waves decreased from 6179 to 3411 m/s, which was a decrease of 44.79%. As a result, the increase in temperature in the concrete samples caused the results in this test to decrease. Similar results were obtained in the research of others [3,4].

3) In XRD analysis, at a temperature of 21 ℃, most of the large peaks occurred in the regions of 16 to 29 and also 60 degrees, and aluminum phosphate compounds, followed by calcium hydroxide, titanium oxide, calcite and dolomite, have the highest dispersion in concrete. However, applying a temperature of 600 ℃ caused a decrease in the height of the peaks in the resulting graph. In this regard, most of the large peaks occurred in the regions of 26 to 29 degrees, and compounds such as calcium manganese carbonate, carbon, hydrated aluminum manganese iron phosphate silicate and hydrated aluminum calcium silicate have the highest dispersion.

4) In SEM analysis, at a temperature of 21 ℃, the tree structure, pores and unhydrated particles are seen in their minimum amount, but after applying heat to the concrete sample at 600 ℃, the volume and number of these values have increased. On the other hand, applying heat to the concrete sample has had destructive effects on the hydrated C-S-H gel and structural disintegration is evident in these gels. Similar results were obtained in the research of others [3-5].

5) At the end of this research, the results of SEM and XRD analysis at room temperature and under high temperature, while coordinating with each other, overlapped with the results of other tests.

menu.

References

[1] Mohammad Mansourghanaei, Milad Biklaryan, and Amir Mardookhpour. “Durability and Mechanical Properties of Granulated Blast Furnace Slag Based Geopolymer Concrete Containing Polyolefin Fibers and Nano Silica.” KSCE Journal of Civil Engineering 28.1 (2024): 209–219. DOI: https://doi.org/10.1007/s12205-023-2202-6 .

[2] Mohammad Mansourghanaei, Milad Biklaryan, and Amir Mardookhpour. “Experimental Study of the Effects of Adding Silica Nanoparticles on the Durability of Geopolymer Concrete.” Australian Journal of Civil Engineering 22.1 (2024): 81–93. DOI: https://doi.org/10.1080/14488353.2022.2120247 .

[3] Mohammad Mansourghanaei, Milad Biklaryan, and Amir Mardookhpour. “Experimental Study of Properties of Green Concrete Based on Geopolymer Materials under High Temperature.” Civil Engineering Infrastructures Journal 56.2 (2023): 365–379. DOI: https://doi.org/10.22059/ceij.2022.90063 .

[4] Mohammad Mansourghanaei and Amir Mardookhpour. “Analysis of the Numerical Results Obtained from the Experimental Examination of the Mechanical Properties of Geopolymer Concrete.” Numerical Methods in Civil Engineering 9.1 (2024): 31–41. DOI: https://doi.org/10.22060/nmce.2024.206415 .

[5] Mohammad Mansourghanaei, Milad Biklaryan, and Amir Mardookhpour. “Experimental Study of Mechanical Properties of Slag Geopolymer Concrete under High Temperature, Used in Road Pavement.” International Journal of Transportation Engineering 11.1 (2023): 1371–1385. DOI: https://doi.org/10.22119/ijte.2023.163982

[6] Mohammad Mansourghanaei and Amir Mardookhpour. “Investigating the Properties of Environmentally Friendly Green Concrete (Geopolymer) Under High Temperature.” Sustainable Earth Trends 3.4 (2023): 62–69. DOI: https://doi.org/10.48308/ser.2024.234846.1038 .

[7] Mohammad Mansourghanaei, Milad Biklaryan, and Amir Mardookhpour. “Experimental Study of Modulus of Elasticity, Capillary Absorption of Water and UPV in Nature-Friendly Concrete Based on Geopolymer Materials.” International Journal of Advanced Structural Engineering 12.2 (2022): 607–615. DOI: https://doi.org/10.1007/s40091-022-00333-1 .

[8] Mohammad Mansourghanaei. “Experimental Evaluation of the Impact Resistance of Alkali-Activated Slag Concrete Under High

Temperature." Journal of Civil Engineering Researchers 6.3 (2024): 47–53. DOI: https://doi.org/10.52547/jcer.6.3.47.

[9] Mohammad Mansourghanaei. "Investigating the Mechanical and Durability Properties of Geopolymer Concrete Based on Granulated Blast Furnace Slag as Green Concrete." Journal of Civil Engineering Researchers 5.3 (2023): 24–34. DOI: https://doi.org/10.52547/jcer.5.3.24 .

[10] Mohammad Mansourghanaei. "Evaluation of Mechanical Properties and Microstructure of Pozzolanic Geopolymer Concrete Reinforced with Polymer Fiber." Journal of Civil Engineering Researchers 5.2 (2023): 1–13. DOI: https://doi.org/10.52547/jcer.5.2.1.

[11] H. K. Lee, Y. J. Shin, and K. M. Kim. "Ultrasonic In-situ Monitoring of Setting Process of High-performance Concrete." Cement and Concrete Research 34.4 (2004): 631–640. DOI: https://doi.org/10.1016/j.cemconres.2003.10.017 .

[12] Edward Gartner. "Industrially Interesting Approaches to 'Low-CO$_2$' Cements." Cement and Concrete Research 34.9 (2004): 1489–1498. DOI: https://doi.org/10.1016/j.cemconres.2004.01.021 .

[13] Hongwei Du, Shun Du, and Xiaojun Liu. "Durability Performances of Concrete with Nano-silica." Construction and Building Materials 73 (2014): 705–712. DOI: https://doi.org/10.1016/j.conbuildmat.2014.10.090 .

[14] H. F. W. Taylor. Cement Chemistry. Thomas Telford, 1997.

[15] Reza Bahramloo and Saeed Gohari. "Investigating the Effect of Cement and Air Entrained Admixture (AEA) on the Capillary Water Absorption in Concrete Lining of Water Conveyance Canals." Concrete Research 12.4 (2019): 123–133. DOI: https://doi.org/10.22124/jcr.2019.12654.1344 .

[16] M. Tadaion, Hani Honarmand, and Moosa Kalhori. "Impact of Plasticizers on the Quality of Concrete and the Reduction of the Cement Content." Concrete Research 3.2 (2010): 49–57.

[17] A. Nosrati, S. Bagheri, and M. Eslami. "Portland Cement Structure and Its Major Oxides and Fineness." Smart Structures and Systems 22.2 (2018): 425–432. DOI: https://doi.org/10.12989/sss.2018.22.2.425 .

[18] Paulo J. M. Monteiro and Perumalsamy N. Balaguru. Concrete: Microstructure, Properties, and Materials. McGraw-Hill Education, 2014.

[19] Kristian D. Hertz. "Concrete Strength for Fire Safety Design." Magazine of Concrete Research 57.8 (2005): 445–453. DOI: https://doi.org/10.1680/macr.2005.57.8.445 .

[20] Mohammad Amiri and Marziyeh Aryanpoor. "The Effects of High Temperatures on Concrete Performance Based on Nanostructural Changes in Calcium Silicate Hydrate (C-S-H)." Concrete Research 12.4 (2019): 69–80. DOI: https://doi.org/10.22124/jcr.2019.12883.1354 .

[21] Dongliang Kong and Jay G. Sanjayan. "Effect of Elevated Temperatures on Geopolymer Paste, Mortar and Concrete." Cement and Concrete Research 40.2 (2010): 334–339. DOI: https://doi.org/10.1016/j.cemconres.2009.10.017 .

[22] Daniel P. Bentz. "Fibers, Percolation, and Spalling of High-Performance Concrete." Materials Journal 97.3 (2000): 351–359. DOI: https://doi.org/10.14359/8880 .

[23] Bin Zhang and Nenad Bicanic. "Residual Fracture Toughness of Normal-and High-strength Gravel Concrete after Heating to 600 °C." Materials Journal 99.3 (2002): 217–226 .

[24] Shao-Gang Hu, Min Wang, and Qun Zhang. "Preparation and Properties of Geopolymer-Lightweight Aggregate Refractory Concrete." Journal of Central South University of Technology 16.6 (2009): 914–918. DOI: https://doi.org/10.1007/s11771-009-0160-0 .

[25] Seyed Hosein Ghasemzadeh Mousavinejad and Behnam Rudy. "Study of Ultrasonic Pulse Wave Velocity in Plain Concrete Using Different Water to Cement Ratio at Different Stress Level." Journal of Civil and Environmental Engineering 50.3 (2020): 37–43. DOI: https://doi.org/10.22034/jcee.2020.16382.1404 .

[26] Bureau of Indian Standards. "IS 13311-1: Method of Non-destructive Testing of Concrete, Part 1: Ultrasonic Pulse Velocity." Bureau of Indian Standards (1992).

[27] E. A. Whitehurst. "Soniscope Tests Concrete Structures." Journal Proceedings 47.2 (1951).

[28] Wai Hoe Kwan, Kamal H. Khayat, and Victor C. Li. "Influence of the Amount of Recycled Coarse Aggregate in Concrete Design and Durability Properties." Construction and Building Materials 26.1 (2012): 565–573. DOI: https://doi.org/10.1016/j.conbuildmat.2011.06.051 .

[29] İbrahim Türkmen, Okan Çopuroğlu, and Ramazan Kocabaş. "Fire Resistance of Geopolymer Concrete Produced from Ferrochrome Slag by Alkali Activation Method." 2013 International Conference on Renewable Energy Research and Applications (ICRERA), IEEE (2013). DOI: https://doi.org/10.1109/ICRERA.2013.6749791 .

[30] Ahmed M. Rashad. "The Effect of Polypropylene, Polyvinyl-Alcohol, Carbon and Glass Fibres on Geopolymers Properties." Materials Science and Technology 35.2 (2019): 127–146. DOI: https://doi.org/10.1080/02670836.2018.1506080 .

[31] Mohamed S. Morsy, Sherif H. Alsayed, and Mohsen S. El-Ghazaly. "Behavior of Blended Cement Mortars Containing Nano-Metakaolin at Elevated Temperatures." Construction and Building Materials 35 (2012): 900–905. DOI: https://doi.org/10.1016/j.conbuildmat.2012.04.132 .

Journal of Civil Engineering Researchers

Journal homepage: www.journals-researchers.com

Methodology for Evaluating and Optimizing the Selection of Concrete Structure Demolition Methods Based on Cost, Time, and Quality (Safety)

Mohsen Asgharinia,[a,*]

[a] Department of Civil and Environmental Engineering, Amirkabir University of Technology, Tehran, Iran

ABSTRACT

Nowadays, with the aging of old structures and the advancement of construction technologies, demolition projects for outdated structures have seen significant growth. this paper focuses on demolition methods in detail. In a case study conducted in Iran, this paper evaluates the demolition methods for a concrete silo using the Analytical Hierarchy Process (AHP) to select the optimal method based on cost, time, and quality (safety).

Time evaluation is performed using MSP software, while cost assessment for each method is estimated based on resources allocated to the activities within the Work Breakdown Structure (WBS) of each approach. Safety evaluation employs a combined application of the AHP and Data Envelopment Analysis (DEA) methods. Required data for constructing pairwise comparison matrices were gathered through questionnaires completed by domain experts.

The results reveal that the demolition method using concrete wire saws scores the highest among the methods evaluated. Furthermore, based on modeling results in Sap2000 software, it is shown that single-stage toppling of the silo by removing its main columns is not feasible. Subsequently, the site layout design and lifting plan calculations for the selected method were carried out.

All outcomes were compared with real-life execution, and the project's success demonstrated the effectiveness of the chosen method due to comprehensive consideration of all construction management aspects of a demolition project. This paper is written with the aim of simplifying technical concepts in the management of demolition methods.

ARTICLE INFO

Received: March 5, 2025
Accepted: April 1, 2025

Keywords:
Demolition methods
Concrete silo
Safety
Cost management
Time management
Concrete wire cutting

DOI: 10.61186/JCER.7.2.76
DOR: 20.1001.1.2538516.2025.7.2.7.5

1. Introduction

1.1. Overview

With the aging of old structures and the advancement of modern construction technologies, the demolition of old structures has experienced significant growth. Construction management provides a comprehensive overview of all factors influencing a project, and by evaluating various criteria, it ensures the project's success. Just as construction methods are popular topics in today's construction management, demolition methods should also be given due attention. This paper focuses on selecting the optimal demolition method for two 10,000-ton concrete

---

[*] Corresponding author. Tel.: +989128026129; e-mail: mohsen76a@aut.ac.ir.

silos at the Gol Gohar Sirjan complex in Kerman Province, Iran. The objective of demolishing these silos is to access the rich iron ore reserves beneath them. The economic justification for demolishing these structures and constructing new ones is supported by the abundant iron ore reserves underneath, and the revenue generated from selling and exporting iron ore to the mine far exceeds the costs of demolition and constructing new silos. This paper addresses the management and selection of demolition methods for the silos in question, and subsequently delves into other aspects of construction management, such as designing the construction site layout plan and calculating the lifting plan. The concrete silos in question have a total height of 26 meters, an external diameter of 15 meters, and a wall thickness of 50 centimeters. Each silo has supports (columns) 7 meters in height and a 2-meter thick concrete slab roof. These silos are situated on a 23 by 35-meter, 3-meter thick, spread foundation. The primary constraints in the demolition method are the presence of a concentration and dust processing plant on the northern side and a distance of 20 meters from the edge of the main mine pit on the southern side.

1.2. Summary of the Literature and Related Studies

Extensive research has been conducted in the field of demolishing old structures. Hufbauer and Severn were among the first, in 1973 [1], to conduct various studies on the demolition of old buildings. Their research focused on the economic analysis of demolishing old buildings and replacing them with new ones, examining factors influencing the decision to demolish old buildings, such as increasing land rent, population growth, and the need for higher density. The results of this research indicate that the demolition of old structures should have an economic justification. In another study conducted by Osama Abudayyeh and his colleagues in 1988 [2], different demolition methods were evaluated in terms of efficiency, advantages, disadvantages, and implementation methods. The study also addressed how to ensure the safety of demolition projects. Similarly, Ravi Patel, in 2019 [3], conducted a brief review and comparison of demolition methods, concluding that explosion was the common method in the early demolition projects in the construction sector. Over time, demolition methods using excavators and diamond wire concrete cutting were employed in demolition projects. Assefa and Ambler, in their research in 2016 [4], investigated the decision to demolish or renovate buildings from the perspective of the life cycle environmental impacts, finding that renovation can significantly reduce environmental impacts and save resources. Furthermore, renovating buildings instead of demolishing and rebuilding can be very beneficial for areas with limited land, such as universities. Baker, Moncaster, and Al-Tabbaa's research in 2017 [5] examined the factors influencing the decision to demolish or renovate existing buildings. They argued that renovating buildings has advantages such as saving embodied energy and preserving heritage values. However, demolition can be a better solution, especially when buildings are of poor technical quality or do not comply with modern building regulations. The decision-making tools in their research include the IconCUR system, a three-dimensional tool designed by Australian researchers for decision-making in the early stages of asset management. This tool has three axes: X, Y, and Z. Axis X assesses the technical condition of the building in terms of design, maintenance, and compliance with regulations. Axis Y assesses the building's compliance with user needs, interior and exterior spaces. Finally, axis Z considers the economic, cultural, and environmental value of the building and stakeholder interests. The tool displays the results in a three-dimensional framework and suggests the best course of action for the building (such as renovation, preservation, conversion, or demolition). Regarding the demolition methods of concrete silos, very little research has been conducted. Julide Yuzbasi, in 2024 [6], conducted the most recent research on this topic, investigating the demolition of silos through one-stage overturning by removing some of the main columns using explosives. Additionally, Xieping Huang and his colleagues [7], in 2024, examined the effects of explosions on underground silos, and their results showed that the number of concrete debris ejected during the explosion would be significant. In a review study conducted by Mohsen Mohammadi and his colleagues in 2024 [8], 21 articles were evaluated based on various criteria for demolition methods, and the results are presented in the Table 1.

1.3. Innovation and Contribution of the Research to the Frontiers of Knowledge and Technology to Address Challenges and Shortcomings

This paper focuses on the comparison and evaluation of demolition methods. The findings of this research can assist construction managers in selecting the optimal demolition method by comparing and evaluating influential factors such as cost, time, and quality (safety). Today, various methods exist for demolishing concrete silos, but determining the most suitable method or combination of methods remains a subject of debate. Each method has its own set of advantages and disadvantages, and comparisons should be based on key criteria. Cost, time, and quality are the three primary criteria for method selection in the construction industry. Experts in this field believe that time, cost, and quality are recognized as the fundamental pillars of any project, and project managers strive to allocate resources appropriately and make the best

Table 1
Evaluation of demolition methods using various criteria [8]

Demolition Method		Demolition Time/Rate	Cost	Need for Skilled Operators	Safety	Environmental Pollution	Waste Reduction	Recyclability of Materials
Conventional Demolition Technologies	Manual Demolition	2	3	3	3	3	3	4
	Mechanical Demolition	4	4	4	3	3	3	3
	Implosion	5	2	5	2	2	2	2
Emerging Demolition Technologies	Static Blasting	3	3	3	4	4	3	3
	Diamond Wire Saws	4	3	4	4	2	5	5
	SCDA	3	3	2	5	2	4	4
	Hydro Demolition	4	4	4	5	2	5	5
	EDT	4	3	5	5	2	4	3
	Demolition Robots	4	3	4	4	3	4	4
	Microwave Heating	3	3	4	5	2	4	4

Extremely low = 1; Low = 2; Moderate = 3; High = 4; Extremely high = 5.

decisions to complete projects in the shortest possible time, at the lowest cost, and with the highest quality. [9], [10].

2. Research Methodology

This research is applied in nature and employs an analytical-descriptive approach. The required data was collected through a literature review. Additionally, part of our study was conducted based on project experiences and the expertise of individuals related to the research topic. Initially, based on a literature review and a review of published articles, the modeling and structural behavior during demolition in each method were examined. In each method, the parameters of cost, time, and quality (safety) were comprehensively analyzed and compared.

In the next stage, using the Analytic Hierarchy Process (AHP) method proposed by Thomas Saaty [11], which is used to solve multi-criteria decision-making problems, and with the help of the Expert Choice software, the demolition methods were compared, and the score of each method was calculated. The proposed research method in this paper for selecting the appropriate demolition method was used in a study by A.J. S´anchez-Garrido in 2022 to select modern construction methods [12].

The use of experts and their experience in multi-criteria decision-making was proposed by Z.-S. Chen in 2021 to evaluate proposals in tendering processes, which considers uncertainty and complexities in human evaluations using fuzzy tools and group decision-making methods [13]. Time assessment was performed using MSP software as suggested by researchers in this field [14]. In this method, based on the schedule obtained for each method using MSP software, to prepare a schedule, a WBS was first prepared for each demolition method, and then by defining the relationship between activities and allocating resources, the duration of activities was calculated, and the total demolition time was obtained using the above method. The basis for calculating the cost criterion is based on the resources allocated to each of the execution operations in the Work Breakdown Structure (WBS) of each method [15]. In this way, in each method, its breakdown structure is prepared, and for the broken-down activities, the required resources and costs, including materials, labor, machinery, and transportation, are allocated, and finally, the amount of execution of that activity is calculated. By summing the costs of each activity, the demolition cost of each method is calculated. Safety assessment was conducted using both AHP and DEA, and the necessary information for forming pairwise comparison matrices in these methods was collected through questionnaires from experts in the field. In the next stage, using the results of the evaluation of each item, the overall evaluation of the method was performed using the AHP method, and the method that obtained the highest score in the evaluation was selected as the optimal method.

In addition to selecting the optimal demolition method, this research also addresses the application of other aspects of construction management such as examining the site setup, designing the project site layout plan, and the role of the lifting plan in the selected method. Given the increasing trend of demolishing old structures, presenting new methods in demolition management and demolition methods

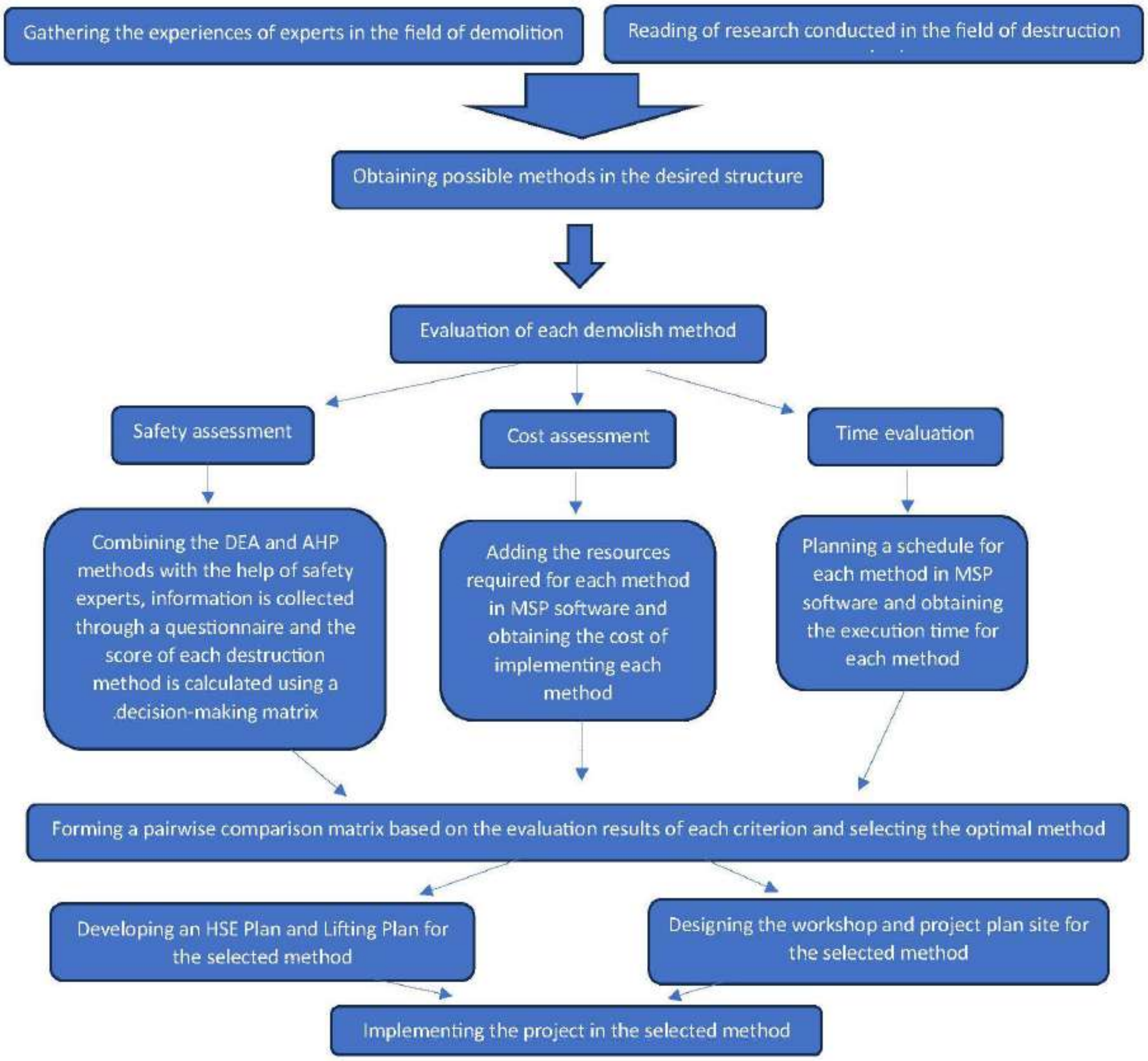

Figure 1: Research methodology and results

is of particular importance. At the end of this paper, we will address how to examine and select the demolition method of the desired structure from various perspectives and, in the next step, by entering other effective factors in site management, to achieve the most optimal project execution method. At the end of this research, the selected method in the research results is compared and validated with the reality of the implemented project case study. Also, the impact of using a suitable site layout plan design and lifting plan for the selected method on the project execution process is investigated.

The flowchart below shows the path and process of the research in this study (Figure 1).

3. Case Study

This research focuses on two 10,000-ton capacity concrete silos at the Gol Gohar Sirjan complex in Kerman Province, Iran. The objective of demolishing these silos is to access the rich iron ore reserves beneath them. This paper specifically addresses the demolition methods for these silos, and while no research has been conducted on constructing new silos, it is recommended that future studies explore and evaluate methods for building new silos.

The concrete silos in question have a total height of 26 meters, an external diameter of 15 meters, and a wall thickness of 50 centimeters. Each silo has supports (columns) 7 meters in height and a 2-meter-thick concrete slab roof. These silos are situated on a 23 by 35-meter, 3-meter thick, spread foundation. The primary constraints in the demolition method are the presence of a concentration and dust processing plant on the northern side and a distance of 20 meters from the edge of the main mine pit on the southern side.

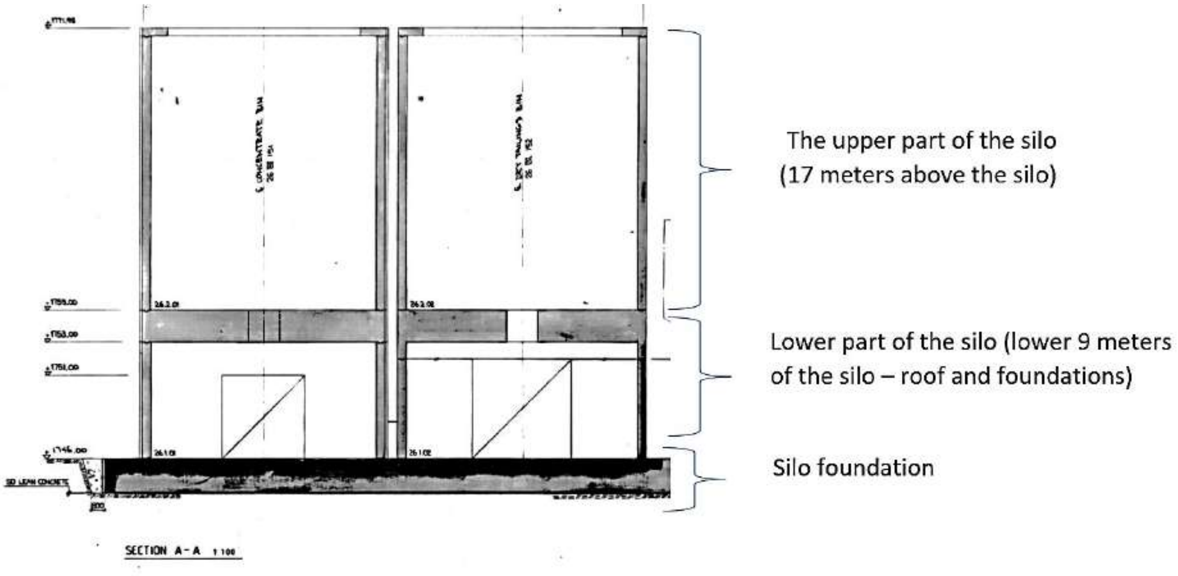

Figure 3 Silo structure division - silo cross-section in height

Figure 4. Transferring the shovel on a metal platform by a dry boom crane at a height for demolition by a hydraulic jaw (scissors) or a pickaxe in stages from top to bottom

In each silo demolition method, the execution steps are divided into three sections of the silo structure, as follows:

- Section 1: Demolition of the upper 17 meters, including the wall and the main body of the silo (where the minerals are stored).
- Section 2: Demolition of the 2-meter-thick roof and the 7-meter-high silo columns.
- Section 3: Demolition of the 3-meter-thick reinforced concrete foundation and 1-meter-thick lean concrete.

The feasible demolition methods for each section will be described in detail in the following sections.

Demolition Methods for the Upper Section of the Silo (17 Meters): Three methods are proposed for demolishing the upper section of the silo, which includes the main silo wall:

Method 1: Demolition using explosives: According to calculations based on Publication 410 (Technical Regulations for Explosives and Blasting in Mines) [16] and blasting demolition relationships [17], holes are drilled at 25 cm intervals around the silo and at the height of the silo using a hand hammer, following safety precautions. These holes are filled with 30-energy emulsion explosives and detonators. The silo is then demolished by a blasting team. Of the 40 cm drilled hole, 30 cm is filled with explosives and 10 cm with sealing material. In this method, using demolition engineering and designing a demolition pattern, and using time delays in detonator explosions, the silo is designed to collapse inward without posing a threat to the surrounding environment. It is worth noting that only the concrete parts of the silo are demolished using this method, and the reinforcements are bent. After the concrete part of the silo is demolished, the reinforcements are cut, and the demolition is completed in this section. At the end of each section, the rebars are separated from the demolished concrete using pneumatic hammers and air cutters and are sorted.

Method 2: Using mechanical equipment: A steel platform is constructed for placing an excavator on it. The excavator, equipped with a breaker, is lifted to a height of 25 meters using a heavy-duty crawler crane and begins to demolish the silo in stages and levels, continuing in this way until the first section of the silo is demolished. The disadvantage of this method is its time-consuming nature. In this method, the inside of the concrete silos can be filled with a mixture of soil, and the excavator can be placed inside the silo on the piled soil and gradually demolish the silo wall and move downwards.

Method 3: Demolition using diamond wire cutting: The execution of this method is carried out according to ACI Report 555 [18]. According to the attached drawings, the wall of each silo is divided into segments, each of which is a quarter of a circle, which is cut at different levels using a concrete diamond wire saw and transferred to the ground by a crane. Before starting the wire cutting process, a scaffolding platform is installed inside the silos so that the equipment can be stationed at different working levels. Two cutting machines are placed inside each silo and simultaneously cut the concrete pieces. At the end of each cut, the section of the wall is cut and transferred to the ground by a crane. The execution of the formwork, according to the design calculated, is carried out using omega (triangular) scaffolding with an arrangement that is as similar as possible to a circle inside the silo and on its roof. The dimensions at the main quadrilateral bases are 1.2 meters by 1.2 meters with a height of 1 meter, which is used for better resistance and performance. The distance between the triangular elements (square bases) is 1 meter. Due to the quarter-circle cut, the scaffolding adheres to the wall only in places where excavation is to be carried out, and in other areas, there will be a distance of about 50 centimeters from the inner edge of the wall. The weight of each cutting machine is about 350 to 400 kilograms, and its dimensions are 1 meter by 1 meter. Two machines are to be operated on each platform. Each machine has two personnel, making a total weight of about 1000 kilograms (1 ton) on the structure. According to the design of the formwork manufacturer, the load-bearing capacity of each square meter is 1 ton, and based on this, the scaffolding platform structure has sufficient strength with a high safety factor.

Demolition Methods for the Second Section of the Silo (2-meter roof and 7-meter columns)

Method 1: Demolition using explosives: In this method, according to calculations based on Publication 410 (Technical Regulations for Explosives and Blasting in Mines) and blasting demolition relationships, holes are drilled at 1-meter intervals in the roof of the silos using a hand hammer, adhering to safety precautions. These holes are drilled to a depth of 150 cm and filled with high-energy emulsion explosives and detonators. The blasting team then detonates the charges to demolish this section of the silo. Of the 150 cm drilled hole, 110 cm is filled with explosives and 40 cm with sealing material.

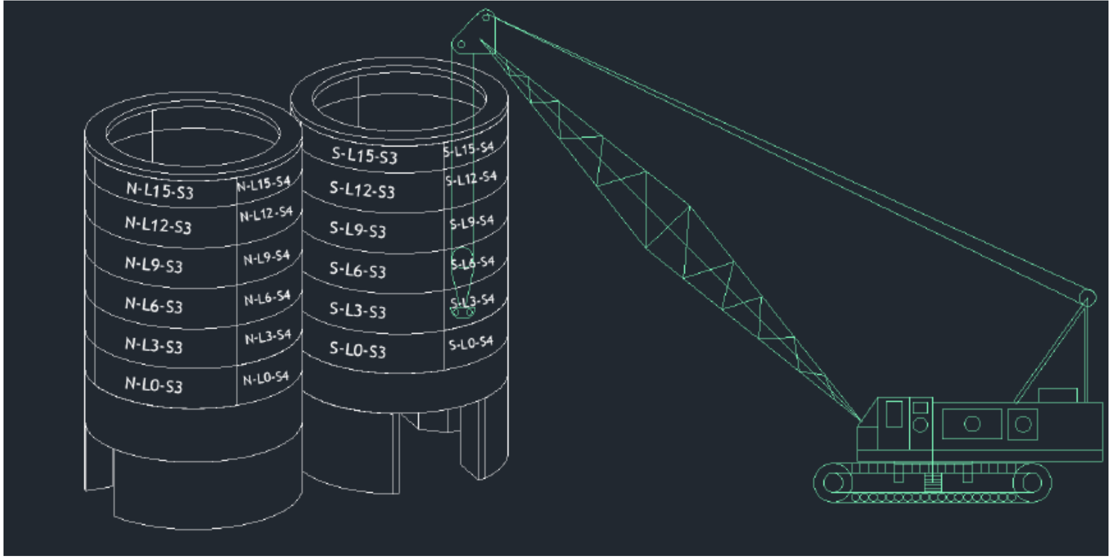

Figure 5. Deploying a crane next to the silo and transferring the cut pieces to the ground using a cutting wire.

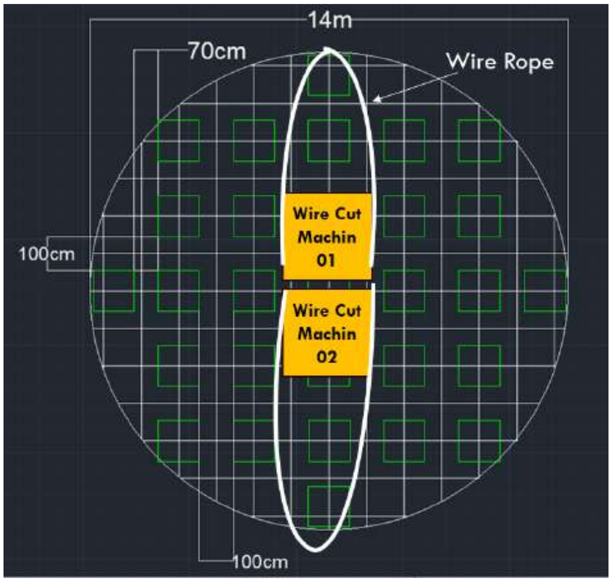

Figure 6 Structure map and cutting path of silo wall concrete

Simultaneously, in areas where the silo's columns are located, the hole depth reaches 7 meters, as the concrete in these areas extends to the ground level. Using demolition engineering and designing a specific demolition pattern, along with time delays in detonating the charges, the design ensures that the roof and columns of the silo collapse inward without endangering the surrounding area. It's important to note that only the concrete parts of the silo are demolished using this method, and the reinforcements are bent. After the concrete portion is demolished, the reinforcements are cut, and the demolition of this section is completed. At the end of each section, rebars are separated from the demolished concrete using pneumatic hammers and air cutters, and they are sorted.

Demolition Methods for the Second Section of the Silo (2-meter roof and 7-meter columns)

Method 2: Using Mechanical Equipment: This method involves using an excavator equipped with a breaker to demolish the concrete in stages. It’s important to note that for demolishing the columns, there's no need for a crane, as the excavator alone can perform the demolition. However, for the roof demolition, due to its 9-meter height, the excavator must be lifted onto the roof using a crane. After the roof is demolished, the excavator is again lowered to the ground using the crane. In this method, the excavator starts demolishing from one point on the roof and moves in the opposite direction of demolition until the entire roof area is demolished.

Method 3: Using Diamond Wire Cutting: In this method, the roof is divided into 25-ton segments using drill holes. A diamond wire cutting machine is then used to divide the roof into smaller pieces, similar to the wall, and these pieces are transferred to the ground using a crane. To cut the columns, each column is cut at the junction with the foundation using a diamond wire saw, and then an external force is applied to cause it to overturn.

Demolition Methods for the Third Section of the Silo (3-meter-thick foundation)

Method 1: Demolition using explosives: In this method, according to calculations based on Publication 410 (Technical Regulations for Explosives and Blasting in Mines) and blasting demolition relationships, holes are drilled at 2-meter intervals throughout the silo foundation using a drill rig, adhering to safety precautions. These holes are drilled to a depth of 150 cm and filled with high-energy emulsion explosives and detonators. The blasting team then detonates the charges to demolish this section of the silo. Of the 150 cm drilled hole, 110 cm is filled with explosives and 40 cm with sealing material. Using demolition engineering and designing a specific demolition pattern, along with time delays in detonating the charges, the design ensures that the silo foundation collapses inward without endangering the surrounding area. It's important to note that only the concrete parts of the silo are demolished using this method, and the reinforcements are bent. After the concrete portion is demolished, the reinforcements are cut, and the demolition of this section is completed. At the end of each section, rebars are separated from the demolished concrete using pneumatic hammers and air cutters, and they are sorted.

Method 2: Using Mechanical Equipment: This method involves using an excavator equipped with a breaker to demolish the concrete in stages. It is estimated that 3 PC300 excavators will be needed to work in two shifts to keep up with the schedule.

One-step overturning of the silo by removing its columns: In this method, a portion of the silo columns is initially demolished at the lower level using an excavator or diamond wire cutting. Then, by placing explosives in the remaining columns and creating an explosion, the other columns are demolished, causing the silo to overturn due to the induced tension and failure in the opposite columns. In this method, a deep pit with dimensions 1.5 times the diameter of the silo (25 meters) must be excavated at the location where the silo is to be overturned to prevent the scattering of concrete debris during the overturning process. For the one-step overturning method, this method must first be modeled in the SAP2000 software, and the results obtained after removing the elements of some of the main columns should be followed, similar to the modeling performed by Julide Yuzbasi in her 2024 research [6]. To do this, the structure is modeled in the SAP software according to the construction drawings. The results of the modeling when two columns are removed from the four columns of the silo show that the stress experienced in the remaining two columns under dead loads and without a factor is 0.928, which means that one-step overturning of the silo by removing the columns is not possible. The figure

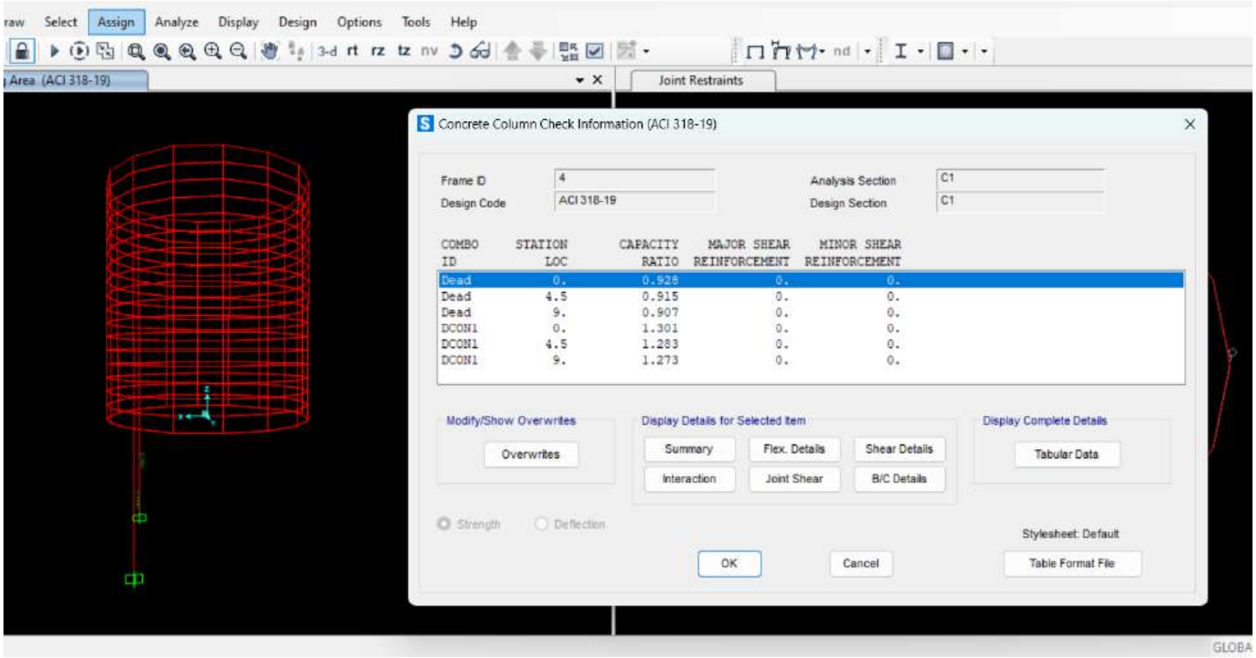

Concrete Column Check Information (ACI 318-19)

Frame ID: 4
Design Code: ACI 318-19
Analysis Section: C1
Design Section: C1

```
COMBO     STATION      CAPACITY   MAJOR SHEAR   MINOR SHEAR
ID            LOC         RATIO REINFORCEMENT REINFORCEMENT
Dead           0.         0.928            0.            0.
Dead          4.5         0.915            0.            0.
Dead           9.         0.907            0.            0.
DCON1          0.         1.301            0.            0.
DCON1         4.5         1.283            0.            0.
DCON1          9.         1.273            0.            0.
```

Figure 7 Silo modeling results by removing 2 columns in Sap2000

7 shows the results of modeling the silos after removing two columns, which indicates that the silo will remain stable after removing two columns.

4. Quality (Safety) Assessment

The basis for calculating quality (safety) is a combination of the AHP and DEA methods. This proposed method, recommended by Mehdi Mohajeri and Abdollah Ardashir in 2016 [19], and applied to the analysis, risk, and safety of construction, allows us to compare and score the risks of each method. The potential risks identified by HSE experts include: projection of concrete fragments during explosions, the possibility of explosions during the placement of explosives, explosions during the transportation of explosives, the projection of crushed concrete during drilling with a drill rig, the projection of crushed concrete during drilling with a core drill, breakage of the concrete cutting wire, electric shock, the projection of concrete pieces during crane lifting, the fall of an excavator from the top of the silo during demolition, breakage of the rebar cutting stone, the projection of splinters during rebar cutting, and the projection of crushed concrete during demolition by an excavator.

In the execution methods, as suggested by Mehdi Mohajeri and Abdollah Ardashir, the probability of occurrence of each of the above events is calculated using two methods, and the results from both methods are used in the risk analysis. First, the probability of occurrence is calculated using the DEA method. In this method, for each of the events mentioned in the safety assessment, the probability of occurrence is obtained based on the opinions of experts. In the second method, using the concentration factor relationship proposed by Badri and his colleagues in 2012 [20], and considering the risk factors and the level of participation of these factors in each of the safety evaluation factors of the demolition method, the probability of occurrence of each of the mentioned incidents in the safety assessment is calculated using the concentration factor formula presented below (Eq. 1).

$$C_{ij} = \frac{X_i Y_{ij}}{\sum_{i=1}^{n} \sum_{j=1}^{m} X_i Y_{ij}} \tag{1}$$

Where X_i is the number of risk factors from the incident factors (Fi) and Y_i is the weight of each risk factor that is important in the occurrence of the incident (and is estimated by experts). The Table 2 shows the ranking of risk factors for calculating the concentration factor.

Table 2.
Risk factor ranking

Num	Dangerous Factor	Grade (1-9)
F1	Inadequate management control	9
F2	Unsafe practices	6
F3	Unfavorable working conditions	7
F4	Personal factors	5

In the subsequent stage, the consequences of human injury and financial loss are evaluated based on the opinions of expert specialists. The weight of the risk level criteria, which include the probability of occurrence (using the DEA method), financial consequences, and human injury consequences, is derived from the research of

Table 3
Survey results regarding risk level

	Criteria	Throwing concrete pieces in an explosion	Possibility of explosion while placing explosives	Explosion while transporting explosives	Crushed concrete being thrown out during drilling by a drill rig	Crushed concrete being thrown out when drilling with a core drill	Concrete cutting wire breaks	Electric shock	Concrete piece thrown out while being moved by crane	Excavator falls from top of silo during demolition	Rebar cutting stone breakage	Throwing of pleats when cutting rebar	Crushed concrete being thrown out during demolition by an excavator
Probability of an accident	scarce	0	7	9	6	3	1	3	7	6	2	2	2
	Sometimes	1	2	1	3	4	1	3	3	4	3	3	5
	Possible	2	1	0	1	3	5	3	0	0	3	3	3
	Common	7	0	0	0	0	3	1	0	0	2	2	0
Life consequences	Minor damage	3	1	0	7	7	2	2	0	0	4	6	4
	Severe injury	3	1	1	3	3	3	3	1	3	3	3	6
	Permanent disability	2	2	3	0	0	3	3	3	6	2	1	0
	Death	2	6	6	0	0	2	2	6	1	1	0	0
Financial consequence	Low	1	1	0	9	8	5	6	6	0	6	8	7
	Medium	1	1	0	1	2	2	4	4	1	4	2	3
	High	3	3	4	0	0	2	0	0	3	0	0	0
	Very High	5	5	6	0	0	1	0	0	6	0	0	0

Ardeshir and colleagues. Based on this, the weight of each sub-criterion is as follows:

- Probability of occurrence: Frequent (0.1), Possible (0.05), Occasional (0.033), and Rare (0.025)
- Human injury consequences: Death (0.146), Permanent disability (0.0731), Severe injury (0.04867), and Minor injury (0.0365)
- Financial consequences: Very high (0.105), High (0.0526), Medium (0.035), and Low (0.0262) Finally, the risk of each hazard is calculated using the relationship proposed by Wang et al. in 2088 [21] for risk assessment (Eq. 2).

In this relationship, W_j represents the weight of the criteria determined by the AHP method, $s^*(H_{jk})$ is the optimal score from the determined evaluation class, and V(Ai) is the final weight of the risks. With the final weight, the risks can be ranked and prioritized.

$$V_{(A_i)} = \sum_{j=1}^{m} W_i V_{ij} = \sum_{j=1}^{m} W_i (\sum_{k=1}^{kj} s^*(H_{jk}) NE_{ijk}) \qquad (2)$$

$$i = 1, \ldots., n$$

In the final stage, based on the weighted score of each of the probability of occurrence criteria (based on risk factors and concentration relationship), probability of occurrence (based on DEA), human injury consequences, and financial consequences, the potential risk of each hazard is calculated. Considering that each of the mentioned hazards is related to which demolition method, the safety assessment score of each method is calculated by the algebraic sum of the hazard scores of each related factor. As mentioned in the research methodology, to evaluate the safety of demolition methods, a combination of the AHP and DEA methods is used, along with questionnaires and opinions of safety experts. The questionnaire results regarding the probability of occurrence, human injury consequences, and financial consequences of each risk level are presented in the following table.

Table 4
Risk score for the qualities being assessed

Dangerous	risk factor concentration	Probability of an accident	Life consequences	Financial consequence	Total Grade of Dangerous
	0.14	**0.14**	**0.64**	**0.08**	
Throwing concrete pieces in an explosion	0.3	0.833	0.6937	0.744	0.662
Possibility of explosion while placing explosives	0.24	0.291	1.1074	0.744	0.843
Explosion while transporting explosives	0.23	0.258	1.144	0.8404	0.868
Crushed concrete being thrown out during drilling	0.24	0.299	0.4015	0.2708	0.354
Crushed concrete being thrown out when drilling	0.22	0.357	0.4015	0.2796	0.360
Concrete cutting wire breaks	0.25	0.608	0.7303	0.4112	0.621
Electric shock	0.22	0.424	0.7303	0.2972	0.582
Concrete piece thrown out while being moved by	0.22	0.274	1.144	0.2972	0.825
Excavator falls from top of silo during demolition	0.24	0.282	0.7306	0.8228	0.606
Rebar cutting stone breakage	0.26	0.499	0.5842	0.2972	0.503
Throwing of pleats when cutting rebar	0.26	0.499	0.4381	0.2796	0.408
Crushed concrete being thrown out during	0.25	0.365	0.438	0.2884	0.389

The numbers presented in the table above represent the number of opinions collected through the questionnaire, which was completed by 10 expert specialists in the field of safety. In the next stage, considering the weight of each criterion mentioned in the previous section, the risk scores are calculated. The table below shows the overall risk score for each risk criterion in the safety assessment. As observed, the risks associated with demolition methods using explosives and concrete cutting have higher scores compared to the demolition method using an excavator, indicating a lower safety score for demolition using these two methods.

In the subsequent stage, based on the obtained risk scores, the safety score of each method is calculated. This is done by algebraically summing the total risk scores of all related factors for each demolition method in the table above, and the safety assessment for each method is obtained. Then, by forming a pairwise comparison matrix for the safety criterion when comparing demolition methods, the first pairwise comparison matrix is constructed in the AHP method. It is worth noting that a higher risk score indicates a lower safety level of the demolition method and entails a higher risk. The table below shows the safety score of each method, and Matrix 1 displays the values of the pairwise comparison matrix for evaluating the safety of demolition methods.

Table 5
Risk score for each destruction method

Demolish Method	Total Risk Score	Safety assessment rating
Explosion	3.648	3
Demolish with Excavator	0.995	1
Wire Cut	2.393	2

$$\begin{pmatrix} S_{11} & S_{12} & S_{13} \\ S_{21} & S_{22} & S_{23} \\ S_{31} & S_{32} & S_{33} \end{pmatrix} = \begin{pmatrix} 1 & 0.27 & 0.65 \\ 3.66 & 1 & 2.4 \\ 1.52 & 0.42 & 1 \end{pmatrix} \quad (3)$$

$$S_{12} = \frac{1}{S_{21}}, S_{13} = \frac{1}{S_{31}}, S_{23} = \frac{1}{S_{32}}$$

Eq. (3) is Pairwise comparison matrix values of destruction methods in assessing the safety of each method.

In the above matrix, the ratios represent the safety score of the explosion method relative to the mechanical excavator method, the safety score of the explosion method relative to the concrete cutting method, and the safety score of the mechanical excavator method relative to the concrete cutting method. The diagonal of the matrix is 1 since the ratio of the safety score of each method to itself is always 1. In this matrix, the higher the value of the matrix elements, the higher the safety (lower risk score) of that method.

5. Cost and Time-Based Evaluation

The cost criterion will be calculated based on the resources allocated to each of the execution activities in the Work Breakdown Structure (WBS) of each method. For each method, its WBS is prepared, and the required resources and costs for executing the activities, including materials, manpower, machinery, and transportation, are allocated. Finally, the cost of executing that activity is calculated. By summing up the costs of each activity, the demolition cost of each method is calculated.

The time is based on the schedule obtained in each method using the MSP software. To prepare the schedule,

Table 6
Results of time and cost of implementing each method

Num	Section	Demolish Method	Time (Days)	Gross cost $	Book value of equipment and machinery after depreciation $	Net cost of Demolish $
1	Wall of Silo	Wire Cut	83	109,850 $	50,750 $	59,100 $
2		Explosion	92	126,861 $	49,263 $	77,599 $
3		Excavator	88	80,513 $	9,669 $	70,844 $
4	Roof & Column of Silo	Explosion	51	85,575 $	23,013 $	62,563 $
5		Excavator	49	49,673 $	9,669 $	40,004 $
6	Foundation	Explosion	42	79,115 $	23,328 $	55,788 $
7		Excavator	32	53,688 $	9,669 $	44,019 $

Table 7
MSP software output for silo wall demolition by explosion method

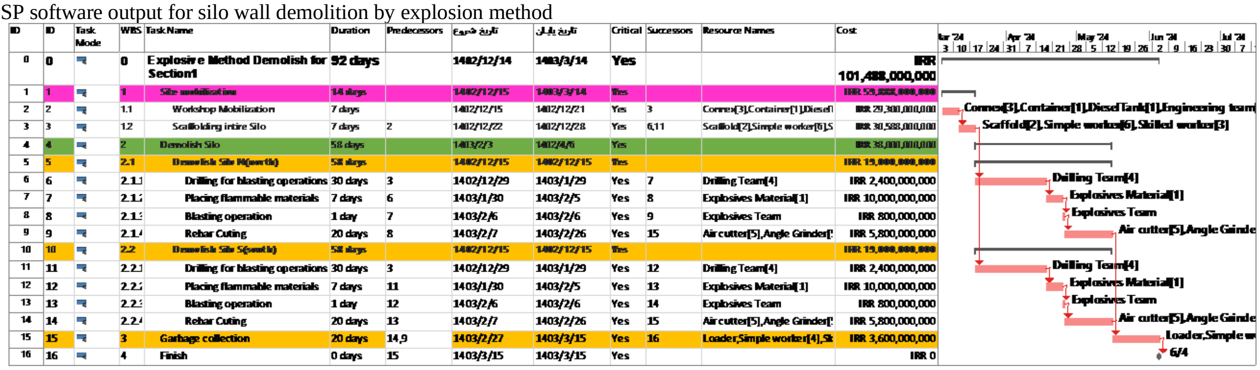

ID	ID	Task Mode	WBS	Task Name	Duration	Predecessors	تاریخ شروع	تاریخ پایان	Critical	Successors	Resource Names	Cost
0	0		0	**Explosive Method Demolish for Section1**	**92 days**		**1402/12/14**	**1403/3/14**	**Yes**			**IRR 101,488,000,000**
1	1		1	Site mobilization	14 days		1402/12/15	1403/3/14	Yes			IRR 59,888,000,000
2	2		1.1	Workshop Mobilization	7 days		1402/12/15	1402/12/21	Yes	3	Connex[3],Container[1],Diesel	IRR 29,300,000,000
3	3		1.2	Scaffolding intire Silo	7 days	2	1402/12/22	1402/12/28	Yes	6,11	Scaffold[2],Simple worker[6],S	IRR 30,588,000,000
4	4		2	Demolish Silo	58 days		1403/2/3	1402/4/6	Yes			IRR 38,000,000,000
5	5		2.1	Demolish Silo N(north)	58 days		1402/12/15	1402/12/15	Yes			IRR 19,000,000,000
6	6		2.1.1	Drilling for blasting operations	30 days	3	1402/12/29	1403/1/29	Yes	7	Drilling Team[4]	IRR 2,400,000,000
7	7		2.1.2	Placing flammable materials	7 days	6	1403/1/30	1403/2/5	Yes	8	Explosives Material[1]	IRR 10,000,000,000
8	8		2.1.3	Blasting operation	1 day	7	1403/2/6	1403/2/6	Yes	9	Explosives Team	IRR 800,000,000
9	9		2.1.4	Rebar Cuting	20 days	8	1403/2/7	1403/2/26	Yes	15	Air cutter[5],Angle Grinder[	IRR 5,800,000,000
10	10		2.2	Demolish Silo S(south)	58 days		1402/12/15	1402/12/15	Yes			IRR 19,000,000,000
11	11		2.2.1	Drilling for blasting operations	30 days	3	1402/12/29	1403/1/29	Yes	12	Drilling Team[4]	IRR 2,400,000,000
12	12		2.2.2	Placing flammable materials	7 days	11	1403/1/30	1403/2/5	Yes	13	Explosives Material[1]	IRR 10,000,000,000
13	13		2.2.3	Blasting operation	1 day	12	1403/2/6	1403/2/6	Yes	14	Explosives Team	IRR 800,000,000
14	14		2.2.4	Rebar Cuting	20 days	13	1403/2/7	1403/2/26	Yes	15	Air cutter[5],Angle Grinder[	IRR 5,800,000,000
15	15		3	Garbage collection	20 days	14,9	1403/2/27	1403/3/15	Yes	16	Loader,Simple worker[4],Sk	IRR 3,600,000,000
16	16		4	Finish	0 days	15	1403/3/15	1403/3/15	Yes			IRR 0

Table 8
MSP software output: Destruction of silo wall using excavator method

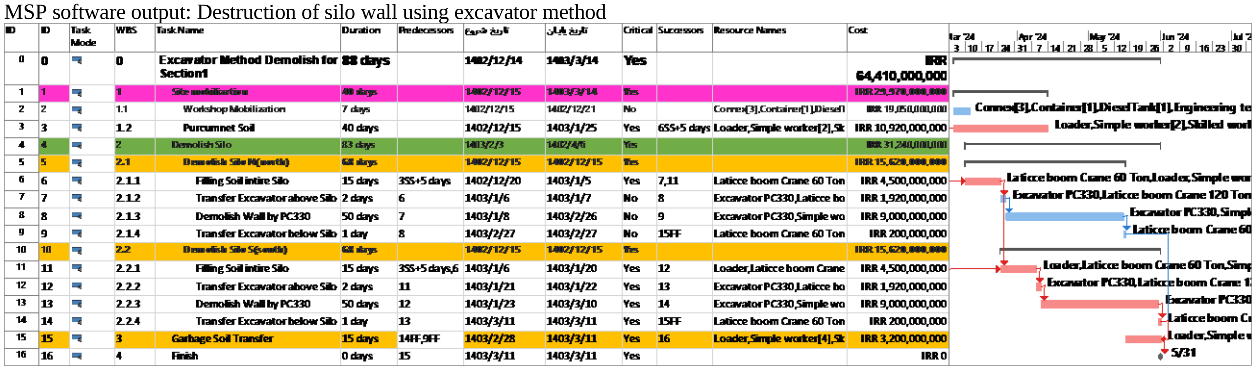

ID	ID	Task Mode	WBS	Task Name	Duration	Predecessors	تاریخ شروع	تاریخ پایان	Critical	Successors	Resource Names	Cost
0	0		0	**Excavator Method Demolish for Section1**	**88 days**		**1402/12/14**	**1403/3/14**	**Yes**			**IRR 64,410,000,000**
1	1		1	Site mobilization	40 days		1402/12/15	1403/3/14	Yes			IRR 29,970,000,000
2	2		1.1	Workshop Mobilization	7 days		1402/12/15	1402/12/21	No		Connex[3],Container[1],Diesel	IRR 19,050,000,000
3	3		1.2	Purcumnet Soil	40 days		1402/12/15	1403/1/25	Yes	6SS+5 days	Loader,Simple worker[2],Sk	IRR 10,920,000,000
4	4		2	Demolish Silo	83 days		1403/2/3	1402/4/6	Yes			IRR 31,240,000,000
5	5		2.1	Demolish Silo N(north)	68 days		1402/12/15	1402/12/15	Yes			IRR 15,620,000,000
6	6		2.1.1	Filling Soil intire Silo	15 days	3SS+5 days	1402/12/20	1403/1/5	Yes	7,11	Laticce boom Crane 60 Ton	IRR 4,500,000,000
7	7		2.1.2	Transfer Excavator above Silo	2 days	6	1403/1/6	1403/1/7	No	8	Excavator PC330,Laticce bo	IRR 1,920,000,000
8	8		2.1.3	Demolish Wall by PC330	50 days	7	1403/1/8	1403/2/26	No	9	Excavator PC330,Simple wo	IRR 9,000,000,000
9	9		2.1.4	Transfer Excavator below Silo	1 day	8	1403/2/27	1403/2/27	No	15FF	Laticce boom Crane 60 Ton	IRR 200,000,000
10	10		2.2	Demolish Silo S(south)	68 days		1402/12/15	1402/12/15	Yes			IRR 15,620,000,000
11	11		2.2.1	Filling Soil intire Silo	15 days	3SS+5 days,6	1403/1/6	1403/1/20	Yes	12	Loader,Laticce boom Crane	IRR 4,500,000,000
12	12		2.2.2	Transfer Excavator above Silo	2 days	11	1403/1/21	1403/1/22	Yes	13	Excavator PC330,Laticce bo	IRR 1,920,000,000
13	13		2.2.3	Demolish Wall by PC330	50 days	12	1403/1/23	1403/3/10	Yes	14	Excavator PC330,Simple wo	IRR 9,000,000,000
14	14		2.2.4	Transfer Excavator below Silo	1 day	13	1403/3/11	1403/3/11	Yes	15FF	Laticce boom Crane 60 Ton	IRR 200,000,000
15	15		3	Garbage Soil Transfer	15 days	14FF,9FF	1403/2/28	1403/3/11	Yes	16	Loader,Simple worker[4],Sk	IRR 3,200,000,000
16	16		4	Finish	0 days	15	1403/3/11	1403/3/11	Yes			IRR 0

the WBS is first prepared for each demolition method, and then by defining the relationship between activities and allocating resources, the duration of activities is calculated, and the total demolition time is obtained using the above method.

The evaluation results of each demolition method based on the time and cost criteria are as follows, according to the predicted schedule output in MSP and the calculation of costs based on the resources allocated to the activities. Table 6 shows Results of time and cost of implementing each method.

Table 6 shows that in the wall area of the silo, the concrete cutting method is the cheapest, but from a safety perspective, the demolition method using an excavator has better safety. In this work area, the choice of demolition method will be made based on the AHP evaluation. In the ceiling, column, and foundation areas of the silos, the shortest time and lowest cost are achieved using the demolition method with an excavator. Also, according to the safety assessment, compared to the explosion method, the demolition method using an excavator has a higher safety factor. Given the absolute superiority of the demolition method using an excavator in terms of cost, time, and safety, the proposed demolition method for the ceiling, column, and foundation sections of the silos is demolition using an excavator. In the concrete cutting method, the gross execution cost is higher than the demolition method using an excavator, but this is due to the purchase of equipment and machinery required for this method. Assuming a 30% depreciation of the required equipment and machinery in this method within 3 months, the book value of the assets after deducting depreciation is less than the demolition method using an excavator. However, it should be noted that if concrete cutting is chosen, the project manager must consider the cost of purchasing the necessary machinery and equipment for this method, which requires a strong financial capacity for the project.

Table 9
MSP software output: Silo wall demolition using concrete wire cutting method

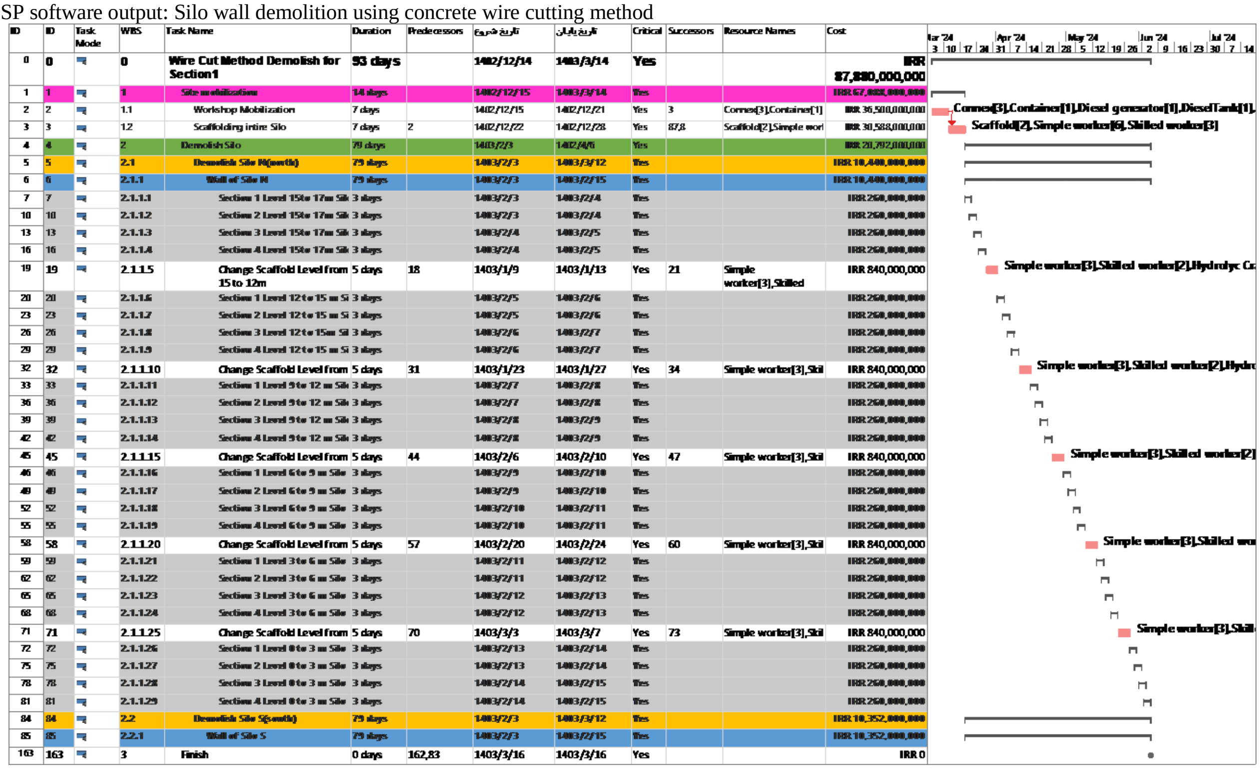

ID	ID	Task Mode	WBS	Task Name	Duration	Predecessors	تاریخ شروع	تاریخ پایان	Critical	Successors	Resource Names	Cost
0	0		0	**Wire Cut Method Demolish for Section1**	**93 days**		**1402/12/14**	**1403/3/14**	**Yes**			**IRR 87,880,000,000**
1	1		1	Site mobilization	14 days		1402/12/15	1403/3/14	Yes			IRR 67,088,000,000
2	2		1.1	Workshop Mobilization	7 days		1402/12/15	1402/12/21	Yes	3	Connex[3],Container[1]	IRR 36,500,000,000
3	3		1.2	Scaffolding intire Silo	7 days	2	1402/12/22	1402/12/28	Yes	87,8	Scaffold[2],Simple worl	IRR 30,588,000,000
4	4		2	Demolish Silo	79 days		1403/2/3	1402/4/6	Yes			IRR 20,792,000,000
5	5		2.1	Demolish Silo N(north)	79 days		1403/2/3	1403/3/12	Yes			IRR 10,440,000,000
6	6		2.1.1	Wall of Silo N	79 days		1403/2/3	1403/2/15	Yes			IRR 10,440,000,000
7	7		2.1.1.1	Section 1 Level 15to 17m Silo	3 days		1403/2/3	1403/2/4	Yes			IRR 260,000,000
10	10		2.1.1.2	Section 2 Level 15to 17m Silo	3 days		1403/2/3	1403/2/4	Yes			IRR 260,000,000
13	13		2.1.1.3	Section 3 Level 15to 17m Silo	3 days		1403/2/4	1403/2/5	Yes			IRR 260,000,000
16	16		2.1.1.4	Section 4 Level 15to 17m Silo	3 days		1403/2/4	1403/2/5	Yes			IRR 260,000,000
19	19		2.1.1.5	Change Scaffold Level from 15 to 12m	5 days	18	1403/1/9	1403/1/13	Yes	21	Simple worker[3],Skilled	IRR 840,000,000
20	20		2.1.1.6	Section 1 Level 12 to 15 m Si	3 days		1403/2/5	1403/2/6	Yes			IRR 260,000,000
23	23		2.1.1.7	Section 2 Level 12 to 15 m Si	3 days		1403/2/5	1403/2/6	Yes			IRR 260,000,000
26	26		2.1.1.8	Section 3 Level 12 to 15m Sil	3 days		1403/2/6	1403/2/7	Yes			IRR 260,000,000
29	29		2.1.1.9	Section 4 Level 12 to 15 m Si	3 days		1403/2/6	1403/2/7	Yes			IRR 260,000,000
32	32		2.1.1.10	Change Scaffold Level from	5 days	31	1403/1/23	1403/1/27	Yes	34	Simple worker[3],Skil	IRR 840,000,000
33	33		2.1.1.11	Section 1 Level 9 to 12 m Silo	3 days		1403/2/7	1403/2/8	Yes			IRR 260,000,000
36	36		2.1.1.12	Section 2 Level 9 to 12 m Silo	3 days		1403/2/7	1403/2/8	Yes			IRR 260,000,000
39	39		2.1.1.13	Section 3 Level 9 to 12 m Silo	3 days		1403/2/8	1403/2/9	Yes			IRR 260,000,000
42	42		2.1.1.14	Section 4 Level 9 to 12 m Silo	3 days		1403/2/8	1403/2/9	Yes			IRR 260,000,000
45	45		2.1.1.15	Change Scaffold Level from	5 days	44	1403/2/6	1403/2/10	Yes	47	Simple worker[3],Skil	IRR 840,000,000
46	46		2.1.1.16	Section 1 Level 6 to 9 m Silo	3 days		1403/2/9	1403/2/10	Yes			IRR 260,000,000
49	49		2.1.1.17	Section 2 Level 6 to 9 m Silo	3 days		1403/2/9	1403/2/10	Yes			IRR 260,000,000
52	52		2.1.1.18	Section 3 Level 6 to 9 m Silo	3 days		1403/2/10	1403/2/11	Yes			IRR 260,000,000
55	55		2.1.1.19	Section 4 Level 6 to 9 m Silo	3 days		1403/2/10	1403/2/11	Yes			IRR 260,000,000
58	58		2.1.1.20	Change Scaffold Level from	5 days	57	1403/2/20	1403/2/24	Yes	60	Simple worker[3],Skil	IRR 840,000,000
59	59		2.1.1.21	Section 1 Level 3 to 6 m Silo	3 days		1403/2/11	1403/2/12	Yes			IRR 260,000,000
62	62		2.1.1.22	Section 2 Level 3 to 6 m Silo	3 days		1403/2/11	1403/2/12	Yes			IRR 260,000,000
65	65		2.1.1.23	Section 3 Level 3 to 6 m Silo	3 days		1403/2/12	1403/2/13	Yes			IRR 260,000,000
68	68		2.1.1.24	Section 4 Level 3 to 6 m Silo	3 days		1403/2/12	1403/2/13	Yes			IRR 260,000,000
71	71		2.1.1.25	Change Scaffold Level from	5 days	70	1403/3/3	1403/3/7	Yes	73	Simple worker[3],Skil	IRR 840,000,000
72	72		2.1.1.26	Section 1 Level 0 to 3 m Silo	3 days		1403/2/13	1403/2/14	Yes			IRR 260,000,000
75	75		2.1.1.27	Section 2 Level 0 to 3 m Silo	3 days		1403/2/13	1403/2/14	Yes			IRR 260,000,000
78	78		2.1.1.28	Section 3 Level 0 to 3 m Silo	3 days		1403/2/14	1403/2/15	Yes			IRR 260,000,000
81	81		2.1.1.29	Section 4 Level 0 to 3 m Silo	3 days		1403/2/14	1403/2/15	Yes			IRR 260,000,000
84	84		2.2	Demolish Silo S(south)	79 days		1403/2/3	1403/3/12	Yes			IRR 10,352,000,000
85	85		2.2.1	Wall of Silo S	79 days		1403/2/3	1403/2/15	Yes			IRR 10,352,000,000
163	163		3	Finish	0 days	162,83	1403/3/16	1403/3/16	Yes			IRR 0

Subsequently, the schedule and cost calculated based on the allocated resources in the MSP software are presented for each demolition method in Table 7,8 and 9.

Given the known cost and time values for each demolition method for the silo wall, pairwise comparison matrices are constructed in the AHP method for evaluating cost and time. Matrices 2 and 3 are the pairwise comparison matrices for evaluating cost and time in the AHP method, as calculated below.

Matrix 2 Pairwise comparison matrix values in the AHP method for cost evaluation:

$$\begin{pmatrix} C_{11} & C_{12} & C_{13} \\ C_{21} & C_{22} & C_{23} \\ C_{31} & C_{32} & C_{33} \end{pmatrix} = \begin{pmatrix} 1 & 0.91 & 0.76 \\ 1.1 & 1 & 0.83 \\ 1.31 & 1.2 & 1 \end{pmatrix}$$

$$C_{12} = \frac{1}{C_{21}}, C_{13} = \frac{1}{C_{31}}, C_{23} = \frac{1}{C_{32}}$$

Matrix 3 Pairwise comparison matrix values in the AHP method for time evaluation:

$$\begin{pmatrix} T_{11} & T_{12} & T_{13} \\ T_{21} & T_{22} & T_{23} \\ T_{31} & T_{32} & T_{33} \end{pmatrix} = \begin{pmatrix} 1 & 0.96 & 0.9 \\ 1.04 & 1 & 0.94 \\ 1.12 & 1.06 & 1 \end{pmatrix}$$

$$T_{12} = \frac{1}{T_{21}}, T_{13} = \frac{1}{T_{31}}, T_{23} = \frac{1}{T_{32}}$$

In the above matrices: C_{12} and T_{12} represent the score ratios (advantages) of the cost and time criteria, respectively, for the blasting method compared to the mechanical excavator method. Similarly, C_{13} and T_{13} denote the score ratios (advantages) of the cost and time criteria, respectively, for the blasting method compared to the concrete wire cutting method. Lastly, C_{23} and T_{23} represent the score ratios (advantages) of the cost and time criteria, respectively, for the mechanical excavator method compared to the concrete wire cutting method.

The diagonal elements of the matrix are equal to 1, as they represent the score ratios of the safety criterion of each method to itself. In these matrices, the higher the matrix element values, the lower the associated cost and time of that method.

6. Discussion and Results

With the obtained evaluation matrices for cost, time, and safety, in the final stage, a pairwise comparison matrix is constructed to make a decision regarding the importance (priority) of cost, time, and safety parameters in this project using the AHP method. The values of the pairwise comparison matrix for the cost, time, and safety parameters in this project are collected through a questionnaire and are based on the opinions of expert specialists in this field. It is worth noting that in each project, a pairwise comparison matrix exists for the decision criteria, and this matrix will be different for each project based on the importance indicators from the perspective of the client and contractor. For example, in this case study, considering the client's request for the earliest possible access to the iron ore reserve under the demolished silos, the importance of time is greater than cost, and due to the high sensitivity of the demolition operations and past accidents, the importance of safety is greater than all other criteria. Matrix 4 shows the values of the pairwise comparison matrix for the final decision criteria for each method in AHP.

Matrix 4 Pairwise comparison matrix values of decision-making criteria in the AHP method:

$$\begin{pmatrix} C(Cost) & C/T & C/S \\ T/C & T(Time) & T/S \\ S/C & S/T & S(Safety) \end{pmatrix} = \begin{pmatrix} 1 & 0.8 & 0.348 \\ 1.25 & 1 & 0.25 \\ 2.875 & 4 & 1 \end{pmatrix}$$

$$C/T = \frac{1}{T/C}, C/S = \frac{1}{S/C}, T/S = \frac{1}{S/T}$$

In the above matrix, the first to third rows correspond to the importance (priority) of the cost, time, and safety criteria, respectively. The inconsistency ratio of this matrix is 0.02, which is within the acceptable range (the inconsistency ratio in a pairwise comparison matrix should be less than 0.1). The result obtained from the hierarchical analysis using the AHP method for selecting the demolition method for silo walls (upper part) shows that the concrete cutting method, with a score of 0.362, is the best method considering cost, time, and safety criteria, followed very closely by the mechanical excavator method with a score of 0.360. The Figure 7 below shows the results of the hierarchical analysis using the AHP method in the Expert Choice software for selecting the demolition method for silo walls (upper part).

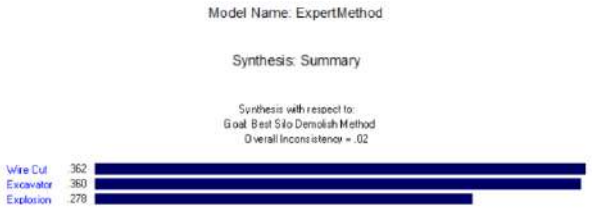

Figure 7 Results of AHP method analysis in Expert Choice software

7. Demolition Using the Selected Method

The wire saw method was chosen as the optimal approach for the upper sections of the silos and for the demolition of silo walls, based on the obtained results. The contractor and client approved this method for execution, and the demolition was carried out accordingly.

The initial concept of using a concrete wire saw and examining its construction management aspects in demolishing concrete structures was introduced by K. Walker and colleagues in 1996 [22], concerning the demolition of concrete chimneys in Arizona, USA. The study summarized and compared three methods: blasting, mechanical demolition, and wire saw cutting with diamond tools. According to their findings, the wire saw method saved approximately 7% in time compared to other methods. By designing the cutting and segmentation process effectively, the project was successfully completed. The study concluded that accurately estimating the structure's geometry and conducting an economic analysis of methods play crucial roles in selecting the optimal method.

Vasiliy Shalenny in 2019 [23] highlighted several key aspects of demolishing concrete structures using diamond wire saws. These include:

1. Installing the cutting device on a temporary support structure rather than directly on the primary structure.
2. Utilizing remote control to operate the cutting device.
3. Using scaffolding for positioning operational personnel and equipment.
4. Establishing reliable methods for lowering cut pieces to the ground.

Based on the results of these studies, the execution procedure, and the silo structural drawings, the walls of each silo were divided into segments, with each segment forming a quarter-circle. These segments were cut at various levels using a concrete wire saw and lowered to the ground using a crane. The weight and dimensions of the cut concrete segments are detailed in the lifting plan calculations provided in the following section.

Notable advantages of this method include precision in concrete cutting, reduced dust and pollution due to water usage, no limitations on the depth and dimensions of the concrete segment owing to the adjustable length of the diamond wire, and no noise or vibration pollution on-site [24]. Additionally, as Shedge concluded in 2024 [25], the wire saw method—also referred to as the "silent demolition method"—is well-suited for sensitive environments due to its reduced noise and vibration.

Sergio Baragetti and colleagues in 2023 [26] developed a numerical FEM model (finite element method) to optimize stress and deformation conditions in diamond wire used for concrete demolition. They found that micro-cracks and small grooves in the wire are primarily due to the misalignment of beads during wire assembly. This allows water penetration, causing corrosion of the metal core, shortening the wire's lifespan, and reducing its fatigue resistance. The study also demonstrated that stress concentration at the wire-to-bead connections is the most critical factor for poor performance. Areas where the wire is in direct contact with the beads are more susceptible to failure due to contact stresses and fatigue from corrosion. To mitigate these stresses, selecting precise parameters such as wire diameter, tensile load, the Young's modulus of the plastic coating, and pulley diameter can reduce Von Mises stresses, increase wire durability, and improve equipment performance.

The introduction of a safety monitoring system during wire saw demolition in concrete structures by Berend Denkena in 2022 [27] further enhances operational reliability. Using inductive sensors adaptable to harsh working conditions, this system identifies minor failures before significant issues arise, monitors wire movement, ensures the stability of the diamond wire, detects positional changes in diamond segments, and predicts tool failures.

Before operating the wire saw equipment, a scaffold platform was constructed inside the silos to facilitate operation at various levels. Two cutting devices were positioned inside each silo, working simultaneously to cut concrete segments. Once a segment was cut, it was lowered to the ground using a crane.

The scaffold design complied with the execution drawings, using Omega (triangular) scaffolding arranged to approximate the circular shape inside the silos and on

Figure 8. From the right, in order, scaffolding is implemented inside the silos to create a platform for the placement of concrete cutting machines, Chinese planks are placed on the scaffolding to place concrete cutting equipment, and concrete cutting equipment is placed.

During the demolition of silo walls using the wire saw method, the creation of three simultaneous work fronts significantly improved project performance by reducing time and labor costs. On this platform, three devices operate concurrently:

1. A horizontal cutting machine that uses a wire to cut concrete horizontally.
2. A vertical cutting machine that performs vertical concrete cutting.
3. A concrete coring machine used to drill boreholes for passing the wire saw and creating connection points for the crane hook.

One of the key requirements for establishing these simultaneous work fronts was ensuring the safety measures for these activities. To protect the operators of the concrete cutting machines, a safety guard and shield were installed

their roofs. The base of the primary structure consisted of square frames measuring 1.2m x 1.2m with a height of 1m. Diagonal bracing was added to enhance resistance and performance. The spacing between the triangular elements (square bases) was 1m.

As only quarter-circle segments were cut where demolition was planned, the scaffolding was in close contact with the silo wall in those areas, while maintaining a distance of approximately 50cm from the inner wall edge in other regions.

Each cutting device weighed about 350–400kg and measured 1m x 1m. Two devices operated on each platform, each requiring two personnel, bringing the total applied load to approximately 1000kg (1 ton). According to the manufacturer’s design, the formwork platform had a load capacity of 1 ton per square meter, ensuring sufficient resistance with a high safety factor.

The execution of the scaffold and the layout of planks to create a platform for positioning the concrete cutting equipment is illustrated in the accompanying diagram. The figure 8 and 9 shows many pictures from this method.

on the platform using scaffolding and metal sheets. This measure ensures no harm or damage occurs to individuals in case the wire saw snaps. Additionally, a separate metal safety guard was installed to ensure the safety of the operator performing the coring activity. To enhance job safety and reduce risks, remote control is utilized for switching the wire saw machines on and off.

Figure 9. Simultaneous creation of three work fronts in the concrete wire cutting demolition method (simultaneous use of two horizontal and vertical cutting machines along with a concrete cutter)

In this method, the sequence of concrete cutting in horizontal and vertical directions is crucial. Initially, horizontal cuts must be executed first, followed by vertical cuts. Alternatively, if both horizontal and vertical cuts are to be performed simultaneously, it must be planned so that the horizontal cutting is completed first and then the vertical cutting. Otherwise, if the vertical cutting is finished before the horizontal cutting, the weight of the cut concrete will rest on the wire saw and its segments. This can cause the wire saw to break frequently due to the immense gravitational load applied to the segments and the wire.

However, if the horizontal cut is completed before the vertical cut, the weight of the concrete does not bear on the wire saw. In this case, because the concrete piece remains connected to the structure at its sides, no significant force is exerted on the wire saw cutting the bottom portion.

Another key consideration in wire saw cutting is accounting for the location of connections and the concentration of structural reinforcements. Cutting should ideally avoid areas where two concrete pieces are joined, especially those with high reinforcement density.

As shown in the figure 10 below, the cutting location has a high concentration of structural reinforcements, which causes frequent breaking of the wire saw and its segments. This, in turn, reduces the execution speed of the operation.

Figure 10. Tearing of cutting wire at the point of compression of structural reinforcements.

In the final stage, before the concrete segment is fully detached from the structure, it is secured to the crane using a 20-mm steel cable. This ensures that when the segment completely separates from the structure, it is already supported by the crane. The crane then transfers the segment to the ground, after which it is transported by a trailer to either a permanent storage site or to be utilized in other parts of the plant. The Figure 11 shows transferring cut concrete pieces to the ground by crane.

Figure 11. Transferring the cut concrete piece to the ground by crane

In this case study, some of the cut concrete segments were repurposed as Jersey barriers for the path of mining dump trucks. The calculations for the load capacity of the crane and the method of securing the segments are detailed in the lifting plan presented later.

8. Lifting Plan

The design and calculation of the lifting plan have been carried out based on the guidelines of the China Work Safety and Health Council (WSH [28]). According to the site plan designed for the project, there are no obstacles within a 500-meter radius of the silos for crane movement. The lifting plan calculations have been performed based on the height of the two silos, which is 25 meters, and their diameter, which is 15 meters.

The following figure 12 shows a view of the two silos. Two lifting plans have been prepared for their demolition. The first plan involves removing the sections on the sides of the silos, assuming that the crane will move to the nearest location for lifting each section.

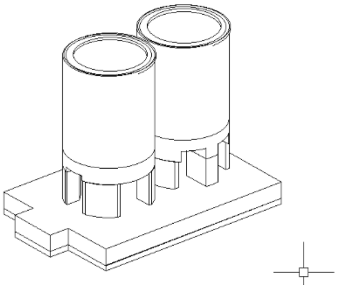

Figure 12. 3D view of existing silos

The second plan considers the scenario where the crane does not have the capability to move and position itself at the closest distance to the silo for lifting the sections.

Crane Specifications Determination: To determine the boom length, boom angle, and lifting radius, we utilize the charts and tables available in the crane’s operation manual [29]. Using this information, the maximum lifting capacity of the crane can be identified. For added safety, up to 75% of the crane's maximum capacity will be used. The figure 13 shows graph of changes in crane boom length and its corresponding angle.

The maximum length of the crane without jib and auxiliary jib is 50 meters. Since the load is not located in an area out of reach, there is no need to use the jib or auxiliary jib.

It is planned for the crane to carry loads between 20 and 25 tons, and to ensure project safety, only 75% of the maximum lifting capacity will be used. Based on the charts and dimensions of the silos, the boom length must be at least 31 meters.

Table 10.
Maximum permissible load based on boom length and crane distance from load center of gravity

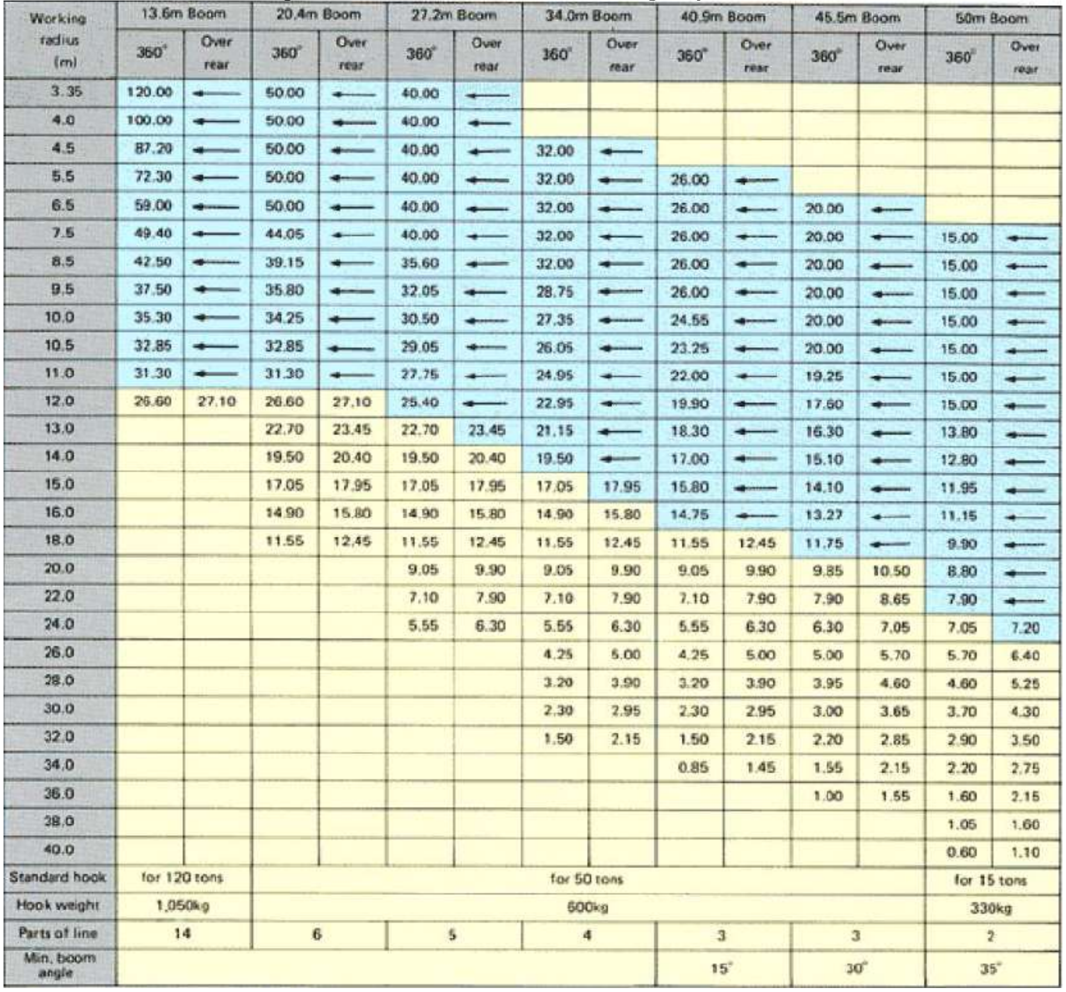

Working radius (m)	13.6m Boom		20.4m Boom		27.2m Boom		34.0m Boom		40.9m Boom		45.5m Boom		50m Boom	
	360°	Over rear	360°	Over rear	360°	Over rear	360°	Over rear	360°	Over rear	360°	Over rear	360°	Over rear
3.35	120.00	←	50.00	←	40.00	←								
4.0	100.00	←	50.00	←	40.00	←								
4.5	87.20	←	50.00	←	40.00	←	32.00	←						
5.5	72.30	←	50.00	←	40.00	←	32.00	←	26.00	←				
6.5	59.00	←	50.00	←	40.00	←	32.00	←	26.00	←	20.00	←		
7.5	49.40	←	44.05	←	40.00	←	32.00	←	26.00	←	20.00	←	15.00	←
8.5	42.50	←	39.15	←	35.60	←	32.00	←	26.00	←	20.00	←	15.00	←
9.5	37.50	←	35.80	←	32.05	←	28.75	←	26.00	←	20.00	←	15.00	←
10.0	35.30	←	34.25	←	30.50	←	27.35	←	24.55	←	20.00	←	15.00	←
10.5	32.85	←	32.85	←	29.05	←	26.05	←	23.25	←	20.00	←	15.00	←
11.0	31.30	←	31.30	←	27.75	←	24.95	←	22.00	←	19.25	←	15.00	←
12.0	26.60	27.10	26.60	27.10	25.40	←	22.95	←	19.90	←	17.60	←	15.00	←
13.0			22.70	23.45	22.70	23.45	21.15	←	18.30	←	16.30	←	13.80	←
14.0			19.50	20.40	19.50	20.40	19.50	←	17.00	←	15.10	←	12.80	←
15.0			17.05	17.95	17.05	17.95	17.05	17.95	15.80	←	14.10	←	11.95	←
16.0			14.90	15.80	14.90	15.80	14.90	15.80	14.75	←	13.27	←	11.15	←
18.0			11.55	12.45	11.55	12.45	11.55	12.45	11.55	12.45	11.75	←	9.90	←
20.0					9.05	9.90	9.05	9.90	9.05	9.90	9.85	10.50	8.80	←
22.0					7.10	7.90	7.10	7.90	7.10	7.90	7.90	8.65	7.90	←
24.0					5.55	6.30	5.55	6.30	5.55	6.30	6.30	7.05	7.05	7.20
26.0							4.25	5.00	4.25	5.00	5.00	5.70	5.70	6.40
28.0							3.20	3.90	3.20	3.90	3.95	4.60	4.60	5.25
30.0							2.30	2.95	2.30	2.95	3.00	3.65	3.70	4.30
32.0							1.50	2.15	1.50	2.15	2.20	2.85	2.90	3.50
34.0									0.85	1.45	1.55	2.15	2.20	2.75
36.0											1.00	1.55	1.60	2.15
38.0													1.05	1.60
40.0													0.60	1.10
Standard hook	for 120 tons		for 50 tons										for 15 tons	
Hook weight	1,050kg		600kg										330kg	
Parts of line	14		6		5		4		3		3		2	
Min. boom angle									15°		30°		35°	

For optimal use of the crane, a boom length of 34 meters will be employed, as shorter boom lengths result in higher lifting capacities.

The maximum length of the crane without jib and auxiliary jib is 50 meters. Since the load is not located in an area out of reach, there is no need to use the jib or auxiliary jib.

It is planned for the crane to carry loads between 20 and 25 tons, and to ensure project safety, only 75% of the maximum lifting capacity will be used. Based on the charts and dimensions of the silos, the boom length must be at least 31 meters. For optimal use of the crane, a boom length of 34 meters will be employed, as shorter boom lengths result in higher lifting capacities.

The closer the boom angle is to a vertical position, the greater the lifting capacity. Similarly, a shorter lifting radius increases lifting capacity. Based on this, a lifting radius of 7.1 meters, a boom length of 34 meters, and an angle of 78 degrees are selected. In this configuration, the maximum load that the crane can lift is 32 tons, with 75% of this being 24 tons.

For the second plan, it is assumed that the crane will lift the load from the center of the silo. Accordingly, the boom length is adjusted to 45.5 meters, and the boom angle is set to 70 degrees. The lifting radius will also increase to 15 meters. Based on the provided charts, the maximum load in this configuration is 14.1 tons. For additional safety, only about 75–80% of this weight will be lifted, which amounts to 10.575 to 11.28 tons. The table 10 shows maximum permissible load based on boom length and crane distance from load center of gravity.

The figure 15 presents a view of a crane, demonstrating its position relative to the silo. The boom is positioned 2.2 meters away from the silo. Additionally, the distance between the tip of the crane and the building is considered to be 2.1 meters.

The Table 13 shows condition of lifting plan B in this project.

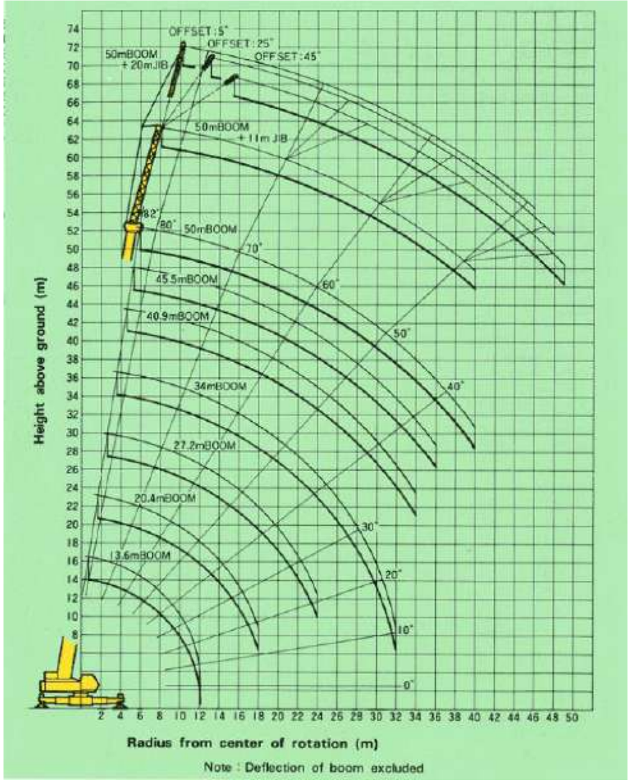

Figure 13. Graph of changes in crane boom length and its corresponding angle

Table 11

Crane Specifications

Boom Length	13.6m-50m
Jib length	11m-20m
Boom derricking Angle	-2-82
Boom derricking time	76sec
Boom Telescoping Speed	0.16m/sec

Table 12

conditions of lifting plan A

Lifting plan A	
crane info	NK-1200(120TON)
Lifting configuration	Main boom
Boom length	34m
Working radius	7.1m
swl	22ton
Height with jib	70m
Load Details	
description	Reinforced concrete parts
Dimension	3mx0.5mx5.8m
Center Of Gravity	Given ☐ Calculated ☐ Unknown ■
Calculation Loads	
Reinforced concrete parts weight	22ton
Extra weight(Hook, Gear,…)	2ton
Total Weight	24ton
Safety Factor	1.33
Crane Capacity Usage	75%
Routine Lift ■	Non Routine Lift ☐

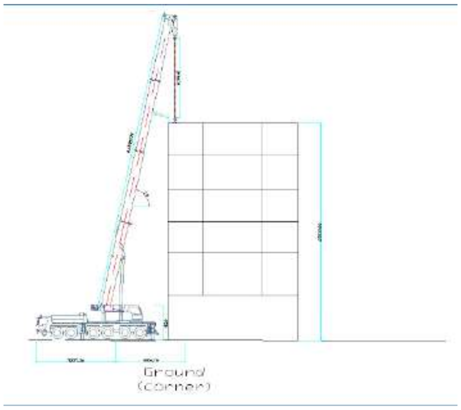

Figure 14. View of the crane in the lifting position of Plan No. 1 to pick up the concrete piece closest to the silo.

The figure 15 shows a crane. The crane's position in relation to the silo is depicted, with the boom one meter away from the silo. Additionally, the distance from the tip of the crane to the building is considered to be 3.8 meters.

The total loads of 24 tons and 10.5 tons represent the combined maximum load the crane can lift in the two presented scenarios. This load includes the weight of the hook and other accessories, which has been conservatively estimated at 2 tons. According to the provided chart, the actual weight of the crane hook is 0.6 tons.

Load Securing: The method of securing loads is critical as it affects the pressure exerted on the slings. The smaller the angle of the slings, the greater the pressure. For example, in some cases, a maximum angle limit of 45 degrees is enforced. Therefore, determining the proper angle during load lifting is essential to control the pressure on the slings.

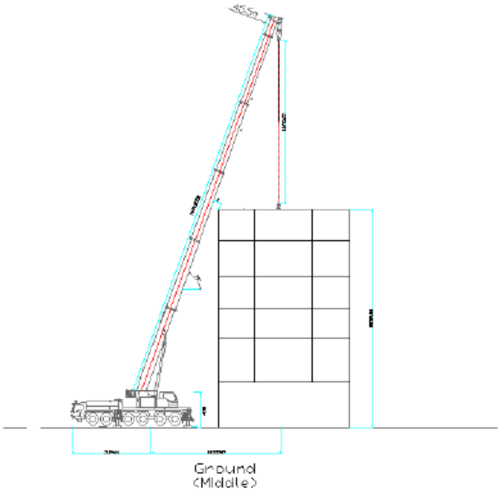

Figure 15. View of the crane in the lifting position of Plan No. 2 to lift the concrete piece at the farthest distance from the silo

Table 13
Condition of lifting plan B

Lifting plan B	
crane info	NK-1200(120TON)
Lifting configuration	Main boom
Boom length	45.5m
Working radius	15m
swl	10.5ton
Load Details	
description	Reinforced concrete parts
Dimension	3mx0.5mx2.26m
Center Of Gravity	Given ☐ Calculated ☐ Unknown ■
Calculation Loads	
Reinforced concrete parts weight	8.5ton
Extra weight(Hook, Gear,…)	2ton
Total Weight	10.5ton
Safety Factor	1.33
Crane Capacity Usage	75%
Routine Lift ■ Non Routine Lift ☐	

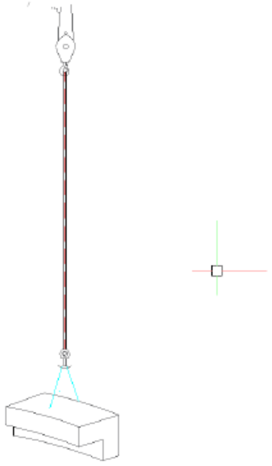

Figure 16. How to fasten and restrain a concrete piece with a crane hook

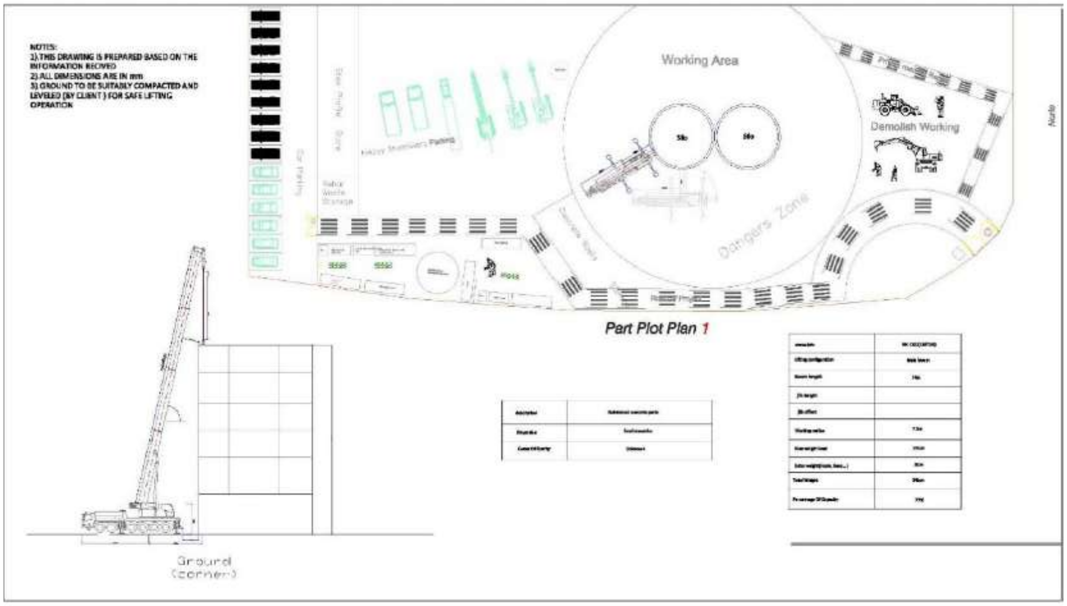

NOTES:
1) THIS DRAWING IS PREPARED BASED ON THE INFORMATION RECIVED
2) ALL DIMENSIONS ARE IN mm
3) GROUND TO BE SUITABLY COMPACTED AND LEVELED (BY CLIENT) FOR SAFE LIFTING OPERATION

Figure 17. Project lifting plan with 120-ton crane

9. Project Workshop Site Plan Design

The design and calculation method for the workshop site plan of this project were prepared based on the research of Mr. Emad Elbeltagi [30]. A site layout includes the placement of buildings, parking areas, storage zones, access roads, and temporary facilities. An optimal site layout ensures maximum utilization of available space, reduces project costs, minimizes material movement during construction, improves accessibility, enhances site security, and promotes workplace safety.

Every project has a unique site layout plan tailored to its specific variables. The most important and primary variable in site layout planning, which drives decisions regarding site logistics, is the size and actual location of the site. A list of the key variables influencing site layout is provided in the illustration.

Elements of Site Layout Planning: A well-planned site that includes all temporary facilities and auxiliary elements results in:

1. Increased productivity and safety.
2. Reduced space required for temporary construction.
3. Maximum utilization of resources.

Table 14
Effective tips for designing a project workshop plan website

No.	Description	Details
1	Fire Prevention	Fire is one of the main causes of damage at construction sites. Therefore, the presence of fire extinguishers is a necessity for any construction project.
2	Medical Services	A first aid kit is essential in construction projects. For remote projects, a well-equipped medical room with a doctor and nurse is important.
3	Safety Gear	Workers must use safety equipment such as safety shoes, helmets, gloves, and protective glasses.
4	Site Access	Easy access to the site improves equipment drivers' morale, reduces the likelihood of accidents, and saves transport time. For large projects, proper planning for road designs leading from nearby highways is necessary. Internal roads are also vital for smooth operations. Parking facilities for the owner, administrative and technical staff, and construction personnel must be planned in available spaces.
5	Site Map	It should outline project details and be displayed at the site manager's or project manager's office as well as at the entrance gate.
6	Traffic Guidance Signs	In large projects, these signs direct site traffic and prevent accidents.
	Display of Safety Rules and Workforce Policies	This can help eliminate disputes between labor and management.
	Emergency Routes and Underground Services	Emergency escape routes should be displayed on every floor as construction progresses. The locations of underground services must be identified to avoid damage.
7	Entrance	Adequate security at the site entrance is essential. All visitors' entries and exits must be recorded.
8	Lighting	A backup generator is necessary to provide site lighting.
9	Fencing	Site boundary fencing is important for security purposes.
10	Accommodation	In large construction projects, providing accommodation facilities for various project personnel is essential.
11	Offices	Offices should be located close to each other, adjacent to the site, and in a secure area. They should also be equipped with appropriate office supplies. The site offices typically include work offices, the general contractor's office, and the subcontractors' and consultants' offices.
12	Water and Sanitation	Providing water and sanitation facilities in appropriate locations for staff is essential.
13	Material Handling	Over one-third of construction operations involve material handling. Using appropriate equipment and advanced planning to reduce material handling can directly lower costs and save time.
14	Storage and Site Cleaning	Planning and reserving areas for storing materials is necessary to avoid multiple relocations.
15	Storage Locations	These are used for temporary or long-term storage of materials and equipment.
16	Covered Warehouses	Materials are stored here until use.
17	Stockpile Areas	These areas are used for short-term material storage close to the work area.
18	Site Cleaning	Cleaning is essential at the workplace, especially in areas generating significant waste. Regular waste disposal must be ensured.
19	Workers' Changing Rooms	These rooms provide appropriate spaces for changing clothes, washing, and resting during waiting periods.
20	Temporary Facilities	Recognizing the characteristics of temporary facilities before site layout planning is important. Key features include: - Compliance with safety and environmental regulations. - Reusability. - Ease of assembly and disassembly.

The table 14 presents the key considerations for proper site layout planning and the design of the workshop site plan.

Table 15
Requirements for equipping a construction project workshop

Facility No.	Facility Name	
1	Job office	*
2	Owner representatives office	*
3	Subcontractors office	*
4	First aid office	
5	Information and guard house	
6	Toilet on site	*
7	Staft/Engineer dormitory	*
8	Statt/Engineer family dormitory	
9	Labor dormitory	
10	Labor family dormitory	
11	Dinning room for labor	
12	Bathroom for labor	
13	Restroom for labor	
14	Equipment maintenance shop	
15	Parking lot for mechanics	*
16	Prefabricated rebar storage yard	*
17	Rebar fabrication yard	
18	Fabricated rebar storage yard	
19	Carpentry shop	
20	Storage yard for lumber	*
21	Storage yard for formed lumber	
22	Cement warehouse	
23	Batch-plant and aggregate storage	
24	Craft change-house	*
25	Sampling / Testing lab	
26	Pipe jointing yard	
27	Pipe storage yard|	
28	Welding shop	*
29	Parking lot	*
30	Tank	*
31	Long tenn laydown storage	
32	Machine room	*
33	Electrical shop	
34	Steel fabrication shop	*
35	Sandblast shop	
36	Painting shop	
37	Scaffold storage yard	*
38	Material warehouse	*

Table 16
Estimating the space required for temporary project facilities

Temporary Facility	Minimum (m2)	Average (m2)	Maximum (m2)
Craft change house per worker	0.09	1.02	2.7
Time office per office worker	5.4	8.7	13.5
Number of people per brass alley (with average area per person)	100 Person	175 Person	250 Person
Number of workers per parking space	1	0.37	4
Area required for each unit parking	22.5	30	36

Once the required temporary facilities have been selected for the site, their necessary sizes must be estimated. The sizing of temporary facilities is primarily determined by labor force requirements, estimated work volume, production rates, site space availability, and cost considerations. Some safety regulations and other criteria for determining the size of temporary facilities are explained in the Table 16, 17 and 18.

Table 17
Space required for temporary offices in the project workshop equipment

Office	Size Range (m²)
Project Manager	12 - 25
Construction Manager	9 - 14
Mechanical, Electrical, Civil Engineer per	9 - 11
Purchasing (total)	46 - 84
Schedule & Cost Control (total)	28 - 93
Accounting (total)	37 - 80
First Aid & Safety per Office	17 - 19
Clerical (total)	28 - 74
Estimator	11

Based on the tables above and the equation 3, the required space for the project's site facilities is calculated:

$$A_n = (Q_{max}/I_m)/q_n \tag{4}$$

Where: $Q_{max} = q_{daily} \times t \times k_{qdaily} = Q_{total}/T$

Q_{max}: Maximum estimated quantity in storage space;

I_m: Utilization index for materials;

q_n: quantity of materials can be stored per m²;

Q_{total}: Total quantity of materials required for the project;

q_{daily}: estimated quantity required per day;

T: construction period (not total project duration);

t: Average stock (days); and

k: Fluctuation factor

10. Conclusion

In today's world, with the aging of old structures and the development of modern construction technologies, demolition projects for obsolete structures have witnessed significant growth. While construction methods are popular topics in modern construction management, this paper delved into demolition methods in detail. At first glance, it may seem that blasting is the most common and suitable method for demolishing concrete structures. However, as demonstrated in this paper, other demolition methods, such as using diamond wire cutting and demolition with excavators, are simpler, cost-effective, and time-saving alternatives. Moreover, they offer higher safety levels.

Project Manager: 1 person → 1 room 18 m^2

Site Manager: 1 Person → 1 room 18 m^2

Construction Manager: 2 Persons → 1 room 18 m^2

technical office (Civil & Mechanical ENG): 4 persons → 1 room 36 m^2

$$\left.\begin{array}{l}\text{Schedule \& Cost Control: 1 person}\\ \text{Accounting: 1 person}\\ \text{Officer: 1 Person}\end{array}\right\}\ \text{1 room 18 } m^2$$

Worker: 20 Persons → 2 room for rest & Lunch 2*18 m^2

Concrete Demolish Team: 10 Persons → 1 room for rest & Lunch 18 m^2

$$\left.\begin{array}{l}\text{Wire rope team: 5 Persons}\\ \text{Drilling team: 5 Person}\end{array}\right\}\ \text{1 room for rest \& Lunch 18 } m^2$$

$$\left.\begin{array}{l}\text{HSE Manager: 1 Person}\\ \text{HSE ENG: 1 person}\end{array}\right\}\ \text{1 room 18 } m^2$$

Total Manpower: 53 Persons → Safety & Area Per Office 10*15 m^2 = 150 m^2

According Table 2:

Time office per worker → 53*13.5 m^2 = 715 m^2

Area Required for each unit car parking → 6*36 m^2 = 216 m^2

Area Required for each unit Pickup parking → 3*40 m^2 = 120 m^2

Area Required for each unit Excavator parking → 2*(30*10) m^2 = 600 m^2

Area Required for each unit Crane parking → 2*(30*10) m^2 = 600 m^2

Area Required for each unit Loder parking → 1*(20*10) m^2 = 200 m^2

Area Required for each unit Truck parking → 2*(15*7) m^2 = 210 m^2

Area Required for each unit Trolley parking → 1*(30*10) m^2 = 300 m^2

Based on the calculations, the site layout and workshop plan for this project shows in Figure 18.

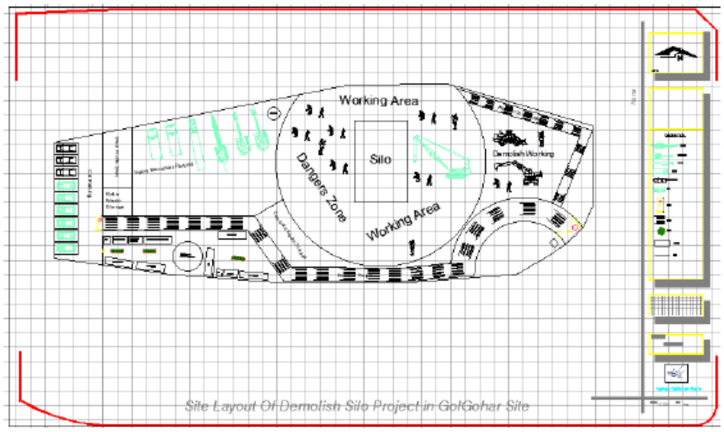

Figure 18 Site design map, project workshop plan

This study used a case study in Iran to analyze the demolition of a concrete silo by comparing various methods from cost, time, and safety perspectives using the Analytic Hierarchy Process (AHP). Time assessment was carried out using MSP software, while the costs for each method were estimated based on resources allocated to each operational phase in the Work Breakdown Structure (WBS). Safety evaluation combined AHP and DEA methods, gathering required data through questionnaires completed by domain experts. Results indicated that diamond wire cutting achieved the highest score among demolition methods. Additionally, according to silo modeling in SAP2000 software, single-stage silo overturning by removing primary columns was determined to be unfeasible.

A construction manager must have comprehensive oversight of all aspects of a construction project. As crucial as management and supervision during execution are, the feasibility study and selection of operational methods hold equal significance before construction begins. This paper aimed to cover essential aspects of demolition management from the initial phase (Phase Zero) through the project's final stages. It also presented a step-by-step approach to managing a demolition project through a case study.

Initially, all potential demolition methods were listed, considering the project’s constraints. This list was compiled using previous research and the experiences of construction managers. Each method was then scored and compared based on core criteria, including cost, time, and safety. Finally, the most suitable demolition method was selected.

A key advantage of the outlined methods is their adaptability to project-specific priorities; in AHP, users can create pairwise comparison matrices based on the relative importance of evaluation criteria. The case study demonstrated that the optimal method was diamond wire cutting. This paper comprehensively reviewed all concrete demolition methods, compared them, and provided a detailed explanation of each.

After selecting the demolition method, a lifting plan was created to optimize its execution. This highlights the need for construction managers to understand operational workflows fully before project commencement to direct progress effectively, avoiding unforeseen circumstances. The final stage involved designing the project’s site plan to maintain order and organization, an essential factor for an efficient workspace. The actual project outcomes, based on the chosen method, were then presented.

Key findings indicate that preliminary evaluations and selecting an appropriate demolition method significantly contribute to project success. In this case study, execution costs totaled 45,000,000,000 IRR compared to the initial estimated cost of 47,280,000,000 IRR, underscoring the impact of an effective site plan in cost reduction. Additionally, while the anticipated execution duration was 73 days, the project was completed in 63 days due to concurrent work fronts and efficient resource management.

Beyond reducing time and costs, this project achieved a remarkable safety record, with no casualties or financial losses due to accidents. Although the highest safety risk associated with diamond wire cutting involved lowering concrete pieces, precise calculations and lifting plans ensured the project's safety. At the time of writing, only the upper sections of the silos were demolished, with the demolition of remaining silo parts planned for subsequent stages.

Lastly, simplicity is a pivotal factor in the success of construction projects. The primary objective of construction managers is project success, and simplifying complex issues in construction methods can undoubtedly increase success rates. This paper was written with the aim of teaching complex issues in a simple manner. Its authors firmly believe that practical applications of the content discussed can significantly aid managers in demolition projects, ensuring success.

For enthusiasts in this field, further exploration of combining Building Information Modeling (BIM) and its impact on demolition method efficiency is recommended. Future research could compare BIM results with this paper’s findings to derive more accurate conclusions and propose effective solutions for demolition method management.

Acknowledgements

I would like to express my sincere gratitude to Mr. Rahman Ghadiri Javan, CEO of Keyhan Gostareh Gharb Company, for his significant assistance in writing this article, especially in the section on demolition methods. I would also like to thank Ms. Atena Abdollahi for her help in preparing the project's lifting plan. Finally, I wholeheartedly thank my dear wife Mrs. Zahra Zare, who has supported me throughout the process of writing this article and has always been a source of strength and encouragement for me to continue on this path.

References

[1] Hufbauer, G. C., and B. W. Severn. "The economic demolition of old buildings." Urban Studies 11.3 (1974): 349-351. https://doi.org/10.1080/00420987420080611 .

[2] Abudayyeh, Osama, et al. "Concrete bridge demolition methods and equipment." Journal of Bridge Engineering 3.3 (1998): 117-125. https://doi.org/10.1061/(ASCE)1084-0702(1998)3:3(117) .

[3] Patel, Ravi. "Demolination method & techniques." Int. J. Res. Sci. Eng. Manag.(nd). (2019).

[4] Assefa, Getachew, and Chelsea Ambler. "To demolish or not to demolish: Life cycle consideration of repurposing buildings." Sustainable cities and society 28 (2017): 146-153. https://doi.org/10.1016/j.scs.2016.09.011 .

[5] Baker, Hannah, Alice Moncaster, and Abir Al-Tabbaa. "Decision-making for the demolition or adaptation of buildings." Proceedings of the Institution of Civil Engineers-Forensic Engineering 170.3 (2017): 144-156. https://doi.org/10.1680/jfoen.16.00026 .

[6] Yuzbasi, Julide. "Experimental verification of full-scale silo structure demolition: Investigating successive column removal with finite element method and progressive collapse simulation through blast load." Structural Concrete 25.6 (2024): 4408-4427. https://doi.org/10.1002/suco.202400017 .

[7] Huang, Xieping, et al. "Failure analysis of underground concrete silo under near-field soil explosion." Tunnelling and Underground Space Technology 147 (2024): 105696. https://doi.org/10.1016/j.tust.2024.105696 .

[8] Mohammadi, Mohsen, et al. "Advances in Concrete Demolition Technologies: A Review of Conventional and Emerging Methods for Sustainable Waste Management." Eng 5.4 (2024): 3174-3191. https://doi.org/10.3390/eng5040167 .

[9] Keshavarz Mirza Mohammadi, Payam, Seyed Hamed Khalilpour, and Pooya Sareh. "Simulating the response of buried structures to external blast loads: methods, challenges, and advances." Engineering Reports 5.6 (2023): e12607. https://doi.org/10.1002/eng2.12607 .

[10] Wang, Tianqi, et al. "Time–cost–quality trade-off analysis for planning construction projects." Engineering, Construction and Architectural Management 28.1 (2021): 82-100. https://doi.org/10.1108/ECAM-12-2017-0271 .

[11] Thomas L. Saaty. Fundamentals of Decision Making and Priority Theory with the Analytic Hierarchy Process. New York: RWS Publications, 2000.

[12] Sánchez-Garrido, Antonio J., Ignacio J. Navarro, and Víctor Yepes. "Multi-criteria decision-making applied to the sustainability of building structures based on Modern Methods of Construction." Journal of Cleaner Production 330 (2022): 129724. https://doi.org/10.1016/j.jclepro.2021.129724 .

[13] Chen, Zhen-Song, et al. "Expertise-based bid evaluation for construction-contractor selection with generalized comparative linguistic ELECTRE III." Automation in Construction 125 (2021): 103578. https://doi.org/10.1016/j.autcon.2021.103578 .

[14] Gharouni Jafari, Kobra, Nozhat Sadat Ghazi Sharyatpanahi, and Esmatullah Noorzai. "BIM-based integrated solution for analysis and management of mismatches during construction." Journal of Engineering, Design and Technology 19.1 (2021): 81-102. DOI: https://doi.org/10.1108/JEDT-02-2020-0044 .

[15] Len Holm and E. John Schaufelberger. Construction Cost Estimating. London & New York: Taylor & Francis, 2021.

[16] Technical Regulations for Explosives and Rock Blasting in Mines No. 410. Islamic Republic of Iran, 2008.

[17] Jangl, Stefan, Vladimir Kavicky, and Michal Pilat. "Design of bridge blasting demolition." MATEC Web of Conferences. Vol. 352. EDP Sciences, 2021. DOI: https://doi.org/10.1051/matecconf/202135200002 .

[18] Lamond, Joseph F., et al. "Removal and reuse of hardened concrete." American Concrete Institute: Farmington Hills, MI, USA 26 (2001)..

[19] Mohajeri, M., and A. Ardeshir. "Analysis of construction safety risks using AHP-DEA integrated method." Amirkabir Journal of Civil Engineering 48.3 (2016): https://doi.org/10.22060/ceej.2016.608

[20] Badri, Adel, Sylvie Nadeau, and André Gbodossou. "Proposal of a risk-factor-based analytical approach for integrating occupational health and safety into project risk evaluation." Accident Analysis & Prevention 48 (2012): 223-234. https://doi.org/10.1016/j.aap.2011.05.009 .

[21] Wang, Ying-Ming, Jun Liu, and Taha MS Elhag. "An integrated AHP–DEA methodology for bridge risk assessment." Computers & industrial engineering 54.3 (2008): 513-525. https://doi.org/10.1016/j.cie.2007.09.002 .

[22] Walker, Kenneth K., et al. "Methods and procedural considerations in demolishing tall concrete chimneys." Journal of construction engineering and management 122.3 (1996): 223-230. https://doi.org/10.1061/(ASCE)0733-9364(1996)122:3(223) .

[23] Shalenny, Vasiliy. "Safe technologies for cutting reinforced concrete structures by means of diamond tools." E3S Web of Conferences. Vol. 97. EDP Sciences, 2019. https://doi.org/10.1051/e3sconf/20199703009 .

[24] Menon, Arathy H., and Geetha K. Jayaraj. "Comparative study of demolition methods." INTERNATIONAL JOURNAL 2.2 (2017).

[25] Vishwajeet Rajkumar Shedge. “Technological Innovations in Demolition Equipment and Methods.” International Journal of Research in Engineering, Science and Management 7.6 (2024): 35–39.

[26] Baragetti, Sergio, Marco Giustinoni, and Fabrizio Ranghetti. "Wire ropes with diamond beads for multi-wire machines optimization by means of DoE: Numerical models and choice of design parameters." Engineering Failure Analysis 143 (2023): 106826. https://doi.org/10.1016/j.engfailanal.2022.106826

[27] Denkena, Berend, Benjamin Bergmann, and Björn-Holger Rahner. "A novel tool monitoring approach for diamond wire sawing." Production Engineering (2021): 1-8. https://doi.org/10.1007/s11740-021-01087-7

[28] Guidelines for Lifting Plan Development. Workplace Safety and Health (WSH) Council, September 2023.

[29] NK-1200 Fully Hydraulic Truck Crane Lifting Capacity 120T. KATO.

[30] D. E. Elbeltagi. Site Layout Planning. Mansoura University.

Author Guidelines EditEdit Author Guidelines

GENERAL GUIDELINES FOR AUTHORS

Journal of civil engineering researches invites unsolicited contributions of several forms: articles, reviews and discussion articles, translations, and fora. Contributions should fall within the broad scope of the journal, as outlined in the statement of scope and focus. Contributors should present their material in a form that is accessible to a general anthropological readership. We especially invite contributions that engage with debates from previously published articles in the journal.

Submissions are double-blind peer-reviewed in accordance with our policy. Submissions will be immediately acknowledged but due to the review process, acceptance may take up to three months. Submissions should be submitted via our website submission form (see links above for registration and login). Once you login, make sure your user profile has "author" selected, then click "new submission" and follow the instructions carefully to submit your article. If problems arise, first check the FAQ and Troubleshooting guide posted below. If you are still experiencing difficulty, articles can be submitted to the editors as email attachments.

Each article should be accompanied by a title page that includes: all authors' names, institutional affiliations, address, telephone numbers and e-mail address. Papers should be no longer than 10,000 words (inclusive of abstract 100-150 words, footnotes, bibliography and notes on contributors), unless permission for a longer submission has been granted in advance by the Editors. Each article must include a 100 words "note on contributor(s)" together will full institutional address details, including email address. We request that you submit this material (title page and notes on the contributors) as "supplementary files" rather than in the article itself, which will need to be blinded for peer-review.

We are unable to pay for permissions to publish pieces whose copyright is not held by the author. Authors should secure rights before submitting translations, illustrations or long quotes. The views expressed in all articles are those of the authors and not necessarily those of the journal or its editors. After acceptance, authors and Special Issue guest editors whose institutions have an Open Access library fund must commit to apply to assist in article production costs. Proof of application will be requested. Though publication is not usually contingent on the availability of funding, the Journal is generally under no obligation to publish a work if funding which can be destined to support open access is not made available.

Word template and guidelines

Our tailored Word template and guidelines will help you format and structure your article, with useful general advice and Word tips.

(La)TeX template and guidelines

We welcome submissions of (La)TeX files. If you have used any .bib files when creating your article, please include these with your submission so that we can generate the reference list and citations in the journal-specific style

Artwork guidelines

Illustrations, pictures and graphs, should be supplied with the highest quality and in an electronic format that helps us to publish your article in the best way possible. Please follow the guidelines below to enable us to prepare your artwork for the printed issue as well as the online version.

Format: TIFF, JPEG: Common format for pictures (containing no text or graphs).

EPS: Preferred format for graphs and line art (retains quality when enlarging/zooming in).

Placement: Figures/charts and tables created in MS Word should be included in the main text rather than at the end of the document.

Figures and other files created outside Word (i.e. Excel, PowerPoint, JPG, TIFF, EPS, and PDF) should be submitted separately. Please add a placeholder note in the running text (i.e. “[insert Figure 1.]")

Resolution: Rasterized based files (i.e. with .tiff or .jpeg extension) require a resolution of at least 300 dpi (dots per inch). Line art should be supplied with a minimum resolution of 800 dpi.

Colour: Please note that images supplied in colour will be published in colour online and black and white in print (unless otherwise arranged). Therefore, it is important that you supply images that are comprehensible in black and white as well (i.e. by using colour with a distinctive pattern or dotted lines). The captions should reflect this by not using words indicating colour.

Dimension: Check that the artworks supplied match or exceed the dimensions of the journal. Images cannot be scaled up after origination

Fonts: The lettering used in the artwork should not vary too much in size and type (usually sans serif font as a default).

Authors services:

For reformatting your manuscript to fit the requirement of the Journal of Civil Engineering Researchers and/or English language editing please send an email to the following address:

researchers.services@gmail.com

Noted: There is a fixed charge for these mentioned services that is a function of the manuscript length. The amount of this charge will be notified through a reply email.

FAQ AND TROUBLESHOOTING FOR AUTHORS

I cannot log in to the system. How do I acquire a new user name and password?

If you cannot remember your username, please write an email to (journals.researchers@gmail.com), who will locate your username and notify you. If you know your username, but cannot remember your password, please click the "Login" link on the left-hand menu at homepage. Below the fields for entering your username and password, you will notice a link that asks "Forgot your password?"; click that link and then enter your email adddress to reset your password. You will be sent an automated message with a temporary password and instructions for how to create a new password. TIP: If you do not receive the automated email in your inbox, please check your SPAM or Junk Mail folder. For any other issues, please contact our Managing Editor,Kamyar Bagherinejad (admin@journals-researchers.com).

How do I locate the online submission form and fill it out?

First you need to register or login (see above). Once you are logged in, make sure the "roles" section of your profile has "Author" selected. Once you assign yourself the role of "Author," save your profile and then click the "New Submission" link on your user home page.

Once you arrive at the submission form page, please read the instructions carefully filling out all necessary information. Unless specified otherwise by the editors, the journal section to be selected for your submission should be "Artlcles." Proceed to the remaining sections, checking all boxes of the submission preparation checklist, and checking the box in the copyright notice section (thus agreeing to journals-researchers's copyright terms). Once the first page is completed, click "Save and Continue." The next page allows you to upload your submission. Use the form to choose your file from your computer. Make sure you click "Upload." The page will refresh and you may then click "Save and Continue." You will then proceed to a page for entering the metadata for your article. Please fill out all required fields and any further information you can provide. Click "Save and Continue." The next page allows you to upload supplementary files (images, audiovisual materials, etc.). These are not required, but if you wish to provide supplementary materials, please upload them here (do no forget to click "Upload." Then click "Save and Continue." This brings you to the final page of the submission form. Please click "Finish Submission" in order to close the submission process. You wil then be notified by email that your article has been successfully submitted. TIP: If you do not receive the automated email in your inbox, please check your SPAM or Junk Mail folder. For any other issues, please contact our Managing Editor, Kamyar Bagherinejad (admin@journals-researchers.com).

Why am I not receiving any email notifications from HAU?

Unfortunately, some automated messages from Open Journal Systems arrive in users' Spam (or Junk Mail) folders. First, check those folders to see if the message was filtered into there. You may also change the settings of your email by editing your preferences to accept all mail from [jcer] and related journals-researchers.com email accounts.

I am trying to upload a revised article following an initial round of peer-review, but I cannot locate where to upload the article. Where do I submit a revised article?

Follow the login process outlined above and when you successfully login you will see on your user home page a link next to "Author" for "active" articles in our system (usually it is only one article, but if you have mulitple submissions currently in our system, the number could be higher. Click the "Active" link and you will be led to a page that lists your authored articles currently in our system. Click the link under the column labeled "Status" and this will take you to a page showing the current review status of your article. At the very bottom of the screen, you will see an upload form under the heading "Editor decision." Here you may upload your revised article. An automated email will be sent to the editors and you may also notify them directly via email. You may then logout.

I successfully submitted an article; how long will it take for the editors to respond to me with a decision.

For all articles that are recommended for peer-review, the editors of JCER strive to notify authors of a decision within 4-6 weeks. You may contact JCER's Managing Editor, Kamyar Bagherinejad (admin@journals-researchers.com). if you have any questions relating to the review process and its duration.

For all other inquiries, please contact: Kamyar Bagherinejad (Managing Editor)

Privacy Statement

The names and email addresses entered in this journal site will be used exclusively for the stated purposes of this journal and will not be made available for any other purpose or to any other party.

Articles

Section default policy

Make a new submission to the Articles section.

Copyright Notice EditEdit Copyright Notice

Journal of Civil Engineering Researchers follows the regulations of the International Committee on Publication Ethics (COPE) and the ethical principles of publishing articles in this journal are set based on the rules of this committee, and in case of problems, it will be treated according to these rules.

This work is licensed under a Creative Commons Attribution 4.0 International License (CC BY 4.0).

In short, copyright for articles published in this journal is retained by the authors, with first publication rights granted to the journal. By virtue of their appearance in this open access journal, articles are free to use, with proper attribution and link to the licensing, in educational, commercial, and non-commercial settings

Privacy Statement EditEdit Privacy Statement

The names and email addresses entered in this journal site will be used exclusively for the stated purposes of this journal and will not be made available for any other purpose or to any other party.

Scholars Pavilion

Scholars Pavilion or **Scholars Chartagi** is a monument donated by the Islamic Republic of Iran to the United Nations Office at Vienna. The monument architecture is claimed by the Islamic Republic News Agency of Iran to be a combination of Islamic and Achaemenid architecture, although the latter clearly predominates in the decorative features, with Persian columns and other features from Persepolis and other remains from the Achaemenid dynasty. The Chahartaq pavilion form runs through the architecture of Persia from pre-Islamic times to the present.

Statues of four famous Persian medieval scholars, Omar Khayyam, Al-Biruni, Muhammad ibn Zakariya al-Razi and Ibn-Sina are inside the pavilion. This monument donated in June 2009 in occasion of Iran's peaceful developments in science.

J-Researchers